NUMERICAL INVESTIGATION OF MICRO-MACRO COUPLING IN MAGNETO-IMPEDANCE SENSORS FOR WEAK FIELD MEASUREMENTS

A Dissertation
Presented to
The Academic Faculty

By

Kwaku Eason

In Partial Fulfillment of the Requirements for the Degree of
Doctor of Philosophy in Mechanical Engineering

Georgia Institute of Technology
December 2008

NUMERICAL INVESTIGATION OF MICRO-MACRO COUPLING IN MAGNETO-IMPEDANCE SENSORS FOR WEAK FIELD MEASUREMENTS

Approved by:

Dr. Kok-Meng Lee, Advisor
School of Mechanical Engineering
Georgia Institute of Technology

Dr. Gary S. May
School of Electrical Engineering
Georgia Institute of Technology

Dr. Peter J. Hesketh
School of Mechanical Engineering
Georgia Institute of Technology

Dr. Mark G. Allen
School of Electrical Engineering
Georgia Institute of Technology

Dr. Suresh K. Sitaraman
School of Mechanical Engineering
Georgia Institute of Technology

Date Approved: August 12, 2008

ACKNOWLEDGEMENTS

There are many who have played a part in helping me to reach this point and I could never thank them all in a finite number of breathes, however, I would like to acknowledge some individuals that have been important in the path of me reaching this point. At the Georgia Institute of Technology, the list begins with my advisor, Dr. Kok-Meng Lee. He has demonstrated the patience, guidance, and support that I have needed to get me to this point and for that I am very thankful. In addition to my advisor, I would also like to thank my committee members who are all faculty at Georgia Tech. They include Dr. Gary May and Dr. Mark Allen of the School of Electrical and Computer Engineering. And also from my home department of Mechanical Engineering, I am grateful for the patience and support of Dr. Suresh Sitaraman and Dr. Peter Hesketh. Their volunteering to serve on my reading committee has made all the difference.

Outside the "walls" of Georgia Tech, I must also acknowledge my family for their continued support and encouragement. I think it worked! In the time that I have lived, they have been the only things constant in my life, and for that I am very grateful. A infinite thanks goes to my dear mom, Beryl J. Davis; my loving sister, Tala R. Davis; and my super-courageous brother, Kojo T. Eason. Thanks to my late father, Lewis Eason, as well. Gratitude is also due to my late maternal grandfather, Asa J. Davis, from whom the first seed of passion in learning was planted; and to my grandmother of manifolding love, Miriam J. Davis, who has kept us all in tact. My ability to get to this point has been made even more possible by them, as well.

To all the great teachers and fellow students in the past with whom the joy of learning was born and rigorously exercised within me, I am also grateful. I could never truly express how thankful I am to all of these lives that have intersected with mine. For now, it will have to suffice as being an acknowledgement that will stand as a permanent part of this document.

TABLE OF CONTENTS

LIST OF TABLES

LIST OF FIGURES

LIST OF SYMBOLS

symbol	description
scalars	
α	, Gilbert phenomenological damping constant, dimensionless
A_X	, magnetization exchange stiffness constant, (Joules/meter)
ε_0	, dielectric constant in vacuum, (Coulombs-Volts^{-1}meters^{-1})
μ_0	, the permeability of free space (Henries/meter)
μ_θ	, transverse magnetic permeability in a circular wire (Henries/meter)
K	, first anisotropy constant, Joules/meter^3
M_s	, saturation magnetization, (Tesla = Volt-seconds-meters^{-2})
$M_{d\theta}$	, transverse or circular equilibrium magnetization in cylindrical wires (Tesla)
M_{dy}	, transverse equilibrium magnetization in ribbon wires (Tesla)
m_e	, apparent electron mass (kilograms)
μ_0	, magnetic permeability in vacuum (Volts-seconds-amp^{-1}meters^{-1})
φ_D	, demagnetization scalar potential, (amps)
q_e	, electron charge (Coulombs)
J_0	, zero order Bessel function of the 1st kind
J_1	, first order Bessel function of the 1st kind
σ	, bulk electrical conductivity (ohms-m)$^{-1}$
ω	, MI sensor current source operating frequency
γ	, micromagnetic gyromagnetic ratio
γ_q	, quantum scale gyromagnetic ratio
R_{dc}	, *dc*-resistance (ohms)
c	, speed of light (meters/second)
L	, MI element axial length (meters)
L_z	, MI element periodic unit length (meters)
T	, temperature (K)
T_r	, reference temperature by T is normalized
g	, g-factor

I_s , source current amplitude (amps)

r_0 , cylindrical MI element radius (meters)

T_∞ , ambient temperature around MI sensor (K)

t , MI ribbon element thickness (meters)

δ_K , Kronecker Delta function

k , thermal conductivity (W/m-K)

c_p , specific heat (J/kg-K)

Ω_c , computational domain

h , convection coefficients (W/m^2-K)

Z_{SL} , single layer composite impedance (Ohms)

Z_{ML} , multi-layer composite impedance (Ohms)

$\hbar$, Planck's constant divided by 2π

q_i , thermal energy rate source per unit volume (W/m^3)

Z_c , circular wire impedance (ohms)

vectors

$\mathbf{M}$, magnetic dipole moment per unit volume or magnetization, (Tesla)

$\mathbf{E}$, Electric field vector (V/m)

$\mathbf{H}$, magnetic field intensity (A/m)

$\mathbf{J}$, current density ($Amps/meter^2$)

$\mathbf{D}$, electric displacement current (Coulombs)

$\mathbf{B}$, magnetic flux density, induction (Tesla)

$\mathbf{H}_T$, total effective field in micromagnetics equation (Amps/meter)

$\mathbf{H}_K$, effective anisotropy field (Amps/meter)

$\mathbf{H}_X$, effective exchange field (Amps/meter)

$\mathbf{H}_D$, effective demagnetization field (Amps/meter)

$\mathbf{e}_K$, preferred anisotropy direction

$\mathbf{M}_d$, equilibrium magnetization (Tesla)

$\mathbf{M}_\sim$, alternating component of the harmonic magnetization

$\mathbf{M}_R$, real component of the alternating magnetization (Tesla)

$\mathbf{M}_I$, imaginary component of the alternating magnetization (Tesla)

$\mathbf{H}_{\sim}$, alternating component of the harmonic magnetic field intensity (Amps/meter)

$\mathbf{H}_R$, real component of the alternating magnetic field intensity (Amps/meter)

$\mathbf{H}_I$, imaginary component of the alternating magnetic field intensity (Amps/meter)

$\boldsymbol{\rho}$, meshless method dilation parameter or support radius vector

$\boldsymbol{\varphi}$, harmonic magnetic field intensity phase angle vector (radians)

$\boldsymbol{\varphi}_M$, harmonic magnetization phase angle vector (radians)

LIST OF ABREVIATIONS

ac	alternating
dc	direct (or constant) current
HP-C or HPC	***Hp*-cloud meshless method shape functions**
FEM	**F**inite **E**lement **M**ethod
MLM	**M**eshless **M**ethods
MI	**M**agneto-**I**mpedance
MR	**M**agneto-**R**esistive
SQUID	**S**uperconducting **Qu**antum **I**nterference **D**evices
LLG	**L**andau-**L**ifshitz-**G**ilbert micromagnetic equation
EM	**e**lectro**m**agnetic
SI	**s**tress-**i**mpedance
MIR	**M**agneto **I**mpedance **R**atio
POU	**P**artition **o**f **U**nity
SPH	**S**mooth **P**article **H**ydrodynamics MLM shape functions
KDFP	**K**ronecker **D**elta **F**unction **P**roperty
RKPM	**R**eproducing **K**ernel **P**article **M**ethod
MLS	**M**oving **L**east **S**quares
MLSRKPM	**M**oving **L**east **S**quares **R**eproducing **K**ernel **P**article **M**ethod
EFG	**E**lement **F**ree **G**alerkin shape functions
NEM	**N**atural **E**lement **M**ethod MLM shape functions
RBF	**R**adial **B**asis **F**unctions
TPS	**T**hin **P**late **S**pline radial basis function
BC	**b**oundary **c**onditions
EBC	**e**ssential **b**oundary **c**ondition = Dirichlet boundary condition
MEG	**M**echano**E**ncephalo**G**ram
ISF	**I**nterpolating **S**hape **F**unction
NISF	**N**on-**ISF**
EOM	**E**quations **o**f **M**otion

SUMMARY

An awareness of magnetism to many is considered antiquated, however, as the size of magnetic specimens have begun to reach vanishingly small proportions, it is found that new knowledge continues to emerge. This new knowledge has subsequently led to new technologies that continue to improve the world in which we live while still showing vast potential areas of exploration. In this spirit, a strong and still growing interest has more recently developed in the use of small low-cost highly sensitive magnetic field sensors for applications ranging from small memory devices (e.g. iPods), to high bandwidth position identification, to biomedical applications requiring detection of subnano ($<10^{-9}$) magnetic fields. Among these sensors, the magneto-impedance (MI) effect sensor has demonstrated a potential absolute resolution on the order of 10^{-11} Tesla. Their behavior is known as the MI effect, which is a sensitive realignment of a periodic magnetization (driven by an *ac* external field) within small ferromagnetic structures in response to second external magnetic field intensity, to be measured. These devices represent a class of alternative low-cost sensitive field detectors in which interest has grown considerably in recent years. However, to date, design optimization of MI sensors, particularly, has involved heavy use of trial and error methods along with reduced models that decouple the micromagnetic and classical electromagnetic equations describing the MI effect. Additionally, these models are generally at odds with common operating conditions as well as an interest weak field behavior.

To promote an improvement in the design optimization process for weak field sensors like MI, in addition to treating a general space-time domain to include thermal effects, this research introduces a coupled nonlinear harmonic formulation and carefully

organizes a numerical modeling approach for solving it, ultimately, predicting MI responses, particularly, in the weak field regime, where previous models are *not* designed to be accurate. The fundamental difference in this numerical-based analytical model is the relaxation of assumptions leading to decoupling. To advance the proposed approach, this thesis is organized largely into three contributing components. (1) We begin with a general formulation of the equations of motion that describe the MI effect, including thermal diffusion, Maxwell, and the Landau-Lifshitz-Gilbert (LLG) equations along with appropriate boundary (and initial) conditions. (2) We selectively choose numerical tools that enable the solution to the equations using a desktop PC. The spatial discretization of the formulation is done using a recently developed tool known as meshless methods (MLM) that frames the problem within a discretization methodology that enables accurate results without the meshing complexities of more traditional finite element methods (FEM). In the case of time discretization, projection methods are utilized to treat the well known temporal instabilities in micromagnetics. Nonlinear solvers are considered carefully to minimize computational demands, as well. (3) In this approach, we are able to directly gauge the coupling effects of micromagnetic and classical dynamics. Influences that have been reported experimentally are examined using this numerical-based analytic model. The effects of temperature, frequency (on the switching mode), and *de*coupling are explored as well as the influence of a known equilibrium magnetic domain structure. Additionally, as a means of validation of the approach, comparisons to linear decoupled models as well as experimental data are made confirming the usefulness of this approach. In all cases discussed, the coupled nonlinear model emphasized in this thesis research is closer to reported experimental data.

The research in this thesis is expected to contribute to an improved understanding of MI effect sensors and provide a means to higher fidelity predictions for weak field responses, potentially extending their use to more applications requiring detection of weak magnetic fields. And although this numerical model is developed in the context of the MI sensor, the methods used here can also be extended to other weak field sensors like Fluxgate and small Hall Effect sensors.

CHAPTER 1
INTRODUCTION & BACKGROUND

In this first chapter, the problem that is the focus of this thesis research is introduced in more detail providing the motivation and its importance, as well as the details of the approach that is taken in this thesis work. With this, we begin with the problem background.

1.1 Background

A number of applications that require highly sensitive magnetic field sensors have emerged in recent years; for example, applications exploiting noninvasive detection of neural signals from the body. Magnetic field amplitudes from the body have been measured for fields as small as 10^{-15} Tesla (T), which have been detected from the brain [1]. While there are several devices capable of measuring magnetic fields, only a subset of them has demonstrated very high sensitivities and the sensitivity of these devices have correlated strongly with shrinking physical features. For magnetic sensors, these small physical features reveal interesting coupling between both commonly regarded large scale phenomena (e.g. voltage) and phenomena associated with these smaller length scales (with nano-sized grains, for example, or magneto-crystalline-anisotropy). Such behavior has become more apparent in the development of small highly sensitive magnetic field sensors, particularly in recent years. This thesis takes an interest in improving the ability to describe the unique coupling between the small scale (micro) and large scale (macro) that is becoming more frequently observed in the development of magnetic field sensors.

Up to the now, the ability to measure a magnetic field as small as those from the brain has only been demonstrated by one type of magnetic field sensor known as a superconducting quantum interference device (SQUID). However, the SQUID sensor operates on a principle known as *superconductivity* which requires very low temperatures to be observed. The phenomenon is triggered by a significant reduction in the kinetic energy of the atoms in the metallic crystal that enables electromagnetic forces to drive currents with virtually no resistance (atom collisions). However, in order to bring the system to the required low temperatures, costly auxiliary refrigeration equipment is necessary and such requirements can limit the applications for the devices. This motivates strong interest in the classes of alternative sensors that do not have these types of limitations.

Alternative magnetic field sensors include small Hall Effect, Magneto-Resistive (MR), Fluxgate, and Magneto-Impedance (MI) sensors. Although these alternative devices have not yet demonstrated an ability to detect fields as small as 10^{-15} T, some may not have far to go as they continue to demonstrate improved sensitivities in their development; for example, the small Hall Effect sensor has continued to show improvements in sensitivity, having demonstrated a resolution at least a couple of order of magnitudes smaller than the earth's magnetic field, known to be on average ~50 μT [2]. The Hall Effect sensor works by building a voltage potential difference in the direction perpendicular to the current flow due to Lorentz forces acting on the charge carriers due to the presence of a magnetic field, which is to be measured. The MR device is another type of sensor which has demonstrated a resolution on the order of 10^{-9} T [3]. MR sensors are very unique as they depend strongly on atomic scale phenomena like the

spin characteristics of the conducting electrons from the metal flowing through layers of thin films where the rotation of the magnetization within a layer, in the presence of an external field, changes the conductivity (or resistance) resulting in a detectable voltage change across the layers of the MR sensor [4]. Also, Fluxgate sensors have demonstrated an improved resolution currently demonstrated to be on the order of 10^{-9} T [3]. Fluxgate sensors operate by a strategic coordination of an *ac* external field and the measured external field; an axially oriented alternating field is created using a transverse *ac* current to drive the axial magnetization. Then, a super-imposed axial external magnetic field generates a detectable *ac* voltage measured transversely with a coil around the fluxgate device. Of interest in this thesis, the MI sensor has demonstrated an absolute resolution on the order of 10^{-11} T; unlike the Fluxgate, the MI sensor exploits two fields in perpendicular directions to measure one of the external fields. These alternative sensors are small, portable, and more cost-effective as they operate at room temperature.

Considering the MI sensor, more potential applications, for example, include detecting neural signals from the heart that have been measured at levels on the order of 10^{-13} T [1]. For such a critical bodily organ, the ability to detect its state in a more flexible way could be a considerable advantage. Considering such limitations for SQUIDs as discussed above, the alternative sensors summarized above are within the radar of the research community where they are actively being developed in hopes of alleviating these types of concerns. Table 1-1 summarizes reported resolutions of this group of highly sensitive magnetic field sensors (with references noted).

Table 1-1 List of *subnano*-sensitive magnetic sensors

sensor	*resolution*	*demonstrated applications*
Hall effect	10^{-7} T [5]	position
MR effect	10^{-9} T [3]	hard-disk drives
Flux Gate	10^{-9} T [3]	hard-disk drives
MI effect	10^{-11} T [6]	limited MEG
SQUID	10^{-15} T [1]	MEG

The MI effect sensor has demonstrated the second best absolute resolution among devices listed. However, a complete understanding of the high sensitivity and how it can be improved follows from a thorough understanding of its operating principle known as the MI effect. Based on the already demonstrated sensitivity, given an improvement of a couple of orders of magnitude, the MI sensor may find use detecting neural signals (noninvasively) from the heart. With even more sensitivity enhancement, also exploiting the ability to detect neural signals from the body, a potential technological application includes wearable robotic systems that can be designed to use detected brain signals for guiding (or amplifying) the subject's motion (or strength). Another perhaps more ready application for the MI sensor is ever shrinking hard-disc drive systems; for example, a computer or even an iPod type media storage device. Also, high bandwidth position measurements in induction motors are another application. Actually, one would be surprised at the list of already demonstrated applications for the MI and stress-impedance (SI) sensor, as it is quite extensive [6].

Therefore, this thesis explores an approach to further the understanding of the MI effect in order to promote the sensitivity enhancement of this class of sensors towards realizing more applications requiring weak-field measurements like those mentioned above. Next, we discuss the setup and operation of the MI effect. Following this, we

review prior and related works in the context of two focal points; first the research in the development of MI sensors; and because this thesis focuses on describing the MI effect using a numerical-based analytical model, a methodology known as meshless methods, used in this thesis, is also reviewed. In this thesis, sufficient details of the numerical tools deployed are discussed in the Appendix. Based on an understanding of these important contributions in both the MI effect sensor development and meshless methods, the problem description is discussed more specifically, highlighting the intended contributions from this thesis work in contrast to previous works. Finally, mapping the flow of information in this thesis, an outline of the chapters and their focal points is given.

1.2 Introduction to the MI Effect Sensor

Figure(s) 1-1 and 1-2 illustrate the basic setup and operating principle in the MI sensor. A current source flows through a small magnetic structure causing a transverse (circumferential) *ac* magnetic field in the wire. The *ac* field "drives" the magnetization causing a corresponding oscillation in the magnetization. Another external magnetic field H_e, the measured field, then modifies the alignment of the oscillating magnetization sensitively as shown in Figure 1-2. The realignment of the magnetization influences the amplitudes of the magnetization oscillation where both the current distribution (e.g. skin effect) as well as the inductive behavior changes. In general, the voltage potential along the axis of the wire and around the wire changes in the MI element, but, without loss of generality, this thesis work focuses on changes in the axial voltage, referred to as V_{MI}.

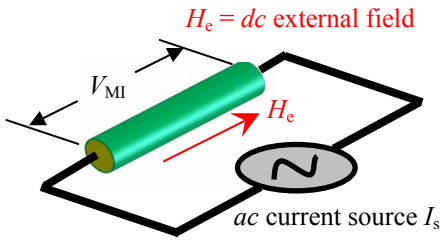

Figure 1-1. Illustration of MI sensor operation.

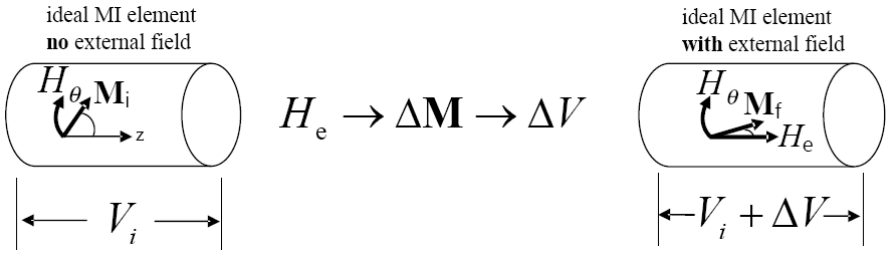

Figure 1-2. Illustration of the magneto-impedance (MI) effect.

1.2.1 Characteristics of the MI Sensor

The MI effect can then be understood as a sensitive realignment of a periodic magnetization where the periodicity is due to a current source I_s. Because the current source is fixed, it is sufficient (and commonly done) to consider only the impedance, Z. The impedance is often expressed in terms of the MI Ratio (in percent), which is a linear metric used to gauge the MI effect sensitivity and is typically defined as

$$\text{MIR}\,(\%) = 100\frac{Z - Z_{ref}}{Z_{ref}} \quad \text{where } Z = V_{MI}/I_s \tag{1-1}$$

In (1-1), Z is the surface impedance and Z_{ref} is a fixed reference impedance value that is usually taken at either the origin $Z(H_e = 0)$ or near the saturation value Z ($H_e \sim H_{sat}$).

Also, an important feature of the MI sensor is the use of a small magnetic structure, known as the MI element. In circular geometries, for example, the radial dimension is

typically on the order of microns (μm) while the longest dimension is typically on the order of several millimeters (mm) or even a centimeter. Figure 1-3 illustrates geometries commonly used in MI sensors. They have been developed primarily in variations of two basic geometries, cylindrical (with single material amorphous and composite metallic wires) and ribbon elements (with single material amorphous and tri-layered wires).

(**a**) Amorphous wire (**b**) Amorphous ribbon (c) Composite wire (d) Multi-ribbon

Figure 1-3. MI device element geometries (not to scale)

In this thesis, the geometries shown in Figure 1-3 (a) and (b) are investigated, however, extending the approach discussed in this work to (c) and (d) is fairly straight forward.

Some additional characteristics of the MI element material are also worth noting. In general, magnetic materials possess a characteristic known as *magnetostriction*. The mechanism results from the coupling that exists between forces generated by magnetic fields within the material and consequent strains (and stresses) in the crystal. Thus, when a small magnetic material is exposed to a magnetic field, a change in strain is observed. This behavior is characterized or "measured" by a parameter known as the magnetostriction coefficient, λ_s, and the smaller the value, the less the degree of this behavior is found. Good MI elements should possess small magnetostriction coefficients ($\lambda_s \sim 10^{-7}$) [7], as this mechanism tends to adversely effect the sensitivity of the MI sensor. In fact, this mechanism is at the root of another sensor known as the Stress-Impedance (SI) sensor [8], using the same configuration as in the MI sensor; however, strains/stresses are measured instead of magnetic fields.

1.2.2 Micro-Macro Coupling in MI Sensors

Given the combination of characteristics summarized above, it is found that MI sensors demonstrate a strong degree of coupling between micro-scale mechanisms and macro-scale. For example, magnetic anisotropy is a mechanism described by micromagnetics where the magnetization demonstrates a preferred direction within the crystal structure even in the absence of an applied external magnetic field. Anisotropy has been shown to sensitively influence measured MI voltages [9] [7] in both shape and scale of the MI voltage behavior. The condition of anisotropy can be controlled by way of experimental treatment to the wire, such as annealing methods, etc.

Another example of a micro-scale mechanism related to the MI effect is the role of domain walls within the magnetic material whose length scales are easily on the order of microns or even smaller [10]. Within a ferromagnetic material, the magnetization can vary spatially in such a way that takes on a lowest energy formation resulting in very narrow regions of transition between other regions of uniform magnetization orientations. These narrow transition regions are referred to as *domain walls*. They can play a significant role in the manner in which the magnetic permeability changes in response to an external magnetic field. According to researchers, the presence of domain walls are also believed to play a role in the observations made in MI sensors. However, unless treated phenomenologically, they must be treated by allowing the magnetization to be independent in space relative to the external field. This can not be achieved in a decoupled model.

1.2.2 Prior Considerations of Coupling

The MI effect is described by the combination of a macro-scale equation known as Maxwell's equation and a micromagnetics equation, which is highly nonlinear in both space and time. Thus, analytical models that describe the MI effect are generally nonlinear and demand assumptions in order to find closed form or linear solutions. Accordingly, in previous efforts to model the relatively young MI effect[1], simplifying assumptions have been made. However, the validity of some of the assumptions made in MI sensor research is often at odds with the actual conditions of operation that have been investigated; for example, in the configuration of the MI element with both a harmonic field and a steady *dc* field (measured field), linearization of the micromagnetic equation that describes the magnetization is appropriate only in near-saturation conditions [11], i.e. when the measured field is very large inducing small changes in the flux density **B**. However, most MI sensors do not operate in saturation, but rather in much smaller *dc* external magnetic fields. Nonetheless, solutions from the linearized model have been used in a large number of previous works [7, 12]. Further, even if previous operating conditions were consistent with saturation in MI sensors, a new interest in operating in a weak-field regime to exploit the high sensitivities would still require a more relaxed modeling approach than what has commonly been used.

To illustrate the degradation of the predictive ability of decoupled models in weak fields, Figure 1-4 shows experimental voltage data reported by Mohri *et al* [9] along with predicted voltages from a decoupled MI effect model presented by Usov *et al*. [7] (using reported *realistic* experimental material parameters and conditions). It is shown that

[1] The MI effect was first reported in the early 90's, which makes it younger than any of the other devices in Table 1-1.

when H_e is small (near the origin of the x-axis), very large errors are observed reaching as high as 221%! These observations suggest that inappropriate assumptions such those leading to decoupling can lead to larger errors between analytical models and experimental data, particularly, in the weak-field regime.

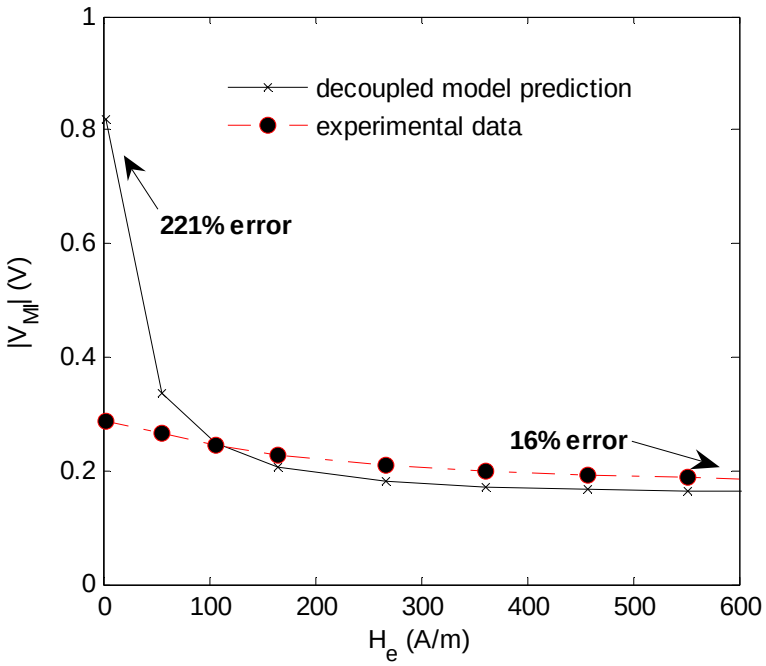

Figure 1-4. Illustration of large weak-field error with decoupled MI model.

Additionally, it is difficult to assess if any pertinent qualitative information is lost along with the observed quantitative disagreement, compromising the completeness of our understanding of the MI effect. This is a relevant consideration that has been demonstrated, for example, in previous MI effect models studying the effects of frequency in ribbon (thin rectangular) elements supposing rigid domain wall motion as the root source of the permeability changes with respect to the magnetic field. One investigation, in particular, by Vulfovich and Panina [13] using a decoupled analytical model relaxing the assumption of a rigid domain wall and, instead, allowing a flexible domain wall, arrived at a permeability dispersion model that tended toward more accurate

results when compared to experimental data. Thus, there is reason to take an interest in information from coupled nonlinear models that describe the MI effect, especially in the weak-field regime.

Then, in order to build up to discussing an approach to address these concerns, we next review prior and related work in MI sensors in more detail and in addition we review the numerical methodology known as meshless methods (MLM) that is deployed in the numerical-based analytical MI effect model emphasized in this thesis for investigating the effects of micro-macro coupling in MI sensors for weak field measurements.

1. 3 Review of Prior and Related Work

A study, by way of a numerical-based analytical model, of the effects of coupling in MI effect sensors, in the manner done here, can be decomposed into two primary areas. This work involves numerical-based modeling of MI sensors solving a more relaxed coupled nonlinear formulation and doing so using a spatial discretization methodology known as meshless methods (MLM). MLMs can be considered as a generalization of finite element methods (FEM) that are developed in such a way that *no mesh* is required for the computational domain. In this work, we have successfully implemented a point collocation (strong form) MLM formulation to solve the coupled nonlinear equations describing the MI effect, which saves considerable time. In choosing the MLM formulation used here, other formulations were considered and therefore the developments in all of those considered are also reviewed in this section.

The review of prior and related work is organized as follows: first, we review prior work in the development of MI sensors and related technologies. In this part, specifically, the discussion is separated into two sub-topics, namely the *modeling* and

experimental efforts, respectively. Then, the review of the work developing meshless methods is given. Also, we note that in Appendix A, a more in-depth review and summary of meshless methods is given, not only because it is a relatively new subject, but in order to facilitate an understanding of the choice of MLM formulations used here, as well.

1.3.1 Decoupled Modeling for MI Sensors

The MI effect has been explained on the basis of classical electrodynamics and micromagnetics (assuming negligible thermal effects) only. This understanding has enabled a direction to build predictive models for these sensors. One of the first MI element geometries studied was the single material amorphous MI element. Mohri *et al*. [14, 15] was one of the first researchers to study the cylindrical geometry experimentally. In [14], although no attempts were made to model the MI effect, the classical impedance relation by Landau and Lifshitz [15] was cited as providing at least a qualitative understanding of the experimental trends observed in the MI effect sensor.

Impedance Models

Landau and Lifshitz had previously derived the solution for the impedance in a cylindrical magnetic conductor [15], which reveals the dependence of the surface impedance, Z, on the bulk transverse magnetic permeability, μ_θ. In the context of modeling MI sensors, this early development suggested to many that what remains in understanding the MI effect is a relationship between μ_θ and the measured external magnetic field, H_e. In a similar order of development, the impedance in a magnetic ribbon conductor had also been derived by Kittel *et al*. [], both models having very similar forms.

Although this thesis research does not focus on the extended composite structures, we highlight some relevant works. In efforts extending beyond the single amorphous element, the impedance model for the cylindrical composite structure (Figure 1-1c) was derived by Usov *et al*. [12]. The multilayered ribbon structures (Figure 1-1d) have been studied intensely in MI sensor designs [16] [17] [18] [19] [20], as well. Analytical expressions for the impedance in a trilayer-ribbon structure has been presented in an analogous way to what has been discussed [21].

In this thesis research, we have also extended the impedance solution for the case of an arbitrary number of layers on the cylindrical MI element. This model enables first order observations of the effects of radial variations in parameters like anisotropy, motivated by experimental findings. The derivation of this model is presented in Chapter 3. The impedance equations so derived represent one part of a decoupled modeling formulation, where the magnetic permeability (which is a parameter on which Z depends) is known to depend on the measured external field H_e. More in-depth modeling efforts followed accordingly.

Permeability Models

With consideration of a specific transverse anisotropy direction, Menard *et al*. [22] presented a "rigorous" (numerical) model in round wires coupling the micromagnetics and Maxwell's equations. However, small amplitudes were assumed for the harmonic fields, which effectively linearizes the micromagnetics equation. The essential difference, compared to other decoupled closed form models, is then given by the solution to the coupled linearized system where exchange is considered to form the full set of linear differential equations.

A MI model for the case of axial and circumferential anisotropy in a cylindrical element was presented by Usov *et al*. [7]. This model involves the Landau-Lifshitz impedance model along with an effective transverse permeability model determined from the solution to the linearized Landau-Liftshitz-Gilbert (LLG) micromagnetics equation. The linearized LLG equation had previously been solved for limited cases by Gurevich and Melkov [11]. The solution to the linearized micromagnetics equation provides a magnetic permeability dispersion (frequency dependent) tensor model (and effective transverse permeability in some cases) as a function of the *dc* external magnetic field H_e.

Panina *et al*. [23, 24] presented a frequency dependent permeability model for the case of transverse anisotropy in both wires and films using a lumped parameter rigid domain wall model, and later a flexible wall model was also investigated by Vulfovich and Panina [13]. In these works, the solutions for **H** and **M** were solved independently of each other, as was done by Usov *et al*. and others. Machado *et al*. [25] also presented a frequency dependent lumped-parameter MI sensor model for the case of transversely anisotropic single ribbon elements, where rigid domain wall motion was also factored into the model, but using phenomenological parameters, similar to Panina *et al*. While useful, such an approach using phenomenological parameters deviates from a more purely analytical model that retains greater qualitative information to explain observations. The permeability model presented by Machado *et al*. was also used with the classical impedance of the ribbon structure in response to frequency.

Using an equilibrium energy approach, Yoon *et al*. [26] presented a lumped parameter real valued transverse permeability model (more useful at low frequencies) that predicts the qualitative effects of tension annealing on the anisotropy of the MI

element, which has been shown experimentally to influence measured MI voltages [14]. In this thesis work, we have also derived a similar real valued transverse permeability model that avoids the assumption of a small transverse field as made by Yoon *et al*. [26] and considering this difference alone, it is shown that relaxing this assumption leads to smaller permeability values in smaller *dc* external fields, roughly one order of magnitude smaller in this case. The derivation and comparisons are presented in Chapter 3.

In all the cases considered above, the analytical approach effectively utilizes an impedance model derived from the decoupled Maxwell equations (assuming a scalar permeability in most cases) along with a permeability tensor (from which an effective scalar is obtained) for modeling the MI effect. Further, a way to validate any modeling approach follows from the abundance of experimental research that has been done with MI sensors. The experimental data is relatively plentiful to provide parallel comparisons between the MI effect predictions and the data. In many cases, with the exception of when phenomenological parameters are introduced (for a more strict set of conditions) into the models, it is generally difficult to obtain good quantitative agreement with the resulting models, as will be shown. However, the amount of experimental data that is available proves to be very useful in building confidence in a predictive model by making comparisons. Therefore, we review relevant experimental work that has been reported on MI sensors that not only provides insight to understanding the MI effect, but also serves here as information to build confidence in the proposed numerical-based MI effect model.

1.3.2 Experimental MI Sensor Work

As previously mentioned, among the first of MI sensors studied experimentally was the cylindrical amorphous MI sensor also reported by Mohri, *et al*. [6, 14, 27], which was presented as a next generation of the magneto-inductive sensor, exploiting the large changes in the ohmic component of the voltages along with the inductive components. In another early work by this same research group, these devices were shown to detect magnetic fields on the order of 10^{-6} Oe (10^{-11} T) for *ac* fields[2]. In [14], the influence of magnetic anisotropy, as well as the source current frequency *f* were investigated for their influence on the MI effect. The influence of anisotropy was most directly demonstrated by the measurement of B-H curves for wires subjected to varying annealing tensions ranging from 2 kg/mm^2 to 40 kg/mm^2, where wires subjected to larger annealing tensions resulted in a more visible transverse anisotropy by visibly "harder" hysteresis curves. A likely explanation of what happens in this case is that the axially applied tension creates an effective shrinkage in the orthogonal dimensions (transverse and radial) due to Poison's ratio, and because the Co-based alloy has a negative (but small) magnetostriction, the resulting strain in the transverse direction generates an additional strain-related effective magnetic field which must be overcome by the external transverse field, or Zeeman energy, of the MI element. The result is a larger *remnant* field or larger value of the field required to demagnetize the material, and thus a "harder" hysteresis curve is observed. This data presented a direct observation of the correlation between micromagnetic parameters like anisotropy and the macroscopic measured voltage output. It is noted that the researchers that presented this work are also well known researchers in

[2] Typcially, the magnetic field intensity (**H**) is expressed in direct unit such as Oe (or A/m), but it is also standard to express a "magnetic field" in Telsa (T), given by multiplying **H** by the permeability in vaccum, μ_0.

this area and this serves to build confidence in using the data reported as a way to validate the numerical models computed here. In this thesis, particularly in circular amorphous wires, data is taken from these works to provide a means of comparisons to the numerical solutions computed here. Some of the experimental data is used in Chapters 3, 4, and 5.

Others have studied the single amorphous wire element experimentally, illustrating behavior under conditions such as effects of wire diameter (controlled by chemical etching) [28]. In this reported data, the MI effect was shown experimentally to diminish with decreasing etched diameter. In an effort to gauge thermal stability of MI sensors, researchers have also studied real-time temperature effects [29] [30]. In these studies, it was shown in one unique case for Co-based alloys that the MI effect is enhanced initially from room temperature up to a relatively low temperature (well below the Curie temperature), and then degrades upon further increase toward the Curie temperature. The Curie temperature is the temperature at which ferromagnetic materials become paramagnetic or weakly magnetized in which the induction **B** is linearly varying with the magnetic field intensity **H**, or in other words, the permeability no longer depends on the magnetic field. Motivated from these works studying thermal effects, the temperature relationship to the MI effect is also investigated in this thesis research where we discuss factors from the model contributing to this observation.

In parallel work, as cylindrical structures were introduced, an interest in MI thin film structures as MI elements grew because of the convenience of existing integrated circuits (IC) manufacturing technology. The technology enables better control of the micron and submicron dimensions of the MI element. With this development, the single layer ribbon

structures have also been studied experimentally as MI elements [31] [32] [33]. Similar to amorphous wires, earlier investigators like Panina *et al*. showed that the amorphous ribbon had very similar and analogous characteristics to the single material cylindrical amorphous wire. Beach *et al*. were also among earlier investigators to present experimental studies for MI ribbons, independently, showing similar behavior to their cylindrical counterparts in response to frequency and other parameters [32]. Also, Machado *et al*. presented experimental work for single MI element ribbon structures prior to his analytical model mentioned above [33]. Machado *et al*. emphasized the effects of 180 ^{o} Neel walls (domain walls) on the MI effect in ribbons. It is an interesting point that Machado was one of first to emphasize the notion that domain wall motion plays an important role in the MI effect, particularly, in ribbon structures, but only ascribing this view to the motion of the equilibrium domain walls that had been observed experimentally. As one of the few reports that provides nearly sufficient data to simulate the problem numerically, data from Machado *et al*. [33] is also used in this thesis research in Chapter 5, in the discussion of the effects of a domain structure in the amorphous ribbon MI element structure on the axially measured MI voltages. However, this conclusion of the role of Neel walls is contrary to what some other researchers believed, alternatively believing that domain wall motion was sufficiently dampened [34] or that there may be no significant domain structure at all [7].

Still, the MI performance in thin films has been shown to depend on analogous parameters, including anisotropy and we may say at this point "possibly" a domain structure. In fact, in this thesis research, it will be shown that domain walls play a significant role in the MI effect. Considering all of the results including our own, it

depends on a number of factors including the operating conditions, material parameters, and geometry. The ribbon structures have, however, demonstrated lower sensitivity than their cylindrical counterparts [35]. Similarly, these structures have more or less been developed primarily using experimental-based trial and error techniques along with decoupled closed form models like those discussed in the previous section.

Although not modeled in this thesis research, composite MI element structures have also been studied experimentally. The cylindrical wire has been modified as a combination of a cylindrical core with a single outer layer of a different metallic material; usually one is magnetic and the other is nonmagnetic [20], but also conductive. The ribbon structures have been studied in tri-layered structures, which were shown experimentally to be the optimum number of layers for stronger MI effects [36]. The composite structures have also demonstrated higher MI ratios, compared to that of single amorphous structures. In fact, the composite cylindrical structures have demonstrated among the highest values for the MI ratio presented experimentally [20], reaching values on the order of 1000s of %, thus far.

In addition to the configurations discussed above, alternative configurations have also been investigated experimentally in MI sensors. One alternative configuration uses a MI element with a surrounding coil (similar to a secondary coil in a Fluxgate sensor) used to detect the circumferential potential variation with the application of a *dc* external field [37].

Also in composite structures, crystalline magnetic properties have been found experimentally to sensitively influence the MI effect. This observation has been shown to be linked to the magnetic softness ascribed to the nano-sized grain structure [38]

within the material. The grains are the regions of homogeneous crystalline structure. As these regions are reduced in size, the accompanying energies that oppose moving neighboring domains are reduced. Such effects tend to reduced the effective anisotropy of the material, increasing the sensitivity (and softness) of the material to externally applied magnetic fields. These crystalline properties of interest can be controlled experimentally in MI elements, for example, by thermal annealing and/or adding non-reacting agents during metallic deposition to control grain size directly [39]. These methods are also examples of controlling micro-scale features experimentally that influence sensitively an observable macroscopic variable of interest, the voltage drop across the MI element.

Additionally, because the MI effect is coupled to magneto-elastic effects, it turns out that magneto-impedance elements also demonstrate an analogous highly sensitive mechanism known as the stress-impedance (SI) effect, which is the result of a voltage change as a result of an applied stress across the SI element axis. This sensitivity makes the MI effect applicable to stress/strain measurement applications. This topic is also one of intense investigation [40] [41] [6] . The focus, however, in this thesis remains with MI, as opposed to SI sensors.

1.3.3 Meshless Methods

Meshless methods (MLM) are a more recently developed generalization to the more classical finite element methods (FEM). The primary difference between the two approaches is that MLMs do not need a mesh and uses nodes or points exclusively to approximate a computational domain. MLMs can be generally broken into two classes: *weak* and *strong* formulations [42]. A weak formulation is an integral formulation of the

equations of motion that has the advantage of reducing the maximum order of the differential equations solved where even ordered systems are reduced by a factor of ½. Alternatively, strong formulations (point collocation) are explicit and involve the discretization of the explicit equations of motion, as opposed to a weakened integral formulation. Although higher derivatives are required in a PC formulation, the method is generally much faster than a weak formulation. In studies comparing these approaches in MLMs (weak *vs* strong), weak formulations have been shown to be very computationally intensive [43], even compared to FEM. Strong formulations have been developed successfully in MLMs that result in very good accuracy and much improved efficiency compared to weak MLM and FEMs, and this thesis successfully deploys one of them in a point collocation formulation to solve the coupled nonlinear equations of motion describing the MI effect.

Then, in this section, the research on MLMs is reviewed. We point out that although one MLM formulation known as the *Hp*-Cloud formulation is chosen in most of the problems discussed in this thesis, many MLM shape functions were considered before making this selection. To provide more insight into all the shape functions considered in this work, in which both weak and strong formulations were considered, the research development of both types are discussed here.

The Smooth Particle Hydrodynamics (SPH) MLM shape functions is considered one of the first presentations of an MLM formulation. It was originally proposed by Gingold and Monaghan [44]. The formulation constructed shape functions without a mesh, only using nodes, with strictly compact radially vanishing weighting functions. The original introduction was applied to astrophysical domains without practical finite boundaries. In

general, one of the characteristics of the resulting SPH shape functions is a lack of possession of what is known as the Kronecker Delta function property (KDFP), i.e. non-interpolation (see Appendix A). The resulting shape functions are, however, well suited for weak formulations without physical finite boundaries or use with strictly natural-type boundary conditions. And although this formulation is recognized as one of the first successful implementations of MLMs using compact weighting functions strictly, some of its weaknesses were later identified and improved upon by other researchers.

One important improvement to the SPH formulation was introduced by Liu, *et al*., and the resulting MLM formulation is known as the reproducing kernel particle method (RKPM) [45]. One of the significant improvements by this method was the augmentation of a *correction* function that restores the "reproducibility" of the shape functions, enabling the *reproduction* of any desired order polynomial. This formulation actually supersedes the demands of the original problem in the SPH, which was a lack of the POU condition, particularly, near the boundaries of the computational domain.

At this point, a remark is in order regarding the concept of *reproducibility* in MLM shape functions. MLM shape functions are not pure polynomials, but rather involve a combination of polynomials and (typically) compact weighting functions. In this case, we may say that the resulting shape functions can "reproduce" polynomials, but are not themselves polynomial basis functions as in FEM shape functions using LaGrange interpolating polynomials. This is discussed in more detail in Appendix A.

Lui *et al*. also presented the moving least square reproducing kernel particle method (MLSRKP) [46]. This formulation can be viewed as a hybrid between a kernel formulation and what is known as a moving least squares (MLS) formulation. As in all

MLS formulations, this formulation naturally includes the polynomial reproducibility characteristic, as well. One of the key improvements in this method, though not explicitly discussed in the introduction of the formulation, is that derivatives of the shape function do not need to be computed, but rather can be approximated well using the information used to construct the shape functions. This characteristic is not unique to the MLSRKPM, but is actually a property of a properly constructed MLS formulation and is exploited in other shape function formulations, as well [47]. In this work (see Appendix A), we show that another improvement resulting from this observation is the ability to approximate the Kronecker Delta Function property well on the boundaries enabling its use without special treatment in problems with essential boundary conditions. This is in contrast to what is done, generally, using the Element Free Galerkin (EFG) formulation, for example. The resulting shape functions in both these formulations are also designed for weak formulations and generally lack the KDFP over the entire computational domain.

In contrast to the kernel methods, the moving least square (MLS) formulation is another very commonly used MLM formulation. One of the first MLS formulations presented in MLMs was proposed by Lancaster and Salkauskas [48]. However, in this work, the study was with surface approximations and not solutions to boundary value problems (BVPs). As a result, very much like the originally proposed SPH, extensions and potential improvements, in the context of solving BVPs, were later identified and investigated by researchers.

A subsequent MLS-MLM formulation (also mentioned earlier) was the Element Free Galerkin (EFG) method. It was originally proposed by Belytschko, *et al*. [49] as an

improvement to the Diffuse Element Method, which was proposed by Nayroles, *et al*. [50].

The MLS based *Hp*-Cloud meshless method shape functions were introduced by Duarte and Oden. [51]. This formulation is unique because it is suitable for both a weak formulation as well as a point collocation (PC) method. Because this method can be used in a PC formulation, it constitutes a truly meshless method. This is because although in weak MLM formulations, only nodes are used for the shape functions, integration must be performed, and therefore some form of a grid must be introduced to numerically solve the problem. Also, treatment of essential boundary conditions is the same as in finite difference approaches, which greatly simplifies the formulation. Based on the earlier remarks regarding derivatives in MLS schemes, derivatives can also be approximated without the need to explicitly calculate them. We exploit this characteristic in this work using the *Hp*-Cloud shape functions, particularly. We also derive this characteristic for the *Hp*-Cloud formulation in Appendix A.

Although kernel methods and MLS formulations are commonly used in MLMs, there are alternative approaches that have been successfully developed. The Partition of Unity (POU) is one such method proposed by Babuska and Melenk, *et al*. [52]. The uniqueness in this approach is the deviation from the use of polynomial basis functions to include basis functions that factor in the behavior of the problem being solved. The advantage is potentially faster convergence of the solution when compared to using polynomial basis functions for problems in which there is knowledge of the solution. This approach also naturally leads to a way to deal with discontinuities.

As mentioned before, interpolation over the entire computational domain is a rare characteristic to obtain for the methods mentioned above, especially when using polynomial basis functions beyond the 1D domain. One way around this is the use of *radial basis functions* (RBFs) [53] [54] [55] . These functions can be used to construct interpolating partitions of unity, but they generally lack compactness, making them more suitable for point-collocation formulations (or lengthened weak formulations). In this work, we also present a simple method we have developed to transform shape functions like these into smoothly vanishing interpolating compact shape functions using what we refer to as an *a posteriori compaction* transformation (this is only discussed in Appendix A). This makes these shape functions more useful in weak formulations.

Lui *et al*. have successfully implemented interpolating shape functions using RBFs to solve BVPs [56]. Other interpolating formulations include the natural element method (NEM), utilizing Veronoi cells to construct the interpolating shape functions [57] [58]. Again, the difference in these formulations is the ability to interpolate naturally over the *whole* computational domain, contrary to the previously mentioned kernel and MLS formulations.

Part of the motivation to use MLMs is to frame the MI sensor problem in such a way that in any future works, more of the advantages of MLMs can be realized. With this, automatic adaptivity is important. Nodal adaptivity in MLMs has also been developed successfully by researchers. Liu, *et al* [59] has implemented a scheme for PC formulations using RBFs. Li and Lee have developed a fully automated adaptive nodal scheme for weak MLMs exploiting shape function properties to implement convergence measures [60]. These methods enable fully automated adaptivity of the nodes much more

easily compared to FEM. These contributions help to more fully realize one of the key benefits of MLMs…no meshing.

All of these methods have been implemented and demonstrated successfully solving numerous BVPs. Development continues in the direction of improving MLMs, however, they have demonstrated (as well as been proven rigorously) as robustly convergent, and in many cases, more accurate than FEM, while also demonstrated as suitable for the use of fully automated nodal adaptivity. For these reasons, the methodology is chosen as the means to discretize space in problems solved in this thesis research.

1.4 Problem Description

Given the landscape summarized above, it is emphasized that the assumptions made in prior modeling works for MI sensors are consistent with saturation (i.e. large external fields) and thus are generally contrary to behavior in weak fields. The assumptions consequently decouple the core equations of motion describing the MI effect, and thus weaken the descriptive ability of the observed small and large scale coupling phenomenon in MI sensors, particularly in the weak field regime. Also, if behavior is unique for some configurations in the weak-field regime, decoupled models loose this information. Consequently, MI sensor development has relied heavily on experimental-based trial-and-error techniques to build the sensors. Given these observations, the advantages of MI sensors are still potentially under-exploited because of under-descriptive models and relatively costly design methods. An improvement in the ability to predict MI responses could be useful in providing a more accurate description in the weak-field regime and thus a better understanding of the behavior of these devices. For these reasons, we present work from this thesis research towards closing this gap between

analytical MI sensor model predictions and experimental data that will not only be useful for the optimization of MI device designs, but other cost-effective devices listed in Table 1-1, as well, such as Fluxgate sensors and small Hall Effect sensors.

1.4.1 How This Work Contributes to MI Effect Research

One can summarize the prior and related work on MI sensors above by saying that the current understanding of MI sensors has generally come from three main types of activities 1) experimental 2) theoretical and 3) numerical, as illustrated in Figure 1-5 below.

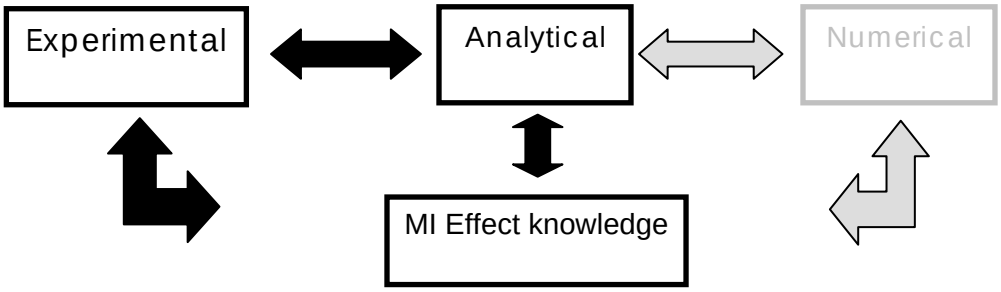

Figure 1-5. MI sensor development research activities.

However, up to this point, *most* of the efforts in studying MI sensors have fallen largely between 1) and 2). Thus, the contributions from this work follow from a focus on a relatively largely under-utilized activity, namely, numerical-based analytical studies of these small relatively young sensors. In this thesis, it will be shown that such a tool not only improves the ability of predictions by analytical models (particularly well below saturation fields), but also enables an improved understanding of the MI effect that is only afforded by using a relaxed numerical-based model to study these devices.

1.4.2 Numerical Considerations

In order to directly allow more relaxed conditions in the coupled nonlinear equations of motion, numerical methods offer promising added value and serve as an important concept in the work presented here. The objective of this thesis research is then two-folded:

1. To combine a more general set of equations including micromagnetics, classical electrodynamics, and thermal diffusion, while preserving coupling in a compact formulation that enables an extended ability for the performance prediction of devices like MI that captures the linkage between both experimentally observed small scale parameters and large scale variables of interest such as voltage.
2. Develop an accurate, efficient, and effective *numerical* formulation using meshless methods along with other numerical tools for solving the set of equations that describe MI type field sensors, while also being easily extendable to other devices, as well.

Considering the potential advantages of MLMs, it is of interest to pose this problem in the framework of a numerical methodology (MLMs) that can potentially be more useful in more general micromagnetic problems, for example, allowing fully automated nodal adaptivity to be implemented. Also, because of the cross-disciplinary nature of MI sensors including heat transfer, classical electrodynamics, and micromagnetics, an "off the shelf" FEM package is not a convenient option to solve the coupled system. Therefore, our approach is to build a customized numerical model using MATLAB code to solve the equations of motion. Further, all of the computations are performed on a desktop PC.

Careful consideration has been given to an approach to solve the system of equations numerically, that minimizes both computational resources on a desktop PC, and time, as will be shown in later discussions. Specifically, the meshless method is deployed to treat space discretization only. Because the equations are nonlinear, a nonlinear solver is also needed; and as the number of degrees of freedom becomes large, it is shown that the use of a quasi-Newton method provides advantages over the more classical Newton's method. This will be shown in the discussion of the effects of Neel walls on the MI effect in Chapter 5. In general, the treatment of time is not trivial for the set of equations being solved in this thesis. Simple methods are implemented known as projection methods [61] (applicable to the micromagnetics equation) in conjunction with a second order Newmark integration scheme. These methods are discussed in more detail in the Appendix.

Given these considerations, a numerical investigation of the effects of coupling is presented in this thesis, where the format of the discussion is summarized next.

1.5 Organization of Thesis

To present the thesis research undertaken here, this thesis follows the given flow of information: In this chapter, we have given a background of the problem addressed in this thesis, reviewing prior and related works aiding in defining the problem considered here.

Next, *Chapter 2* organizes, in a general fashion, the equations of motion (EOM) and relevant boundary conditions that describe the MI effect. First, the general equations including electrodynamics, micromagnetics, and thermal diffusion equations in the space-

time domain are given. Following this, a coupled nonlinear harmonic formulation is introduced, originally introduced in this thesis research [62], for modeling the MI effect.

In *Chapter 3*, we consider approaches to solving the equations of motion, examining two of the three approaches considered overall in this thesis research. We introduce incremental extensions in some decoupled models. The approach of decoupling is primarily used in this thesis as a basis for comparison to coupled nonlinear models emphasized in this thesis research, while the more general space-time modeling approach is also considered to study the MI effect and build an improved understanding the characteristics of the general equations of motion describing the MI effect.

Observations made in Chapter 3 motivate the third approach emphasized in this thesis research and is used in subsequent chapters, where we make efficient use of a coupled nonlinear harmonic formulation that will be shown to provide improvements in describing the MI effect, particularly in the weak-field regime. The formulation preserves nonlinear coupling, while eliminating the time variable t to improve computational efficiency. Additionally, the work from this particular discussion has been presented (published) in [62].

In addition to improvements in predicting the MI effect and improving the understanding of the costs of decoupling, in *Chapter 5*, the nonlinear coupled harmonic formulation is also used to study some effects that are not directly accessible in decoupled models. In particular, we investigate the effects of experimentally observed magnetic domain structures on the MI effect. The work in this discussion has been accepted for publication, as well [63].

Finally, Chapter 6 summarizes the key observations and contributions from this thesis research. Suggestions for future work are also discussed.

CHAPTER 2
MI EFFECT EQUATIONS OF MOTION

In this chapter, the equations of motion that describe the thermo-electro-magnetic behavior of MI sensors are organized. All of what is discussed in future discussions draws from the set of equations organized here.

The format of this chapter is as follows: first, we summarize the assumptions made that lead to the use of the final equations for MI sensors. Then based on the assumptions, the general space-time equations of motion are organized. Following the space-time formulation, we introduce a coupled nonlinear harmonic formulation used in this work that will be shown to also demonstrate an improved ability to describe MI effect sensors compared to decoupled harmonic models.

2.1 Assumptions for MI Effect EOM

The equations of motion, as used here, are built on a foundation of assumptions upon which the equations are considered appropriate. Recall that MI elements typically possess at least one mesoscopic (small) length scale dimension on the order of microns or smaller. The role of dynamics within this dimension plays a crucial role in the behavior of these devices. Therefore, a modeling formulation must be consistent with behavior on this length scale, at least. This observation enables the admission of what is known as a micromagnetics formulation that describes the magnetization **M** in small structures with good "resolution" with respect to influences from small scale mechanisms. With this understanding, the assumptions for modeling MI sensors are summarized next, followed by an organization of the equations of motion ultimately leading to a more general

coupled nonlinear formulation that enables the effects of fully coupling the micromagnetics formulation and classical electrodynamics to be directly investigated in this thesis research.

The assumptions for modeling MI effect sensors in this work include:

1. The minimum length scale of variations in the fields involved (**H** [magnetic field intensity], **M** [magnetization], φ_D [demagnetization scalar potential], and T [temperature]) in the MI sensor is large compared to characteristic atomic length scales, making continuum approaches allowed. This assumption also influences the way in which the thermal diffusion equation is treated, namely, using a bulk thermal conductivity, k. For extremely small dimensions, surface effects become appreciable and these nano-sized effects must be accounted for in the determination of k [64]. We assume the bulk value applies.
2. Assuming (1), the operating frequencies are low enough (or the conductivities are high enough) to satisfy quasi-static conditions, i.e. $2\pi f << \sigma/\varepsilon$ where f is the operating frequency; σ is the bulk electrical conductivity; ε is the dielectric constant. Based on this, displacement currents given by **D** are ignored. **Note**: For the materials more commonly considered in MI sensors, it is shown in this chapter that this condition is well satisfied, although if dielectrics are to be considered, then this assumption may not be appropriate.
3. The wavelengths of the fields involved are large compared to the length of the mean free path of conducting electrons. This assumption enables the linear approximation given by Ohm's law; $\mathbf{J} = \sigma\mathbf{E}$. **J** is the electrical current density and **E** is the electric field.

4. Although length scales of the variations are assumed sufficiently large for continuum approximations, they are still assumed small enough for the admissibility of micromagnetics formulations to characterize spatial distributions of the magnetization, **M**, directly. It is noted that this key assumption is what is not fully exploited in previous MI sensor models as spatial dispersion (independent **M** distributions in space) is assumed appreciable in this work, which means that the **M** is not generally proportional to **H** in space.
5. Assuming (4), and based on ample experimental data, contributions from magnetoelastic effects (and stress) are neglected based on the assumed use of near-zero magnetostriction materials (and annealed treatments) in MI elements. In this work, two particular amorphous MI element geometries are considered where this assumption has been shown to be valid.

In short, we are allowing a continuum approach, but on the smallest admissible length scale, which provides a finer "resolution" for observing the behavior of MI sensors.

2.2 Space-Time Equations of Motion

Consider the example cylindrical MI element geometry shown in Figure 2-1, where an alternating current is forced axially through the MI element establishing an axially directed *ac* electric field which also corresponds to a circumferentially oriented *ac* magnetic field, ($\mathbf{H}_\theta$=$\mathbf{H}_S$ in diagram). The additional application of a *dc* (or steady) external field H_e along the axis of the wire influences a steady state condition locally in the magnetization, **M**, within the ferromagnetic structure that ultimately influences the dynamics of the system, as well. The local orientations of the magnetization are known to influence the MI effect through such effects as anisotropy and domain structure. Using

the field solutions that are influenced by effects such as these, a further interest in this problem is to also predict the output voltage (or impedance) across the length L, of the MI element in response to the *dc* external magnetic field H_e while considering such mechanisms such as temperature, anisotropy, exchange, and domain structure.

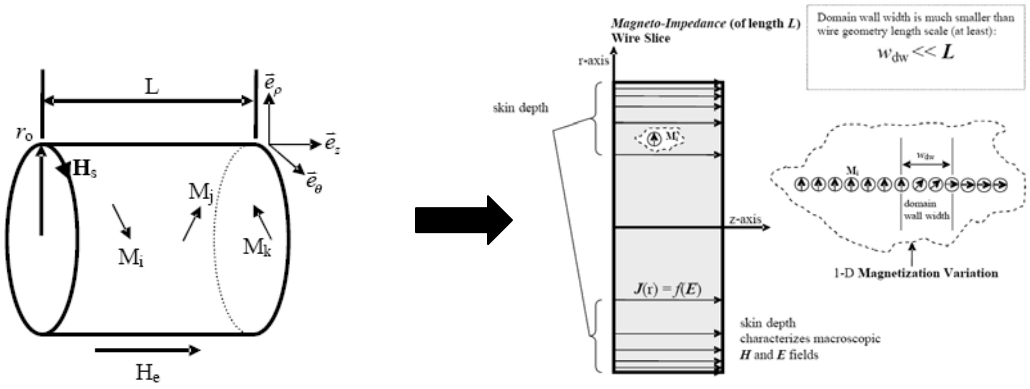

(a) MI element set up

(b) MI element slice showing magnetization phenomena

Figure 2-1 MI element (a) and a slice (b) showing MI effect variables and parameters.

We begin with the most general form of equations abiding by the assumptions above describing the relationships, directly, between the above mechanisms and key variables of interest such as **H** , **M** and *T*.

2.2.1 Maxwell Equations

In electromagnetic materials, the magnetic field intensity (or strength), **H**, magnetic flux density, **B**, as well as the electric field **E** and the electric displacements **D** are described on a continuum basis by the dynamic form of the classical macroscopic Maxwell's equations:

$$\nabla \times \mathbf{H} = \mathbf{J} + \frac{\partial \mathbf{D}}{\partial t} \tag{2-1}$$

$$\nabla \times \mathbf{E} = -\frac{\partial \mathbf{B}}{\partial t}, \text{ where } \mathbf{B} = \mu_0 \mathbf{H} + \mathbf{M} \qquad \text{(2-2a,b)}$$

Similar to remarks in assumption (1), the term, macroscopic, implies that the variations of the fields represented are on length scales large compared to characteristic atomic length scales. The variables in (2-1) and (2-2) thus represent volume averages of their respective small scale quantities. Roughly speaking, the macroscopic Maxwell equations are assumed appropriate for geometries with variations on length scales on the order of $l_{\min} = 10^{-8}$ m [65], based on the observation that *x*-rays are not adequately described by Maxwell's equations and thus can be used as a sort of "limit" for length scales in continuum field descriptions. MI devices operate well below this limit, typically at frequencies between 100 kHz and 500 MHz, corresponding to wavelengths between 0.6 – 3000 m, which are much larger than $l_{\min} = 10^{-8}$ m. Thus, a continuum theory for **E** and **H** should be admissible per assumption (1) above.

Quasi-Static Condition

In the Maxwell equations, under certain assumptions, typically, the last term on the RHS of Ampere's law, equation (2-1), is neglected based on to what is known as the quasi-static condition. The condition loosely means that the electromagnetic field variations in time are relatively slow, thus the term "quasi-static". The condition can be revealed by examining the terms of Amperes law in the frequency domain, which becomes

$$\nabla \times \mathbf{H} = \mathbf{J} - j\omega \mathbf{D} \qquad \text{(2-3)}$$

In (2-3), the fields are assumed proportional to $e^{-j\omega t}$. Next, replace **J** and **D** with the linear classical constitutive laws relating them to the electric field, given by

$$\mathbf{J} = \sigma\mathbf{E} \text{ and } \mathbf{D} = \varepsilon\mathbf{E} \tag{2-4 a,b}$$

The symbol, σ, represents the bulk electrical conductivity, and the symbol, ε, represents the bulk dielectric constant. Substitution into Ampere's Law then gives

$$\nabla \times \mathbf{H} = \left(\sigma - j\omega\varepsilon\right)\mathbf{E} \tag{2-5}$$

The scalar coefficient on the right hand side (RHS) for the electric field involves the sum of two terms. The quasi-static condition results from comparing amplitudes of both terms and usually the first of the two terms is significantly larger than the second, i.e.:

$$\sigma / \varepsilon >> 2\pi f \tag{2-6}$$

This is known as the quasi-static condition and applies in most problems with metallic conductors. For the magnetic alloys considered in this work, along with additional more conductive materials, such as copper (Cu), this is easily shown to be the case. For example, using the experimentally determined values for the amorphous Permalloy, CoFeSiB taken from Ref. [27], operating at 1 MHz, the comparison becomes:

$$7.69 \bullet 10^{5} >> 5.56 \bullet 10^{-5} \tag{2-7}$$

Then, under these assumptions, Amperes law is reduced to the following:

$$\nabla \times \mathbf{H} = \mathbf{J} \tag{2-8}$$

Using the reduced equation in (2-8) along with (2-2), a single equation that describes either **E** or **H** can be formed. The equation describing **H** is used exclusively in this work. It is found by first taking the curl of (2-8). Then **J** can be replaced using (2-4a). Then interchanging the linear operators of curl and time differentiation and substituting (2-2) then leads to

$$\nabla \times \nabla \times \mathbf{H} = \sigma \nabla \times \mathbf{E} = -\sigma \frac{\partial \mathbf{B}}{\partial t} = -\sigma(\mu_0 \frac{\partial \mathbf{H}}{\partial t} + \frac{\partial \mathbf{M}}{\partial t}) \tag{2-9}$$

Equation (2-9) is then the independent equation that describes the space-time variation of the magnetic field intensity, **H**. Notice that equation (2-9) is *coupled* to the time variation of the magnetization, **M**.

2.2.2 Micromagnetics Formulation

For the MI effect, Maxwell equations alone do not provide the sufficient "resolution" to observe many of the coupled mechanisms that have been observed in MI devices experimentally. For example, the sensitivity of MI sensors has shown to be affected by the magnetic anisotropy as observed in both amorphous single materials, as well as composite MI sensors and this is a not a mechanism explicitly captured by Maxwell equations. Another mechanism that plays a role in the MI effect is domain walls, also described by micromagnetics. The aim is then a further examine at a "finer" scale, these additional mechanisms and how they influence the MI effect.

Typically, the equations above also require the constitutive relationship relating **B** and **H** where

$$\mathbf{B} = \mu_0 \mathbf{H} + \mathbf{M} = \left(\mu_0 \mathbf{I} + \left[\chi(\mathbf{H})\right]\right)\mathbf{H} = \left[\mu(\mathbf{H})\right]\mathbf{H} \tag{2-10}$$

For magnetic materials, this generally poses the nonlinear equation. If one is now tasked with solving a nonlinear equation based on (2-10), for small magnetic sensors satisfying assumptions (1) – (5), there is an alternative to using the empirically determined constitutive law in (2-10). This alternative (and more general) approach enables the "finer resolution" in observing the influences of the mechanisms on the fields involved in the MI effect. Also, because the micromagnetics equation is somewhat the "heart" of the

equations of motion, we spend relatively more time in this thesis research developing and explaining this formulation (and its characteristics). Thus, we begin with a "derivation" of the micromagnetics formulation used in this work. The word "derivation" is in quotes here because the micromagnetics equation is not derivable fully from first principles, but invokes phenomenological elements to arrive at the final equations. This is discussed in more details in the next section.

Derivation of Micromagnetics Formulation from Quantum Relations

To present the continuum micromagnetics equation, we begin by expressing a non-dissipative form of the micromagnetics equation which can be readily derived from quantum relations, given by

$$\frac{\partial \mathbf{M}}{\partial t} = -\gamma \mathbf{M} \times \mathbf{H}^* \tag{2-11}$$

In the derivation outlined here, **H*** is assumed to already be a volume averaged quantity, or consistent with Maxwell equations. The micromagnetics equation can be derived based on a volume average of the quantum mechanics relation given by

$$\hbar \frac{\partial \mathbf{J}_q}{\partial t} = \mathbf{M}_q \times \mathbf{H}^* \tag{2-12}$$

The parameter, $\hbar$, is Planck's constant divided by 2π, $\mathbf{J}_q$ is the atomic (quantum) angular momenta and $\mathbf{M}_q$ is the corresponding quantum magnetic moment, generally comprised of both atomic orbital moments and spin moments. For the electron, which is responsible for the net magnetic moment in ferromagnets[3], the total magnetic moment is related to the angular momenta by

[3] In ferromagnets, the magnetization (exchange) is known to be due to the electrons primarily in the 3d orbital of the metal's atoms.

$$\mathbf{M}_q = -\gamma_q \hbar \mathbf{J}_q \tag{2-13}$$

The symbol, γ_q, represents the quantum scale gyromagnetic ratio, which is not exactly the same as the value in the continuum relation, (2-11), as will be seen later. $\mathbf{J}_q$ takes on discrete values, which are determined by solving what is known as the Schrödinger equation [2]. Using (2-13), (2-12) is expressed as

$$\frac{\hbar}{\hbar\gamma_q}\frac{\partial \mathbf{M}_q}{\partial t} = -\mathbf{M}_q \times \mathbf{H}^* \rightarrow \frac{\partial \mathbf{M}_q}{\partial t} = -\gamma_q \mathbf{M}_q \times \mathbf{H}^* \tag{2-14a,b}$$

Contrary to (2-11), the equation in (2-14) is on the quantum scale. However, a continuum form can be derived by a volume average of the equation using the following definition of volume averaging with respect to a weighting function $f(\mathrm{x})$, defined by the relation [65]:

$$\int_V f(\mathbf{y}) F(\mathbf{x}-\mathbf{y},t)\, d\mathbf{y} = \langle F(\mathbf{x},t) \rangle \tag{2-15}$$

Using (2-15) with (2-14), averaging leads to the following:

$$\int_V f(\mathbf{y}) \left(\frac{\partial \mathbf{M}_q}{\partial t} + \gamma_q \mathbf{M}_q \times \mathbf{H}^* \right) d\mathbf{y} = \int_V f(\mathbf{y}) \frac{\partial \mathbf{M}_q}{\partial t} d\mathbf{y} + \int_V f(\mathbf{y}) \gamma_q \mathbf{M}_q \times \mathbf{H}^* d\mathbf{y} \tag{2-16}$$

Reordering the linear operator of integration and time differentiation leads to

$$\int_V f(\mathbf{y}) \frac{\partial \mathbf{M}_q}{\partial t} d\mathbf{y} + \int_V f(\mathbf{y}) \gamma_q \mathbf{M}_q \times \mathbf{H}^* d\mathbf{y} = \frac{\partial}{\partial t} \int_V f(\mathbf{y}) \mathbf{M}_q d\mathbf{y} + \int_V f(\mathbf{y}) \gamma_q \mathbf{M}_q \times \mathbf{H}^* d\mathbf{y} \tag{2-17}$$

From (2-17), it follows that

$$\frac{\partial \langle \mathbf{M}_q \rangle}{\partial t} + \gamma_q \int_V f(\mathbf{y}) \mathbf{M}_q \times \mathbf{H}^* d\mathbf{y} = 0 \tag{2-18}$$

The cross product can alternatively be written as a skew matrix operation

$$\mathbf{M}_q \times \mathbf{H}^* = -\begin{bmatrix} 0 & -H_3^* & H_2^* \\ H_3^* & 0 & -H_1^* \\ -H_2^* & H_1^* & 0 \end{bmatrix} \begin{bmatrix} M_{q1} \\ M_{q2} \\ M_{q3} \end{bmatrix} \tag{2-19}$$

The first of the vector equations has the form

$$\frac{\partial \langle M_{q1} \rangle}{\partial t} = -\int_V \gamma_q f(\mathbf{y}) M_{q2} H_3^* d\mathbf{y} + \int_V \gamma_q f(\mathbf{y}) M_{q3} H_2^* d\mathbf{y} = 0 \tag{2-20}$$

At this point, a distinction regarding the magnetic field, **H*** can be made. If, in fact, there are enough particles within V to justify volume averaging (assumed to be the case), then, volume averaging holds true for the independently described magnetic field (and its constituents fields), as well, i.e.

$$H_i^*(\mathbf{x}) = \int_V f(\mathbf{y}) H_{qi}(\mathbf{x}-\mathbf{y}) d\mathbf{y} = \langle H_{qi} \rangle \tag{2-21}$$

In general, **H*** includes more than the external field, and recall that Maxwell's equations are volume averages of the corresponding small scale values, as well. Then, H_i^* is non-varying over the volume integral in (2-20). Then it becomes

$$\frac{\partial \langle M_{q1} \rangle}{\partial t} = -\left(\int_V \gamma_q f(\mathbf{y}) M_{q2} d\mathbf{y} \right) H_3^* + \left(\int_V \gamma_q f(\mathbf{y}) M_{q3} d\mathbf{y} \right) H_2^* \tag{2-22}$$

In general, γ_q may vary through out the atomic structure. In more compact form, we have

$$\frac{\partial \langle M_{q1} \rangle}{\partial t} = -\langle \gamma_q M_{q2} \rangle H_3^* + \langle \gamma_q M_{q3} \rangle H_2^* \tag{2-23}$$

An effective continuum scale gyroscopic ratio can then be defined for each independent direction in terms of the quantum scale value such that

$$\gamma_c\left[-\left\langle M_{q2}\right\rangle H_3^* + \left\langle M_{q3}\right\rangle H_2^*\right] = -\left\langle \gamma_q M_{q2}\right\rangle H_3^* + \left\langle \gamma_q M_{q3}\right\rangle H_2^* \tag{2-24}$$

Extending the same arguments to all components of the vector equation (2-18), a volume averaged form of the magnetic momenta equation is given by

$$\frac{\partial\left\langle \mathbf{M}_{\mathrm{q}}\right\rangle}{\partial t} = -\left[\gamma_c\right]\left\langle \mathbf{M}_q\right\rangle \times \left\langle \mathbf{H}_q\right\rangle = -\gamma\left\langle \mathbf{M}_q\right\rangle \times \left\langle \mathbf{H}_q\right\rangle \tag{2-25}$$

As is commonly done with ferromagnets, the general gyroscopic tensor is assumed equal to an effective scalar. The equation in (2-25) is a non-dissipative form of the equation of motion. In quantum systems, the magnetic momenta are undampened and continue without any apparent loss of energy; however, in bulk magnetic materials (collections of atoms) with interactions with external magnetic fields, dampening is generally observed due to "friction" and other irreversibilities such as imperfections in the material. This affiliated energy loss is most evident by hysteresis in magnetic materials. To account for observations like this, the equation given in (2-25) is modified to reflect this peculiar nonlinearity with a purely phenomenologically inspired dampening term yielding the final form given by

$$\frac{\partial\left\langle \mathbf{M}_q\right\rangle}{\partial t} = -\gamma\left\langle \mathbf{M}_q\right\rangle \times \left\langle \mathbf{H}_q\right\rangle + \frac{\alpha}{M_{\mathrm{s}}}\left\langle \mathbf{M}_q\right\rangle \times \frac{\partial\left\langle \mathbf{M}_q\right\rangle}{\partial t} \tag{2-26}$$

This equation form is known as the Gilbert equation, similar to the more well-known Landau-Lifhitz equation which pre-dates the Gilbert equation form of the micromagnetics equation. From here, we drop the volume averaging notation and it can be assumed from this point forward that all quantities are volume averaged, where $\langle \mathbf{H}_q \rangle = \mathbf{H}^* = \mathbf{H}_T$, where $\mathbf{H}_T$ is the total effective magnetic field. We then have the following form known as the Gilbert equation expressed in continuum form

$$\frac{\partial \mathbf{M}}{\partial t} = -\gamma \mathbf{M} \times \mathbf{H}_{\mathrm{T}} + \frac{\alpha}{M_s} \mathbf{M} \times \frac{\partial \mathbf{M}}{\partial t} \tag{2-27}$$

The Gilbert equation is equivalent to another micromagnetics formulation referred to as the Landau-Lifshitz-Gilbert (LLG) equation. In (2-27), γ is the continuum gyromagnetic ratio given in SI units by $\gamma = \mu_0 g q_{\mathrm{e}} / 2m_{\mathrm{e}}$ [66]; where in this work, the g-factor $g \approx 2$, q_{e} is the electron charge; and m_{e} is the electron mass. The total effective field, $\mathbf{H}_T$, includes "effective" fields generally accounting for the effects of magnetic anisotropy, magnetization exchange, demagnetization, magnetoelastic (and stress-related), as well as the total external magnetic field described by Maxwell's equations. The parameter α is the phenomenological Gilbert damping constant; M_{s} is the saturation magnetization, where it is assumed that $||\mathbf{M}|| = M_{\mathrm{s}}$. This condition is shown for the micromagnetics relation used in this work in the Appendix. Based on the assumptions outlined above, the total effective field used here is then given by (ignoring stress-related terms)

$$\mathbf{H}_T = \mathbf{H} + \mathbf{H}_K + \mathbf{H}_X + \mathbf{H}_D \tag{2-28}$$

$\mathbf{H}_{\mathrm{K}}$ is the effective anisotropy field owing to the coupling between spin and orbital motion; $\mathbf{H}_{\mathrm{X}}$ is the effective exchange field owing the quantum mechanical exchange force; and $\mathbf{H}_{\mathrm{D}}$ is the demagnetizing field due to the presence of dipoles both inside and on the surface of a magnet, also known as the magnetostatic field. The effective anisotropy field, $\mathbf{H}_{\mathrm{K}}$, is expressed as

$$\mathbf{H}_K = \left(2K / M_s^2\right)\left(\mathbf{M} \cdot \mathbf{e}_K\right)\mathbf{e}_K \tag{2-29}$$

K is the first anisotropy constant. The vector, $\mathbf{e}_K$, represents the material preferred anisotropy direction unit vector. $\mathbf{H}_X$ is the exchange field given by

$$\mathbf{H}_X = A_X \nabla^2 \mathbf{M} \tag{2-30}$$

A_X is a scalar known as the exchange stiffness scalar. $\mathbf{H}_D$ is the demagnetization field. This long range field is generated within any magnetic material, independent of an externally applied magnetic field, as a result of the magnetic dipoles of the structure, both inside and on the surface. An analytic form of the demagnetizing field, based on potential theory, exists for computing $\mathbf{H}_D$, however, it is more computationally demanding as it requires both volume and surface integration [67]. Alternatively, more fit for the numerical modeling process deployed here, the relation characterizing the demagnetization field follows from combining one of the static Maxwell equations along with the magnetostatic form of Ampere's Law, where both are given by

$$\nabla \cdot \mathbf{B} = \mu_0 \nabla \cdot \mathbf{H}_D + \nabla \cdot \mathbf{M} = 0 \tag{2-31}$$

$$\nabla \times \mathbf{H}_D = 0 \tag{2-32}$$

Equation (2-32) implies that the demagnetizing field can be expressed as the gradient of a demagnetization scalar potential, φ_D, resulting in the following:

$$\nabla \cdot \mathbf{M} - \mu_0 \nabla^2 \varphi_D = 0 \tag{2-33}$$

The demagnetizing field is thus defined as

$$\mathbf{H}_D = -\nabla \varphi_D \tag{2-34}$$

The uniqueness of the potential, φ_D, is not guaranteed in general, defined in this way, and in order to ensure uniqueness, φ_D is specified as zero at the axis of symmetry (or anti-symmetry) in all geometries modeled.

2.2.3 Thermal Diffusion Equation

Of the three modes of heat transfer (conduction, convection, and radiation), it is assumed in this work that radiation is negligible, due to use of metals at near-room temperature. Conduction is the dominant mode in the interior of the MI element while convection takes place at the wire surface between the wire and surrounding air environment. Temperature changes can then result potentially from two primary sources: 1) joule heating due to electrical current flow and 2) surrounding temperature. In this work, only the effects from elevated surrounding temperature are investigated. Results from the first case (joule heating) can actually be inferred from the results of the considered case, as well, since the result in either case is to elevate the temperature leading to different temperature dependent parameters in the equations of motion. To include the effects of temperature in the model, the thermal diffusion equation is added to the system of equations, which can generally be expressed in the following form:

$$\rho c_{\mathrm{p}} \frac{\partial T}{\partial t} = \nabla \bullet \left(k \nabla T \right) + q_{\mathrm{i}} \tag{2-49}$$

In (2-49), q_{i} represents an internal thermal power source. In the MI element, this energy is provided by the electromagnetic energy via current flow where the energy rate per unit volume is generally given by:

$$q_{\mathrm{i}} = \mathbf{J} \bullet \mathbf{E} \tag{2-50}$$

However, (2-50) is modified to use only the magnetic field intensity, **H**, leading to the following form:

$$q_{\mathrm{i}} = 1/\sigma \left\| \nabla \times \mathbf{H} \right\|^2 \tag{2-51}$$

In (2-51), we have used Ampere's law given in (2-8) along with (2-4) to replace the current density, **J**. Then, the form of the thermal diffusion equation used in this formulation is given by

$$\rho c_p \frac{\partial T}{\partial t} = \nabla \bullet \left(k \nabla T \right) + 1/\sigma \left\| \nabla \times \mathbf{H} \right\|^2 \tag{2-52}$$

Therefore, in the space- time domain, the complete set of equations that describe the MI effect is given by

$$\nabla \times \nabla \times \mathbf{H} = -\mu_0 \sigma \frac{\partial \mathbf{H}}{\partial t} - \sigma \frac{\partial \mathbf{M}}{\partial t} \tag{2-53a}$$

$$\frac{\partial \mathbf{M}}{\partial t} = -\gamma \mathbf{M} \times \mathbf{H}_{\mathrm{T}} + \frac{\alpha}{M_s} \mathbf{M} \times \frac{\partial \mathbf{M}}{\partial t} \tag{2-53b}$$

$$\rho c_p \frac{\partial T}{\partial t} = \nabla \bullet \left(k \nabla T \right) + 1/\sigma \left\| \nabla \times \mathbf{H} \right\|^2 \tag{2-53c}$$

2.2.4 Normalized Form of the Equations of Motion

It a numerical formulation, it is useful to normalize the equations of motion in space and time as this often achieves a few practical advantages:

1) The numerical solution is more general in such a way that often leads to more information in a single solution.
2) Parameters that may have physical significance are sometimes revealed that often govern the characteristics of the equations of motion.
3) Normalizing can also stabilize calculations, as well, by limiting the range of values in the unknowns normalizing both the independent and dependent variables.

For the spatial coordinate, a single length scale is used by which each spatial coordinate is normalized, referred to as L^*. Similarly, **H**, **M**, and φ_{D} are normalized by a single

parameter M_s. Also, a time parameter, τ, is used by which time is normalized. Then appropriate substitutions are made in the equations of motion leading to the following:

$$\frac{\partial \mathbf{h}}{\partial \bar{t}} = -\frac{\tau}{\mu_0 \sigma L_*^2} \nabla \times \nabla \times \mathbf{h} - \frac{1}{\mu_0} \frac{\partial \mathbf{m}}{\partial \bar{t}} \tag{2-54a}$$

$$\frac{\partial \mathbf{m}}{\partial \bar{t}} = -\tau\gamma \mathbf{m} \times \mathbf{h}_T + \alpha M_s \mathbf{m} \times \frac{\partial \mathbf{m}}{\partial \bar{t}} \tag{2-54b}$$

$$\frac{\partial \bar{T}}{\partial \bar{t}} = \frac{1}{L_*^2} \frac{\tau}{\rho c_p} \nabla \bullet \left(k \nabla \bar{T} \right) + \frac{\tau}{\rho c_p} \frac{M_s^2}{\sigma T_r L_*^2} \left\| \nabla \times \mathbf{h} \right\|^2 \tag{2-54c}$$

In this thesis, we use formulations of various forms of (2-54) in order to investigate the effects of coupling between diffusion, Maxwell's, and the Gilbert equations.

The MI voltages generated across the length of the MI element are composed of two components, the ohmic voltage, which follows from the axial current, and the inductive currents, which is a consequence of the resulting flux change within the wire. The MI voltage is thus given by

$$V_{MI} = V_R + V_L \tag{2-55}$$

The ohmic and inductive voltages are given by

$$V_R = R_{dc} I_s \text{ and } V_L = \frac{d}{dt} \int_A (\mu_0 \mathbf{H} + \mathbf{M}) \cdot d\mathbf{A} \tag{2-56a,b}$$

2.3 Coupled Harmonic Micromagnetics Formulation

It will be shown in Chapter 3 that for small enough currents in the MI elements while simultaneously operated in ambient conditions, thermal effects can be considered negligible. This distinction is of interest because temporal integration can add considerable computational time. However, in systems under these conditions, the

explicit time dependence can be eliminated and the problem can be cast into a reduced coupled nonlinear harmonic form without the thermal diffusion equation. In general, because the input is harmonic and the system is nonlinear, there is no guarantee that the output will be harmonic at the same single frequency as the input current source. This is only the case for linear systems. However, experimental data for MI sensors shows that the magnetization variation is also at least harmonic at the same input frequency, although in some cases, the voltage output wave is not purely sinusoidal [68]. Based on a purely periodic output voltage of the MI sensor, it is, in general, represented by a Fourier series such that

$$V_{\mathrm{MI}} = \sum_{k=1}^{\infty} A_k \sin(n_k \omega) + B_k \cos(n_k \omega) \tag{2-55}$$

Therefore, to approximate the general expression of (2-55), a single mode is assumed to dominate the series. The assumption of a monochromatic harmonic field representation has been used, without exception, in modeling MI sensors; however, prior works have also effectively decoupled and/or linearized the equations of motion. Thus, reducing the general nonlinear harmonic waveform in (2-55) to that consisting of a single dominant mode leads to a form that can be expressed as a simple complex number. This is done with the use of a harmonic model.

Still, preserving a coupled nonlinear formulation also allows more direct comparisons to linearized models to gauge the costs of linearizing and decoupling the system equations of motion. Here, a fully coupled nonlinear harmonic formulation is presented [62], from which a linearized formulation consistent with other models can readily be deduced.

To begin, the Gilbert equation is expressed using a skew matrix representation [62]:

$$\left(\mathbf{I}-\frac{\alpha}{M_s}\text{skew}\left(\mathbf{M}\right)\right)\frac{\partial\mathbf{M}}{\partial t}=\mathbf{\Gamma}\frac{\partial\mathbf{M}}{\partial t}=-\gamma\mathbf{M}\times\mathbf{H}_T \tag{2-56}$$

Then, the system of equations becomes:

$$\mu_0\frac{\partial\mathbf{H}}{\partial\text{t}}+\frac{\partial\mathbf{M}}{\partial t}=-1/\sigma\nabla\times\nabla\times\mathbf{H} \tag{2-57}$$

$$\mathbf{\Gamma}\left(\mathbf{M};\alpha,M_s\right)\frac{\partial\mathbf{M}}{\partial t}=-\gamma\mathbf{M}\times\mathbf{H}_T, \tag{2-58}$$

Following the approach by Gurevich *et al*. [11], it is assumed that **H** and **M** can be expressed as the sum of an equilibrium (or steady) component and an alternating component, which, for the problem considered, is expressed as

$$\mathbf{H}=\mathbf{H}_\text{d}+\mathbf{H}_\sim=\mathbf{H}_\text{d}+\left|\mathbf{H}_\sim\right|e^{-j\omega t+\phi}=\mathbf{H}_\text{e}+\mathbf{H}_\text{R}+j\mathbf{H}_\text{I} \tag{2-59}$$

$$\mathbf{M}=\mathbf{M}_\text{d}+\mathbf{M}_\sim=\mathbf{M}_\text{d}+\left|\mathbf{M}_\sim\right|e^{-j\omega t+\phi_\text{M}}=\mathbf{M}_\text{d}+\mathbf{M}_\text{R}+j\mathbf{M}_\text{I} \tag{2-60}$$

From (2-59) and (2-60), it is assumed that the time derivatives are then given by

$$\frac{\partial\mathbf{H}_\sim}{\partial\text{t}}=-j\omega\upsilon_s\left(\mathbf{H}_\text{R}+j\mathbf{H}_\text{I}\right)=\omega\upsilon_s\left(\mathbf{H}_\text{I}-j\mathbf{H}_\text{R}\right) \tag{2-61a}$$

$$\frac{\partial\mathbf{M}_\sim}{\partial\text{t}}=-j\omega\upsilon_s\left(\mathbf{M}_\text{R}+j\mathbf{M}_\text{I}\right)=\omega\upsilon_s\left(\mathbf{M}_\text{I}-j\mathbf{M}_\text{R}\right) \tag{2-61b}$$

Due to the nonlinear nature of the degrees of freedom, the parameter υ_s has been introduced in order to reflect that although the derivative is harmonic (indicated by the reported experimental voltages), it may not be exactly sinusoidal (or cosinal) as a derivative, thus a scaling parameter is added to account for this observation. For our calculations, however, υ_s is assumed unity. In this formulation, the value of $\mathbf{M}_\text{d}$ is assumed to be known. Physically, it represents the equilibrium magnetization which is essentially given by the domain structure within the MI element. For the formulation

organized here, it is assumed that this information is known *a priori*. This is reasonable based on known previous observations of the domain structures in both amorphous cylindrical wires as well as the ribbon wires [69] [70]. Therefore, given the equilibrium state and using the assumed form of **M** and **H**, all effective fields can similarly be represented as the sum of steady and alternating components, where we have:

$$\mathbf{H}_{\mathrm{X}} = A_{\mathrm{X}}\nabla^2\mathbf{M} = \mathbf{H}_{\mathrm{Xd}} + \mathbf{H}_{\mathrm{X}\sim} = A_{\mathrm{X}}\nabla^2\mathbf{M}_{\mathrm{d}} + A_{\mathrm{X}}\nabla^2\mathbf{M}_{\sim} \tag{2-62}$$

$$\mathbf{H}_{\mathrm{K}} = \frac{2K}{M_s^2}\left(\mathbf{M}\cdot\mathbf{e}_{\mathrm{K}}\right)\mathbf{e}_{\mathrm{K}} = \mathbf{H}_{\mathrm{Kd}} + \mathbf{H}_{\mathrm{K}\sim} = \frac{2K}{M_s^2}\left(\mathbf{M}_{\mathrm{d}}\cdot\mathbf{e}_{\mathrm{K}}\right)\mathbf{e}_{\mathrm{K}} + \frac{2K}{M_s^2}\left(\mathbf{M}_{\sim}\cdot\mathbf{e}_{\mathrm{K}}\right)\mathbf{e}_{\mathrm{K}} \tag{2-63}$$

The demagnetizing relation also results in a steady and alternating formulation given by

$$\nabla\cdot\left(\mathbf{M}_{\mathrm{d}} + \mathbf{M}_{\sim}\right) - \mu_0\left(\nabla^2\varphi_{\mathrm{Dd}} + \nabla^2\varphi_{\mathrm{D}\sim}\right) = 0 \tag{2-64}$$

Then, the steady and alternating equations separate naturally yielding

$$\nabla\cdot\mathbf{M}_{\mathrm{d}} - \mu_0\nabla^2\varphi_{\mathrm{Dd}} = 0 \tag{2-65a}$$

$$\nabla\cdot\mathbf{M}_{\sim} - \mu_0\nabla^2\varphi_{\mathrm{D}\sim} = 0 \tag{2-65b}$$

The formulation now defines the demagnetizing field as the sum of a steady and alternating component, where the *dc* component is given by

$$\mathbf{H}_{\mathrm{Dd}} = \left(-1/\mu_0\right)\mathbf{M}_{\mathrm{d}} \tag{2-66a}$$

$$\mathbf{H}_{D\sim} = -\nabla\varphi_{D\sim} \tag{2-66b}$$

Substitution into the equations of motion yields

$$\nabla\times\nabla\times\left(\mathbf{H}_{\mathrm{R}} + j\mathbf{H}_{\mathrm{I}}\right) - j\omega\sigma\left(\mu_0\mathbf{H}_{\mathrm{R}} + \mathbf{M}_{\mathrm{R}}\right) + \omega\sigma\left(\mu_0\mathbf{H}_{\mathrm{I}} + \mathbf{M}_{\mathrm{I}}\right) = 0 \tag{2-67}$$

$$\omega\left(\boldsymbol{\Gamma}_{\mathrm{R}} + j\boldsymbol{\Gamma}_{\mathrm{I}}\right)\left(\mathbf{M}_{\mathrm{I}} - j\mathbf{M}_{\mathrm{R}}\right) = -\gamma\left(\mathbf{M}_{\mathrm{d}} + \mathbf{M}_{\mathrm{R}} + j\mathbf{M}_{\mathrm{I}}\right)\times\mathbf{H}_{\mathrm{TR}} + -\gamma\left(\mathbf{M}_{\mathrm{d}} + \mathbf{M}_{\mathrm{R}} + j\mathbf{M}_{\mathrm{I}}\right)\times j\mathbf{H}_{\mathrm{TI}} \tag{2-68}$$

The matrix, **Γ**, has been separated into its real and imaginary components. The micromagnetics equation is then given by

$$\begin{aligned}&\omega\boldsymbol{\Gamma}_{\mathrm{R}}\mathbf{M}_{\mathrm{I}}+j\omega\boldsymbol{\Gamma}_{\mathrm{I}}\mathbf{M}_{\mathrm{I}}-j\omega\boldsymbol{\Gamma}_{\mathrm{R}}\mathbf{M}_{\mathrm{R}}+\omega\boldsymbol{\Gamma}_{\mathrm{I}}\mathbf{M}_{\mathrm{R}}=\\&-\gamma\left(\mathbf{M}_{\mathrm{d}}+\mathbf{M}_{\mathrm{R}}\right)\times\mathbf{H}_{\mathrm{TR}}+-j\gamma\mathbf{M}_{\mathrm{I}}\times\mathbf{H}_{\mathrm{TR}}-\gamma\left(\mathbf{M}_{\mathrm{d}}+\mathbf{M}_{\mathrm{R}}\right)\times j\mathbf{H}_{\mathrm{TI}}-j\gamma\mathbf{M}_{\mathrm{I}}\times j\mathbf{H}_{\mathrm{TI}}\end{aligned} \tag{2-69}$$

Separating real and imaginary terms, the fully coupled nonlinear harmonic equations of motion for **H** and **M** are then given by

$$1/\sigma\nabla\times\nabla\times\mathbf{H}_{\mathrm{R}}+\omega\left(\mu_0\mathbf{H}_{\mathrm{I}}+\mathbf{M}_{\mathrm{I}}\right)=0 \tag{2-70}$$

$$1/\sigma\nabla\times\nabla\times\mathbf{H}_{\mathrm{I}}-\omega\left(\mu_0\mathbf{H}_{\mathrm{R}}+\mathbf{M}_{\mathrm{R}}\right)=0 \tag{2-71}$$

$$\omega\left(\boldsymbol{\Gamma}_{\mathrm{I}}\mathbf{M}_{\mathrm{R}}+\boldsymbol{\Gamma}_{\mathrm{R}}\mathbf{M}_{\mathrm{I}}\right)+\gamma\left(\mathbf{M}_{\mathrm{d}}+\mathbf{M}_{\mathrm{R}}\right)\times\mathbf{M}_{\mathrm{TR}}-\gamma\mathbf{M}_{\mathrm{I}}\times\mathbf{H}_{\mathrm{TI}}=0 \tag{2-72}$$

$$\omega\left(\boldsymbol{\Gamma}_{\mathrm{I}}\mathbf{M}_{\mathrm{I}}\text{-}\boldsymbol{\Gamma}_{\mathrm{R}}\mathbf{M}_{\mathrm{R}}\right)+\gamma\mathbf{M}_{\mathrm{I}}\times\mathbf{H}_{\mathrm{TR}}+\gamma\left(\mathbf{M}_{\mathrm{d}}+\mathbf{M}_{\mathrm{R}}\right)\times\mathbf{H}_{\mathrm{TI}}=0 \tag{2-73}$$

This summarizes the set of equations used to model the MI effect in this work.

2.4 Boundary Conditions

In this section, we discuss the relevant boundary conditions (BCs) that supplement the equations summarized above. Boundary conditions are needed for **H**, **M**, φ_{D}, and T to determine the relevant solution for the MI sensor. First, we derive the general interface boundary condition for the tangential magnetic field intensity component as this is the only type of component present on the surface of the MI element. This is followed by an analytical derivation of the BC for the magnetization that is sufficient to deduce the boundary conditions for the MI element. Lastly, the BCs for the demagnetization potential and temperature are expressed.

2.3.1 Tangential Magnetic Field Strength Boundary Condition

The diagram below illustrates a differential element of an interface between two electromagnetic materials, material 1 and material 2. Each material has a respective magnetic field $\mathbf{H}_1$ and $\mathbf{H}_2$ whose relationship is needed.

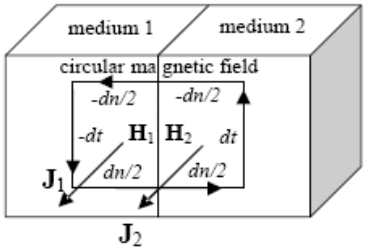

Figure 2-2 Interface of tangential magnetic field boundary condition

To derive the interfacial boundary condition between $\mathbf{H}_1$ and $\mathbf{H}_2$, a general form of Ampere's Law is used given by

$$\nabla \times \mathbf{H} = \mathbf{J} + \frac{\partial \mathbf{D}}{\partial \mathrm{t}} \tag{2-74}$$

Integrating (2-74) over the Gaussian rectangular surface shown in Figure 2-3 leads to

$$\mathrm{RHS} = \int_{d\mathbf{S}_1} \mathbf{J}_1 d\tau d\eta + \int_{d\mathbf{S}_2} \mathbf{J}_2 d\tau d\eta + \int_{d\mathbf{S}} \frac{\partial \mathbf{D}}{\partial \mathrm{t}} d\tau d\eta \tag{2-75}$$

$d\tau$ and $d\eta$ represent the sub-differentials of dt and dn, respectively, used to integrate over the Gaussian surface, d$\mathbf{S}$. The last term on the RHS has not been divided between the two mediums because it follows that in the limit as dn approaches zero, this term vanishes. This result follows from the fact that the time derivative of the electric displacement is a finite term and is not influenced by the local area of integration, i.e.

$$\lim_{dn\to 0} \int_{d\mathbf{S}} \frac{\partial \mathbf{D}}{\partial \mathrm{t}} d\tau d\eta = \lim_{dn\to 0} \left[dt \cdot dn \cdot \left. \frac{\partial \mathbf{D}}{\partial \mathrm{t}} \right|_{avg} \right] = 0 \tag{2-76}$$

The vanishing of the integral in general, however, is not the case for the current density term, $\mathbf{J}$, and this difference is exploited in deriving the final boundary condition. For example, in a wire with a current source, the current density can approach infinity as the wire area is gradually reduced, all other things remaining the same. Since the end goal is

to take the limit as *dn* approaches 0, the RHS can alternatively be written in the following way:

$$\int_{d\mathbf{S}_1} \mathbf{J}_1 d\tau d\eta + \int_{d\mathbf{S}_2} \mathbf{J}_2 d\tau d\eta = \int_0^{dt} \mathbf{J}_1^* d\tau + \int_0^{dt} \mathbf{J}_2^* d\tau \tag{2-77}$$

Where **J*** now represents the local current per unit length along the tangential direction. The RHS of (2-77) is now written as proportional to d*t*. This is done using the integral average, i.e.

$$\int \mathbf{J}_1^* d\tau = dt\left[\frac{1}{dt}\int_0^{dt} \mathbf{J}_1^* d\tau\right] = \mathbf{J}_{1,avg}^* dt \tag{2-78}$$

Substituting (2-60) into (2-59), we now have:

$$\text{RHS} = \left(\mathbf{J}_{1,avg}^* + \mathbf{J}_{2,avg}^*\right) dt \tag{2-79}$$

The LHS of (2-74), which has the curl of **H**, is transformed using *Stokes Theorem*, resulting in the following

$$\begin{aligned}\int \nabla \times \mathbf{H} dS = \oint \mathbf{H} \cdot dl = &-\left(\mathrm{H}_1 - \frac{\partial \mathrm{H}_1}{\partial n}\frac{dn}{2}\right)dt + \left(\mathrm{H}_1 + \frac{\partial \mathrm{H}_1}{\partial t}\frac{dt}{2}\right)\frac{dn}{2} - \left(\mathrm{H}_1 - \frac{\partial \mathrm{H}_1}{\partial t}\frac{dt}{2}\right)\frac{dn}{2} \\ &+ \left(\mathrm{H}_2 + \frac{\partial \mathrm{H}_2}{\partial n}\frac{dn}{2}\right)dt + \left(\mathrm{H}_2 + \frac{\partial \mathrm{H}_2}{\partial t}\frac{dt}{2}\right)\frac{dn}{2} - \left(\mathrm{H}_2 - \frac{\partial \mathrm{H}_2}{\partial t}\frac{dt}{2}\right)\frac{dn}{2}\end{aligned} \tag{2-80}$$

The limit of (2-80), as *dn* approaches zero, assuming all finite derivatives, reduces to:

$$\oint \mathbf{H} \cdot dl = \left(\mathbf{H}_2 - \mathbf{H}_1\right) dt \tag{2-81}$$

The following tangential boundary condition results

$$\mathbf{H}_2 - \mathbf{H}_1 = \mathbf{J}_{1,avg}^* + \mathbf{J}_{2,avg}^* \tag{2-82}$$

The terms on the RHS are commonly referred as surface currents [65]. This equation is applied analogously to any tangential field component. They represent the current per unit length in the transverse direction, having units of current per unit length (A/m).

In problems with good electrical conductors, the current distributes within the interior of the structure enough and thus surface currents are relatively small, especially for the frequencies and dimensions considered in this work. Thus, the approximation of a continuity condition results given by

$$\mathbf{H}_2 - \mathbf{H}_1 = 0 \tag{2-83}$$

Because the materials of interest in this work involve only conductors, the continuity condition is assumed valid and is used throughout this work. Next, a similar analytical condition is derived from the EOM for the magnetization, **M**.

2.4.2 Analytic Magnetization Interfacial Boundary Condition

The diagram above illustrates a differential element in the shape of a "pill box" or cylinder, across an interface between two magnetic materials, with magnetizations $\mathbf{M}_1$ and $\mathbf{M}_2$, both ideally at the interface.

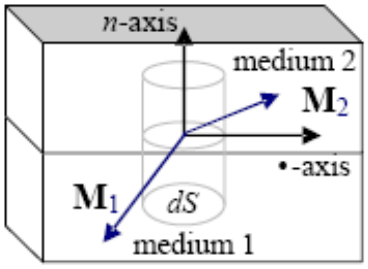

Figure 2-3 Interface for boundary condition for magnetization

To derive the interior boundary condition between $\mathbf{M}_1$ and $\mathbf{M}_2$, at the interface, the Gilbert equation is used leading to the following:

$$\frac{\partial \mathbf{M}}{\partial t} = \underbrace{-\gamma\left(\mathbf{M}\times\mathbf{H}_{nX}\right)}_{T_{nX}} - \gamma\left(\mathbf{M}\times A_X\nabla^2\mathbf{M}\right) + \frac{\alpha}{M_s}\left(\mathbf{M}\times\frac{\partial \mathbf{M}}{\partial t}\right) \tag{2-84}$$

For convenience, we have expressed the effective field as the sum of two components; the exchange field, $\mathbf{H}_X = A_X \nabla^2 \mathbf{M}$; and the non-exchange fields have all been lumped together, labeled as $\mathbf{H}_{nX}$. The symbol $\mathbf{T}_{nX}$ is used to represent the non-exchange related torques. Equation (2-84) is modified further by bringing the dampening term over to the LHS using a skew matrix representation, as done above. Equation (2-84) is then integrated over the volume of the Gaussian pill box shown in Figure 2-4, resulting in the following:

$$\int \left(\mathbf{\Gamma}\left(\mathbf{M};\alpha,M_s\right)\frac{\partial \mathbf{M}}{\partial t} - \mathbf{T}_{nX} \right) dV = \varsigma \int \mathbf{M} \times \nabla^2 \mathbf{M} dV \tag{2-85}$$

The symbol, $\varsigma = -\gamma A_X$. Greens theorem can now be used to transform the volume integral to a surface integral. Greens theorem is given by

$$\int \left(\psi \nabla^2 \phi - \phi \nabla^2 \psi \right) dV = \int \left(\psi \frac{\partial \phi}{\partial n} - \phi \frac{\partial \psi}{\partial n} \right) dS \tag{2-86}$$

Equation (2-86) is used recognizing that each row of the vector equation in the integrand of the RHS of (2-85) has the form given in the LHS of Greens theorem, giving:

$$\int \left(\mathbf{\Gamma}\left(\mathbf{M};\alpha,M_s\right)\frac{\partial \mathbf{M}}{\partial t} - \mathbf{T}_{nX} \right) dV = \varsigma \int \left(\mathbf{M} \times \frac{\partial \mathbf{M}}{\partial n} \right) d\mathbf{S} \tag{2-87}$$

In representing the surface integral, we must sum the integrand over both circular surfaces, dS_1 and dS_2, as well as the cylindrically shaped surface, $dS_{1,cyl}$ and $dS_{2,cyl}$. For the surfaces, dS_1 and dS_2, both equal to dS, we have:

$$\mathbf{M}_{S,1} = \mathbf{M}_1 + \frac{\partial \mathbf{M}_1}{\partial n} dn \text{ and } \mathbf{M}_{S,2} = \mathbf{M}_2 - \frac{\partial \mathbf{M}_2}{\partial n} dn \tag{2-88}$$

Along the cylindrical surfaces, $dsdn = \rho d\theta dn$, of the pill box, we have:

$$\mathbf{M}_{S,1,cyl} = \mathbf{M}_1 \pm \frac{\partial \mathbf{M}_1}{\partial \rho} d\rho \text{ and } \mathbf{M}_{S,1,cyl} = \mathbf{M}_1 \pm \frac{\partial \mathbf{M}_1}{\partial \rho} d\rho \tag{2-89}$$

Substituting (2-88) and (2-89) into (2-87), we have:

$$\int \left(\mathbf{\Gamma} \frac{\partial \mathbf{M}}{\partial t} - \mathbf{T}_{nX} \right) dV = \int \sum_{i=1}^{2} \varsigma_i \left(\mathbf{M}_{S,i} \times \frac{\partial \mathbf{M}_{S,i}}{\partial n} \right) dS + \int \sum_{i=1}^{2} \varsigma_i \left(\mathbf{M}_{S,i,cyl} \times \frac{\partial \mathbf{M}_{S,i,cyl}}{\partial \rho} d\rho \right) \rho d\theta dn_{i,cyl} \tag{2-90}$$

The limit is taken as the volume goes to zero by way of *dn*. Because all terms in the integrand of the LHS are finite, this term vanishes. By the same argument, the last term on the RHS accounting for the cylindrical sides also vanishes. The result is the following analytic general boundary condition between two magnetic materials:

$$\varsigma_1 \left(\mathbf{M}_1 \times \frac{\partial \mathbf{M}_1}{\partial n} \right) - \varsigma_2 \left(\mathbf{M}_2 \times \frac{\partial \mathbf{M}_2}{\partial n} \right) = 0 \tag{2-91}$$

The boundary condition in (2-91) results in the more commonly used condition between a nonmagnetic and magnetic material known as the free spinning condition. This follows naturally, since, in this case, $\mathbf{M}_i = 0$, for a nonmagnetic medium, while $\mathbf{M}_j \neq 0$ for the magnetic medium, resulting in

$$\frac{\partial \mathbf{M}_j}{\partial n} = \frac{\partial \mathbf{M}}{\partial n} = 0 \tag{2-92}$$

It is assumed that no additional surface torque is present in the structure. Additional phenomenalogical surface torques are sometime present in the absence of a free-spinning condition, for example, from a relatively thin magnetic layer adjacent to the magnetic material surface or perhaps special treatments that arise sharply at the surface, such as a form of metallic oxidation, for example. More details of an inclusion of such effects can be found in [71] [67].

Summarizing the boundary conditions for **H** and **M** in MI element structures, we have:

$$\left(\mathbf{H}_2 - \mathbf{H}_1\right)\Big|_{\partial\Omega} \times \mathbf{n} = 0 \tag{2-93}$$

$$\left.\frac{\partial \mathbf{M}}{\partial \mathrm{n}}\right|_{\partial\Omega} = 0 \tag{2-94}$$

The vector, **n**, is the unit vector normal to the interface.

2.4.3 Demagnetization Potential Boundary Condition

The boundary condition for the demagnetization potential follows from the boundary condition for the normal components of the magnetic flux density, which is a continuity condition given by

$$\left(\mathbf{B}_2 - \mathbf{B}_1\right)\Big|_{\partial\Omega} \bullet \mathbf{n} = 0 \tag{2-95}$$

This relation follows from a similar derivation of the tangential field components where a Gaussian volume is used. Plugging in the definition of **B** in terms of $\mathbf{H}_D$ and the magnetization **M** leads to the following demagnetization potential boundary condition:

$$\left(-\mu_0 \nabla \varphi_{D,2} + \mathbf{M}_2 - \left[-\mu_0 \nabla \varphi_{D,1} + \mathbf{M}_1\right]\right)\Big|_{\partial\Omega} \bullet \mathbf{n} = 0 \tag{2-96}$$

2.4.4 Temperature Boundary Condition

Only conduction and convection are considered in the MI element under the conditions of the MI effect, and convection is present only on the surface of the wire. Thus, a convective surface condition assumed to describe the thermal condition of the MI wire surface is given by

$$-k\nabla T\big|_{\partial\Omega} \bullet \mathbf{n} = h\left(\mathrm{T}\big|_{\partial\Omega} - T_\infty\right) \tag{2-97}$$

In (2-97), h is the convection coefficient expressed in units of W/(m^2-K) and T_∞ is the temperature of the surrounding environment in Kelvins (K).

2.5 MLM Formulation for MI Effect Model

Given the equations of motion for the MI effect sensor, a maximum of 8 scalar variables ($\mathbf{H}(\mathbf{x},t)$, $\mathbf{M}(\mathbf{x},t)$, $\varphi_D(\mathbf{x},t)$, and $T(\mathbf{x},t)$) in the space-time model (or 14 in the nonlinear harmonic formulation) must be determined over a spatial computational domain Ω_c. Further, when time is considered, this must be done at each time step. The use of a numerical-based analytical model requires these variables and their derivatives be approximated in a discrete fashion over a spatially discretized computational domain, in this case the ferromagnetic conducting MI element.

As mentioned earlier, in this thesis research, a unique approach used to solve this numerical-based model is that the spatial discretization is done using an MLM formulation in a point collocation scheme. By using MLMs, the computational domain only requires nodes to be placed in the interior as well as on the boundaries, for a total of N independent nodes, without any meshing or connectivity requirements, etc. Using this discretized computational domain, the degrees of freedom can then be approximated.

2.5.1 MLM Point Collocation Formulation

Given $\mathbf{H}(\mathbf{x},t)$, $\mathbf{M}(\mathbf{x},t)$, $\varphi_D(\mathbf{x},t)$, and $T(\mathbf{x},t)$, each component, for example, of the vector unknown $\mathbf{H}$ is an independent scalar degree of freedom, u. In the EOM, each degree of freedom is discretized using a linear combination of what is known as *shape functions*. To derive the MLM shape functions used here, which are not closed form functions, each degree of freedom, u, begins with a definition given by

$$u_i(\mathrm{x}) \cong u^{\rho}(\mathrm{x}, \mathrm{x}_k; \rho) = \sum_{j=1}^{p} \varphi_j \, a_j = \varphi_v \mathbf{A} \tag{2-98}$$

x and $\mathbf{x}_k$ are global (from anywhere in the domain) and local (only near **x**) positions, respectively, within the computational domain. In (2-98), φ_j are known as *basis functions*, which are generally not equal to the *shape functions*; and ρ is the referred to as the dilation parameter or support radius that determines the local support nodes influencing the value, $u(\mathbf{x})$. The basis function coefficients, a_j, (which are unknown) are associated with each independent basis function, φ_j and are often taken from the set of monomials that span the set of polynomials in $\boldsymbol{R}^n$. For example, the one dimensional basis functions, φ_j, for a 3rd order *reproducible* formulation, are given by

$$\{\varphi\} = \{1, x, x^2, x^3\} \tag{2-99}$$

Then, to determine the coefficients **A** uniquely, in the case of the *Hp*-Cloud formulation, a discrete moving least square problem is solved. A localized discrete cost function, $\boldsymbol{J}_d$, is defined by

$$J_d := \sum_{k=1}^{n} w\left(\frac{\mathrm{x} - \mathrm{x}_k}{\rho}\right)\left(u_k - \sum_{j=1}^{p} \varphi_j\left(\frac{\mathrm{x} - \mathrm{x}_k}{\rho}\right) a_j\right)^2 \tag{2-100}$$

The weighting function, w, is chosen to provide compact support (see Appendix A for details on w). n is the number of local support nodes, $\mathbf{x}_k$, referred to as a local support node resulting from those determined using the dilation parameter ρ around **x**. Minimizing the cost function then results in the following normal equations:

$$\begin{aligned}
&\frac{\partial J_d}{\partial a_1} = 0 \Rightarrow \sum_{k=1}^{p} w\left(\frac{\mathrm{x}-\mathrm{x}_k}{\rho}\right)\cdot u_k \cdot \varphi_1\left(\frac{\mathrm{x}-\mathrm{x}_k}{\rho}\right) = \sum_{k=1}^{n} \varphi_1(\mathrm{x}_k) w\left(\frac{\mathrm{x}-\mathrm{x}_k}{\rho}\right)\sum_{j=1}^{p} \varphi_j\left(\frac{\mathrm{x}-\mathrm{x}_k}{\rho}\right) a_j \\
&\quad\vdots \qquad\qquad\qquad\qquad\qquad\qquad\qquad\qquad \vdots \\
&\frac{\partial J_d}{\partial a_p} = 0 \Rightarrow \sum_{k=1}^{n} w\left(\frac{\mathrm{x}-\mathrm{x}_k}{\rho}\right)\cdot u_k \cdot \varphi_p\left(\frac{\mathrm{x}-\mathrm{x}_k}{\rho}\right) = \sum_{k=1}^{n} \varphi_p(\mathrm{x}_k) w\left(\frac{\mathrm{x}-\mathrm{x}_k}{\rho}\right)\sum_{j=1}^{p} \varphi_j\left(\frac{\mathrm{x}-\mathrm{x}_k}{\rho}\right) a_j
\end{aligned} \tag{2-101}$$

Commuting the summations in the last term on the RHS, (2-101) can be written as

$$\begin{aligned}
&\sum_{k=1}^{n} w\left(\frac{\mathrm{x}-\mathrm{x}_k}{\rho}\right)\cdot u_k \cdot \varphi_1\left(\frac{\mathrm{x}-\mathrm{x}_k}{\rho}\right) = \sum_{j=1}^{p}\left(\sum_{k=1}^{n} \varphi_1(\mathrm{x}_k) w\left(\frac{\mathrm{x}-\mathrm{x}_k}{\rho}\right)\varphi_j\left(\frac{\mathrm{x}-\mathrm{x}_k}{\rho}\right)\right) a_j \\
&\quad\vdots \qquad\qquad\qquad\qquad\qquad\qquad\qquad\qquad \vdots \\
&\sum_{k=1}^{n} w\left(\frac{\mathrm{x}-\mathrm{x}_k}{\rho}\right)\cdot u_k \cdot \varphi_p\left(\frac{\mathrm{x}-\mathrm{x}_k}{\rho}\right) = \sum_{j=1}^{p}\left(\sum_{k=1}^{n} \varphi_p(\mathrm{x}_k) w\left(\frac{\mathrm{x}-\mathrm{x}_k}{\rho}\right)\varphi_j\left(\frac{\mathrm{x}-\mathrm{x}_k}{\rho}\right)\right) a_j
\end{aligned} \tag{2-102}$$

From equations (2-102), the following matrix equation is given by

$$\mathbf{TU} = \mathbf{M}_m \mathbf{A} \Rightarrow \mathbf{A} = \mathbf{M}_m^{-1}\mathbf{TU} \tag{2-103}$$

From this, the final shape functions can be computed as

$$u(\mathrm{x}) \cong \varphi_v \mathbf{M}_m^{-1}\mathbf{TU} = \Psi_v^S \mathbf{U} \tag{2-104}$$

$\mathbf{M}_\mathrm{m}$ is a $p \times p$ matrix, often referred to as a moment matrix, and p is the number of monomial basis functions (e.g. in (2-99) $p = 4$), whose matrix elements are given by

$$M_{m,ij} = \sum_{k=1}^{n} \varphi_i\left(\frac{\mathrm{x}-\mathrm{x}_k}{\rho}\right) w\left(\frac{\mathrm{x}-\mathrm{x}_k}{\rho}\right)\varphi_j\left(\frac{\mathrm{x}-\mathrm{x}_k}{\rho}\right) \tag{2-105}$$

T is a $p \times n$ matrix, whose elements are given by

$$T_{ij} = w\left(\frac{\mathrm{x}-\mathrm{x}_j}{\rho}\right)\cdot \varphi_i\left(\frac{\mathrm{x}-\mathrm{x}_j}{\rho}\right) \tag{2-106}$$

The result is an approximation of the degree of freedom u in terms of the final shape functions given by

$$u^\rho(\mathrm{x}) = \sum_{j=1}^{n} \Psi_j^S u_j \tag{2-107}$$

Ψ_j^S are the MLM shape functions which are not polynomials, but are a combination of the weighting function and the monomials. The approximation in (2-107) is then used explicitly in a point collocation scheme to define each degree of freedom, where, for the MI effect variables, we have

$$\mathbf{H}(\mathrm{x}) \cong \sum_{j=1}^{n} \Psi_j^s \mathbf{H}_j \,, \mathbf{M}_I(\mathrm{x}) \cong \sum_{j=1}^{n} \Psi_j^s \mathbf{M}_j$$
$$\varphi_{\mathrm{D}}(\mathrm{x}) \cong \sum_{j=1}^{n} \Psi_j^s \varphi_{\mathrm{D},,j} \quad T(\mathrm{x}) \cong \sum_{j=1}^{n} \Psi_j^s T_j \tag{2-108}$$

After discretization, the final equations then pose a system of equations with 8 x N unknowns in the space-time model and 14 x N for the coupled nonlinear harmonic formulation presented above. Because of the large number of unknowns at each spatial node, the equations of motion can become computationally intensive, motivating the need to carefully consider the methods for solving the system of equations. This motivates the use of a MLM point collocation method, also. It will be shown that for the problem considered, this approach results in much improved efficiency without compromising accuracy. Additionally, the equations of motion themselves have characteristics that also motivate such a choice.

In MLMs, the ability to solve arbitrary nonlinear BVPs has not always been apparent. One reason for this observation was because MLM shape functions do not generally interpolate across the entire computational domain. This subtle characteristic has been investigated by researchers where it was shown that this non-interpolating characteristic of MLMs in a point collocation formulation can lead to instability in numerical solutions [43]. Based on research in this thesis, it is believed that this is due to

the fact that the minimum requirement is that the shape functions possess boundary interpolation (without any special treatment). In this thesis research, we implement a nice feature of the *Hp*-Cloud formulation that provides flexibility with the choice of a weighting function leading to shape function interpolation at least on the boundaries of the computational domain. This implementation appears to stabilize the formulation, particularly, in the computation of the solutions to nonlinear BVPs. See the Appendix A for details of how this is achieved.

CHAPTER 3
ANALYTICAL APPROACHES

Given the equations of the motion describing the MI effect, there are number of ways to approach an analytical model. It is noted that by *analytical models*, the intention is to avoid the introduction of data fitting parameters. Instead, the explicit analytical equations of motion are used explicitly to model the problem. Three approaches considered in this thesis research are listed below:

1) *Decoupled Linear Harmonic MI Effect Model*
2) *Space-Time MI Effect Model*
3) *Coupled Nonlinear Harmonic MI Effect Model*

In this chapter, we will discuss two of the three, beginning with decoupled MI sensor models.

3.1 Decoupled Harmonic MI Effect Modeling Approach

A decoupled model offers the least amount of computational effort as the solutions are typically closed form. In some cases, a nonlinear lumped parameter permeability model has also been used in combination with a closed form impedance expression, however, still in a decoupled setting [72]. As we have said, this was one of the first approaches to model the MI sensor and it is used as a basis for comparison in this thesis research, as well. Relevant decoupled models are therefore summarized where we introduce two decoupled models that are incremental improvements to previously introduced decoupled models. In addition to being used as basis for comparison, a

relevant analysis of the equations to examine the characteristics of the decoupled models is also given.

Thus, the discussion of these approaches follows the given format: first, useful decoupled models are derived, where we first introduce a "generalized" multilayer impedance model from which previous single material [15] and single layer composite impedance models [12] in the round wire can be obtained. The impedance model for the single material ribbon element is also used in this work but details of its derivation can be found in the Appendix. We then derive two permeability models to be used with the impedance models completing the decoupled MI effect model. One permeability model is very similar to that presented by Yoon *et al*., however, it is slightly modified by deriving it *without assuming a small transverse field*, as done in [73]. We will see that this relaxation in a lumped parameter decoupled model leads to an order of magnitude difference in the predicted permeabilities well below saturation. Then, we derive a state-space model of the permeability tensor consistent with what was introduced by Gurevich and Melkov [11] (obtained from the linearized micromagnetics equation) and later used by Usov *et al* [7]. These permeability models provide the link between the impedance and the measured external field, H_e. They represent the decoupled MI sensor modeling approach that has been used extensively in previous works describing the MI effect.

Then, as the second modeling approach, we discuss a space-time model that includes the more general degrees of freedom, $\mathbf{H}(\mathbf{x},t)$ (magnetic field intensity), $\mathbf{M}(\mathbf{x},t)$ (magnetization), $\varphi_D(\mathbf{x},t)$ (demagnetization potential), and $T(\mathbf{x},t)$ (temperature). For this approach, we discuss the effects of elevated surrounding temperature on the MI effect switching mode; particularly, we discuss the initial increase in the MI voltages from room

temperature that has been reported in single material Co-based amorphous wires [29]. Also, we discuss dynamic effects such as the approach to a frequency peak after which the MI voltage diminishes with frequency. The study uses realistic material properties, most of which have been reported experimentally. Of additional importance, we also briefly consider the computational times.

3.1.1 MI Effect Decoupled Model(s)

Decoupled equations allow the separate solutions to both the macroscopic voltage (impedance) and the permeability, which depends on the measured external field H_e. Using this approach, impedances in the circular and ribbon elements are discussed first, followed by permeability models.

3.1.2 Generalized Cylindrical Impedance Model for Arbitrary Layers

A solution for the impedance in a cylindrical single layer *composite* MI element has been presented in [12]. The model considered only a single layer over a core material. Here, we extend the model for the case of the circular wire to one with an arbitrary number of layers. The motivation for such a model not only comes from experiments of MI elements with more than a single layer, but such a model can also be used to examine first order effects of variations in the material properties along the small scale dimension, e.g. radius in the case of the round wire. Given the manufacturing processes of the MI elements, including stress and thermal treatments, nonuniform material properties are likely in some structures and can be explored using a multilayered model.

Equations for the Multilayered Impedance

For a circular wire, the reduced Maxwell's equations describing the amplitudes of the electric field and magnetic field intensity, E_z and H_θ, in linear harmonic form, are given by

$$\frac{1}{r}\frac{\partial(rH_\theta)}{\partial r} = J_z \tag{3-1}$$

$$\frac{\partial E_z}{\partial r} = -j\omega\mu_\theta(H_e)H_\theta \tag{3-2}$$

H_θ is the circular or transverse component of the magnetic field intensity and J_z is the corresponding axial current density; j is the complex operator defined as $\sqrt{-1}$. μ_θ is the transverse permeability, which for the MI effect, depends on the measured field H_e. The assumptions leading to (3-1) and (3-2) include that the permeability μ_θ is a scalar (complex or real). With the assumption of linear material properties, (3-1) and (3-2) leads to the following equation

$$\frac{1}{r}\frac{\partial}{\partial r}\left(r\frac{\partial E_z}{\partial r}\right) = -j\omega\sigma\mu_\theta E_z \tag{3-3}$$

Equation (3-3) can alternatively be expressed as

$$\frac{1}{r}\frac{\partial}{\partial r}\left(r\frac{\partial E_z}{\partial r}\right) + k^2 E_z = 0 \tag{3-4}$$

In (3-4), the parameter k is then defined by $k = \sqrt{j\omega\sigma\mu_\theta}$. It can be easily shown that an analogous equation is formed for the corresponding magnetic field H_θ.

Additionally, in the case of conductive materials in the composite, the interfacial boundaries of the MI element consist of tangential field components parallel to the wire

surface. Then, for multilayered MI elements using a series of materials, the following boundary conditions are given for all interior interfacial tangential field components:

$$E_i = E_{i+1} \tag{3-5}$$

$$H_i = H_{i+1} \tag{3-6}$$

Equation (3-4) poses a particular case of the well known Bessel equation where for the core material, the solution is given by the zero order Bessel function of the first kind:

$$E_1 = c_1 J_0\left(k_1 r\right) \tag{3-7}$$

$$H_1 = c_1 \gamma_1 J_1\left(k_1 r\right) \tag{3-8}$$

c_1 is constant determined by a boundary condition. In general, γ_i is given by

$$\gamma_i = -j\frac{k_i}{\mu_i \omega} \tag{3-9}$$

k_i is given by the i^{th} material where $k_i = \sqrt{j\sigma_i \mu_i \omega}$. For all layers beyond the core of the wire, the fields are given by a more general Bessel equation solution:

$$E_i = c_2^i J_0\left(k_i r\right) + c_3^i Y_0\left(k_i r\right) \tag{3-10}$$

$$H_i = \gamma_i\left(c_2^i J_1\left(k_i r\right) + c_3^i Y_1\left(k_i r\right)\right) \tag{3-11}$$

J_0 and Y_0 are Bessel functions of the first and second kind, respectively. The superscript denotes the material number where the core starts as material 1 and continues outward. Using the boundary conditions for the first interface, a linear system can be expressed as follows:

$$c_1 J_0\left(k_1 R_1\right) = c_2^2 J_0\left(k_2 R_1\right) + c_3^2 Y_0\left(k_2 R_1\right) \tag{3-12}$$

$$\gamma_1 c_1 J_1\left(k_1 R_1\right) = \gamma_2\left(c_2^2 J_1\left(k_2 R_1\right) + c_3^2 Y_1\left(k_2 R_1\right)\right) \tag{3-13}$$

Normalizing the set of equations by c_1, the linear system becomes

$$\underbrace{\begin{bmatrix} J_0(k_2R_1) & Y_0(k_2R_1) \\ (\gamma_2/\gamma_1)J_1(k_2R_1) & (\gamma_2/\gamma_1)Y_1(k_2R_1) \end{bmatrix}}_{[\mathbf{A}_1]} \begin{bmatrix} c_2^{2*} \\ c_3^{2*} \end{bmatrix} = \underbrace{\begin{bmatrix} J_0(k_1R_1) \\ J_1(k_1R_1) \end{bmatrix}}_{\mathbf{b}_1} \tag{3-14}$$

The symbol * is added as a superscript to denote the normalization by c_1 from the core material (material 1). The solution for the normalized coefficients in the second material (or first layer) is then given by

$$\begin{bmatrix} c_2^{2*} \\ c_3^{2*} \end{bmatrix} = \underbrace{\frac{1}{\|\mathrm{A}_1\|}\begin{bmatrix} (\gamma_2/\gamma_1)Y_1(k_2R_1) & -Y_0(k_2R_1) \\ -(\gamma_2/\gamma_1)J_1(k_2R_1) & J_0(k_2R_1) \end{bmatrix}}_{[\mathbf{A}_1^{-1}]} \underbrace{\begin{bmatrix} J_0(k_1R_1) \\ J_1(k_1R_1) \end{bmatrix}}_{\mathbf{b}_1} \tag{3-15}$$

The determinant evaluated at R_1 is given by:

$$\|\mathrm{A}_1\| = (\gamma_2/\gamma_1)\cdot\left(J_0(k_2R_1)\cdot Y_1(k_2R_1) - Y_0(k_2R_1)\cdot J_1(k_2R_1)\right) \tag{3-16}$$

Equation (3-15) provides the coefficients for the field solutions in the 2nd material. Because the impedance is proportional to the electric field E_z on the surface of the outer material, observing the determinant of A_1, it follows that if there were only a single layer (2 materials), the impedance is found to be such that:

$$Z_{SL} \propto (\gamma_1/\gamma_2) \Rightarrow Z_{SL} \propto \sqrt{\sigma_1/\sigma_2} \tag{3-17}$$

Equation (3-17) suggests that having a more conductive core leads to larger voltage amplitudes. This observation is a potential factor why many experimentally designed single layer composite cylindrical (and ribbon) wires tend to have the higher conductivity in the core (e.g. Cu) with a magnetic material surrounding the core (e.g. Ni). Such a configuration generates larger voltage amplitudes (impedances). Some very sensitive

composite sensors developed successfully have this order [74]. This point was previously discussed on the basis of an analytical model in [12].

For additional layers, following the same process for the next interface, equating the fields at each interface, we have:

$$\underbrace{\begin{bmatrix} J_0(k_3R_2) & Y_0(k_3R_2) \\ (\gamma_3/\gamma_2)J_1(k_3R_2) & (\gamma_3/\gamma_2)Y_1(k_3R_2) \end{bmatrix}}_{[\mathbf{A}_2]}\begin{bmatrix} c_2^{3*} \\ c_3^{3*} \end{bmatrix} = \underbrace{\begin{bmatrix} J_0(k_2R_2) & Y_0(k_2R_2) \\ J_1(k_2R_2) & Y_1(k_2R_2) \end{bmatrix}}_{[\mathbf{B}_2]}\begin{bmatrix} c_2^{2*} \\ c_3^{2*} \end{bmatrix} \tag{3-18}$$

The next set of solutions for the normalized coefficients is then given by

$$\begin{bmatrix} c_2^{3*} \\ c_3^{3*} \end{bmatrix} = \left[\mathbf{A}_2^{-1}\mathbf{B}_2\right]\left[\mathbf{A}_1^{-1}\right]\mathbf{b}_1 \tag{3-19}$$

It follows that all the normalized coefficients have solutions that can then be generalized for any layer as follows:

$$\begin{bmatrix} c_2^{k*} \\ c_3^{k*} \end{bmatrix} = \left[\prod_{i=2}^{k-1}\mathbf{A}_i^{-1}\mathbf{B}_i\right]\left[\mathbf{A}_1^{-1}\right]\mathbf{b}_1 \tag{3-20}$$

For the problem of the MI element, the total current is known, however, for more general problems, the current can also be determined in terms of normalized coefficients. Continuing the form using coefficient normalization by c_1, the normalized current in the core is given by

$$I_1^* = 2\pi\sigma_1\int_{a_1} rJ_0(k_1r)dr = \frac{2\pi\sigma_1}{k_1}R_1J_1(k_1R_1) \tag{3-21}$$

a_1 is the cross sectional area of the core material. R_1 is the core radius. Following the same process outside of the core, in any layer, the normalized current is given by

$$I_i^* = \int_{a_i} J_i da = \frac{2\pi\sigma_i}{k_i}\left[c_2^{i*}\left(R_iJ_1(k_iR_i) - R_{i-1}J_1(k_iR_{i-1})\right) + c_3^{i*}\left(R_iY_1(k_iR_i) - R_{i-1}Y_1(k_iR_{i-1})\right)\right] \tag{3-22}$$

Then, a positive axial voltage drop on the surface of the MI element is determined using the value of the axially uniform electric field on the surface

$$E_z\big|_{r=R_o} = \nabla V\big|_{r=R_n} \Rightarrow \Delta V_z = I_s Z = L\, E_z\big|_{r=R_n} \tag{3-23}$$

n is the index counting the number of materials. It then follows that the impedance for a multilayer cylindrical wire is given by

$$Z_{ML} = \frac{\left[\prod_{i=2}^{k-1} \mathbf{A}_i^{-1}\mathbf{B}_i\right]\mathbf{A}_1^{-1}\mathbf{b}_1 \bullet \begin{bmatrix} J_0\left(k_n R_n\right) \\ Y_0\left(k_n R_n\right) \end{bmatrix}}{I_1^* + \sum_{i=2}^{n} I_i^*} \tag{3-24}$$

Since all parameters are normalized by the core coefficient, c_1, the ratio defining Z_{ML} is given in absolute units e.g. ohms (Ω).

It follows from (3-24) by assuming only a core without any layers that the impedance in a single circular material is given by

$$Z_{SL} = L_z \frac{J_0\left(k_1 r_0\right)}{I_1^*} = \frac{1}{2} R_{dc} \cdot k \cdot r_0 \frac{J_0\left(k r_0\right)}{J_1\left(k r_0\right)} \tag{3-25}$$

This is the expression commonly used in the literature for the impedance across a linear magnetic conductor, originally given by Landau and Lifshitz [15].

3.1.3 Ribbon Impedance

There is an analog of (3-25) for the ribbon structure which is also used in this thesis research and is given by

$$Z = \frac{1}{2} R_{dc} kt \coth\left(k \frac{t}{2}\right) \tag{3-26}$$

R_{dc} is the *dc* resistance and *t* is the ribbon thickness. The derivation of (3-26) from the equations of motion is given in Appendix E. Additionally, a generalized impedance

model can be determined analogously to what was done above yielding an expression similar to (3-24), replacing the Bessel functions with the proper hyperbolic sine and cosine functions.

3.1.4 A Transverse Permeability Using Micromagnetic Energy

For a decoupled system at relatively low frequencies, a relevant real valued permeability can be derived considering the micromagnetic energy of the system. Consider the schematic in Figure 3-1, showing the magnetization vector **M** and the external field vectors H_e and the transverse field, labeled as H_t. Here, only Zeeman and anisotropy energies are assumed dominant, where the anisotropy direction is indicated by $\mathbf{e}_K$. The angle θ_K is the anisotropy direction relative to the transverse direction (y-axis). The angle of the magnetization is then given by the sum of θ and θ_K

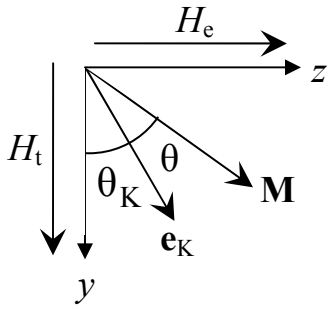

Figure 3-1 Lumped parameter magnetic system with external fields and anisotropy.

Then, adding the magnetic energy (per unit volume) of the system including only anisotropy and Zeeman energy (due to external fields), the energy is given by

$$E = K\sin^2\theta - M_s H_e \sin\left(\theta+\theta_k\right) - M_s H_t \cos\left(\theta+\theta_k\right) \tag{3-27}$$

In (3-27), K is the first anisotropy constant, M_s is the saturation magnetization and both can be used to determine the anisotropy field amplitude $H_K=2K/M_s$. The permeability

solution can be obtained by finding the solution that minimizes (3-27). To do this, a determination of the optimum angle, θ^*, that minimizes the energy is found using the relation:

$$\frac{\partial E}{\partial \theta} = 2K\sin(\theta^*)\cos(\theta^*) - M_s H_e \cos(\theta^* + \theta_K) - M_s H_t \sin(\theta^* + \theta_K) = 0 \tag{3-28}$$

The transverse field, H_t, is then expressed as a function of the optimum angle, θ^* by rearranging equation (3-28):

$$H_t = \frac{M_s H_e \cos(\theta^* + \theta_k) - 2K\sin\theta^*\cos\theta}{M_s \sin(\theta^* + \theta_k)} \tag{3-29}$$

The (differential) transverse susceptibility can then be found using the definition given by

$$\chi_t = \frac{\partial M_t}{\partial H_t} = \frac{\partial M_t}{\partial \theta^*} \div \frac{\partial H_t}{\partial \theta^*} \tag{3-30}$$

For the case considered (refer to Figure 3-1), **M** is given by

$$M = \underbrace{M_s \cos(\theta^* + \theta_k)}_{M_t}\, \vec{e}_t + M_s \sin(\theta^* + \theta_k)\, \vec{e}_z \tag{3-31}$$

It follows that

$$\frac{\partial M_t}{\partial \theta^*} = -M_s \sin(\theta^* + \theta_k) \tag{3-32}$$

The other term needed is given by

$$\frac{dH_t}{d\theta^*} = \frac{2KM_s \sin\theta^* \cos\theta^* \cos(\theta^* + \theta_k) - 2KM_s \sin(\theta^* + \theta_k)\cos 2\theta^* - M_s^2 H_e}{M_s{}^2 \sin^2(\theta^* + \theta_k)} \tag{3-33}$$

The transverse differential susceptibility is then given by

$$\chi_t = \frac{M_s{}^2 \sin^3(\theta^* + \theta_k)}{M_s H_e + 2K\sin(\theta^* + \theta_k)\cos 2\theta^* - 2K\sin\theta^*\cos\theta^*\cos(\theta^* + \theta_k)} \tag{3-34a}$$

In terms of the anisotropy field H_K (3-34a) can be expressed as

$$\chi_t = \frac{M_s \sin^3\left(\theta^* + \theta_k\right)}{M_s H_e + H_K \sin\left(\theta^* + \theta_k\right)\cos 2\theta^* - .5 H_K \sin 2\theta^* \cos\left(\theta^* + \theta_k\right)} \tag{3-34b}$$

For the limiting case of saturation, as H_e approaches ∞, the susceptibility vanishes like $1/H_e$ independent of the material parameters and

$$\lim_{H_e \to \infty} \chi_t = 0 \tag{3-35}$$

Condition (3-35) is a well established characteristic of the MI effect. While in the case of zero measured field, we see a distinct generally nonzero value given by

$$\chi_t(H_e = 0) = \frac{M_s \sin^3(\theta^* + \theta_K)}{H_K \sin(\theta^* + \theta_K)\cos 2\theta^* - .5 H_K \sin 2\theta^* \cos(\theta^* + \theta_K)} \tag{3-36}$$

Therefore, using the definition of the transverse magnetic permeability, we have

$$\mu_t = \mu_0 + \frac{M_s \sin^3(\theta^* + \theta_K)}{M_s H_e + H_K \left[\sin(\theta^* + \theta_K)\cos 2\theta^* - .5 \sin 2\theta^* \cos(\theta^* + \theta_K)\right]} \tag{3-37}$$

The relation given in (3-37) does not assume small transverse field amplitudes as is made by Yoon *et al* [75]. Figure 3-2 shows results from the equilibrium calculations used to compute (3-37) and Figure 3-3c compares both ((3-37) vs Yoon) predicted permeabilities.

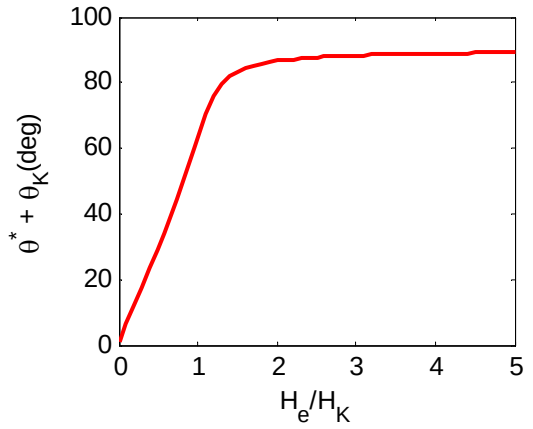

(a) orientation angle of M_y

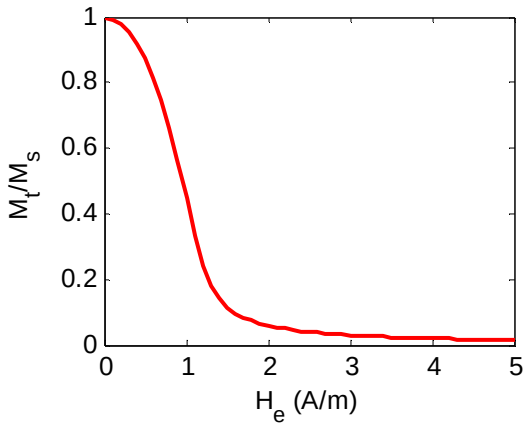

(b) M_t/M_s versus H_e

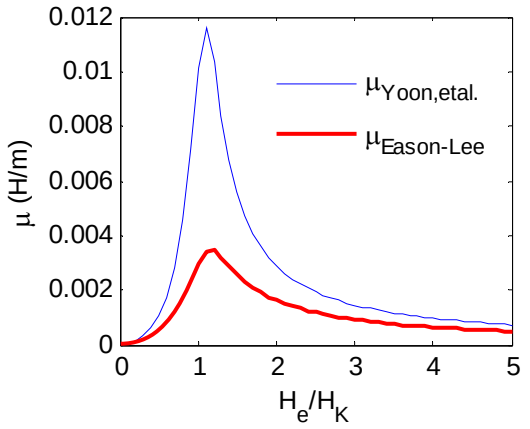

(c) permeability comparisons Yoon *et al*. versus (3-33) labeled as Eason-Lee

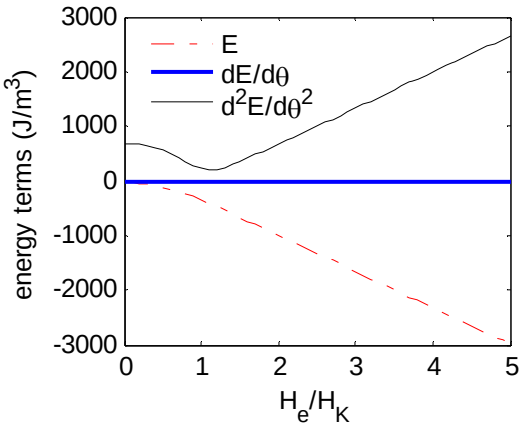

(d) resulting energy terms showing that angle minimizes energy.

Figure 3-2 Comparisons of permeability models with/without small amplitude for transverse anisotropy.

It is observed that relaxing the assumption of a small transverse field leads to smaller predicted permeability values compared to the model by Yoon *et al*. But this is very similar to the difference between coupled and decoupled models pointed out earlier by an assumption of a small transverse field amplitude which results in decoupling the explicit equations of motion. The difference is particularly large in the vicinity of the critical point of the anisotropy field, $H_e \approx H_K$, and well below the saturation field, which is the region of interest in this thesis.

3.1.5 Permeability From Linearized skewed-Gilbert Equation

There is another closed form solution approach useful at higher frequencies. The approach is to reduce the coupled nonlinear equations including Maxwell's and the Gilbert equation to a more tractable form by directly *decoupling* the electromagnetic from the magnetization motion equation by approximating $\mathbf{M} \approx [\chi]\mathbf{H}$ where $[\chi]$ is the magnetic susceptibility tensor thus leading to

$$\mathbf{B} \approx \left[\boldsymbol{\mu}(H_e)\right]\mathbf{H} \text{ where } \left[\boldsymbol{\mu}\right] = \mu_0\left[\mathbf{I}\right] + \left[\boldsymbol{\chi}(H_e)\right] \tag{3-38}$$

With (3-38), the Maxwell's equations no longer explicitly depend on **M;** and the linear system can be solved for an impedance model in terms of the permeability, possibly leading to a scalar form like that derived using the energy approach. The solution for the permeability tensor, [**μ**], can then be derived separately and strictly from the micromagnetics equation, capturing the dependence on both frequency *f* as well as the external field, H_e.

In particular, a permeability model can be derived in closed form from the linearized LLG (or Gilbert) equation for a quasi-static problem which satisfies the following assumptions:

1) The amplitudes of the *ac* fields are small compared to that of the *dc* fields.

2) Equilibrium total effective field ($\mathbf{H}_{Td}$) and magnetization ($\mathbf{M}_d$) are known *a priori* at the equilibrium state defined by [76]

$$\mathbf{M}_d \times \mathbf{H}_{Td} = 0 \text{ where } \left\|\mathbf{M}_d\right\| = M_s \tag{3-39}$$

3) Exchange and demagnetization effects are neglected leading to

$$\mathbf{H}_T \approx \mathbf{H} + \mathbf{H}_K \tag{3-40}$$

Under assumptions 1 and 2, the linearized LLG equation can be obtained by removing all products of *ac* terms leading to the following:

$$\left[\boldsymbol{\Gamma}_d\right]\left(\partial \mathbf{M}_\sim / \partial t\right) = -\gamma\left(\mathbf{M}_d \times \mathbf{H}_{T\sim} + \mathbf{M}_\sim \times \mathbf{H}_{Td}\right) \tag{3-41}$$

$\boldsymbol{\Gamma}_d$ is given by $\boldsymbol{\Gamma}_d = \mathbf{I} - (\alpha/M_s)\text{skew}(\mathbf{M}_d)$. Substituting a general harmonic form of $\mathbf{M} = \mathbf{M}_d + \mathbf{M}_\sim$ into the anisotropy field equation, the anisotropy field can alternatively be expressed as

$$\mathbf{H}_{\mathrm{K}} = \left[\mathbf{M}_{\mathrm{K}}\right]\left(\mathbf{M}_{\mathrm{d}} + \mathbf{M}_{\sim}\right) \tag{3-42}$$

The matrix, $[\mathbf{M}_{\mathrm{K}}]$ is a matrix of all zeros except for a single element, depending on the preferred anisotropy direction. For example, in the case of axial anisotropy, matrix element $\mathrm{M_K}(3,3)$ equals $H_{\mathrm{K}}/M_{\mathrm{s}}$. It follows from (3-42) with assumption 3 that

$$\mathbf{H}_{\mathrm{Td}} = \mathbf{H}_{\mathrm{e}} + \left[\mathbf{M}_{\mathrm{K}}\right]\mathbf{M}_{\mathrm{d}} \tag{3-43}$$

$$\mathbf{H}_{\mathrm{T}\sim} = \mathbf{H}_{\sim} + \left[\mathbf{M}_{\mathrm{K}}\right]\mathbf{M}_{\sim} \tag{3-44}$$

Permeability Tensor for the Case of Axial Anisotropy

For the case of axial anisotropy, the equilibrium magnetization $\mathbf{M}_{\mathrm{d}}$ and corresponding anisotropy matrix, $[\mathbf{M}_{\mathrm{K}}]$, is given by

$$\mathbf{M}_{\mathrm{d}} = \begin{bmatrix} 0 & 0 & M_{\mathrm{s}} \end{bmatrix}^{T} \tag{3-45}$$

$$\left[\mathbf{M}_{\mathrm{K}}\right] = \left|\mathbf{H}_{\mathrm{K}} / M_{\mathrm{s}}\right| \begin{bmatrix} 0 & 0 & 0 \\ 0 & 0 & 0 \\ 0 & 0 & 1 \end{bmatrix} \tag{3-46}$$

Using these relations, solving for $[\boldsymbol{\chi}]$, we have [62]

$$\frac{[\boldsymbol{\mu}]}{\mu_0} = [\mathbf{I}] + \frac{\gamma}{\mu_0}\left[-j\omega\left[\boldsymbol{\Gamma}_d\right] + \gamma \mathbf{S}_1 \mathbf{M}_{\mathrm{K}} + \gamma\left[\mathrm{S}_2\right]\right]^{-1}\left[\mathrm{S}_1\right] \tag{3-47}$$

$\left[\boldsymbol{\Gamma}_{\mathrm{d}}\right] = [\mathbf{I}] - \left(\alpha / M_{\mathrm{s}}\right) Skew(\mathbf{M}_{\mathrm{d}})$; $[S_1] = Skew\left(\mathbf{M}_{\mathrm{d}}\right)$; and $[S_2] = Skew\left(\mathbf{H}_{\mathrm{e}} + \left[\mathbf{M}_{\mathrm{K}}\right]\mathbf{M}_{\mathrm{d}}\right)$. In the case when the equilibrium direction is parallel to the preferred anisotropy direction, (3-47) reduces to

$$\frac{[\boldsymbol{\mu}]}{\mu_0} = [\mathbf{I}] + \frac{\gamma}{\mu_0}\left[-j\omega\left[\boldsymbol{\Gamma}_{\mathrm{d}}\right] + \gamma\left[\mathrm{S}_2\right]\right]^{-1}\left[\mathrm{S}_1\right] \tag{3-48}$$

Given the solution in (3-48), it can be shown that for the axially aligned case considered, the permeability tensor take the form [11]:

$$[\boldsymbol{\mu}] = \begin{bmatrix} \mu & j\mu_a & 0 \\ -j\mu_a & \mu & 0 \\ 0 & 0 & \mu_0 \end{bmatrix} \tag{3-49}$$

where μ and μ_a depend on both the input frequency ω and the external magnetic field, H_e. In SI units,

$$\mu_a = \mu_0 + \frac{\omega_H \gamma M_s}{\omega_H^2 - \omega^2} \text{ and } \mu = \frac{\omega \gamma M_s}{\omega_H^2 - \omega^2} \tag{3-50}$$

where $\omega_H = \gamma\left(H_e + H_K\right) - j\omega\alpha M_s$.

In the case of axial anisotropy, one can determine an effective scalar permeability from (3-49) that can be used with the impedance model for the MI element. One expression derived from [**μ**], presented by Gurevich *et al*. and used later by Usov *et al*. for the lumped-parameter transverse permeability for the problem considered is given by

$$\mu_{1\theta} = \mu - \mu_a^2 / \mu \tag{3-51}$$

A second lumped parameter permeability expression which follows from computing the eigenvalue(s) of [**μ**] is given by

$$\mu_{2\theta} = \mu + \mu_a \tag{3-52}$$

Figure 3-4 is a plot of the amplitudes of their values for the case of axial anisotropy versus the external field, H_e.

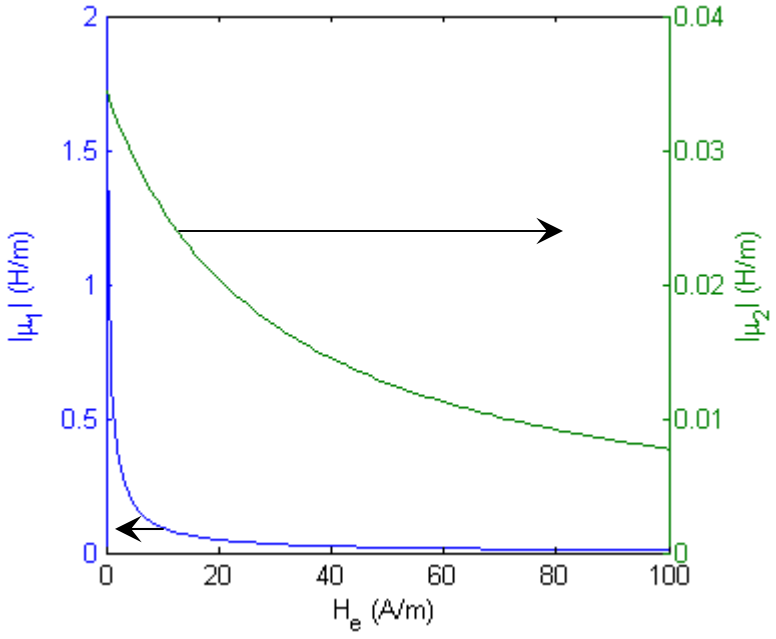

Figure 3-3 Permeability comparisons. μ_1 is given by (3-52) and μ_2 is given by (3-51)

Figure 3-3 illustrates both permeability models where the second effective permeability definition given in (3-52) is one order of magnitude smaller than that of (3-51). Also, computing an impedance using the smaller permeability (3-52) results in voltages more closer to experiment, as will be shown in Chapter 4 with comparisons of this model against a coupled nonlinear harmonic model and experimental data. Also, it is noted that the smaller of the two models in Figure 3-3 corresponds to magnetization domain wall propagation along the radial direction while the other corresponds to one along the axis of the wire [11].

3.2 Space-Time MI Effect Model Approach

The previous decoupled MI effect model results from a reduction of a more general space-time MI effect model. Using numerical tools, the more general approach is considered here in the context of the cylindrical MI element solved using a meshless

method as summarized in Chapter 2 and using additional numerical tools discussed in the Appendix. As a more general approach, in addition to analyzing the results from the model predicting the MI effect, particularly in a weak-field (H_e=0), computational costs are briefly discussed.

3.2.1 Simulation Background

The space-time model describes the variables **H**(**x**,*t*) (magnetic field intensity), **M**(**x**,*t*) (magnetization), φ_D(**x**,*t*) (demagnetization potential), and *T*(**x**,*t*) (temperature). With this model, we simulate predictions investigating the influence of temperature and frequency on the predicted switching mode for the transverse magnetization. The effects of temperature on the MI effect have been studied experimentally in MI sensors. In an earlier study [29] of amorphous *Co*-based MI elements, it was found that the MI effect increases initially (from room temperature) with temperature over a range of approximately 50-100 ^{o}C from room temperature. However, after passing this range, the MI voltage vanishes as the temperature continues to increase towards what is known as the Curie temperature (or Curie point). In another study before the introduction of MI sensors, the effects of temperature on the magnetic permeability was investigated in Co-based wires where consistent behavior was observed near room temperature [77]. It is noted however, that the observations have been made on the initial temperature sweep only. It has been shown that different behavior is observed on the temperature reversal.

For many magnetic materials, the decline of the permeability with temperature is due to a well known decrease in the saturation magnetization M_s with temperature (along with other magnetic parameters) [78]. However, the peculiar initial increase in the regular

amorphous Co-based MI element wire does not follow the typical monotonic trend and this is examined here using the space-time modeling approach.

The discussion of modeling the MI effect using this approach is organized as follows: first, the explicit general space-time equations of motion are reduced for the cylindrical amorphous MI element. Then, computational results are discussed considering temperature, frequency, and their effects on the mode of switching.

Amorphous Circular Element

The reduction of the equations of motion is made to describe a uniform axially oriented domain structure in an amorphous circular wire element. This configuration in the MI element is an approximation based on experimental observations made in MI element wires where such Co-based amorphous wires have been shown to posses a large volume of axially oriented domains in the core with transversely oriented alternating domains in the exterior using Bitter patterns[4] [69]. Also, the observed experimental trends in these wires were very consistent with axially oriented domains, where the peak MI voltage appears at the origin. This approximation in the space-time model leads to a reduction in the equations of motion such that spatial variations exist only in the radial dimension of the wire.

Meshless methods (MLMs) are used to discretize the spatial coordinate. In particular, the *Hp*-Cloud MLM shape functions are used with a 3rd order reproducibility in a point collocation scheme (see Chapter 2 and/or Appendix A). The time integration performed is implicit, using a second order Newmark integration scheme which is discussed in

[4] Bitter patterns techniques are a "classical" method used to observe static (or slow) magnetic domain patterns using magnetic colloidal suspension in fluids where more particles accumulate (coagulate) near domain walls. A good summary of the method can be found in [67].

Appendix B. At each time step, the nonlinear problem is solved using a Broyden (quasi-Newton) scheme with an optimal line search and the details of this approach are discussed in Appendix C.

3.2.2 Reduced Equations of Motion

In the case of only radial variation, the Maxwell's equations reduce to the following:

$$\mu_0 \frac{\partial H_{\mathrm{r}}}{\partial t} + \frac{\partial M_{\mathrm{r}}}{\partial t} = 0 \tag{3-53}$$

$$\mu_0 \frac{\partial H_{\theta}}{\partial t} + \frac{\partial M_{\theta}}{\partial t} = \frac{\partial^2 H_{\theta}}{\partial r^2} + \frac{1}{r}\frac{\partial H_{\theta}}{\partial r} - \frac{H_{\theta}}{r^2} \tag{3-54}$$

$$\mu_0 \frac{\partial H_{\mathrm{z}}}{\partial t} + \frac{\partial M_{\mathrm{z}}}{\partial t} = \frac{\partial^2 H_{\mathrm{z}}}{\partial r^2} + \frac{1}{r}\frac{\partial H_{\mathrm{z}}}{\partial r} \tag{3-55}$$

In the micromagnetics formulation, all three magnetization components are generally nonzero and the form given in Chapter 2 does not reduce from how it is presented. It is given by

$$\left[\mathbf{I} - \frac{\alpha}{M_s}\mathrm{skew}(\mathbf{M})\right]\frac{\partial \mathbf{M}}{\partial t} = -\gamma \mathbf{M} \times \mathbf{H}_T \tag{3-56}$$

However, the components of the total effective field $\mathbf{H}_{\mathrm{T}}$ are reduced. Particularly, the magnetization exchange ($\mathbf{H}_{\mathrm{X}}$) and demagnetization ($\mathbf{H}_{\mathrm{D}}$) reduce to

$$\nabla^2 \mathbf{M} = \left[\left(\frac{\partial^2 M_{\mathrm{r}}}{\partial r^2} + \frac{1}{r}\frac{\partial M_{\mathrm{r}}}{\partial r} - \frac{M_{\mathrm{r}}}{r^2}\right) \quad \left(\frac{\partial^2 M_{\theta}}{\partial r^2} + \frac{1}{r}\frac{\partial M_{\theta}}{\partial r} - \frac{M_{\theta}}{r^2}\right) \quad \left(\frac{\partial^2 M_{\mathrm{z}}}{\partial r^2} + \frac{1}{r}\frac{\partial M_{\mathrm{z}}}{\partial r}\right)\right]^T \tag{3-57}$$

$$\nabla \varphi_{\mathrm{D}} = -\left[\partial \varphi_{\mathrm{D}} / \partial r \quad 0 \quad 0\right]^T \tag{3-58}$$

The demagnetization equation reduces to

$$\mu_0\left(\frac{\partial^2\varphi_{\mathrm{D}}}{\partial r^2}+\frac{1}{r}\frac{\partial\varphi_{\mathrm{D}}}{\partial r}\right)-\left(\frac{\partial M_{\mathrm{r}}}{\partial r}\right)=0 \tag{3-59}$$

Lastly, the thermal diffusion equation for the circular wire reduces to

$$\sigma(T)\rho c_p(T)\frac{\partial T}{\partial t}=\sigma(T)\frac{\partial}{\partial r}\cdot\left(k(T)\frac{\partial T}{\partial r}\right)+\left\|\nabla\times\mathbf{H}\right\|^2 \tag{3-60}$$

In (3-60), the curl of **H** is given by

$$\nabla\times\mathbf{H}=\left[0\quad -\frac{\partial H_{\mathrm{z}}}{\partial r}\quad \frac{1}{r}\frac{\partial(rH_{\theta})}{\partial r}\right]^T \tag{3-61}$$

3.2.3 Temperature Dependence of Parameters

The parameters that depend on temperature considered in the model are $\sigma(T)$, $k(T)$, $M_{\mathrm{s}}(T)$, $K(\mathrm{T})$, and $c_{\mathrm{p}}(T)$. To our knowledge, for the temperature range considered here (300 – 450K), the experimental material given by $Co_{68.15}Fe_{4.35}Si_{12.5}B_{15}$, has not had all of these material properties reported and thus their values are estimated. In many cases, however, a single data point (at room temperature) has been measured and reported, and thus the temperature dependence of the parameters has been approximated using commonly used characteristic curves that pass through these single data points reported for the material. Taking this approach, the material parameters are then expected to not only demonstrate the proper variation with temperature, but be reasonably close to an expected value, as well. A summary of the final relations is given next.

Electrical Conductivity Dependence on Temperature

The temperature dependence of the electrical conductivity $\sigma(T)$, particularly, in alloys, is approximated where the bulk resistivity ($1/\sigma$) is given as a second order parabolic temperature dependence, given by

$$\rho_1(T) = \frac{1}{\sigma(T)} \approx \rho_0 + CT^2 \tag{3-62}$$

ρ_0 is the resistivity at $T = 0$ and C is a rate control parameter.

Thermal Conductivity Dependence on Temperature

The thermal conductivity, $k(T)$, is approximated by computing an interpolated volume compositional average (with cobalt and iron) using measured values for the respective materials over the temperature range considered [64].

Saturation Magnetization Dependence on Temperature

The saturation magnetization dependence on temperature in magnetic alloys has been studied considerably in the past and relations that approximate the dependence have been presented in previous works, and one in particular, is used here [38]. The saturation magnetization is approximated by

$$M_s(T) = M_{s0}(1 - T/T_c)^{\beta} \tag{3-63}$$

M_{s0} is the value at $T = 0$; T_c is the Curie temperature, given in [79] as 310 ^{o}C; and the value for β that has been reported from experimental measurements in both iron and cobalt is $\beta = 0.36$ [38].

Anisotropy Dependence on Temperature

The variation of the first anisotropy constant with temperature has been approximated using a hyperbolic tangent function, inspired by classical curves reported for cobalt and iron [10]. The curve has also been scaled to be consistent with the *as cast* data point reported in [68], and subsequently estimated after annealing [23], for the experimental material considered. The general relation is given by

$$K(T) = -K_0 \tanh(\varsigma(T - T_0)) + K_{\mathrm{m}} \tag{3-64}$$

The parameter ζ controls the variation rate with temperature and has been estimated based on previously reported values of K(T) for cobalt and iron [10].

Heat Capacity Dependence on Temperature

Similar to the thermal conductivity, $c_{\mathrm{p}}(T)$, is approximated by computing an interpolated volume compositional average (with cobalt and iron) using measured values for the constituent materials over the temperature range considered [64].

3.2.4 Boundary Conditions

The boundary conditions are reduced in such a way that the equation for the radial component of the magnetic field is described by a scalar equation given by:

scalar equation

$$\mu_o H_r = -M_r \tag{3-65}$$

Then, the remaining boundary conditions are given by

boundary conditions

(t, 0)
$$\partial \mathbf{H} / \partial r = \partial \mathbf{M} / \partial r = \varphi_{\mathrm{D}} = \partial T / \partial r = 0 \tag{3-66a}$$

(t, r_o)
$$H_\theta = I_s / 2\pi r_0 \text{ and } H_z = H_e = 0 \tag{3-67a,b}$$
$$\partial \mathbf{M} / \partial r = 0 \tag{3-67c}$$
$$\mu_0 \partial \phi_D / \partial r = M_r \tag{3-67d}$$
$$k \partial T / \partial r = h\left[T(t, r_0) - T_\infty\right] \tag{3-67e}$$

3.2.5 Initial Condition

For simplicity, the initial condition is assumed uniform at $t = 0$. The magnetization is assumed *initially* "saturated" along the axis of the wire leading to the initial condition given by

$$\mathbf{H}(0, r) = \varphi_{\mathrm{D}}(0, r) = 0\,,\ \mathbf{M}(0, r) = \begin{bmatrix} 0 & 0 & M_s \end{bmatrix}^T,\ T(0, r) = T_\infty \tag{3-68}$$

3.2.6 Discussion of Computational Results

The model simulates the experimental cylindrical amorphous Permalloy $(Fe_{0.06}Co_{0.94})Si_{12.5}B_{15}$ [14] and the material parameters used in the model are taken from reported experimental data and are provided in Tables 3-1 and Tables 3-2, where Table 3-2 provides the parameters that are temperature dependent obtained from the relations summarized above.

Table 3-1 Non-temperature dependent simulation parameters for circular wire

f (MHz)	I_s *(mA)*	H_K (A/m)	α	A_X J/m^2	γ
1-1000	15	7.8	0.01	10^{-11}	q_e/m_e

Table 3-2 Temperature dependent simulation parameters for circular wire

(K)	T_1 (K) 300	T_2 (K) 400	T_3 (K) 500	T_4 (K) 600
σ ($\mu\Omega$-m)$^{-1}$	0.769	0.500	0.345	0.250
k (kW/m-K)	74.23	61.22	54.77	48.31
M_s (T)	0.8101	0.6926	0.5212	-
K (J/m^3)	0.1912	0.1547	0.1148	0.763
c_p (kJ/kg-K)	301.49	327.99	347.88	367.76

The highlighted columns represent the temperature range of calculations discussed here. In the model calculations, a lookup table like that shown in Table 3-2 is used.

Effects of Elevated Ambient Temperatures

For temperature effects, the MI effect is simulated at T_∞ = 27, 77, and 127 ^oC. The convective boundary condition is modified such that the ambient temperature, T_∞, has a higher fixed temperature. Recall the convective boundary condition is given by

$$-k\nabla T(t,r_0) = h\left(T(t,r_0) - T_\infty\right) \tag{3-69}$$

Figure 3-5 shows the dynamic response of **H** and **M** components where the left column shows **H** components and the right column shows **M**.

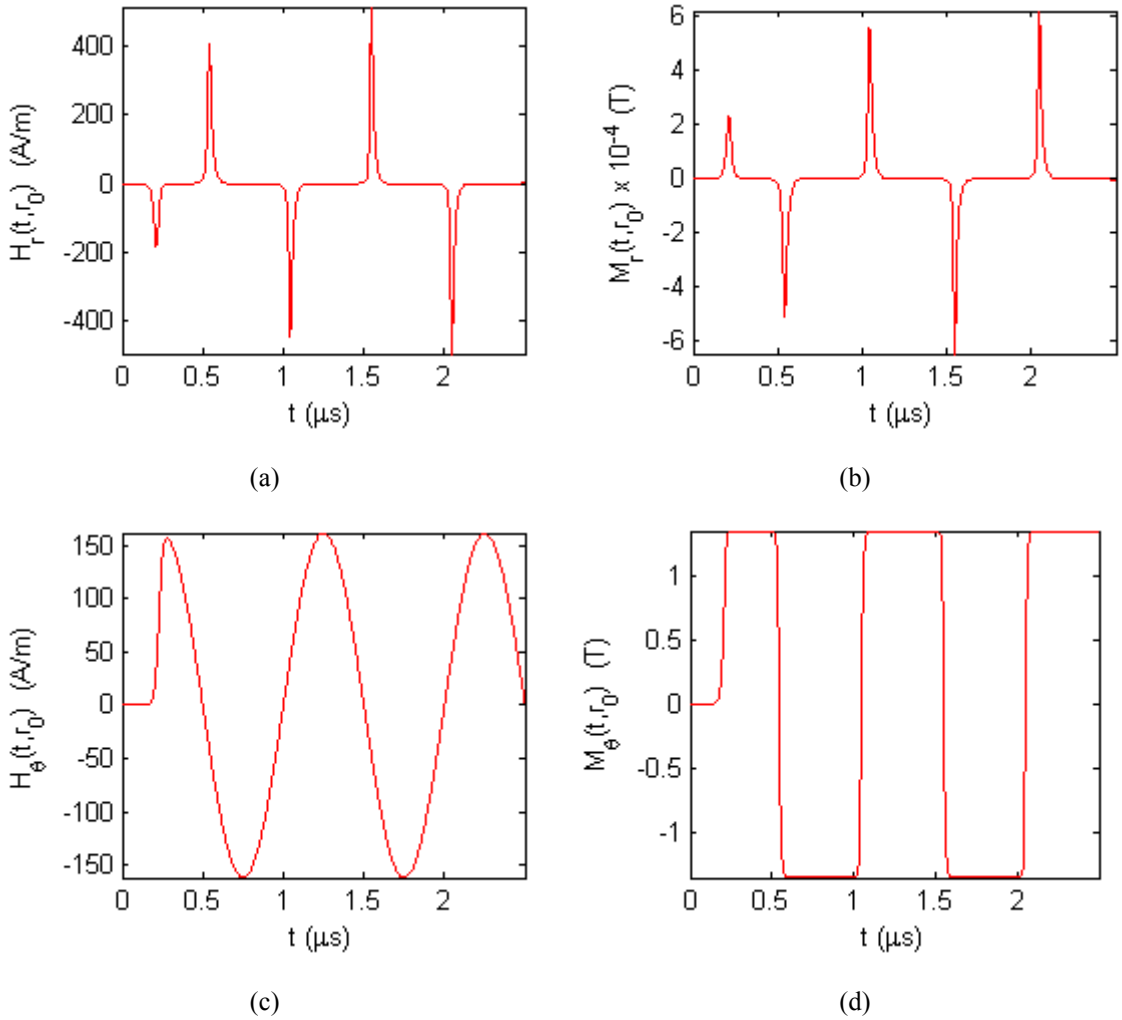

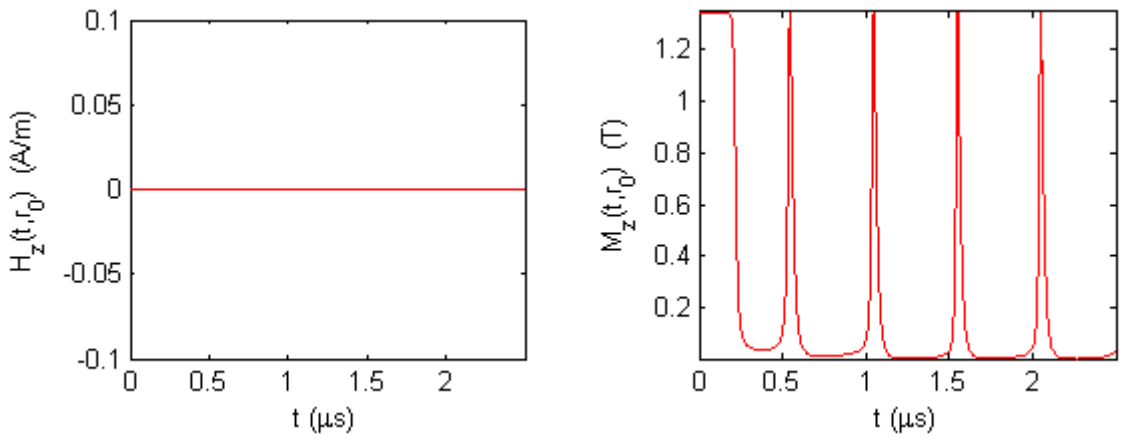

(e) (f)

Figure 3-4. Temporal solutions of **H** and **M** components on the wire surface at 27° C.

Figure 3-4 shows the "nature" of the field responses over 2.5 current cycles which are computed at a current frequency of 1 MHz with a current amplitude of 15 *m*A. The corresponding components, H_r and M_r, in Figures 3-4 (a) and (b), respectively, have an anticipated relationship based on equation (3-65). The coupling between these two components is evident where both show such peaks in the dynamic transitions of the magnetization being the temporal regions of precession.

The other two components are of more interest as they more directly contribute to the MI effect. Figure 3-4 (c) and (d) show H_θ and M_θ components, respectively. It is seen that as the transverse magnetic field transitions to a large enough amplitude in either direction, the magnetization responds by switching to a saturated state very rapidly. This is expected in a soft magnetic material, which is the case for the amorphous annealed treated alloy considered, based on their B-H curves that have been previously reported [14].

Even though the *z* component of the magnetic field intensity, H_z, is zero, M_z is clearly influenced by the dynamics of the current source and the transverse component. This is a

consequence of the constraint condition of the micromagnetics equation (see Appendix D), where as the transverse component is harmonically driven by the current, as it passes through a value of zero, the *z* component then must be at a maximum amplitude since the magnetization switching takes place primarily in the θ-*z* plane. The result is a peculiar double-peaking of the z component. In other words, in one cycle, the *z* component peaks twice in the same direction (positive).

Magnetization Switching Mode: Origin of the Dynamic Domain Wall

In magnetic materials, *switching mode* refers to the manner in which the magnetization domains align themselves with the driving *ac* external field over the volume of the wire. In this case, the driving field is the transverse magnetic field H_θ. The question arises as to whether all the magnetization changes in the MI element structure are simultaneous or do domain walls play a role in achieving the reorientation of all of the domains. Recall that a domain wall is defined as a region of transition (typically much more narrow compared to the domain size) between two differently oriented magnetization regions within a magnetic material. Figure 3-6 shows a simplified diagram of one type of domain wall known as a 180° Bloch wall [10].

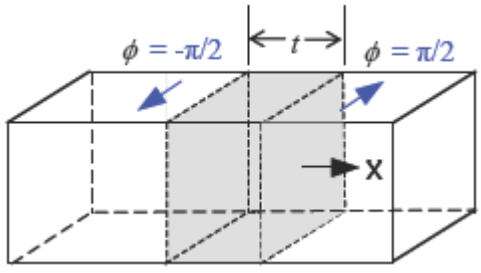

Figure 3-5. A 180° Bloch wall illustration. (The domain wall is within the t_w region)

When a harmonic field is introduced into a wire, the question as to how the magnetization switches from one orientation to another is relevant because the answer is obviously *not* always the same for all materials and conditions. For example, in very low input frequencies and at low amplitudes (of the external field), the switching mode can take place by way of reversible domain wall motion [10]. While, under the same conditions, but with larger fields, additional switching modes can take place including irreversible domain wall motion including conditions with combinations of things like Barkhausen jumps as well as pure rotation. Additionally, when the frequencies are relatively high, the domain wall motion may be somewhat unfavorable due to the fact that domain walls have dynamic attributes. If the variation of the magnetic field happens too rapidly and exceeds the amount of time required for the formation of a domain wall, then their formation and propagation become less favorable and this is referred to as domain wall dampening.

If a domain wall participates in the switching mode, it is common that one way of switching of the magnetization is for a domain wall(s) to serve as means to "sweep" an orientation through the structure, where one side of the wall is oriented in one direction while as the wall moves, the other side that is "growing" occupying the increasing volume until all domains are oriented along the direction of the external field.

The computational results from the space-time model reveal that for the conditions here, which have been taken from real MI sensors, domain wall motion, including radial propagation, is a key mode of switching. In general, such an observation would be difficult to make by experiments and, to our knowledge, has not been made for the case of MI elements.

Figure 3-6 illustrates the motion of the dynamic domain wall displaying a series of "snapshots" of the transverse magnetization in a cycle of the magnetic field intensity in a quarter geometry model.

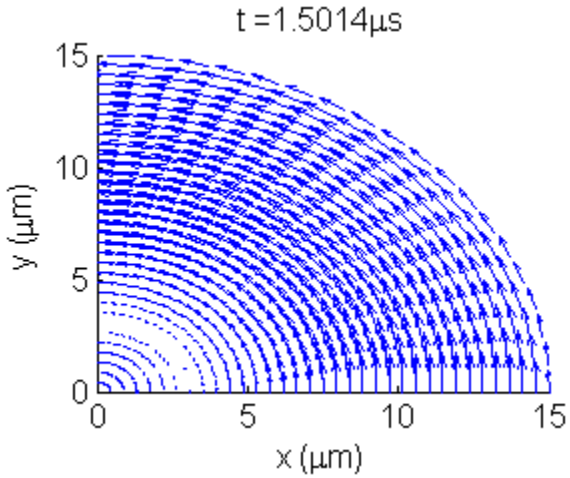

(a) M_θ distribution showing radially translating domain wall at t_1

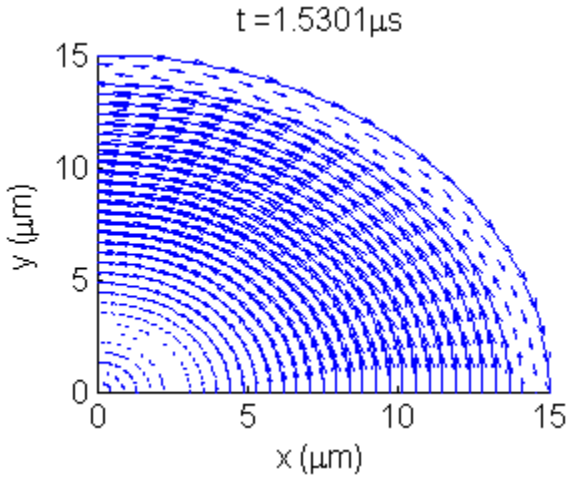

(b) M_θ distribution showing radially translating domain wall at t_2

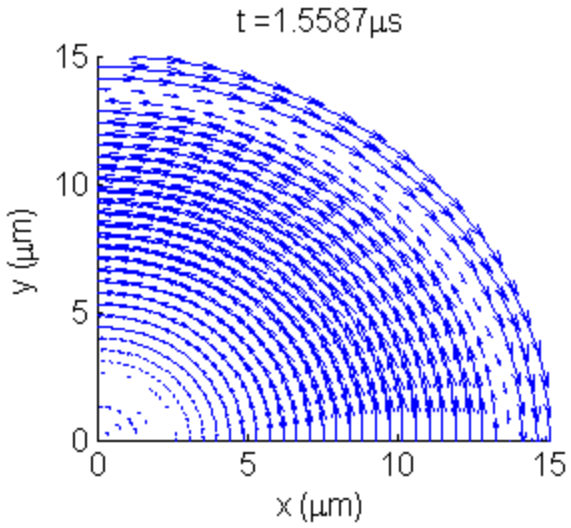

(c) M_θ distribution showing radially translating domain wall at t_3

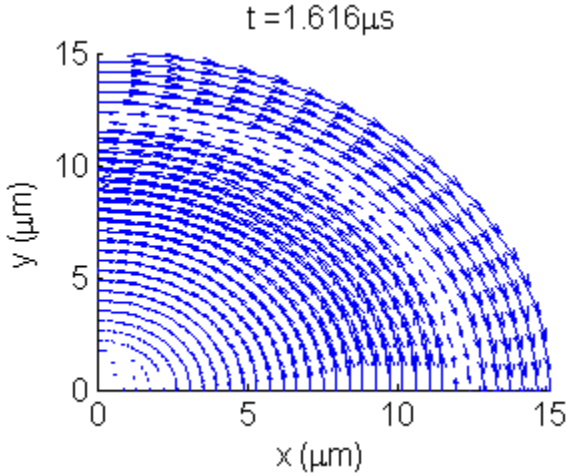

(d) M_θ distribution showing radially translating domain wall at t_4

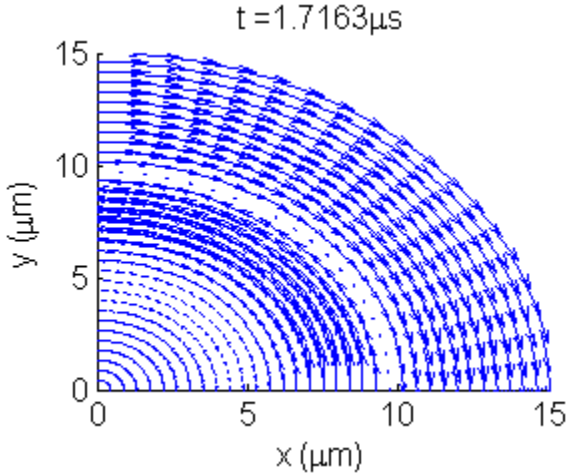

(e) M_θ distribution showing radially translating domain wall at t_5

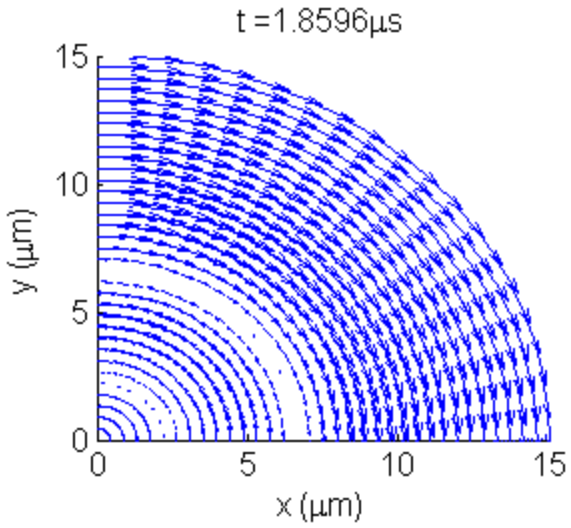

(f) M_θ distribution showing radially translating domain wall at t_6

Figure 3-6. Illustrations of radially propagating 180° Bloch wall in MI element with "snapshots".

It is seen that the dynamic domain wall develops on the surface of the MI element and propagates into the core until the wire is homogeneously transverse in one direction. We point out that for the conditions simulated; there has been mention of the belief that for 1MHz, domain wall motion is dampened [34]. However, a more general analytical coupled nonlinear model reveals that the structure prefers switching by developing propagating dynamic domain walls. Thus, even at 1 MHz, the role of domain walls in the dynamics of the MI effect may be much more significant that originally believed.

Increasing V_{MI} With Temperature

Figure 3-7 shows the transverse magnetic field intensity radial distribution in the wire, $H_\theta(r,t_p)$, and the corresponding magnetization distribution, $M_\theta(r,t_p)$, at three different temperatures of 27, 77, and 127° C. The point in time is taken at the peak t_p of the current in the last cycle of calculations. The data is normalized to fit all curves on the same axes. Figure 3-7(a) shows the transverse magnetic field intensity component (H_θ), (b) shows the corresponding magnetization component, M_θ.

(a) magnetic field distribution at the time of current peak

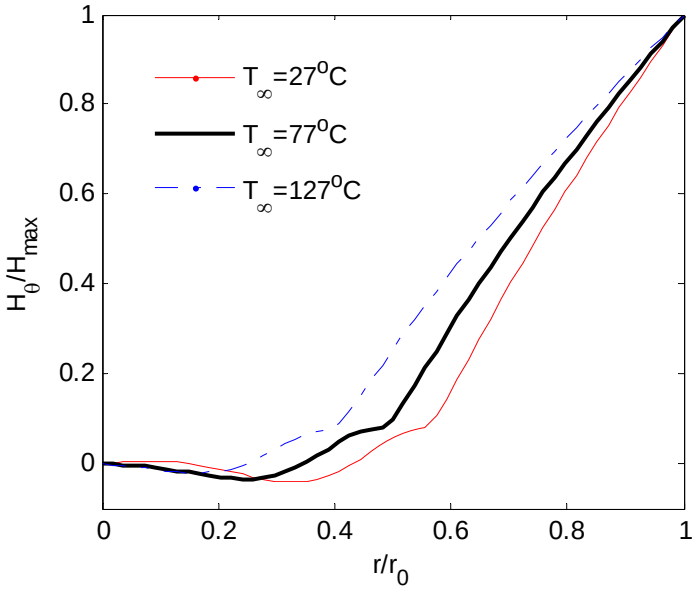

(b) magnetization distribution at the time of current peak

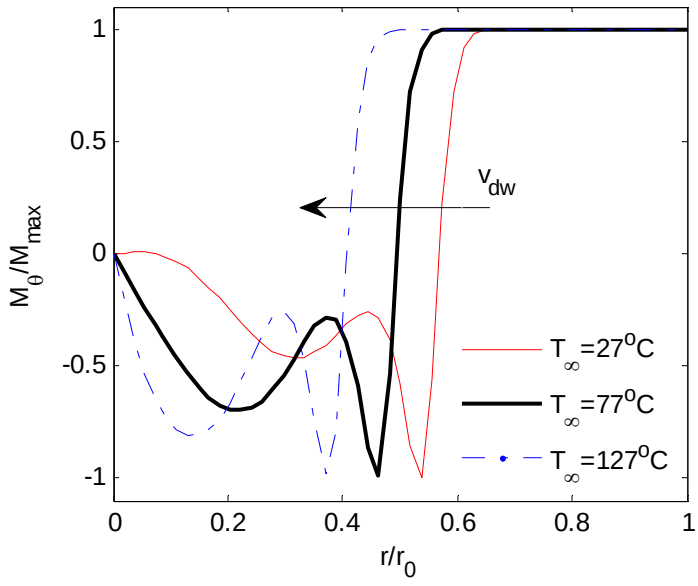

Figure 3-7. H_θ and M_θ spatial distribution with T (a) and (b).

These figures suggest an interesting contribution to the rise in the MI voltage with temperature. Figure 3-7a shows that the influence of elevated temperature from room temperature is to "gently" widen the distribution of the magnetic field intensity H_θ. The observation in the magnetic field can be explained by way of well known characteristics of Maxwell's equations. Firstly, the use of an *ac* current source in the MI element introduces the dynamic phenomena known as the skin effect. Recall the equation for the magnetic field given by

$$\nabla \times \nabla \times \mathbf{H} = -\sigma(\mu_0 \frac{\partial \mathbf{H}}{\partial t} + \frac{\partial \mathbf{M}}{\partial t}) \tag{3-71}$$

Equation (3-71) leads to a length scale for the distribution within the wire (skin effect) where the length scale is known to be such that

$$\delta_s \propto 1/\sqrt{\sigma(T)\mu_\theta \omega} \tag{3-72}$$

Thus, a factor in the distribution widening in H_θ is given by a reduction in the electrical conductivity as temperature increases, causing a wider distribution (or larger skin depth, δ_s).

It is noted that the abrupt change in the corresponding magnetization curves in Figure 3-7(b) is a dynamic *domain wall*. A *dynamic* domain wall must be distinguished from an *equilibrium* domain wall, which typically forms permanently in minimizing the energy of the magnetic structure at room temperature in the absence of external fields. In the dynamic wall seen here, the formation is in the presence of a very active external field H_θ. Figure 3-7(b) shows that as the temperature increases, the dynamic domain wall is seen to increase in speed v_{dw}, propagating from the surface towards the center. Even for seemingly small changes in the magnetic field, this observation is reasonable based on

the well known characteristic of domain walls: they can be moved with very small external fields. Thus, the "small" increase in the distribution (or average H_θ) with temperature gives rise to faster moving domain wall in the MI element wire.

The resulting increase in the inductive voltage V_L with temperature can then be explained by the micro-scale domain wall dynamics. To illustrate this, Figure 3-8 shows a simple schematic of the switching domain wall motion near the surface of the wire as predicted by the model used here.

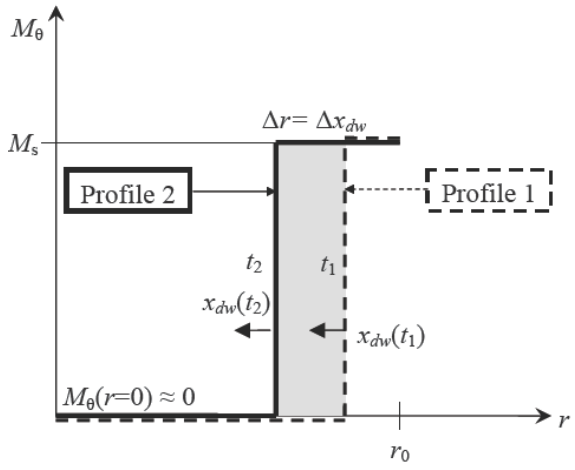

Figure 3-8. Simplified MI element domain wall motion

In the circular wire, because $H_\theta(r=0)=0$, the transverse magnetization is also small at the center for the circular wire. Thus, $M(r=0)\approx 0$, leading to the simple illustrative diagram shown above (also see Fig. 3-7). Figure 3-8 shows that the change in flux is given by the difference between the area under Profile 1 and 2. Thus, the shaded area in Figure 3-8 represents the change in flux. It follows that the inductive voltage can be approximated as follows

$$V_L \propto L_z \frac{d}{dt}\int_0^{r_0} M_\theta dr \approx L_z M_s(T)\frac{\Delta r}{\Delta t} = L_z M_s(T) v_{dw} \tag{3-70}$$

A_{eff} is an effective flux area. Then, an increase in the magnetic field causes an increase in the domain wall velocity, v_{dw}, which gives rise to an increasing voltage based on (3-70). However, (3-70) also suggests that eventually the effects of $M_s(T)$ and possibly other parameters such as anisotropy $K(T)$ begin to dominate causing the expected eventual decline of the MI voltage with temperature.

Temperature Profiles in the MI Element

For a 15 μm radius wire under the given conditions, the wire temperature turns out to be nearly uniform in the wire, taking on the surrounding ambient temperature. Figure 3-9 shows corresponding temperature profiles for the various temperatures of 300 K (27 ^{o}C), 350 K (77 ^{o}C), and 400 K (127 ^{o}C) illustrating the very weak distributions, for a current source I_s = 15 mA at f = 1 MHz.

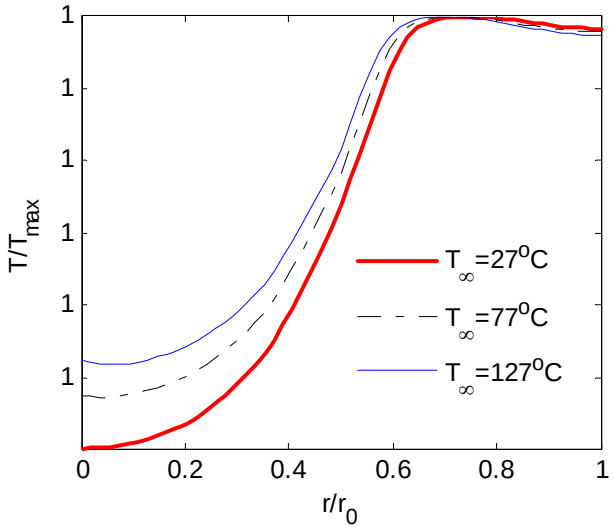

Figure 3-9. Normalized temperature profiles taken a peak current in cycle.

Such a weakly distributed temperature profile is expected based on the wire being very small (r_0=~15μm) along with a large thermal diffusivity given

by $\alpha_d = k / \rho c_p \approx 0.003$ m-s^{-2}, which means heat diffuses quickly in the wire. Thus, for a current source of I_s = 15 mA (and smaller), the steady state temperature profiles should be expected to be uniform in the wire and close to the surrounding temperature, T_∞.

Even for such a mild spatial temperature variation as shown in Figure 3-9, the volume averaged temperature is used and computed by

$$T_{avg} = \frac{1}{r_0}\int_0^{r_0} T(r)dr \tag{3-71}$$

Figure 3-10 shows the corresponding components of the MI voltage components in response to temperature T. In this simulation, because the current is known to be distributed throughout the wire (i.e. weak skin effect), the components of the MI voltage are computed by

$$V_R = \frac{L}{\pi\sigma(T)r_0^2} I_s(t) \text{ and } V_L = -\frac{d\Phi}{dt} \tag{3-72a,b}$$

Where in (3-72b),

$$\Phi = \int_S (\mu_0 \mathbf{H} + \mathbf{M}) \bullet d\mathbf{s} \tag{3-73}$$

Their sum at each point in time provides the total MI voltage across the cylindrical MI element and the amplitude is then taken from the resulting harmonic waveform.

It is seen that from room temperature, the MI voltage increases initially, instead of decreasing.

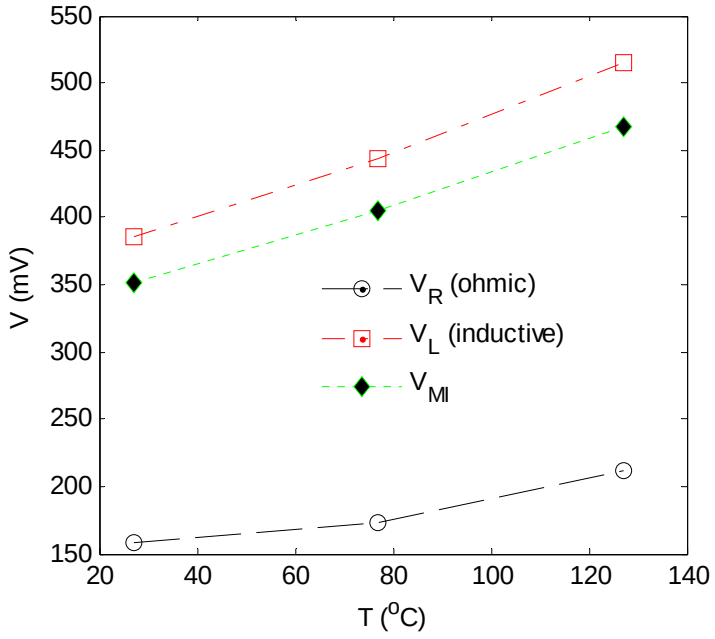

Figure 3-10. Voltage components over 3 temperatures 27, 77, 127 °C.

Table 3-3 shows the same data plotted in Figure 3-10 where an approximation to the thermal sensitivity has been also added in the right-most column.

Table 3-3. MI voltage components vs temperature (at 1 MHz)

	T_1 27 (°C)	T_2 77 (°C)	T_3 127 (°C)	*max dV/dT* (mV/°C)
V_R (mV)	138	173	212	0.78
V_L (mV)	386	444	515	1.42
V_{MI} (mV)	355	405	467	1.24
experiment*	325	-----	-----	-----

Based on the approximated temperature sensitivity, then, for example, on a given day where the temperature may vary approximately 30° C, a drift of approximately 37 mV may occur. Given a MI voltage of 355 mV, this corresponds to a ~10 % deviation. Thus, using an amorphous circular Co-based MI element wire, methods may be needed to reduce the thermal drift in this case.

Therefore, the coupled nonlinear space-time model suggests a mechanism linked to influenced dynamic domain wall motion where increasing temperature near room temperature leads to increased inductive voltages. It is noted that the ohmic component also increases by way of the skin effect increasing the effective resistance in the wire. Generally speaking for both components, it may be stated that the root cause of the observations discussed here are attributed to temperature dependence of the electrical conductivity $\sigma(T)$ in the Co-based alloy.

Effects of Frequency

Experimentally (and theoretically), it has been established that the MI effect has a relatively strong dependence on the frequency f up to a certain limiting peak frequency after which the MI voltage begins to diminish. Many researchers have shown this experimentally and it has also been shown with proposed models using decoupled linear harmonic formulations [31] [80] [22], as well.

Figure 3-11 shows that resulting magnetic fluxes in the wire for frequencies f = 10 and 100 MHz.

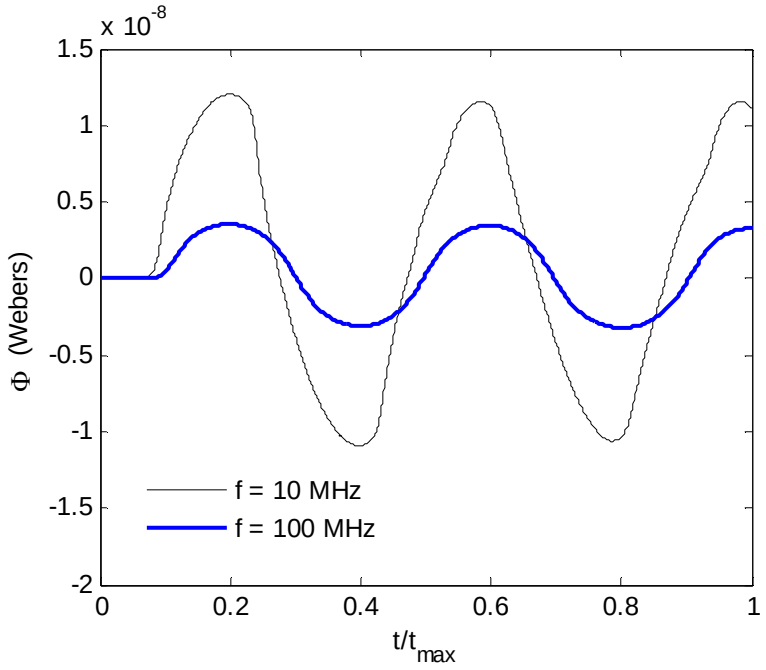

Figure 3-11. Flux over time for f=10 and 100 MHz, I_s=15 mA.

In trying to understand the behavior of the MI effect with frequency, we may try to interpret the behavior in accordance with the switching mode as in the observations from the short range temperature effects near room temperature. It was shown that increasing the wire temperature tends to create faster domain wall propagation which increases the inductive voltage. With this physical picture, consider that the boundary condition on the surface of the wire is given by $I_s/2\pi r_0$, at the location which was shown to be where the formation of the domain wall takes place then moves toward the center. Thus, as the frequency of the current is increased, two mechanisms may be considered to contribute to the rise in the voltage, and then to the subsequent fall in the MI voltage in f.

Rise in the MI Voltage With f

First, note that the resulting amplitude of the flux is greater for 10 MHz than it is for 100 MHz. However, Figure 3-12 (b) shows the resulting amplitudes of the voltage as they increase with the frequency (below ~1GHz), despite the fact that the flux amplitudes

simultaneously decrease with frequency as shown in Figure 3-12. In this situation, the inductive voltage is given by

$$V_{\mathrm{L}} \propto \frac{d\Phi}{dt} \approx \frac{\Delta\Phi}{\Delta t} \tag{3-76}$$

As the frequency changes, the changing flux is due to the evolving skin effect cause by an *ac* current source. The skin effect is a phenomenon predicted by classical electromagnetics (Maxwells equations) in dynamic problems and predicts the degree to which the field distribution is confined more and more to the surface of the structure. Thus, the faster the variation of the source, the more near the surface the field will be, hence the name, the skin effect. Despite this behavior, the increasing rate of variation of the transverse magnetic field results in turning the magnetic moments faster, which produces faster domain walls while increasing (low) frequencies. This mechanism results in relatively rapid changes in the flux Φ. Thus, V_{L} increases as the dynamics is such that the relative change in the flux ($\Delta\Phi$) is faster than the corresponding change in time (Δt). The result is that MI effect demonstrates an increase with frequency (up to a critical point), as discussed next

Decline in the MI Voltage With f

At ultra-high frequencies, the MI voltage begins to flatten out and decrease with frequency as shown in Figure 3-12(b). This has been shown experimentally in MI elements [22]. Figure 3-12 and Table 3-4 show that this occurs on the order of 100s of MHz - 1GHz, which is consistent with experiments in similar Co-based wires. Based on results computed here, a factor contributing to the decrease in the MI voltage is as follows: As the frequency increases, the profile of H_θ becomes increasingly confined to

the surface due to the skin effect, while the values in the core are negligible. However, because the wire prefers that a domain wall form on the surface, these conditions are not conducive to propagate the wall towards to core. For zero transverse field values in most of the wire, the domain wall velocity practically vanishes resulting in a vanishing inductive voltage by way of both a lack of a driving force in the wire and dynamic domain wall dampening as the variation of the source becomes too fast. The end result is that the MI voltage diminishes with frequency from such conditions. We may equivalently state that the relative ratio of the deviations expressed in (3-76) between the flux and time evolves in such a way that the change in time becomes much more rapid compared to the flux change. Since fewer domains are switching within the core, the result is a reduced flux.

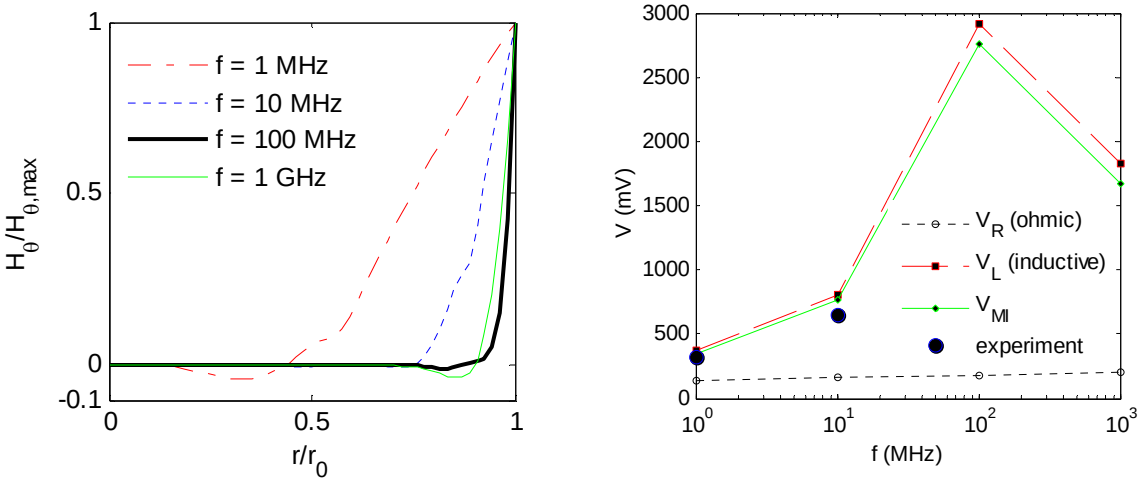

(a) H_θ profile vs f. (at current peak) (b) Voltage components vs f.

Figure 3-12 Transverse magnetic field profiles vs f (a) and MI voltage components (b)

Table 3-4. MI voltage components *vs* frequency at 27°C

	f_1 1 MHz	f_2 10 MHz	f_3 100 MHz	f_4 1000 MHz
V_R (mV)	138	157.3	173.1	197.9
V_L (mV)	378	800	2914	1824
V_{MI} (mV)	351(error=8%)	761(error=17%)	2752	1670

experiment*	325	650	-----	-----

Comparisons To Experiment

Table 3-5 shows computed voltage components with reported experimental measurements. It is seen that the space-time MI effect model is in good agreement with experiments for both frequencies reported with a maximum error of 17 % and the other being 8 %. In the calculations above, M_s was computed using reported measured values (found just recently) of the parameter from researchers working with the same *Co*-based wire alloys [68]. It is seen that the space-time model results in very good agreement with experimental values for all the reported MI voltage values.

3.2.6 Computational Costs

While the model above has been extremely useful in better understanding the MI effect in the conditions considered, it must be recognized that computation times for the problems above are very high. Using a desktop PC, each computation discussed spanning 2.5 cycles, *took on the order 100 hours* for each simulation! This is on the order of several days to compute the MI response for a single external field value. And this is considering that the dimensional space was reduced to (r,t), for example. These characteristics are obviously undesirable, particularly if another approach can be used that alleviates such high computational costs and still preserves the nonlinear coupling between the degrees of freedom.

3.2.7 Summary of Space-Time MI Effect Model

Therefore, the coupled nonlinear space-time model is shown to be capable of describing the MI effect in weak fields, resulting in good fidelity (compared with

frequency data) and very plausible explanations for experimental observations (with temperature). Also, the model results in good qualitative agreement when considering the peculiar increase in the MI voltage with temperature from room temperature.

However, given the benefits of the model, it was also mentioned that the space-time formulation has high computational costs. This observation motivates the question as to whether a different approach can be used that is not too under-descriptive, as we have discussed in decoupled models, and yet maintains good fidelity, resulting in consistent enough behavior with experiments, especially in a weak field.

3.3 Motivation of a Coupled Nonlinear Harmonic MI Effect Model

Given the two approaches considered above, the third approach, introduced in this thesis research, represents a modeling approach in between the two. Benefits include that it preserves nonlinear coupling between the small and large scale mechanisms, while reducing computational demands greatly by eliminating the independent variable of time *t*. A coupled nonlinear harmonic approach, to our knowledge, is one that has not been considered in treating the equations of motion describing the MI effect prior to this research. As such, we introduce this formulation as a way to model the MI effect in a way that strikes a balance between the two previously summarized approaches. In the following two chapters, this modeling approach will be shown to be valuable in predicting the MI effect, providing an improvement in MI effect descriptions over decoupled models, especially in the weak field regime.

CHAPTER 4
THE EFFECTS OF NONLINEAR COUPLING

Using the numerical tools organized in this thesis research, in the previous chapter, we have solved a space-time model predicting the MI effect. While decoupled models are known to be under-descriptive in weak fields, it was also pointed out that the main drawback to a space-time model is that it takes a long time to solve a harmonic problem. In this chapter, a coupled nonlinear harmonic model, which is originally introduced in this work, is used to model the MI effect. To use this approach, it is noted that based on results from the space-time model that showed that at room temperature at a current of ~15 mA, thermal effects are negligible because the temperature in the wire is near ambient and possess a flat spatial distribution. This condition is exploited in the coupled nonlinear harmonic model by eliminating the thermal diffusion equation of motion.

The coupled nonlinear harmonic model is then used to study the effects of both the measured external field H_e and current frequency f, both of which have been studied extensively in MI sensors. In this chapter, the spatial dimension is again reduced to the radial dimension. Because the formulation is harmonic (more consistent with decoupled models), the differences between both approaches are carefully studied to examine the effects of coupling (or decoupling) the EOM as it applies to predicting the MI effect.

This chapter is thus organized as follows: first, we further discuss the notion of studying the effects of nonlinear coupling using harmonic models. From there, we review and summarize the specific coupled nonlinear harmonic formulation used in the problem considered. Following this, results and discussions are presented. Then, summary

remarks are given, highlighting observations from the study of the effects of nonlinear coupling in modeling the MI effect.

4.1 Introduction and Motivation for a Case Study of Coupling in the MI Effect

Given the reductions in the EOM, the system now reduces to three equations describing only **H**, **M**, and φ_D. From this point, the question arises as to whether the remaining equations can be reduced further into a harmonic (complex) form in order to simplify the problem and still predict the MI effect. A relevant point for a harmonic formulation is that based on ample experimental data from MI sensors, the output voltage has consistently been shown to be periodic at the same frequency as the input current source. Therefore, given any periodic function, it is known by way of a Fourier series that such a function can be expressed as a linear combination of periodic basis functions where in this case, $V_{\mathrm{MI}} = \sum_{k=1}^{\infty} A_k \sin(n_k \omega) + B_k \cos(n_k \omega)$ (see (2-55)). However, the observation of a periodic MI voltage at the input frequency does not necessarily mean that a single harmonic basis dominates, leading to the use of a single component to approximate the wave form. But, this is a result of any complex harmonic model with a single amplitude and phase. Thus, in the formulations used in this chapter (and the next), it is assumed that one component dominates the Fourier series. Consequent reductions in the equations should keep this additional source of error in mind.

In this investigation, using a harmonic formulation, the influence of the external field H_e as well as frequency f are studied, showing that a coupled nonlinear harmonic model results in significant improvements in predicting the MI effect, particularly, in the weak field regime.

The study of the effects of coupling is carried out in three principle tasks:

1. We deploy a general harmonic nonlinear formulation for modeling the magnetic field **H** and magnetization **M** in the MI sensor element in the circular wire. While relaxing assumptions commonly made, this model provides a means to explicitly solve the Maxwell and Gilbert (or LLG) equations simultaneously for the real and imaginary parts of the magnetic fields and magnetization in both MI element structures *without* decoupling.
2. In solving the proposed model, spatial discretization is also done using a meshless method (MLM) formulation in a point collocation scheme with the *Hp*-cloud shape functions (see Appendix A). We also validate the numerical method (referred to here as HP-PC MLM) for the specific problem considered with the circular wire by comparing results against those using a Galerkin finite element (weak) method (FEM) solving the same problem, which shows excellent agreement as well as a clear advantage of the HP-PC MLM in terms of computational time.
3. We investigate the effects of nonlinear coupling on the MI effect by comparing the coupled nonlinear model computed using the HP-PC MLM against a decoupled linear model which has a closed form solution, taken from the first part of Chapter 3. The computed impedances/voltages are also compared against published experimental data from Ref. [14]. As will be shown, the nonlinear coupled model agrees in a much improved way not only qualitatively with the experimental data compared to linearized models but also results in much closer predicted data compared to experimental data in the weak field regime.

4.2 Review of Coupled Nonlinear Harmonic Formulation

For the problem of the MI element with an *ac* input current under a *dc* external field, recall from the harmonic EOM developed in chapter 2 that **M** and **H** are assumed to take the form:

$$\mathbf{H} = \mathbf{H}_{\mathrm{e}} + \left|\mathbf{H}_{\sim}\right| e^{-j\omega t+\phi} = \mathbf{H}_{\mathrm{e}} + \mathbf{H}_{\mathrm{R}} + j\mathbf{H}_{\mathrm{I}} \tag{4-1}$$

$$\mathbf{M} = \mathbf{M}_{\mathrm{d}} + \left|\mathbf{M}_{\sim}\right| e^{-j\omega t+\phi_{\mathrm{M}}} = \mathbf{M}_{\mathrm{d}} + \mathbf{M}_{\mathrm{R}} + j\mathbf{M}_{\mathrm{I}} \tag{4-2}$$

ϕ and ϕ_{M} are phase angles with respect to the operating frequency angle, ωt, of the *ac* source, I_{s}. The value of $\mathbf{M}_{\mathrm{d}}$ is given *a priori* by the equilibrium state of the wire, where a uniform axial alignment is again assumed (i.e. $\mathbf{M}_{\mathrm{d}} = [0\ 0\ M_{\mathrm{s}}]^{\mathrm{T}}$).

Substitution of (4-1) and (4-2) into the Maxwell's and Gilbert equations leads to the final form of the equations given by

$$\nabla\times\nabla\times\mathbf{H}_R + \sigma\omega\left(\mu_0\mathbf{H}_I + \mathbf{M}_I\right) = 0 \tag{4-3}$$

$$\nabla\times\nabla\times\mathbf{H}_I - \sigma\omega\left(\mu_0\mathbf{H}_R + \mathbf{M}_R\right) = 0 \tag{4-4}$$

$$\frac{\omega}{\gamma}\left(\left[\boldsymbol{\Gamma}_I\right]\mathbf{M}_R + \left[\boldsymbol{\Gamma}_R\right]\mathbf{M}_I\right) = \mathbf{M}_I\times\mathbf{H}_{TI} - \left(\mathbf{M}_d + \mathbf{M}_R\right)\times\mathbf{H}_{TR} \tag{4-5}$$

$$\frac{\omega}{\gamma}\left(\left[\boldsymbol{\Gamma}_R\right]\mathbf{M}_R - \left[\boldsymbol{\Gamma}_I\right]\mathbf{M}_I\right) = \mathbf{M}_I\times\mathbf{H}_{TR} + \left(\mathbf{M}_d + \mathbf{M}_R\right)\times\mathbf{H}_{TI} \tag{4-6}$$

$$\mu_0\nabla^2\varphi_{DR} = \nabla\bullet\mathbf{M}_R \tag{4-7}$$

$$\mu_0\nabla^2\varphi_{DI} = \nabla\bullet\mathbf{M}_I \tag{4-8}$$

Equations (4-3) - (4-8) are referred to as the *coupled nonlinear harmonic* model, which enables explicitly solving the Maxwell and Gilbert micromagnetics equations, in a coupled nonlinear fashion, simultaneously for the real and imaginary parts of the magnetic field intensity ($\mathbf{H}_{\mathrm{R}}$ and $\mathbf{H}_{\mathrm{I}}$), magnetization ($\mathbf{M}_{\mathrm{R}}$ and $\mathbf{M}_{\mathrm{I}}$) and demagnetization

field potential (φ_{DR} and φ_{DI}). They are equivalent to the formulation known as the Maxwell-Landau-Lifshitz-Gilbert equations [81] and the formulation used here has also been referred to as the Maxwell-skewed-Landau-Lifhshitz-Gilbert (MsLLG) equations [62].

4.3 Numerical Considerations

Recall that the idea of coupling versus decoupling is appropriate based on the relative amplitudes between the harmonic and steady field components of the problem expressed in (4-1) and (4-2). In general, for decoupling, it is assumed that all alternating components are much smaller in amplitude than that of the steady components. As will be shown, it is easily the case that this is not consistent with the operation of MI sensors as $||\mathbf{H}_{\sim}||>||H_e||$ inside the MI element, which *il*legitimizes the linearization assumption, particularly in the weak field regime. Since the only independent variable in this formulation is space, the solutions to the coupled nonlinear harmonic model are again solved numerically using a meshless method (MLM) in a point collocation scheme. The reader can refer to Appendix A (and cited references) for more details on the *Hp*-Cloud MLM and other formulations.

4.3.1 1D Boundary conditions

To determine unique and relevant solutions for the MI voltage in the wire element and ribbon, an appropriate set of consistent boundary conditions (*BC'*s) must also be specified. Since **M** and **H** only vary in *r*, it follows from the equations of motion that the radially oriented components are described by a scalar equation

(a) circular wire radial EOM

$$\mu_o(H_{Rr} + jH_{Ir}) = -(M_{Rr} + jM_{Ir}) \tag{4-9}$$

The remaining twelve coupled nonlinear component equations are solved with the following boundary conditions:

(a) circular wire BCs

$r = 0$ $$\partial \mathbf{H} / \partial r = \partial \mathbf{M} / \partial r = \varphi_{\mathrm{D}} = 0 \quad \text{(4-10a)}$$

$r = r_{\mathrm{o}}$ $$H_{\mathrm{R}\theta} = I_{\mathrm{s}} / 2\pi R \; ; \; H_{I\theta} = 0 \quad \text{(4-10b)}$$

$$H_{\mathrm{Rz}} = H_{\mathrm{Iz}} = 0 \quad \text{(4-10c)}$$

$$\partial \mathbf{M} / \partial r = 0 \quad \text{(4-10d)}$$

$$\mu_0 \partial \left(\phi_{\mathrm{RD}} + j\phi_{\mathrm{ID}} \right) / \partial r = M_{\mathrm{Rr}} + jM_{\mathrm{Ir}} \quad \text{(4-10e)}$$

It is noted that equation (4-10d) assumes the free-spinning condition [71]. See Chapter 2 for a deduction of the free spinning condition from a more general analytically derived magnetization boundary condition.

4.3.2 Discussion of Computational Results

Using mostly material parameters from experimental studies, a numerical simulation has been performed on a circular amorphous wire (diameter of 30 μm and length of 5 mm) with an *ac* source amplitude of 15 *m*A at 1MHz input current frequency within the external field ranging from 0 to 1000 A/m. The values for the parameters used in the numerical investigation are summarized in Table 4-1, where M_{s} for the magnetic alloy is computed from the volume compositional average using published values for cobalt (Co) and iron (Fe) in the material $Co_{68.15}Fe_{4.35}Si_{12.5}B_{15}$.

Validation Comparisons to FEM

Since all computations for this problem are performed on a desktop PC, for the circular wire, both a MLM point collocation method and an FEM (weak) formulation were preliminarily tested for accuracy and computational efficiency leading to the choice

of an MLM formulation using a point-collocation method with the *Hp*-cloud shape functions. For short, the formulation is referred to as the HP-PC MLM. All solutions presented here were computed using a quasi-Newton (Broyden) family nonlinear solver with an optimized line-search. See Appendix C for details of this method as deployed here. All models were implemented in MATLAB®.

In comparing the convergence characteristics, the norm of the approximate error e_a, defined by $e_a^{i+1} \doteq \|y_{i+1} - y_i\| / \|y_{i+1}\|$, is used as a convergence metric; the computation was terminated when e_a (and $|f(y_i)|$) $< 10^{-8}$.

Table 4-1 Circular wire simulation parameters

M_s (T)	I_s (mA)	σ (kΩ-m)$^{-1}$	H_K (A/m)	α	f (kHz)	A_X
1.35	15	67.367	0.78	0.01	100-1000	10^{-11}

In addition of the field solution in space, a key interest in the MI sensor model is its response to the external field H_e over the region from zero field to near saturation. The sensor response is often measured in terms of the voltage amplitude across the MI sensor, $|V_{MI}|$. Recall (2-2b) provides the magnetic flux density **B** in terms of **H** and **M**. The circular component of **B** determines the axial inductive voltage, while the total voltage amplitude for the considered problem[5] is given by

$$V_{MI} = \left| I_s R_{dc} + V_L \right| \tag{4-18}$$

Figure 4-1a graphs the magnitude of the voltage across the MI element, $|V_{MI}|$, as a function of the external *dc* field H_e. The computational time to solve the coupled nonlinear model follows the same trend as the MI voltage where the "stiffness" is increased in the small field region. To provide a means to validate the numerical

[5] Because the problem is known to have a weak skin effect, the current is throughout leading to the *dc* voltage expression for the ohmic voltage. Otherwise, the skin effect should be taken into consideration.

computation, the $|V_{MI}|$ results (computed using the HP-PC MLM) are compared with those using a Galerkin FEM, which shows very good agreement. However, the HP-PC MLM needs significantly less time than the FEM for the same number of nodes (N=55) as shown in Figure 4-1b, where the computation time is normalized to the largest respective time observed at $H_e=0$.

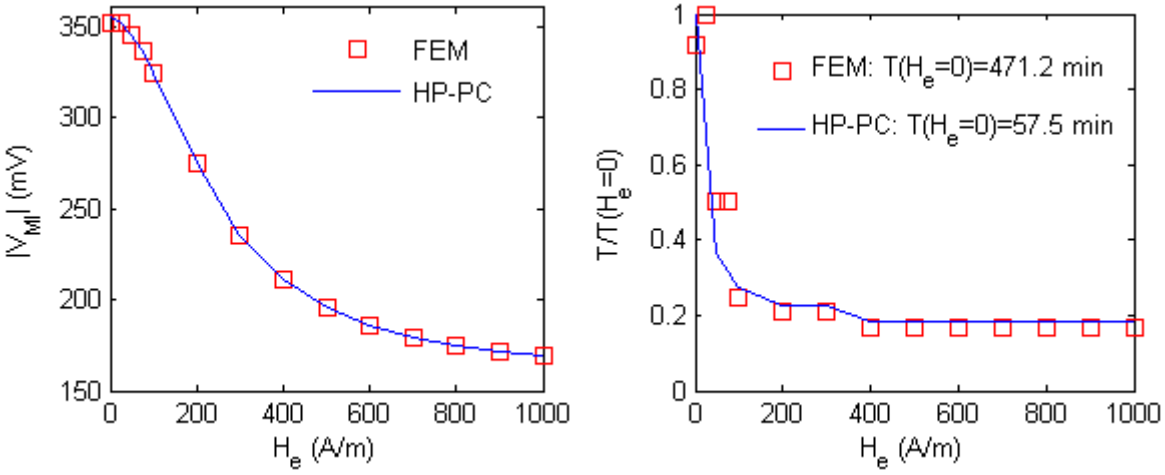

(a) $|V_{MI}|$ comparison as a function of H_e (b) Computation time, T, comparison

Figure 4-1 Computed $|V_{MI}|$ versus H_e (n=55 nodes) and computation times, T (HP-PC *vs* Galerkin FEM).

For $|V_{MI}|$ at $H_e=0$, FEM took more than 8 hour to compute the solution using 55 nodes (or 27 second-order elements) while the HP-PC-MLM computed the same result in less than an hour! The above results emphasize that using an MLM point collocation scheme saves a considerable amount of computation time, without sacrificing accuracy, and this is a motivating factor for using a point collocation scheme. It is easier to implement and it is much more efficient. Figure 4-1b illustrates the efficiency of the HP-PC very clearly where nearly a 9-fold decrease in computational time is obtained by simply deploying the HP-PC formulation.

Given this observation, a discussion of the investigation of the effects of coupling between micromagnetics and electrodynamics on the magneto-impedance effect follows.

To gauge the effects of decoupling, in the circular wire, comparisons are made between the coupled nonlinear harmonic model and a decoupled linear harmonic model, formed by combining the Landau-Lifshitz impedance model with a scalar effective permeability like used by Usov *et al*.[7] and as derived in Chapter 3. Also, most of the values of the material parameters used are *realistic* values taken mostly from experimentally measured (and reported) values summarized in Table 4-1. Here, the spatial grid has been discretized into an equally distributed nodal set of 55 nodes.

Discussion of Results

Computed results (using the HP-PC MLM) are shown in Figures 4-2 to 4-6:

A. $|V_{MI}|$ is plotted as a function of the external *dc* field H_e (measured field) in Figure 4-2 and as a function of the source frequency *f* in Figure 4-3 where H_e= 800A/m, as reported in [9]. In Figures 4-2 and 4-3, def_1 and def_2 refer to the solutions of the decoupled linear model with $\mu_{1\theta}$ and $\mu_{2\theta}$ given in Chapter 3, in equations (3-47) and (3-48), respectively. Computed MI voltages are also compared against reported experimental data in order to observe which model demonstrates better fidelity according to experimental data.

B. Figure 4-4 shows the amplitudes of the transverse components of both **H** (H_θ) and **B** (B_θ) for H_e=0 and 900A/m computed from the coupled nonlinear model. With this information, the resulting distributions can be compared in the case of a weak field (H_e=0) and a near-saturation field (H_e=900 A/m) so the assumptions leading to linearization can be more closely examined.

C. In an effort to offer better intuitive insights into the effect of coupling, particularly, in a very weak external field, the following results are also computed at $H_e = 0$:

1) Figures 4-5a and 4-5b compare the distributions of the amplitudes of $B_\theta(r)$ in the MI element simulated using both the coupled and decoupled models. In both figures, the vector lengths indicate the amplitudes.

D. Figure 4-6 shows the distribution of each of the total effective field components ($\mathbf{H}_T = \mathbf{H} + \mathbf{H}_K + \mathbf{H}_X + \mathbf{H}_D$), by way of their vector amplitudes, within the MI element. This information shows the relative contributions of each total effective field component for the problem considered.

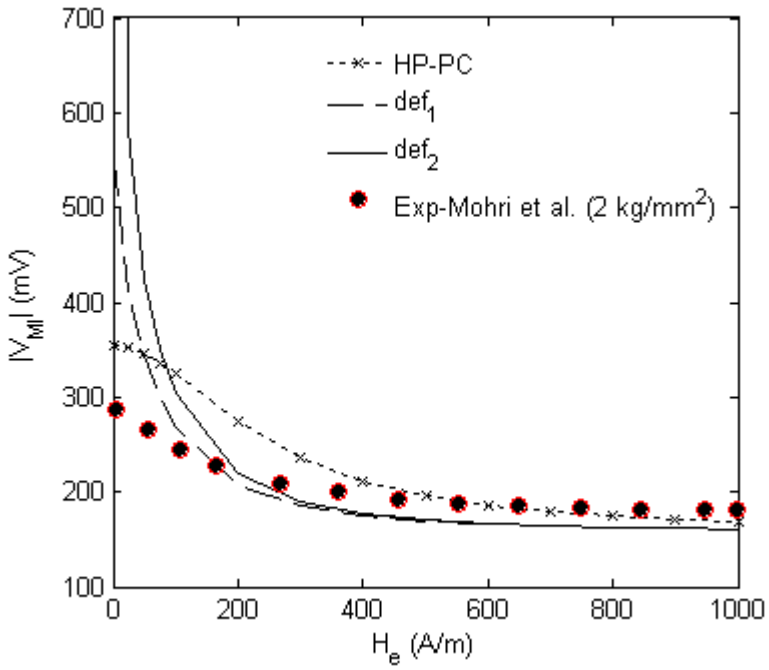

Figure 4-2 MI voltages versus external field (f =1MHz)

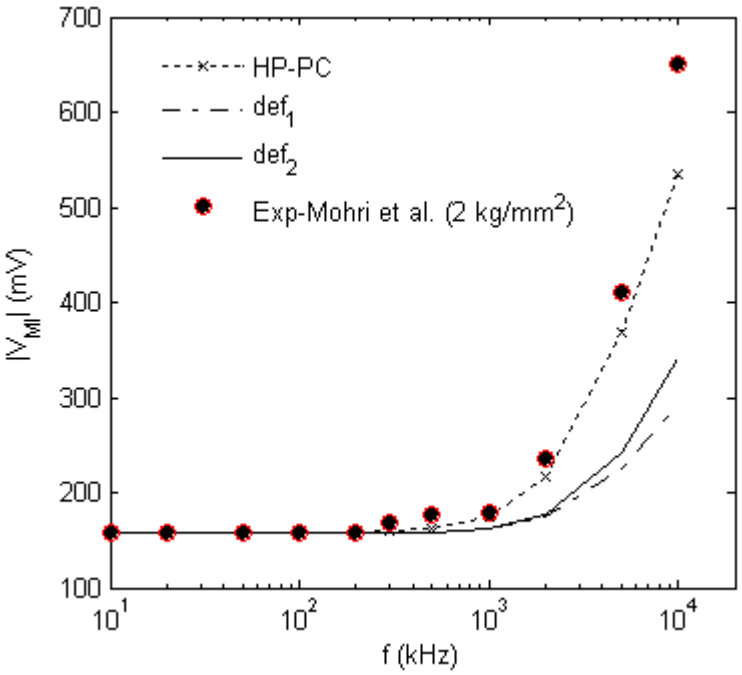

Figure 4-3 MI voltages versus frequency (H_e =800A/m)

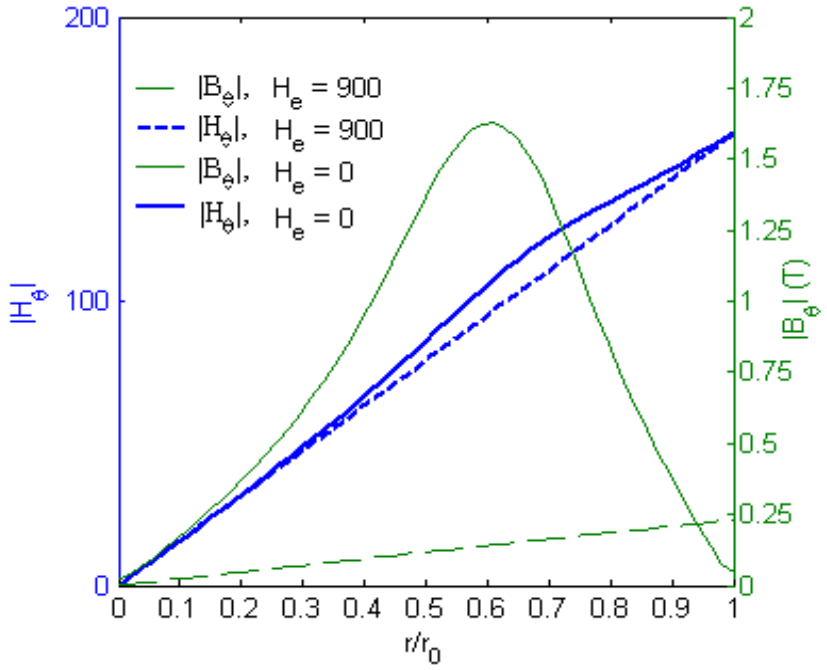

Figure 4-4 Illustration of dispersion for small H_e on the radial variations of $|H_\theta|$ and $|B_\theta|$

Improvements in Predictions Comparing Coupled vs Decoupled

As shown in Figure 4-2, the decoupled linear model agrees well with experimental data in predicting $|V_{MI}|$ for relatively large H_e (i.e. saturation), but does not predict very well in the weak field region, where the error is seen to be very large. The values increase much more sharply as H_e is reduced. The decoupled model and experimental data do not agree well. Between both linear models, the smallest MI voltage is ~550 mV, which amounts to a *minimal* experimental error of 96% (221 % max), whereas that of the coupled nonlinear model leads to ~25% experimental error. Recall that the assumptions for linearization include that the amplitude of the harmonic field is much larger than that of the *dc* field, H_e. This condition is clearly *not* met for the problem considered when H_e is very small. Similar quantitative experimental discrepancies are observed for higher frequencies, also, as shown in Figure 4-4. In this case, the data "falls off much faster as the frequency increases, according to decoupled models, and it is noted that this is in the high field regime, where conditions are more consistent with decoupling.

Spatial Dispersion In Weak Fields

Since the decoupled model assumes $\mathbf{M} \approx [\chi]\mathbf{H}$ and thus $\mathbf{B} \approx \mu_\theta \mathbf{H}$, the scalar permeability μ_θ does not depend on space implying that $|B_\theta|$ and $|H_\theta|$ vary the same in space. This relative spatial variation of the permeability is referred to as *spatial dispersion*. In the linearized model, spatial dispersion is consequently negligible as it is not considered. However, Figure 4-4 shows that this assumption deteriorates as H_e decreases into the weak field region. The amplitude of the transverse field is clearly not proportional (in space) to the induction in the weak field region. Meanwhile, we can see that for H_e = 900 A/m (near saturation), both distributions are linear and consistent with

the assumption of spatial proportionality (i.e. no spatial dispersion). The presence of spatial dispersion in the weak field region definitely influences the MI voltage, as the area of the curve determines the flux in the wire. This provides at least one mechanism that leads to reduced voltages for the coupled nonlinear model (compared to the decoupled), as illustrated in Figure 4-4.

The analytical models also offer an intuitive means to visualize the effect that decoupling has on the transverse magnetic flux density, particularly, in the weak field regime. Figures 4-5a and 4-5b show two very different $B_\theta(r)$ wire images predicted by the coupled nonlinear and decoupled linear models, respectively.

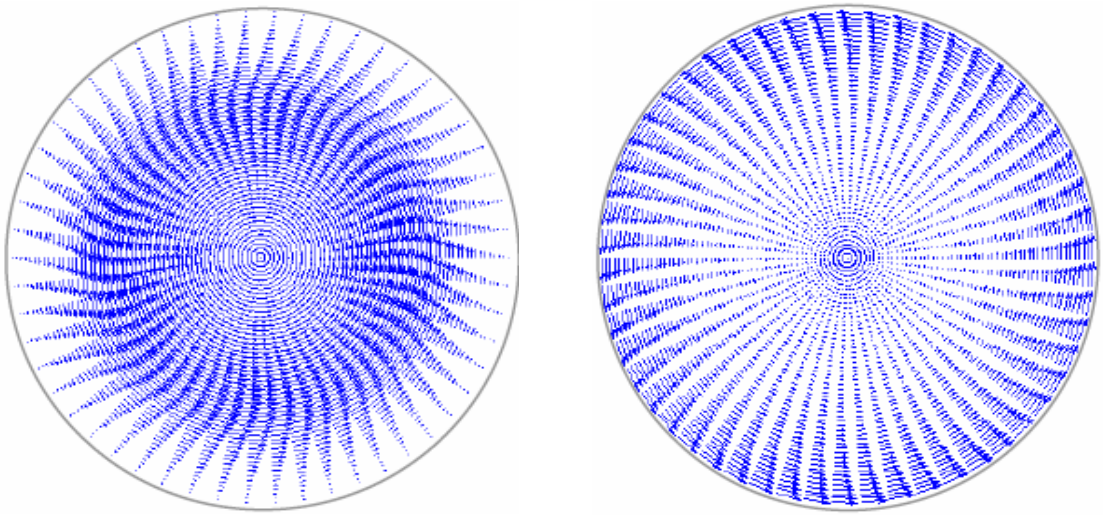

(a) $|\mathbf{B}_0|$ from coupled nonlinear model (b) $|\mathbf{B}_0|$ from decoupled linear model

Figure 4-5 Transverse magnetic flux density amplitude, $|B_0|$

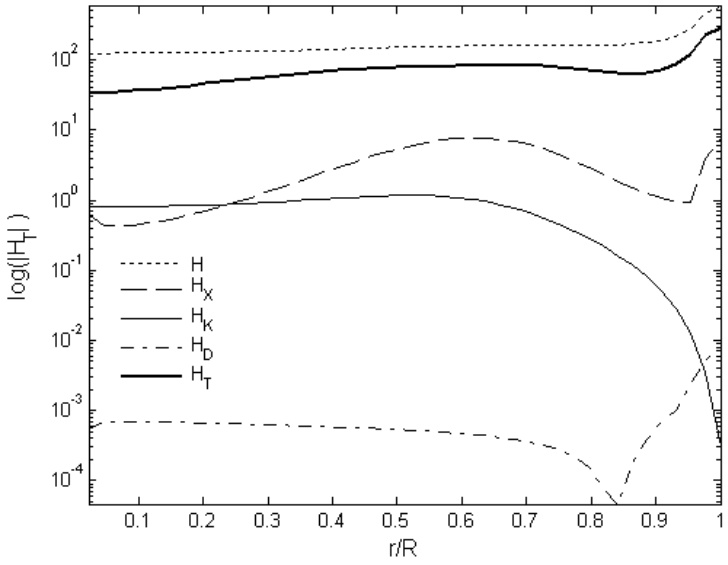

Figure 4-6 Relative component contributions to H_T (H_e =0)

The nonlinear coupled model (Figure 4-5a) results in a solution showing that the bulk of the transverse induction oscillations occur within the core of the wire, and not more towards the surface as decoupled classical models suggest. This qualitative feature of internal oscillations is consistent with experimental data with Co-based amorphous wires subjected to harmonic fields reported in [69]. Yamasaki *et al*. observed experimentally in similar wires that no switching activity was found on the wire surface (where Neel walls were visible) while induction changes were still observed. Also, the magnetic domains participating in the switching could only be made visible by polishing away part of the wire where axially oriented domains were seen. On the other hand, the decoupled linear model (Figure 4-5b) predicts a monotonically increasing induction with maximums near the surface (even for the case of weak H_e). Given both sets of results, it is more likely that the transverse magnetic field distribution evolves qualitatively from Figure 4-5a to that of Figure 4-5b over the range $0 < H_e < H_{sat}$.

Once the coupled nonlinear harmonic equations are solved, the effective field components in the total effective field $\mathbf{H}_T$ can be computed (see Chapter 2) for a given external field H_e. Figure 4-6 shows the vector magnitudes of each component including the external field $\mathbf{H}$, anisotropy $\mathbf{H}_K$, exchange $\mathbf{H}_X$, and demagnetization $\mathbf{H}_D$. As shown in Figure 4-6, the magnitude of $\mathbf{H}_D$ is nearly two orders smaller than that of $\mathbf{H}_K$ and $\mathbf{H}_X$, in the core of the wire. The dominance of the total effective field by $|\mathbf{H}_{\sim}|$, evident in Figure 4-6, also suggests that the nonlinear dependence of $\mathbf{M}$ on $\mathbf{H}$ can not be neglected; in other words, this dynamic component has a relatively strong contribution on the magnetization, $\mathbf{M}_{\sim}$ In a decoupled model, the influence of this component is assumed relatively small because $|\mathbf{H}_{\sim}| << |\mathbf{H}_e|$.

Thus, it has been shown that decoupling can be strongly divergent from the more general formulation when the external field is very weak. The coupled nonlinear formulation used here results in predictions that are much more representative of the actual behavior of MI devices, and thus treating nonlinear coupling can be very important to more accurately predict the MI effect, particularly, in the weak field behavior.

4.4 Conclusions on Effects of Coupling in MI Elements

In this chapter, we have investigated the effects of coupling, in a nonlinear fashion, the Maxwell and micromagnetic equations describing the MI effect. We have achieved such an investigation studying the MI effect using numerical methods. To motivate the numerical model, the choice of a MLM point collocation method was shown to offer a considerable advantage in computational efficiency in solving the equations, particularly, compared to FEM. This numerical approach enables a study that offers new insight into the effect of decoupling the originally coupled nonlinear equations. This was shown by

comparing two analytical (coupled and decoupled) models, to data from published experimental results.

In the weak field regime, it was shown that the more commonly used linear approximation leads to much larger errors; also, the coupled nonlinear model agrees very well qualitatively, and reveals a clear improvement quantitatively, compared with independently published experimental data. This was shown in predicting the behavior in both the dependence on H_e and frequency f. There are at least two likely factors for the discrepancy near the very weak field regime: we have ignored any possible domain walls and their effects (which have been shown to be present in the considered material). Also, an over-estimation of the saturation magnetization M_s is also a factor[6].

Additionally, it was shown that both models for the circular wire lead to strikingly different distributions within the wire in the weak field regime, providing a different qualitative understanding of the magnetization behavior within the wire and providing direct evidence of spatial dispersion associated with the MI effect in a weak field.

[6] Very recently, we have found better estimations of M_s for these materials [68] that would improve the computed results even further.

CHAPTER 5
EFFECTS OF EQUILIBRIUM DOMAIN STRUCTURE

In this chapter, further use of the coupled nonlinear model is made by examining magnetic structural effects that are not accessible directly via decoupled models, but only using a coupled nonlinear model. Specifically, the effect of an equilibrium magnetic domain structure on the MI effect is investigated. This is examined primarily in the ribbon MI element where 180^o Neels walls are investigated. Additionally, we examine the effect of a 90^o radial Bloch wall in the circular wire. The domain structures investigated have all been observed experimentally, as well, and the structure used is modeled after these observations.

5.1 Background for the Problem of Domain Structure in MI Sensors

The coupled nonlinear harmonic model can be used to study the influence of an equilibrium magnetization domain structure in an explicit manner, as we will see. In decoupled models, these effects are considered phenomenologically, at best [72]. Here, the effects are explored in the ribbon where 180^o Neel walls are the domain walls of primary focus however the effects of Bloch walls are also studied in the case of the circular wire, both of which have been observed experimentally [70] [69].

As mentioned earlier, MI sensors utilize soft magnetic materials in the MI element whose electromagnetic state determines the behavior of the MI sensor. Based on these observations, an understanding of the influence of a domain structure begins with a study

including the equilibrium magnetization state of these small magnetic structures subjected to harmonic conditions, due to an *ac* input current source, I_s.

According to earlier works with MI sensors, the influence of equilibrium domain walls has not unanimously been considered as generally playing a key role in the MI effect. For example, some earlier works suggested that for an operating frequency of 1 MHz, domain wall motion is sufficiently dampened and, therefore, there may be no need to consider domain walls in modeling efforts [34] for the MI effect. However, it was shown in Chapter 3 that the predicted mode of switching in the amorphous round wires at 1 MHz is by way of dynamic domain wall formation and propagation starting at the surface. Also, consistent remarks, expressing little confidence in an influence by domain walls, have been put forth by others [7]. But, some experimental evidence has also been presented, for example, in amorphous ribbon elements that suggest domain walls play a very influential role in the MI effect of ribbons [70] [80]. In this case, however, the operating frequency, *f*, was on the order of *k*Hz, not MHz. Similar conclusions have been supposed by other researchers for the case of the circular amorphous wires, as well [31].

Given the details of the models discussed, experimental evidence suggests that the influence of domain walls likely depends on a variety of conditions, where the MI effect may or may not be influenced by a domain structure. The coupled nonlinear harmonic model will be shown to add some insight to the questions about the role of the domain walls known to be present within the MI elements. It is of interest to use the coupled nonlinear harmonic model because it also has the advantage of accommodating an equilibrium domain structure explicitly in the model. In this way, an improved understanding of the role of a domain structure shown to be present experimentally in

some MI element structures is possible. A good understanding of the role of a domain structure within magnetic materials also has broader implications to a wider of class of magnetic materials used in sensors that may also possess domain walls. For example, fluxgate sensors use amorphous magnetic alloys that may also possess a domain structure.

According to observations in MI ribbons, *Co*-based amorphous ribbons possess the "stripe" domain structure with each pair of domains separated purely by 180^{o} Neel walls throughout the thickness of the ribbon. The domain structure in MI ribbon elements has been observed using a longitudinal magneto-optical Kerr effect (LMOKE) technique which exploits the peculiar tendency of electromagnetic waves to be reflected from a magnetic surface in varying polarization planes depending on the local magnetization [70]. Figure 5-1(a) shows an actual image taken by researchers illustrating from an exterior view, the domains in ribbon wires (a) and the corresponding domain structure in the round wire (b).

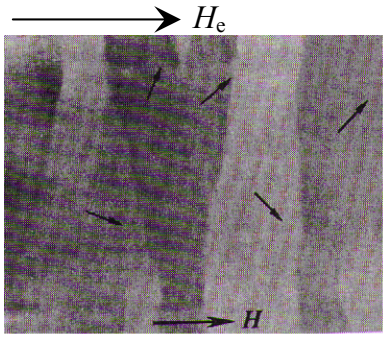

(a) Experimentally observed similar striped domain structure in MI ribbon domains; the ribbon domain width is ~50 μm.

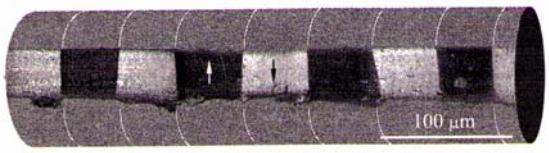

(b) Domain structure observed experimentally by Yamasaki *et al* in CoFeSiB wires

Figure 5-1 Magnetic domain structure in amorphous MI elements. Photos taken from [67]

The existence of a domain structure in MI elements has been confirmed in both amorphous near-zero negative magnetostrictive circular wires [69]. Even before the

formal introduction of MI sensors, amorphous magnetic materials, now used in some MI sensors, had been investigated for their soft magnetic properties, particularly in *Co*-based and *Fe*-based amorphous wires. According to observations by Yamasaki *et al*., circular *Co*-based amorphous wires possess the "bamboo" domain structure with nearly 180^o Neel walls visible from the wire surface using Bitter pattern techniques [67] (also see Figure 5-1b). It was found that in the amorphous *Co*-based wire, there is also present a 90^o radial Bloch wall extending along the entire length of the wire. Then, the equilibrium configuration is such that the core magnetization is axially aligned, while the exterior region contains alternating transverse magnetic domains.

Therefore, given a domain structure within the amorphous MI element, there exists two types of domain walls (90^o Bloch and 180^o Neel), of which their respective roles in the MI effect are a natural inquiry. For the ribbon, the Neel wall effects are by default of primary concern as they are the only type found in ribbon elements, while for the circular wire, the focus in this chapter is only on the effects of the 90^o Bloch wall. In the case of the circular wire, a motivating factor for the limited focus on the Bloch wall alone is due to the computational intensity preliminarily discovered in computing the 2D solution considering both the Neel and Bloch walls within the circular wire. In order to properly compute the solution to the more general 2D problem in this case, more robust computing resources are required than what is currently and "conveniently" available in these research efforts.

Thus, considering the treatment of domain walls, it of interest to not only more accurately predict the MI effect quantitatively using the numerical model deployed here,

but to better understand the role(s) of the observed domain walls, as well, which is information that is not directly accessible using decoupled linearized models.

The ability to observe the domain structure, experimentally, enables the modeling approach used here, since this information essentially provides the solution to the equilibrium micromagnetics problem, defined by a zero balance of torque, i.e.

$$\mathbf{M}_{\mathrm{d}}(\mathbf{x}) \times \mathbf{H}_{\mathrm{T}} = 0 \text{ where } \left\| \mathbf{M}_{\mathrm{d}}(\mathbf{x}) \right\| = M_s \tag{5-1a,b}$$

$\mathbf{M}_{\mathrm{d}}$ is, by definition, the equilibrium or steady magnetization as it results from (5-1); $\mathbf{H}_{\mathrm{T}}$, again, is the total effective magnetic field (defined in Chapter 2); M_{s} is the saturation magnetization.

The work discussed here presents with the following key features:

1. Again, we deploy the general harmonic coupled nonlinear formulation (presented in Chapter 2 and used previously in Chapter 4) describing the MI effect (under negligible thermal effects), easily adapted to accommodate an *a priori* known domain structure, particularly, when experimental observations of them have been made. The equations of motion describe the real and imaginary components of the magnetic field intensity ($\mathbf{H}_{\sim} = \mathbf{H}_{\mathrm{R}} + \mathrm{j}\mathbf{H}_{\mathrm{I}}$) and magnetization ($\mathbf{M}_{\sim} = \mathbf{M}_{\mathrm{R}} + \mathrm{j}\mathbf{M}_{\mathrm{I}}$).

2. The nonlinear coupled equations describing the MI effect have again been spatially discretized using a meshless method (MLM) deploying the *Hp*-Cloud shape functions in a point collocation scheme. Similar to previous motivations, the choice has been made based on good accuracy along with a reduction in computation time compared to classical approaches such as a Galerkin finite element method (FEM). This is demonstrated here via a numerical example solving the classical nonlinear 180^{o} Bloch wall model numerically.

3. Using this formulation, we investigate the effects of the experimentally observed domain structure within the MI ribbon element, studying Neel walls, and the circular elements, studying only the 90^o radial Bloch wall. Relevant comparisons are made including that to a coupled nonlinear model ignoring domain structure, and resulting voltages are also compared to reported experimental results. In both cases, it will be shown that factoring in the experimentally observed domain structure results in:

- reduced voltages compared to predictions with a uniform domain structure and the mechanisms leading to this are discussed
- improved agreement with experimental results

With this, the discussion takes the following format: *first*, the motivation for the choice of the *Hp*-Cloud MLM shape functions for this particular problem is discussed further in the context of domain walls by examining a numerical solution to the 180^o Bloch wall (different from the Neel wall structure); the nonlinear solver method is also investigated in the 2D ribbon problem; *second*, the model formulation, applying to both ribbon and circular elements, is summarized for the problems considered, where the approach to explicitly account for the experimentally observed domain structure in the model is also summarized; *third*, we discuss the role and influence of the domain structure based on computed results from the harmonic coupled nonlinear model. Finally, we conclude with a summary of key points and observations on the effects of the equilibrium domain structure on the MI effect.

5.1.1 180^o Bloch Wall: New Motivation for the Hp-Cloud Shape Functions

For this particular problem, the choice of an MLM shape function is not arbitrary. But rather, it follows from comparisons considering various formulations. Since we are

modeling a problem with a domain wall, in order to validate the numerical algorithm selected using the *Hp*-Cloud shape functions, the well known analytical 180° Bloch wall problem is solved numerically before choosing the better formulation for the problem considered (2D ribbon model with Neel walls). The Bloch wall is a nonlinear problem involving a domain wall that has an exact solution and therefore a reliable basis for comparison is available.

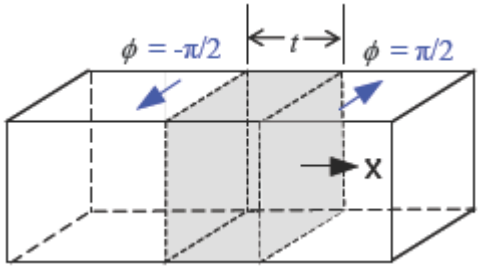

Figure 5-2 Illustration of domains separated by a 180° Bloch wall.

Figure 5-2 illustrates a 180° Bloch wall where the magnetization "turns" along the *x*-axis from -90° to +90° degrees. For the 180° Bloch wall, the equilibrium magnetization is found from minimizing the total magnetic energy of the system. For a B*loch* wall, the total magnetization energy (per unit area in the *y*-*z* plane) is given by

$$\varepsilon_m = \int_{-\infty}^{\infty} \left(A\left(\frac{d\phi}{dx}\right)^2 + K\cos^2\phi \right) dx \tag{5-2}$$

The sum accounts for only the exchange and anisotropy energies in a uniaxial anisotropy structure such as Cobalt, using only the 1st anisotropy constant, $K_1 = K$. The boundary conditions are such that on both sides of the wall, 180° domains are set up, leading to Dirichlet BCs at the axial extents (far along $\pm x$) given by

$$\phi(-\infty) = -\frac{\pi}{2}\ ;\ \phi(+\infty) = +\frac{\pi}{2} \tag{5-3}$$

To be a minimum, the solution must satisfy

$$\frac{d\varepsilon_m}{dx} = \frac{d}{dx}\int_{-\infty}^{\infty}\left(A\left(\frac{d\phi}{dx}\right)^2 + K\cos^2\phi \right)dx = 0 \tag{5-4}$$

After "absorbing" the derivative into the integral, (5-4) becomes

$$\int_{-\infty}^{\infty}\left(A\frac{d}{dx}\left(\frac{d\phi}{dx}\right)^2 + K\frac{d}{dx}\left[\cos^2\phi\right] \right)dx = 0 \tag{5-5}$$

Equation (5-5) then leads to the following

$$\int_{-\infty}^{\infty}\left(2A\frac{d\phi}{dx}\frac{d^2\phi}{dx^2} - 2K\cos\phi\sin\phi\frac{d\phi}{dx} \right)dx = 0 \tag{5-6}$$

From (5-6), the differential equation equivalent to the variational form, known as the Euler-Lagrange form of the equation, is then given by [10]

$$A\frac{d^2\phi}{dx^2} - K\cos\phi\sin\phi = 0 \tag{5-7}$$

Equation (5-7) is the differential equation solved here numerically, using the methods we have prescribed deploying MLMs. The exact solution to (5-7) is also available because the integral in (5-6) is directly solvable using integration by parts. It can be shown that the exact solution is given by [10]

$$\phi(x) = 2\tan^{-1}\left(e^{x/\sqrt{\frac{A}{K}}} \right) - \frac{\pi}{2} \tag{5-8}$$

A plot of the exact solution is shown in Figure 5-3 along with the resulting minimized energy profile across the wall.

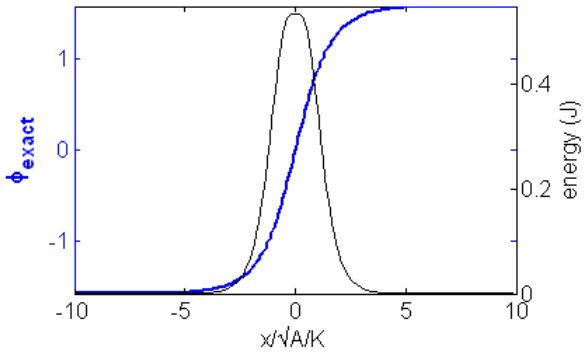

Figure 5-3 Exact solution for 180° Bloch wall and minimized energy profile

Figure 5-3 shows that in the Bloch wall, there is self-energy stored by way of anisotropy and exchange energy within the wall.

Given an exact solution, next, the numerical solution to (5-7) is discussed where MLMs have been used in addition to a more classical Galerkin FEM formulation.

Bloch wall Calculations

Since all simulations in this research are performed on a desktop PC, two spatial discretization methods are compared for computational efficiency; namely,

1. Point collocation (strong form) MLM formulations

   a) *Hp* cloud shape functions with 2nd order reproducibility (HP-PC) [51]

   b) Radial Basis Functions using thin plate splines (TPS) also with 2nd order reproducibility (RBF-PC) [56]

2. Galerkin FEM with standard 2nd order LaGrange basis functions (FEM).

Comparisons of the results are evaluated in terms of the energy norm, $\|E\|_2$, normalized computation time T/T_{max}, and the approximate error, e_a:

$$\|E\|_2 \doteq \sqrt{\int_\Omega \left(\phi(x)-\phi_{\text{exact}}\right)^2 dx} \quad \text{and} \quad e_a = \left|\phi_{i+1}-\phi_i\right| / \left|\phi_{i+1}\right| \qquad (5\text{-}9a,b)$$

In (5-9), ϕ_{exact} is the exact solution, given in (5-8); and the maximum computation time

is T_{max} = 89 minutes, from the computation time using the FEM with 115 nodes. The results are shown in Figures 5-4a,b, and c.

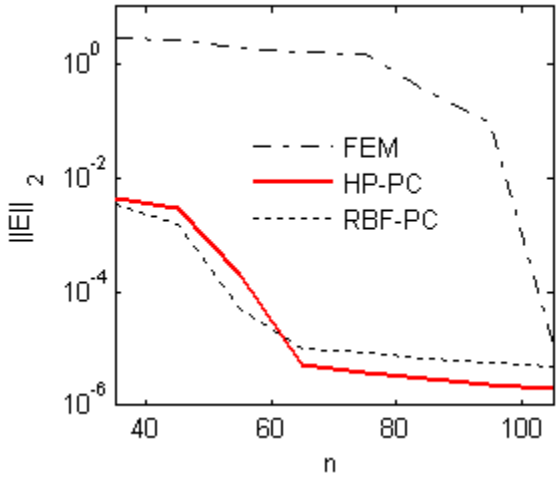

(a) convergence of error norm, E_2

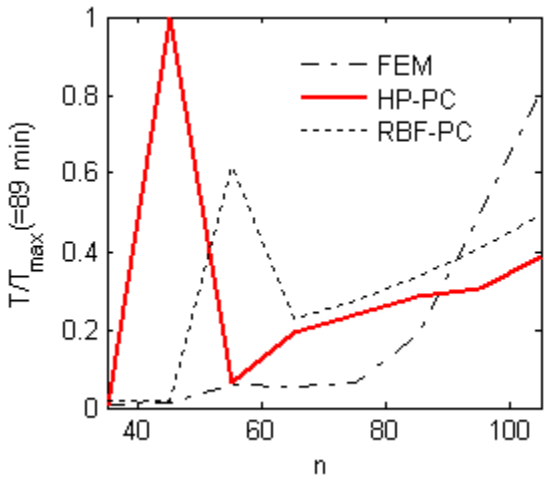

(b) computation time versus number of nodes *n*.

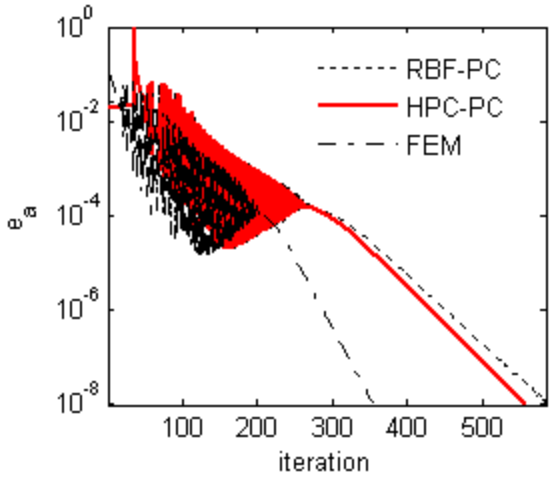

(c) comparisons of convergence of approximate error, e_a.

Figure 5-4 180° Bloch wall convergence characteristics using equally spaced nodes.

Figure 5-4 shows the validation and convergence of the numerical algorithms compared where the polynomial order of all shape functions is two.

Discussion of Validation of Numerical Formulation

For this problem, the MLM point collocation schemes converge to an acceptable error $e_a < 10^{-4}$ faster than FEM, while for FEM, significantly more nodes are required before "catching up" to the MLM point collocation error. Also, between both point collocation schemes, the HP-PC scheme appears slightly better than the RBF-PC scheme. This slight difference is believed to be attributed to the compact nature of the *Hp*-Cloud shape functions used here, whereas the RBF using TPS (see Appendix A for details) are not generally compact. The compactness of the HP-PC shape functions leads to a more diagonally dominant Jacobian matrix in the nonlinear solver, which is used for this 180° Bloch wall problem with a relatively small number of degrees of freedom.

Both point-collocation schemes are initially somewhat unstable and non-characteristic (requiring longer computation time) when too few nodes are used as shown in Figure 5-

4b. However, note that this is *not* reflected in the error at all, where accurate solutions are still obtained. When calculations with 65 or more nodes are made, consistency in computation time is apparent in both point collocation schemes. Beyond the proper number of nodes, the point collocation schemes show approximately linear computation times with the number of nodes, while FEM computation times increase at an even faster rate. For an acceptable accuracy, however, the point collocation schemes need significantly less computation time than FEM, where in this case, nearly 1/3 the computation time is observed.

As shown in Fig 5-4(c), which compares the approximate error e_a with iterations, the highly oscillatory region early in the iterations indicates a variable stiffness in the problem. This is because at each new step, the function value is not reduced initially, but rather increased. To combat this, numerical damping is performed, after which a value that reduces the norm of the function is found. This behavior continues throughout the stiff region until a smooth region is approached that manifests as a smoothly decreasing error. This smooth region is reflected in the "smooth" part of the approximate error. As the average norm reaches a certain threshold value between 200 and 300 iterations, the system converges more smoothly. Although FEM has the fastest convergence rate, it is of little value as the computation time still takes much longer. Also, the HP-PC demonstrates a slightly faster convergence than the RBF-PC formulation possible for reasons discussed above.

Then, based on the calculations for the 180^o Bloch wall problem, the HP-PC scheme is used for the remainder of calculations that follow, studying the effects of domain structure. However, the monomial basis functions have been increased up to order three.

5.2 Formulation Review

Given the final solutions for **H** and **M**, the inductive voltage, for a stationary circuit in a time varying magnetic field, V_L, in harmonic form, takes the form:

$$V_L = -j\omega \int_S (\mu_0 \mathbf{H} + \mathbf{M}) \bullet d\mathbf{s} \tag{5-10}$$

ω is the input current operating frequency; μ_o is the permeability of free space; **H** and **M** are the magnetic field intensity and magnetization respectively; and *S* is the magnetic flux crossing area. In the ribbon, this area is within the *x-z* (thickness-axial) plane, while in the circular wire, it is the *r-z* (radial-axial) plane. The solution from the harmonic coupled nonlinear formulation provides the values for **H** and **M** used to compute the inductive voltage.

For the problem of the MI element, subjected to an *ac* current source, and under a *dc* external field H_e, recall **M** and **H** have an assumed representation in the general harmonic form, discussed in Chapter 2, given by

$$\mathbf{H} = H_e \mathbf{e_z} + \mathbf{H}_R + j\mathbf{H}_I \; ; \; \mathbf{M} = \mathbf{M}_d(\mathbf{x}) + \mathbf{M}_R + j\mathbf{M}_I \tag{5-11a,b}$$

The subscripts "R" and "I" denote the real and imaginary parts; $\mathbf{M}_d(\mathbf{x})$ represents the equilibrium magnetization which is provided by knowing the experimentally observed domain structure. Substitution of (5-11a,b) into harmonic forms of the Maxwell and Gilbert equation leads to the following real valued partial differential equations (see Chapter 2):

$$\nabla \times \nabla \times \mathbf{H}_R + \sigma\omega(\mu_0 \mathbf{H}_I + \mathbf{M}_I) = 0 \tag{5-12a}$$

$$\nabla \times \nabla \times \mathbf{H}_I - \sigma\omega(\mu_0 \mathbf{H}_R + \mathbf{M}_R) = 0 \tag{5-12b}$$

$$\frac{\omega}{\gamma}\left([\Gamma_I]\mathbf{M}_R + [\Gamma_R]\mathbf{M}_I\right) = \mathbf{M}_I \times \mathbf{H}_{TI} - (\mathbf{M}_d + \mathbf{M}_R) \times \mathbf{H}_{TR} \tag{5-13a}$$

$$\frac{\omega}{\gamma}\left(\mathbf{M}_{\mathrm{R}}-\mathbf{M}_{\mathrm{I}}\right)=\mathbf{M}_{\mathrm{I}}\times\mathbf{H}_{\mathrm{TR}}+\left(\mathbf{M}_{\mathrm{d}}+\mathbf{M}_{\mathrm{R}}\right)\times\mathbf{H}_{\mathrm{TI}} \tag{5-13b}$$

$$\mu_0\nabla^2\varphi_{\mathrm{DR}}=\nabla\bullet\mathbf{M}_R \tag{5-14a}$$

$$\mu_0\nabla^2\varphi_{\mathrm{DI}}=\nabla\bullet\mathbf{M}_{\mathrm{I}} \tag{5-14b}$$

The unknowns are the real and imaginary parts of the magnetic field ($\mathbf{H}_{\mathrm{R}}$ and $\mathbf{H}_{\mathrm{I}}$), magnetization ($\mathbf{M}_{\mathrm{R}}$ and $\mathbf{M}_{\mathrm{I}}$) and demagnetization field potential (φ_{DR} and φ_{DI}).

5.3 Domain-wall Effect Considerations for Ribbon Elements

The magnetic ribbon wire is considered first which has an alternating input current source along the axis of the ribbon with an external magnetic field intensity H_{e}. The limited range of the external field is chosen where the values are less than or equal to the anisotropy field, H_{K} ($0\leq He\leq H_{\mathrm{K}}$). Using the coupled nonlinear harmonic model summarized above, a primary interest is to directly investigate the effects of the domain structure that have been observed in the amorphous ribbon MI element experimentally [70]. This effort is possible by using the coupled nonlinear harmonic formulation, resulting from the use of a harmonic vector form for the magnetic field intensity and magnetization where

$$\mathbf{H}=H_{\mathrm{e}}\mathbf{e}_{\mathbf{z}}+\mathbf{H}_{\sim}\text{ and }\mathbf{M}=\mathbf{M}_{\mathrm{d}}\left(\mathbf{x}\right)+\mathbf{M}_{\sim} \tag{5-15}$$

Both vectors are written as the sum of steady ($H_{\mathrm{e}}\mathbf{e}_{\mathrm{z}}$, $\mathbf{M}_{\mathrm{d}}$) and *ac* components ($\mathbf{H}_{\sim}$, $\mathbf{M}_{\sim}$). In the expression for $\mathbf{H}$, H_{e} is the measured *dc* external field, while the harmonic component of the magnetic field is due to the input current source, I_{s}. For the magnetization $\mathbf{M}$, one can imagine a picture where $\mathbf{M}_{\mathrm{d}}$ represents the stable orientation of the magnetization from which oscillations occur, i.e. the equilibrium magnetization (requiring the least energy and thus the physical system prefers this orientation and it is stable). We therefore exploit the fact that the formulation accommodates a prior knowledge of this

equilibrium domain structure, given as $\mathbf{M}_d$. The harmonic magnetization component $\mathbf{M}_\sim$ then represents the unknown magnetization components or deviations from $\mathbf{M}_d$.

Generally, the equilibrium magnetization is quantitatively described by (5-1). However, an explicit solution to (5-1) is nontrivial for MI elements; however, because the domain structure for the ribbon materials in MI elements has been observed experimentally, it is known to possess stripe domains given by alternating transverse domains separated by 180^o Neel walls. These observations in amorphous *Co*-based ribbons provide, at least qualitatively, the domain structure, i.e. $\mathbf{M}_d$, illustrated schematically (and ideally) in Figure 5-5.

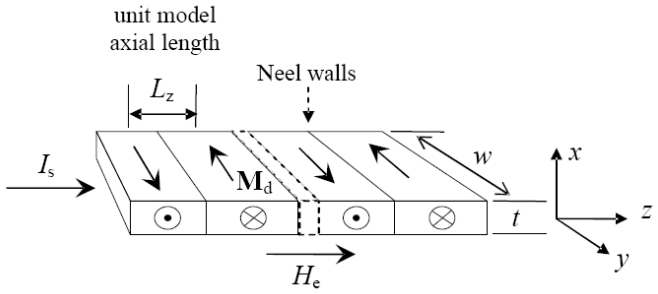

(a) Domain structure illustration

Figure 5-5 MI element *Co*-based amorphous ribbon domain structure.

Figure 5-5 is a schematic representation of the experimentally observed domain structure. In order to account for the domain structure in the coupled nonlinear harmonic model, $\mathbf{M}_d(\mathbf{x})$ is modeled analytically and included in the nonlinear harmonic model.

With an approach to include the domain structure, more is needed in order to be able to solve the problem practically using a desktop PC. The actual "length" of the individual domains is approximately 50 microns, while the length of the MI element is on the order of several millimeters or even a centimeter. Given these length scales, the physical number of domains along the axial length is estimated by 1.5 cm/50μm which

suggests on the order of several hundred domains. However, they are periodic and a relevant observation is that the domain wall widths are much narrower in their width compared to the overall domain width. This suggests that not all the domains need to be considered in the model. Thus, in this work, these conditions are exploited where only a periodic slice of length, L_z, is considered for the model (see Figure 5-5). This reduction down to a single periodic unit slice is important as it actually enables the direct study of the effects of the observed striped domain structure by reducing computational demands greatly, particularly for a desktop PC machine. Additionally, based on Figure 5-5, the following assumptions are made:

1) The domain structure is uniform in the *y* direction.

2) The *x* component equilibrium magnetization is negligible.

Based on these assumptions, $\mathbf{M}_d$ remains in the *y*-*z* plane and the *z*-component of the equilibrium magnetization is always given by the constraint $\overline{\mathrm{M}}_{dz} = \sqrt{1 - \overline{\mathrm{M}}_{dy}^{\,2}}$; where $\overline{\mathbf{M}}_d = \mathbf{M}_d / M_s$. From this, we adopt the following tensor form, using factors, for the transverse equilibrium component M_{dy}:

$$\overline{M}_{dy} = \overline{M}_N(z)\,\overline{M}_H(H_e) \tag{5-16}$$

The components describe the respective dependence on the Neel wall and external field H_e.

A complete geometrical representation including all domains in the MI element, for numerical modeling of the structure represented in Figure 5-1 would be prohibitively expensive computationally on a desktop PC. However, based on the approximations summarized above, the model is reduced to a general periodic unit slice as shown in

Figure 5-5 (see L_z) and 5-6, enabling the formulation to run on a desktop PC (Pentium 4, 3.5 MHz, 3.5 GB RAM)

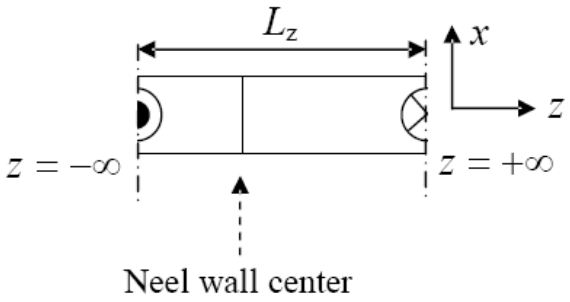

Figure 5-6 Reduced unit periodic slice

From the solutions for the unit slice, the field solutions can then be computed on a per unit length basis, the results of which can be scaled to suit the full element length. Using such an approach to model the MI effect in ribbons considering Neel walls directly, analytic forms for the Neel wall and the dependence on H_e are summarized next.

5.3.1 Analytic Neel Wall Model for $\mathbf{M}_d$ *in Ribbon*

The Neel wall introduces variations along the z direction. However, in regions sufficiently far from the center of the Neel walls moving along the axis of the ribbon element, i.e. z = ± ∞, the boundary conditions are given by

$$\overline{\mathbf{M}}_d\Big|_{z=\mp} = \begin{bmatrix} 0 & \mp 1 & 0 \end{bmatrix}^T \tag{5-17}$$

Sufficiently far away from the Neel wall is approximated as the region in the middle of each domain. In order to express a z dependent variation that rotates 180° across the unit length L_z, a function that meets these conditions is given in relevant form by

$$\bar{M}_N(z) = \tanh\left[\left(p_1 z + z_p\right)/L_c\right] \tag{5-18}$$

Thus, equation (5-18) describes the Neel wall related variation. The parameter p_1 scales the wall width, while the parameter z_p locates the center of the domain wall within the

computational domain or along L_z. The characteristic domain wall width is taken as $L_c = \sqrt{A/K}$ from the characteristics of the 180° Bloch wall model above. From this analytic model, this parameter represents a length scale for the domain wall width and is used throughout the calculations discussed. The parameter z_p is chosen such that the center of the wall is located at the position midway along the z domain range ($-L_z/2$, $+L_z/2$). Figure 5-7 illustrates an example of the resulting analytic model of the transverse equilibrium magnetization M_{dy}/M_s over the computational range.

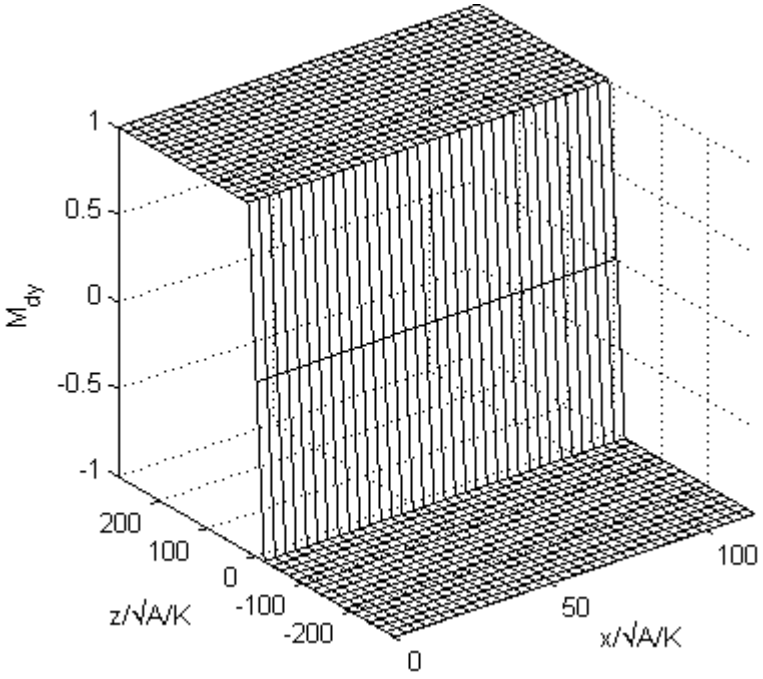

Figure 5-7 Analytic transverse equilibrium magnetization (H_e=0)

5.3.2 Dependence on H_e for M_{dy} in the Ribbon

The equilibrium magnetization not only depends on the z coordinate, but the measured external magnetic field H_e. This dependence should be treated in the absence of time varying fields, i.e. equilibrium. Without this, the formulation only describes the system at H_e=0. Thus, to approximate the dependence on H_e, a simplified equilibrium analysis is used to build a lookup table to determine the transverse component of $\mathbf{M}_d$ as a

function of the external field H_e. The specific approach that is used here is the same as what has been discussed in Chapter 3 for the case of transverse anisotropy (see 3.1.3). In this approach, the anisotropy and Zeeman energy (including H_e) are considered and minimized to determine $\mathbf{M}_d$.

5.4 Boundary Conditions for the 2D Ribbon Model

The boundary conditions are discussed here, where the treatment of the surface conditions and the axial ends of the periodic unit slice are discussed separately.

5.4.1 Boundary Conditions for x (thickness)

The resulting computational model contains variations in the *x*-*z* plane. The most straightforward of the boundary conditions are those of the wire surface (in the thickness dimension) and with both anti-symmetry and symmetry axis conditions at the center of the ribbon, we have

$x = 0$ $$\partial \mathbf{H}_{x,z} / \partial x = \mathbf{H}_y = \partial \mathbf{M} / \partial x = \varphi_D = 0 \quad (5\text{-}19)$$

$x = t/2$ $$\mu_0 (H_{Rx} + jH_{Ix}) = -(M_{Rx} + jM_{Ix}) \quad (5\text{-}20a)$$

$$H_{Ry} = I_s / 2w \text{ and } H_{Iy}=0 \quad (5\text{-}20b)$$

$$H_{Rz} = 0 ;\ H_{Iz} = 0 \quad (5\text{-}20c)$$

$$\partial \mathbf{M} / \partial x = 0 \quad (5\text{-}21)$$

$$\mu_0 \partial \left(\varphi_{DR} + j\varphi_{DI} \right) / \partial x = M_{Rx} + jM_{Ix} \quad (5\text{-}22)$$

Equation 5-19 uses both symmetry ($H_{x,z}$) and anti-symmetry (H_y) conditions. Also, we note that equation (5-21) assumes the free spinning condition discussed in more detail in Chapter 2.

5.4.2 Boundary Conditions for z (axial BC for periodic unit slice)

In order reduce the computational domain down to a single periodic unit "slice", at positions near the middle of each Neel type domain, represented by the left and right

"edges" in Figure 5-6, the variation in z is expected to be negligible because the Neel walls are so thin that as one moves very far from the center of the Neel walls, all variations in z are extremely small. Thus, on these boundaries, all variables can be assumed to vary only with x, as it is sufficiently far from the neighboring Neel walls at $z = \mp\infty$. With this, we equivalently assume that at $z = \mp\infty$, the 2D model converges to the 1D model solution that includes no domain structure, but only an equilibrium orientation that is purely transverse. Using this approximation, a high density solution of the 1D problem is enforced at the axial ends of the "slice", expressed as follows:

$$z = \mp\infty: \qquad \mathbf{f}(x, z; H_e)\big|_{z=\mp\infty} = \mathbf{f}(x; H_e)\big|_{z=\mp\infty} \tag{5-23}$$

We also note that because we are using a point collocation MLM scheme, oftentimes, treatment of the corners of the computational domain requires special attention to avoid numerical instability [43]. In this approach, however, the boundary conditions used are all consistent, and thus, no special treatment is necessary for corners of the computational domain.

5.5 Results and Discussion of Neel Wall Effects

Using the approach summarized above, the results are discussed in the following format: *first*, another important topic is discussed in solving for the numerical solution of the 2D model in particular, is the choice of the nonlinear solver used, as will be shown; *second*, we discuss the solutions of the boundary conditions at $z = \mp\infty$; *then*, we discuss 2D calculations of the ribbon MI element with a Neel wall domain structure.

In the discussion of the results, resulting MI ratios (MIR) are also computed, where in this problem, the MIR is defined as

$$\mathrm{MIR}(\%) \doteq 100 \cdot \left[V(H_e) - V(0) \right] / V(0) \tag{5-24}$$

To gauge the effects of Neel walls on the MI effect, the computed MIR is compared to published experimental data for the ribbon material considered, reported in Ref. [33]. Also, comparisons are made to the coupled nonlinear solution where all conditions and parameters are the same except that here; the assumption of a uniform transverse domain structure is made, reducing the model to 1D.

5.5.1 Remarks on Nonlinear Solver for 2D MI Effect Model

One of the most widely used nonlinear solvers is Newton's method (or Newton-Raphson). However, for systems with a large number of variables, Newton's method becomes increasingly inefficient due to excessive computational demands associated with the Jacobian matrix, **J**. At each iteration of Newton's method, the Jacobian matrix must be computed along with its inverse. For the 2D problem considered, each node has 14 degrees of freedom (real and imaginary components of vectors $\mathbf{H}_{\sim}$ and $\mathbf{M}_{\sim}$, and scalar φ_D). For Newton's method applied to this problem, this leads to an approximate total number of function evaluations at each iteration given by

$$n_{\mathrm{feval}} \approx 28n^2 + 14\vartheta(n^3) \tag{5-25}$$

n is the number of nodes in the computational domain and the last term on the RHS often dominates and is understood as "on the order of n^3". For calculations on a desktop PC, this becomes computationally expensive in 2D and 3D problems of this kind, particularly using a MATLAB programming environment on a desktop PC. Thus, for the 2D MI element model considered here, a quasi-Newton method (discussed in more detail in Appendix C) has been deployed using a *Broyden* update rule [82] with an optimized line

search [83]. The Broyden's update rule is very similar in appearance to the Newton's update rule given by

$$\mathbf{x}^{k+1} = \mathbf{x}^k - \hat{\alpha}\tilde{\mathbf{J}}_k^{-1}\mathbf{f}(\mathbf{x}^k) \tag{5-26}$$

In the Broyden's scheme, however, $\tilde{\mathbf{J}}_k^{-1}$ is generally computed from a law that approximates the inverse of the Jacobian directly by updating the previous value. Thus, $\tilde{\mathbf{J}}_k^{-1}$ can be computed from $\tilde{\mathbf{J}}_{k-1}^{-1}$, eliminating the need for a matrix inversion with each iteration. The final form of the resulting inverted update matrix used here is given by

$$\tilde{\mathbf{J}}_k^{-1} = \tilde{\mathbf{J}}_{k-1}^{-1} + \frac{\left(\boldsymbol{\delta} - \tilde{\mathbf{J}}_{k-1}^{-1}\boldsymbol{\gamma}\right)}{\boldsymbol{\delta}^T\tilde{\mathbf{J}}_{k-1}^{-1}\boldsymbol{\gamma}}\boldsymbol{\delta}^T\tilde{\mathbf{J}}_{k-1}^{-1} \tag{5-27}$$

In (5-27),

$$\boldsymbol{\delta} = \mathbf{x}_{k-1} - \mathbf{x}_{k-2} \text{ and } \boldsymbol{\gamma} = \mathbf{f}(\mathbf{x}_{k-1}) - \mathbf{f}(\mathbf{x}_{k-2}) \tag{5-28}$$

In (5-27), $\hat{\alpha}$ is found from a line search by approximating the solution to the optimization problem defined by

$$\frac{\partial}{\partial\alpha}\left\|\mathbf{f}(\alpha)\right\|^2 = 0 \tag{5-29}$$

More details of the line search are also given in Appendix C. While the quadratic convergence of Newton's solver is lost to *super*linear convergence, the quasi-Newton method requires only $\vartheta(n_c^2)$ function evaluations and as will be shown in the 2D solutions computed here, the Broyden update scheme offers a more than acceptable trade-off for the time savings as the computation time is reduced significantly.

To illustrate the time savings using a Broyden (*vs* Newton) solver, Figure 5-8 shows comparisons of the 2D solution convergence behavior and computation times, *T*. Both

methods use an optimized line step, where results are shown for 5x5, 7x7, 9x9, and 11x11 nodal sets.

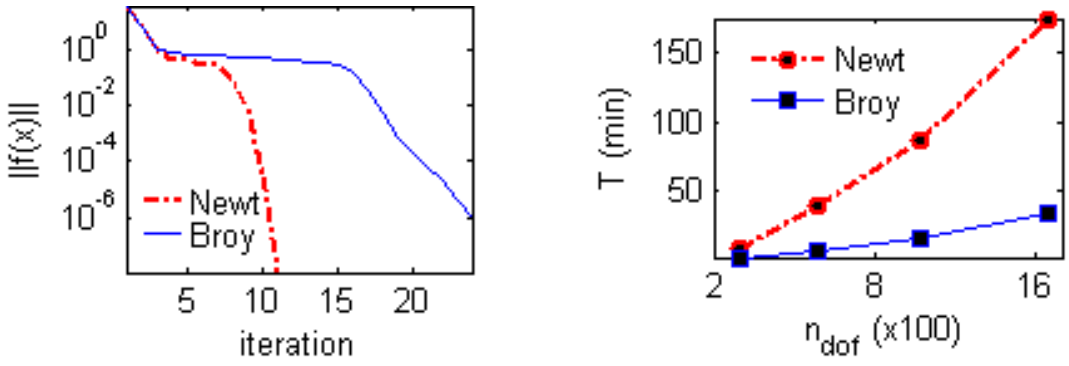

(a) convergence of f(x)

(b) solver computation time, T

Figure 5-8 Newton and Broyden solver convergence and computation times comps. (tol = 1e-6)

Figure 5-8 shows that the reduction in the number of iterations seen in the Newton's solver adds no value because each iteration of Newton's method takes considerably more time due to the need to compute the Jacobian and its inverse. Thus, using a quasi-Newton method for the problem considered saves considerable computation time, particularly as the number of degrees of freedom becomes large. A Broyden update law is therefore used in the calculations presented for the domain wall problems in the MI sensor.

Additionally, for all calculations presented for the ribbon MI element, Table 5-1 provides the remaining parameters used to simulate a 40 μm thick amorphous ribbon element subjected to an *ac* current source, I_s, at an operating frequency f = 120 *k*Hz taken from experimental data reported in Ref. [33]

Table 5-1 2D Harmonic Ribbon Wire Simulation Parameters

M_s (T)	I_s (mA)	f (kHz)	σ (mΩ-cm)$^{-1}$	H_K (A/m)	α	L_z (μm)	t (μm)	A (J-m^{-1})
1.39	10	120	7.6923	478	0.01	100	40	10^{-11}

M_s was computed using the volume compositional average based on published M_s values for *Co* and *Fe* [4], for the experimental material, $Co_{70.4}Fe_{4.6}Si_{12.5}B_{10}$. The preferred anisotropy direction is assumed uniformly transverse throughout the ribbon given by the direction $\mathbf{e}_K = [0\ 1\ 0]^T$.

5.5.2 Boundary Solutions at z=±∞

An initial insight into the effects of a domain structure in ribbon MI elements is given by considering the boundary condition solutions discussed in the previous section, at z = ± ∞. The equilibrium magnetization in these regions occupies a large extent of the volume, thus the behavior in this region possibly constitutes behavior for a large percentage of the volume of the ribbon, as well. Here, the 1D boundary model is solved at both axial ends (of the periodic unit slice) keeping uniform transverse anisotropy throughout the thickness of the structure, only accounting for the alternating 180^o equilibrium magnetization configuration. Figure 5-9 shows comparisons of the field intensity and magnetization transverse component amplitudes that have been computed at $H_e = H_K$ and corresponding phase angles ϕ and ϕ_M.

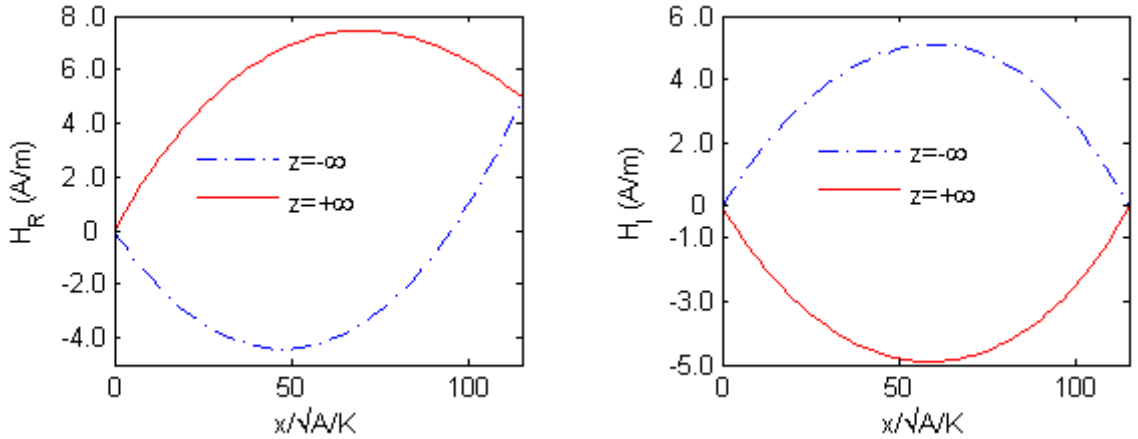

(a) H_{Ry} solutions

(b) H_{Iy} solutions

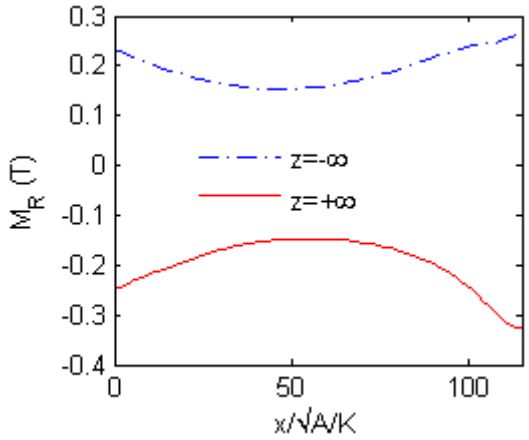

(c) M_{Ry} solutions

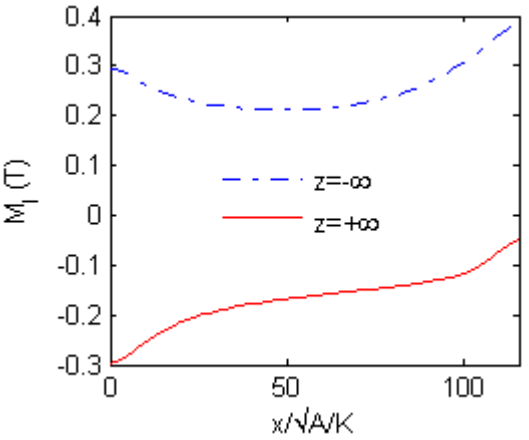

(d) M_{Iy} solutions

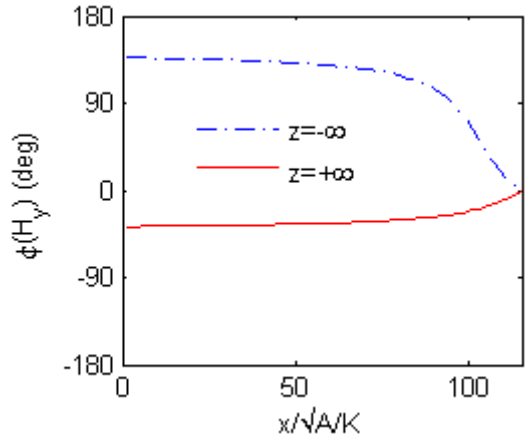

(e) H_y phase, ϕ

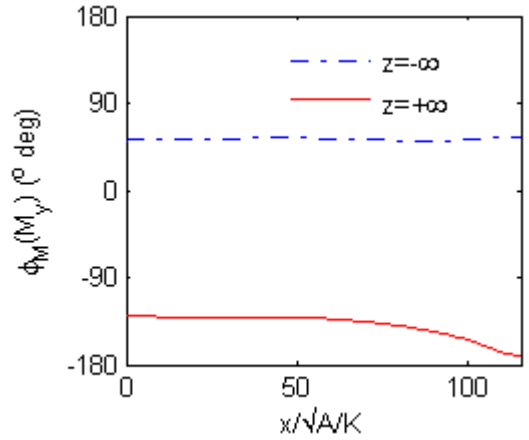

(f) M_y phase, ϕ

Figure 5-9 H_y and M_y solution (and phases), at z=±∞.

The boundary solutions in Figure 5-9 show that both the magnetic field intensity and magnetization both depend on the equilibrium magnetization distribution. This type of

information is not obtainable using decoupled models, where independent magnetization distributions are "given up" because both are assumed proportional to one another in space. In the more general coupled nonlinear model, however, the phase difference between magnetic field intensity solutions in both domains are approximately 180^o, clearly indicating an influence from the 180^o alternating domains along the ribbon axis.

Figure 5-9(e) and (f) show the phases of the both the magnetic field intensity and magnetization clearly indicating a 180^o phase difference, with the exception that for the magnetic field at the surface. It is seen that the phase difference vanishes close to the surface of the ribbon, due to the current source. The presence of the current in the MI ribbon element contributes to "breaking symmetry" (like that seen in H_{Iy}) by ensuring a positive nonzero boundary condition on the surface for the real component of H_{Ry} on both sides of the domain wall.

These results are consistent with a physical picture of partly axially aligned magnetization vectors (due to $H_e = H_K$), each predominantly responding to the transverse field when the "sign" of the input wave is in the opposite sense of the equilibrium domain orientation. This generates a phase between 0^o and -180^o. Such a picture is also expected to generate a 180^o phase difference between both ends of the unit periodic slice as each domain responds according to the respective upwards and downwards peaks of the input, which are 180^o apart. Additionally, the difference in phase between H_y and M_y is approximately 90^o, which is also consistent with this physical picture, as the magnetization is switching while the local transverse field is approaching its maximum amplitude.

Additionally, to see the dominant components of the total effective field, $\mathbf{H}_T$, the norms of the components including $\mathbf{H}_K$, $\mathbf{H}_X$, $\mathbf{H}_D$, and the total external field, $\mathbf{H}_Z$=$\mathbf{H}$, are shown in Figure 5-10 for the boundary solution at $z = +\infty$.

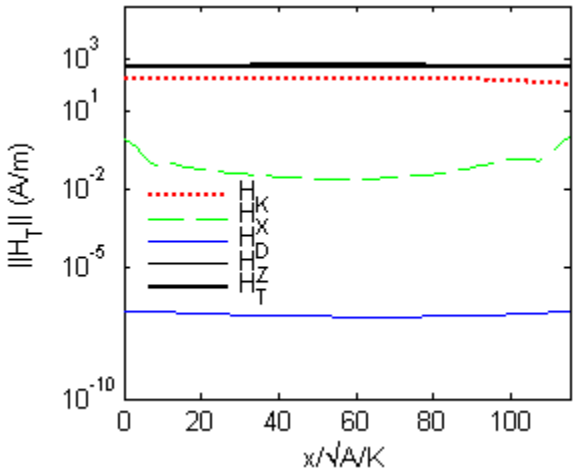

Figure 5-10 $|H_T|$ components at $z = +\infty$. Note: $|H_z|$ is underneath $|H_T|$

Figure 5-10 shows that the external field and anisotropy field dominate in the problem by several orders of magnitude, particularly when $H_e \approx H_K$. This also further justifies the simplified approach for describing the dependence of the analytic equilibrium domain model M_{dy} on the *dc* external field H_e where the only contributions considered are the external field related (Zeeman) and the anisotropy energies (discussed in Chapter 3).

5.5.3 Discussion of 2D MI Ribbon Model Results with Neel Walls

For transverse anisotropy, the peak of the MI voltage is known to occur when the external field, H_e, is in the vicinity of the anisotropy field H_K. Based on this, we compute a data point at the point $H_e = H_K$ and 2 additional values at $0.1H_K$ and $0.6H_K$. Figure 5-11 and 5-12 show the solutions for H_y and M_y components for all three data points, where the top-most set of figures (Figure 5-11) show H_y solutions and M_y in the second set of figures (Figure 5-12).

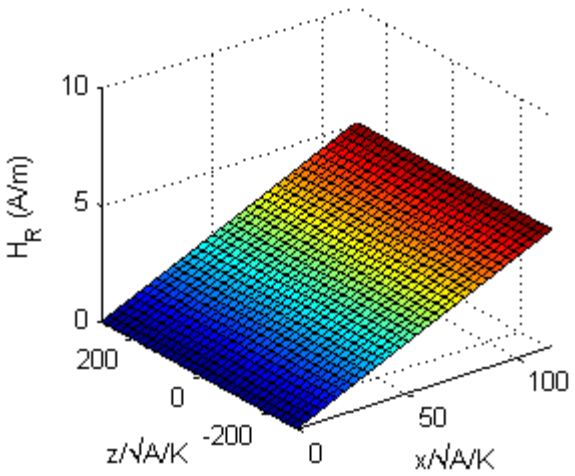

(a) H_{Ry} at $H_e/ H_K = 0.1$

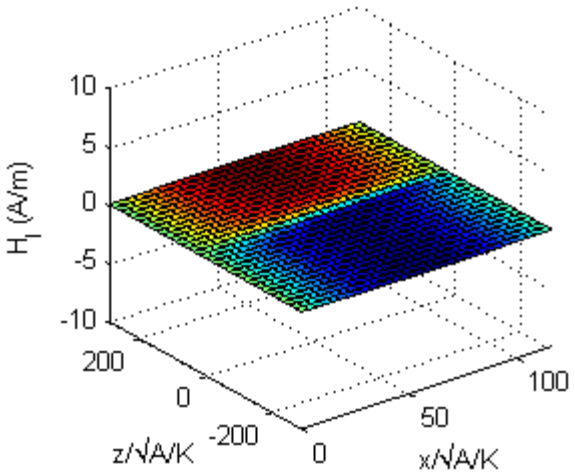

(b) H_{Iy} at $H_e/ H_K = 0.1$

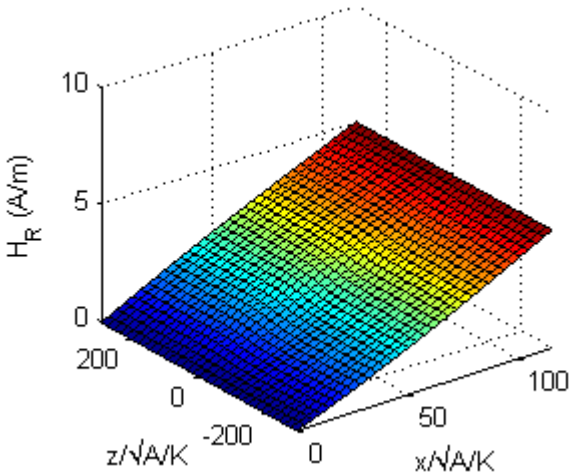

(c) H_{Ry} at $H_e/ H_K = 0.6$

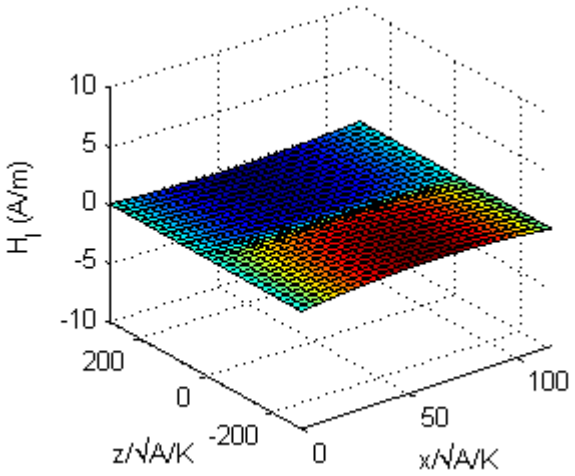

(d) H_{Iy} at $H_e/ H_K = 0.6$

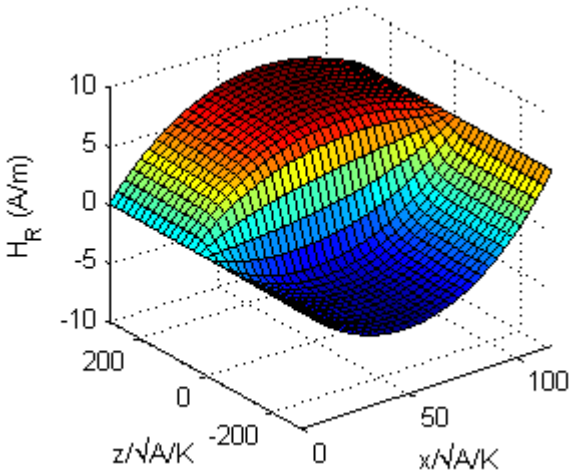

(e) H_{Ry} at $H_e/ H_K = 1.0$

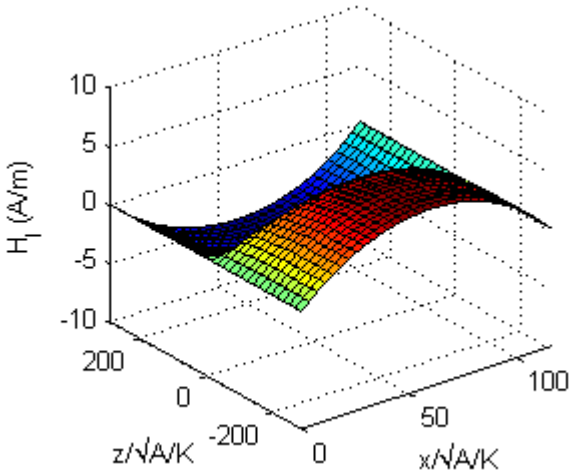

(f) H_{Iy} at $H_e/ H_K = 1.0$

Figure 5-11 H_y components versus H_e

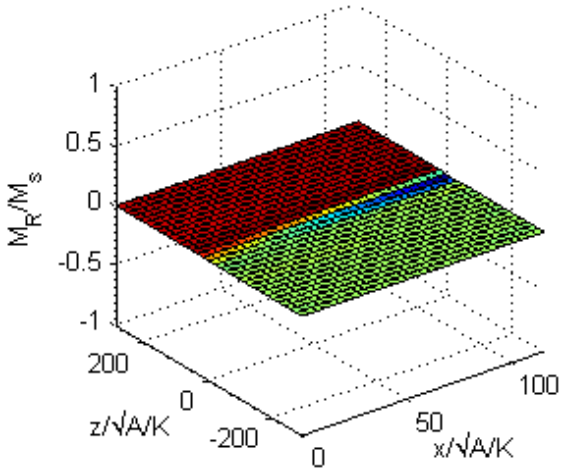

(a) M_{Ry} at $H_e/ H_K = 0.1$

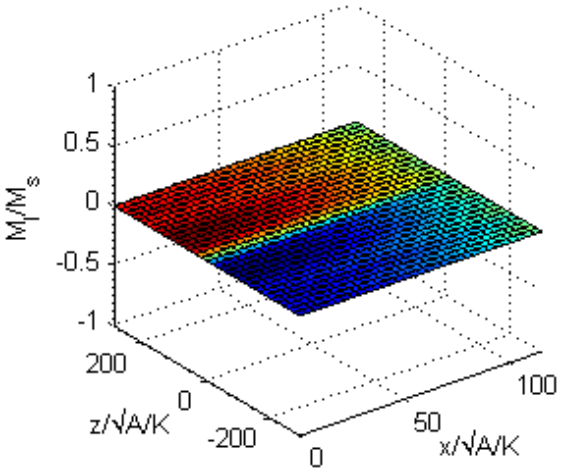

(b) M_{Iy} at $H_e/ H_K = 0.1$

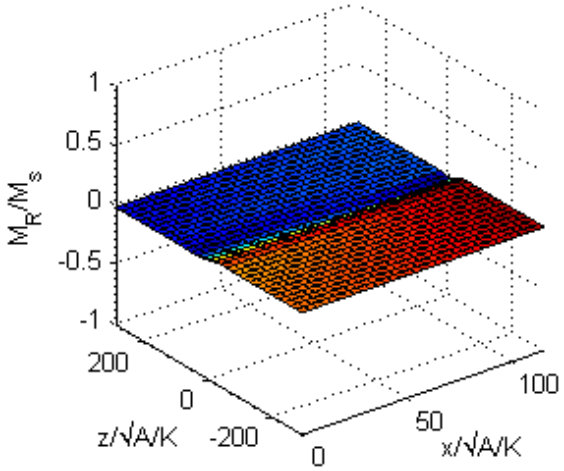

(c) M_{Ry} at $H_e/ H_K = 0.6$

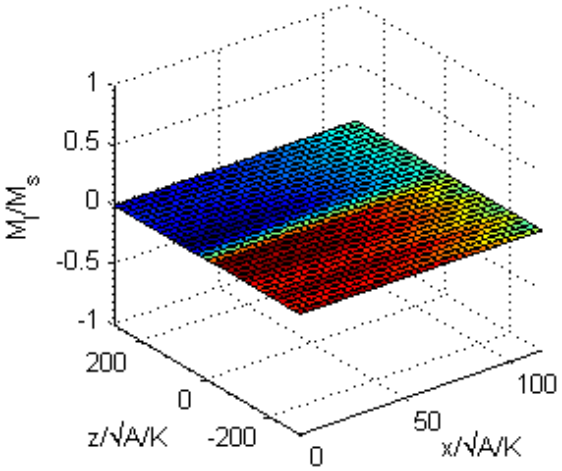

(d) M_{Iy} at $H_e/ H_K = 0.6$

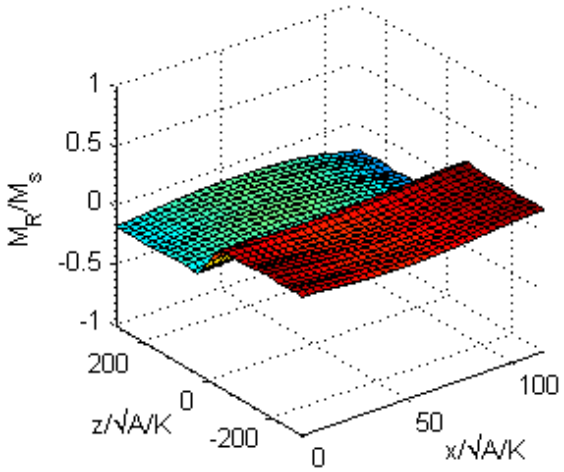

(e) M_{Ry} at $H_e/ H_K = 1.0$

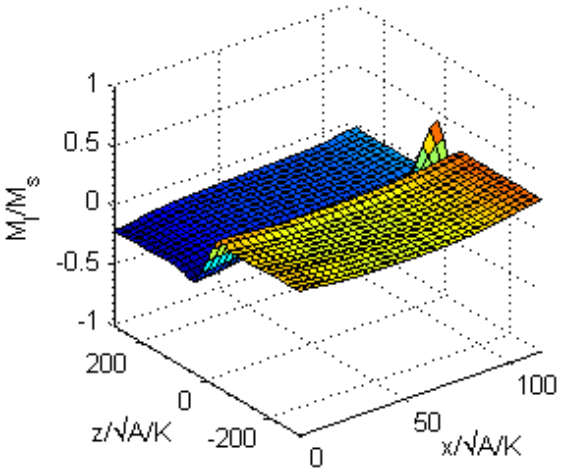

(f) M_{Iy} at $H_e/ H_K = 1.0$

Figure 5-12 M_y components versus H_e

Figures 5-11 and 5-12 both show that the Neel wall region provides the conditions that facilitate an analogous narrow transition region for the harmonic components of both **H** and **M**. It is also seen that a large portion of the ribbon favors the boundary condition solutions and thus the behavior in this region contributes strongly to the flux. This transition between oppositely oriented oscillations is significant in the MI effect because this condition leads to *flux cancellation* along the axis of the ribbon which reduces the axially measured inductive voltage V_L. Integrating over the area (x-z) of such a periodic pattern leads to a significant degree of equal and opposite cancellations over the integral, similar to integrating the sine function over the range 0 to 2π. This flux cancellation is possibly a factor in experimental observations that show that ribbon MI elements are less sensitive than their cylindrical counterparts including both single material amorphous and composite wires. Within *Co*-based cylindrical amorphous MI elements, the domain structure is such that Neel walls are only in the outer part of the wire, while the core is axially aligned. Also, in composites MI elements, no domain walls exists, and this geometry has reported the highest MI ratios observed among all MI element geometries [20] being on the order of 1000s of %. *Thus, the coupled nonlinear harmonic model suggests that the Neel wall domain structure ultimately reduces the measured inductive voltage drop along the axis of the MI element.*

The solutions also suggest by Figure 5-11(f), the bulk of the switching takes place within the core of the ribbon, especially when $H_e \sim H_K$. These conditions are very consistent qualitatively with computations in the circular wire, discussed in the previous chapter (and in Ref. [62]).

The effects of the external field on the model are also consistent with experiments in that all of the "action" takes place when H_e is in close proximity to H_K. To illustrate this predictive feature of the model, the surfaces in Figure 5-11 and Figure 5-12 are shown for all three data points, $H_e = H_K$, H_e=0.6H_K, and H_e=0.1H_K where the variations with H_e are along the vertical direction. The oscillation amplitudes are clearly diminishing as the amplitude of H_e approaches zero. In other words, the profile comparison shows that the distributions develop rapidly in both x and z, but not until H_e is much closer to H_K. For H_e = 0.6H_K, the amplitudes are actually an order of magnitude smaller than that of H_e = H_K.

Physically, the vanishing of the transverse amplitudes can be explained as follows: In the weak field region, the magnetization is firmly oriented by the transverse anisotropy field. This field has a value of ~478 A/m in comparison to a maximum value of ~10 A/m for the *ac* field generated by the *ac* current source. Therefore, when the measured external field (H_e) is small and $\mathbf{M}_d$ is naturally aligned in a transverse direction (due to $\mathbf{H}_K$), it does not respond sensitively to the relatively weak transverse *ac* field, H_y. This condition is relieved as H_e approaches H_K causing the steady component of the magnetization to re-orient more along the z axis. This subtle re-orientation introduces a growing sensitivity to the overall oscillation of the magnetization by way of developing ferromagnetic resonance (FMR). In these developing conditions, **M** rotates towards both transverse directions over a cycle in response to the current, however, because much more "swing" is present when oscillating in the opposite sense, the net result is an oscillation with reduced amplitude in the opposite direction. This corresponds to the phase between 0 and -180^o as discussed earlier. Additionally, as H_e begins to increase

further past H_K (H_e>H_K), the same "stiffening" effect occurs with respect to H_e, where the sensitivity to the transverse field intensity diminishes again due to being more "stiffly" aligned in the *dc* external field direction. This description is better known as ferromagnetic resonance (FMR), where the interplay of the magnetization using both a steady field and harmonic field create the necessary conditions for FMR.

5.5.4 MIR Comparisons

In discussing the MIR, the values at the three data points have been computed for H_e = $0.1H_K$, $0.6H_K$, and H_K. Given the MI voltages, the MI ratio (MIR) is found from (5-24). To gauge the effects of the domain walls in the material considered, published experimental MIR values are used for comparison to the model along with results ignoring domain walls completely. This is shown in Table 5-2.

Table 5-2 2D Ribbon MIR % comparisons

	experiment (Machado[33])	2D model with domain structure	1D model ignoring domain structure
H_e=H_K	45 %	211 %	1187 %
H_e=$0.6H_K$	10 %	13.2 %	75 %
H_e=$0.1H_K$	1 %	1.6 %	16 %

The MIR values result in much smaller MIR values (or voltages) when a domain structure is present, and tend more towards the experimental data that has been reported. Based on the discussion above, this reduction follows from the *flux cancellation* which is a direct result of the domain structure.

Sources For Error in Coupled Model

It is also important to understand the sources for the differences between the coupled nonlinear model and experimental measurements. Likely contributors to the error include:

1) Errors in the analytical domain model representation

2) The method of treatment of the equilibrium state as a function of H_e.

3) Additionally, the estimated saturation magnetization M_s is also likely to be smaller than what has been estimated using volume compositional averages, particularly based on a recently discovered report on measured saturation magnetization values in similar magnetic alloys [68].

5.6 Conclusions for Effects of Neel Walls in Ribbons

In this first case study of the effects of a domain structure, we have investigated the effects of the experimentally observed 180^o Neel wall domain structure in ribbon MI elements. This problem has been shown to serve as a good example to illutrate the benefits of using a Broyden nonlinear solver as opposed to a Newton solver in combination with a point collocated MLM formulation. Results for the ribbon model show that the equilibrium domain structure influences both the magnetic field intensity ($\mathbf{H}_{\sim}$) *and* the magnetization ($\mathbf{M}_{\sim}$) amplitudes. Considering a Neel wall structure in the MI ribbon element, this distinct condition has lead to a peculiar flux reduction mechanism resulting from oppositely oriented oscillations in the ribbon that effectively reduces the amount of voltage drop across the axis of the ribbon. This leads to greatly reduced MIR values more consistent with published experimental data.

Also, these observations are made in the small external field region $0 \leq H_e \leq H_K$, where the domain structure is more "in tact" well below saturation. Otherwise, a linearized model should be a good approximation of behavior, even allowing a coupled formulation where exchange is the primary difference.

5.7 Effects of 90° Bloch Wall in Circular Wire

Analogous to the MI ribbon element, the circular amorphous element possesses a domain structure that has been observed experimentally. According to observations by Yamasaki *et al*., circular *Co*-based amorphous wires possess the so-called "bamboo" domain structure with 180° Neel walls only in the exterior portion of the wire. In this case, they were observed using Bitter pattern techniques. In this structure, it was also found that there is an interior 90° radial Bloch wall extending along the entire length of the wire.

5.7.1 Analytic Domain Structure Representation

Figures 5-13(a) and 5-13(b) are schematic representations of the experimentally observed domain structure illustrating both exterior and interior perspectives.

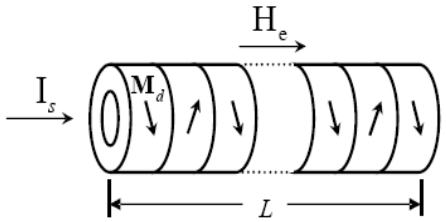

(a) Domain wall illustration (exterior)

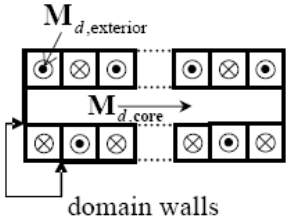

(b) Domain wall illustration (interior)

Figure 5-13 Circular Co-based amorphous wire bamboo domain structure

In order to account for $\mathbf{M}_d$ in the model, the arrangement shown is Figure 5-10 is also represented analytically using closed form mathematical functions for $\mathbf{M}_d(\mathbf{x})$. Using the

general formulation in the 2D domain (to be discussed next), only the radial Bloch wall is considered in these calculations. As mentioned before, this limited case was due to an apparent extreme stiffness of the problem considering both domain walls for computation on a desktop PC.

Nonetheless, based on these experimental observations of the domain structure, similar to the case of the ribbon element, it is still assumed that

1) The domain structure is uniform in the transverse (circumferential) direction and

2) The equilibrium magnetization radial component is negligible.

An analogous tensor form is then used for the circumferential equilibrium component leading to

$$\bar{\mathrm{M}}_{\mathrm{d}\theta}\left(r,z;H_e\right)=\bar{\mathrm{M}}_{\mathrm{B}}\left(r\right)\bar{\mathrm{M}}_{\mathrm{N}}\left(z\right)\bar{\mathrm{M}}_{\mathrm{H_e}}\left(H_{\mathrm{e}}\right) \tag{5-31}$$

The normalized equilibrium magnetization vector is given by

$$\bar{\mathbf{M}}_{\mathrm{d}}=\left[0 \quad \mathrm{M}_{\mathrm{d}\theta}/M_{\mathrm{s}} \quad \mathrm{M}_{\mathrm{dz}}/M_{\mathrm{s}}\right]^T=\left[0 \quad \bar{\mathrm{M}}_{\mathrm{d}\theta} \quad \bar{\mathrm{M}}_{\mathrm{dz}}\right]^T \tag{5-32}$$

$\bar{\mathrm{M}}_{\mathrm{B}}\left(r\right)$ describes the radial 90° Bloch wall-related variation, $\bar{\mathrm{M}}_{\mathrm{N}}\left(z\right)$ describes the 180° Neel wall-related variation as in the ribbon and $\bar{\mathrm{M}}_{\mathrm{H}}\left(H_{\mathrm{e}}\right)$ describes the dependence everywhere on the *dc* external field H_{e}.

For the case of a "tangential" equilibrium magnetization structure, where $\mathbf{M}_{\mathrm{d}}$ remains in the θ-z plane, the z-component of the *dc* magnetization is always given by the constraint $\bar{\mathrm{M}}_{\mathrm{dz}}==\sqrt{1-\bar{\mathrm{M}}_{\mathrm{d}\theta}{}^2}$. Based on the shape of the 90° Bloch wall, the radial variation must vary exponentially while meeting necessary boundary conditions from the center of the wire to the surface given by

$$\bar{\mathbf{M}}_{\mathrm{d}}\Big|_{r=0} = \begin{bmatrix} 0 & 0 & 1 \end{bmatrix}^T \text{ and } \bar{\mathbf{M}}_{\mathrm{d}}\Big|_{r=r_0} = \begin{bmatrix} 0 & \pm 1 & 0 \end{bmatrix}^T \tag{5-33a,b}$$

An analytic function that provides a representation for $\bar{\mathrm{M}}_{\mathrm{B}}$ is given by a sigmoid function:

$$\bar{\mathrm{M}}_{\mathrm{B}}(r) = \frac{1}{1 + e^{-\left[(p_1 r + r_i)/\sqrt{A/K}\right]}} \tag{5-34}$$

The exponent in the denominator of the function in (5-34) also contains two parameters, p_1 and r_{i}. The first parameter, p_1, scales the domain wall width. The second parameter, r_{i}, controls the location of the center of the domain wall along the radial dimension of the wire. The value of r_{i} is estimated from discussions of experimental observations by Yamasaki *et al*. The radial location of the experimentally observed domain structure was estimated to be between the half-radius and the surface for *as-cast* wires, while the wall is expected to shift inward for stronger transverse anisotropy induced with annealing where a tension is applied to the wire in parallel [14]. The wires modeled here have been annealed at a tension of 2 kg/mm^2 and therefore the wall is assumed to have shifted inward to be located approximately at the half-radius of the wire in its initial configuration, i.e. $r_i / r_0 \approx 0.5$.

As in the case of ribbon element, an analytic function describing Neel wall related variation is given by a hyperbolic tangent function:

$$\bar{\mathrm{M}}_{\mathrm{N}}(z) = \tanh\left[\left(p_3 z + z_i\right)/\sqrt{A/K}\right] \tag{5-35}$$

For illustration, Figure 5-14 shows the resulting analytical representation of the equilibrium magnetization (at H_{e}=0), including $\bar{\mathrm{M}}_{\mathrm{B}}$ (at $z = +\infty$), $\bar{\mathrm{M}}_{\mathrm{N}}$ (at the surface), and the resulting transverse magnetization component over the computational domain.

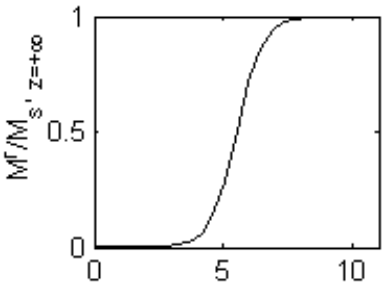

(a) $M_{d\theta}$(r) versus normalized r

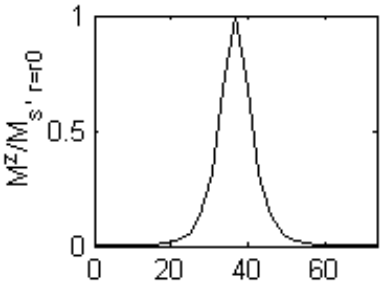

(b) M_{dz}(z) versus normalized z.

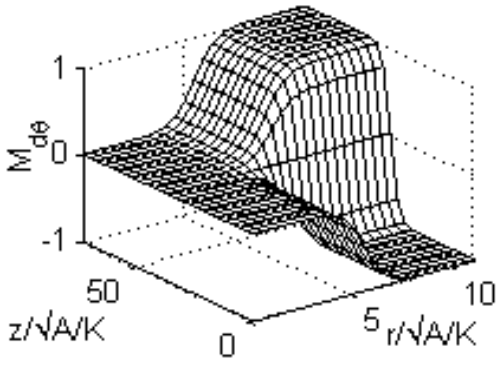

(c) transverse equilibrium surface

Figure 5-14 Analytic transverse equilibrium magnetization component.

5.7.2 Boundary Conditions (circular wire)

The most straightforward of the BCs are those pertaining to the radial dimension, where we have

$r = 0$ $$\partial \mathbf{H} / \partial r = \partial \mathbf{M} / \partial r = \varphi_D = 0 \quad (5\text{-}36)$$

$r = r_0$ $$\mu_0 (H_{Rr} + jH_{Ir}) = -(M_{Rr} + jM_{Ir}) \quad (5\text{-}37a,b)$$

$$H_{R\theta} = I_s / 2\pi r_0 \text{ and } H_{I\theta} = 0 \quad (5\text{-}37c,d)$$

$$H_{Rz} = 0 \text{ and } H_{Iz} = 0 \quad (5\text{-}37e)$$

$$\partial M_{r,\theta} / \partial r + (1/r) M_{r,\theta} = 0;\ \partial M_z / \partial r = 0 \quad (5\text{-}38)$$

$$\mu_0 \partial (\phi_{DR} + j\phi_{DI}) / \partial r = M_{Rr} + jM_{Ir} \quad (5\text{-}39)$$

The reduction of the MI element computational domain down to a unit periodic slice follows the same logic as in the case of the ribbon. At positions near the middle of each domain, indicated by the vertical dashed lines in Figure 5-15, the variables can be assumed to vary only with r, as it is sufficiently far from the neighboring Neel walls. Then, the MI element between these positions is assumed to be periodic along the entire

length of the MI element. Figure 5-15 illustrates a region with two magnetic domains containing a periodic unit slice bounded at $z = \mp\infty$.

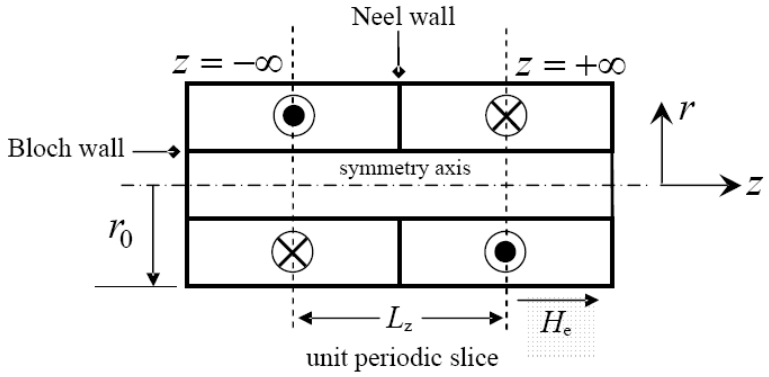

Figure 5-15. Slice containing a unit domain structure model, of length, L_z.

The 2D model (at these z boundaries) is then assumed to converge to the 1D model solution that only includes the radially varying 90° Bloch wall. A high density solution of the 1D problem at the axial ends of the "slice" is enforced as a Dirichlet boundary condition, expressed as

$$z = \mp\infty \qquad y(r,z;H_e)\big|_{z=\mp\infty} = y(r;H_e)\big|_{z=\mp\infty} \tag{5-40}$$

5.7.3 Results and Discussion of 90° Bloch Wall Effects

Again, the *Hp*-Cloud MLM shape functions are deployed in a point collocation formulation. The discussion considers only the effects of the 90° radial Bloch wall (the edges) in the weak field region, $H_e = 0$, where these effects can be put into context by considering the solution ignoring domain structure, to see the effects of their presence. Resulting MI voltages are also discussed and compared to experimental data, as well.

For all calculations presented for the circular wire with a 90° Bloch wall, Table 5-3 provides all additional parameters used to simulate a 15 μm (r_0 = 15 μm) radius amorphous MI wire element with an *ac* current source, I_s = 15 mA and f = 1 MHz [9].

Table 5-3 Harmonic Bloch Wall Model Simulation Parameters

M_s (T)	σ $(k\Omega\text{-m})^{-1}$	K (J-m^{-3})	α	L_z (μm)	A ($J\text{-}m^{-1}$)	γ	p_1	r_i
1.35	67.367	0.697	0.01	100	10^{-11}	m_e/q_e	1	0.5

M_s was computed using the volume compositional average based on published values for both Cobalt and Iron [4] for the experimental material, $Co_{68.15}Fe_{4.35}Si_{12.5}B_{15}$ [9]. The preferred anisotropy direction is assumed radially distributed and equal to the exponential variation of $\bar{M}_B$, equation (5-34), at $z = +\infty$ throughout the wire.

An initial insight into the effects of the experimentally observed domain structure is given by considering only the 90^o Bloch wall. Additionally, we note that all earlier investigations (to our knowledge) of the MI effect that have considered domain walls in MI element structures at all have only considered the effects of the axially distributed Neel walls in a lumped parameter model, while ignoring Bloch walls altogether [24]. Because the pure Bloch wall regions (away from Neel walls) span the entire length of the element, it is likely that behavior from this domain wall influences the resulting magnetic flux linking to the MI voltage.

The effect of the Bloch wall is seen clearly in Figure 5-16, illustrating the transverse component of both **H** and **M.**

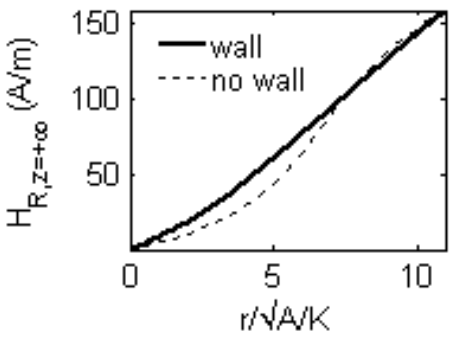

(a) $H_{R\theta}$ at z = +∞

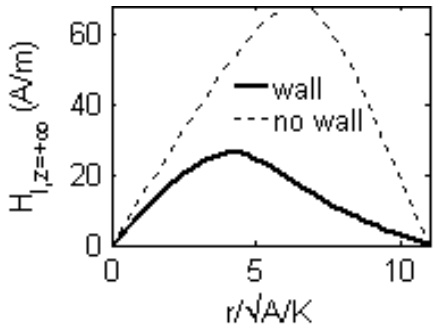

(b) $H_{I\theta}$ at z = +∞

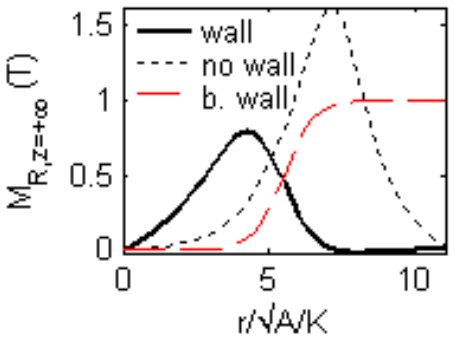

(c) $M_{R\theta}$ at z = +∞

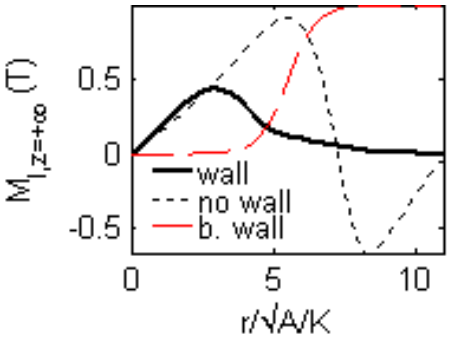

(d) $M_{I\theta}$ at z = +∞

Figure 5-16 Radial field/magnetization with and without Bloch wall (Bloch wall shown for reference)

Figure 5-16 shows comparisons of the field intensity and magnetization amplitudes with and without a 90° Bloch wall present at $H_e = 0$. It is seen that the Bloch wall tends to reduce the amplitude distributions across the radius of the wire. The domain wall is also shown in Figure 5-16(c) and (d) clearly indicating that the interior region (one side of the domain wall), is much more active than the outer part of the wire magnetization.

For an intuitive feel of the resulting profile in the Bloch wall regions of the wire, Figure 5-17 illustrates $|B_\theta|$ within the MI element for both cases where (a) is without any domain wall, while (b) includes the 90° Bloch wall.

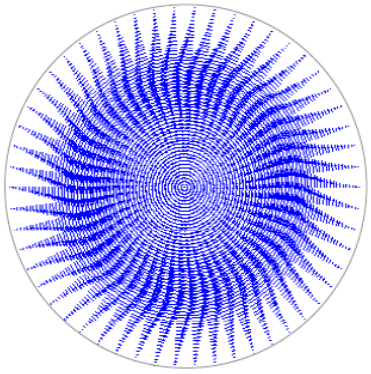

(a) $|B_\theta(r)|$ with no wall

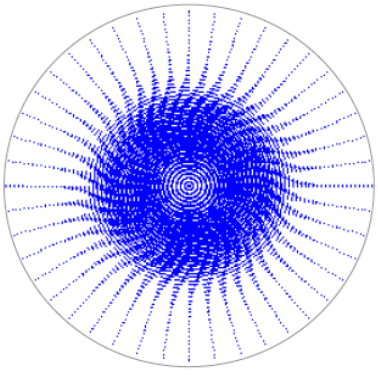

(b) $|B_\theta(r)|$ with 90° Bloch wall

Figure 5-17 $|B_\theta|$ profile comparisons with and without Bloch wall. ($H_e = 0$)

A suppressing effect of the radial Bloch wall is very apparent in both the magnetic

field intensity, as well as, the magnetization. For this problem, the inductive component of the MI voltage is determined largely by the magnetization distribution, which shows that the presence of the Bloch wall leads to a reduced inductive voltage, by way of a *reduced average magnetization*.

Physically, we can describe this observation in the following way: In this case, at zero *dc* external field, the exterior domains, in particular, remain aligned in the transverse direction in the configuration where the equilibrium domains are parallel to both the anisotropy direction and the transverse field. However, in the interior domains, the magnetization is more sensitive to the *ac* transverse field, which dominates among total effective field components. The interior domains are more "loosely" aligned along the axis of the wire, and are more sensitive or more relatively influenced by the alternating transverse field. Therefore, the presence of the Bloch wall leads to a relatively stronger interior switching phenomenon in the core separated by Bloch walls.

Comparisons To Experiment With Bloch Walls

The suppressed profile shown in Figure 5-16 and 5-17 lead to a total MI voltage amplitude of ~255 mV with a Bloch wall in the MI element compared to ~350 mV without the Bloch wall domain structure. The experimental voltage for the wire is reported as ≈ 275 mV, for $H_e = 0$. Thus, including the Bloch wall leads to smaller MI voltages due to the effect of a reduced average magnetization within the wire, and in this case leads to an error of ~7 % in the case where the Bloch wall is considered.

5.9 Conclusions on Effects of the 90^o Bloch Wall

We have presented the effects of the experimentally observed domain structure on the

MI effect by investigating a 90^o radial Bloch wall, experimentally shown to be present in amorphous cylindrical MI elements. The 90^o Bloch wall has been shown to contribute to a reduction in the average transverse magnetization amplitudes, which leads to smaller MI voltages. This is consistent with the effects of the Neel walls discussed previously, where they also caused reduced MI voltages.

5.10 Conclusions on Effects of a Domain Structure

Overall, in this chapter, using the coupled nonlinear harmonic model, we have considered the effects of an equilibrium domain structure within the MI element explicitly. The domain structures considered have been observed experimentally in MI wires. Both 180^o Neel walls in ribbon elements and 90^o Bloch walls in circular wires have been considered, where general results can be summarized as follows: equilibrium domain walls effectively reduce the MI voltages. The way these reductions take place are different between the types of domain walls considered where the Neel walls have been shown to induce a type of flux cancellation. However, in the case of the Bloch wall, the reductions in the MI voltage are by way of a reduction in the average magnetization due to a "tighter" distribution. Both lead to reduced MI voltages which have been shown in both cases to lead to results tending towards the experimental data.

CHAPTER 6
CONCLUSIONS & FUTURE WORK

A key goal in this thesis research has been to develop an analytical model that describes the MI effect in such a way that new and improved prediction capability as well as new information can be retrieved with its use for weak field measurements. In the modeling approach introduced here, it has been shown to provide improved accuracy in comparison to experimental data as well as an overall improved understanding of the MI effect. However, in order to arrive at such a model, careful thought was required in organizing the needed tools that would be supportive of this overall goal. The use of numerical methods for this problem demands considerable time due the following reasons:

1) Treatment of such a cross-disciplinary subject like the MI effect does not have a convenient option of an "off the shelf" software package, thus custom code was more practical.

2) Additionally, in order to build a numerical model using a standard PC, additional efforts were required to aim at reducing computational costs and discussions have summarized these efforts showing the additional computational savings by use of the selected point collocation meshless formulation as well as a quasi-Newton nonlinear solver, all motivated by illustrated shortcomings in the approach using decoupled models.

6.1 Limitations of Decoupled Models

We have discussed previous works studying the MI effect (as well as meshless methods). What has emerged from studying previous works is that the limitations of the

decoupled approach are most times due to inconsistency with experimental conditions, where saturation is not the operating condition. Such an approach assumes that one mode out of the three modes of the magnetization is much more dominant than the other two. In this case, the combined effects are well represented by the dominant mode and thus a scalar permeability, for example, approximates the behavior well. In studying the MI effect, this distinction turns out to be very important if the interest is in the behavior and prediction when a weak magnetic field is measured (well below the saturating field). This has been the interest taken up in this thesis research.

Previous models have been shown incapable of resolving behaviors that are dominant in the weak field region. For example, domain structure is typically an influence observed well below saturation. Decoupled models can not treat a domain structure directly, but can only attempt to describe their effects phenomenologically, at best. It has been an interest here to reduce the number of phenomenological parameters to regain a higher fidelity description of the MI effect. Such efforts alleviate these kinds of concerns and build more confidence in the ability to predict the behavior of the MI effect with a domain structure, particularly in these kinds of weak field condition and over a broader range of conditions.

6.2 Benefits of Numerical Models

Numerical models of the MI effect have been shown to offer an approach to improve upon the previous decoupled models and provide an alternative way to model the MI effect in such a way that allows a focus on the region in which decoupled models are not designed to treat accurately (weak fields). Specifically, the assumption(s) that lead to decoupling can be relaxed more easily to allow this kind of investigation.

A numerical approach, however, also has a large number of possible approaches to formulate the problem. With this, we have systematically selected an approach that apparently reduces the computational times without sacrificing the accuracy of the solution. The *Hp*-Cloud MLM shape functions have served very well in achieving this goal. It was shown in two different test cases that such a formulation helps to achieve the goal of improved efficiency with good accuracy. MLMs have been a very important part of the realization of the numerical-based MI effect model.

The approach to modeling the MI effect using numerical methods has more obvious advantages by accessing more information. However, achieving the results discussed here involved the successful deployment of a point collocation MLM formulation. This has enabled a more efficient way to discretize the system in space which has led to the ability to solve the problems of interest here using a desktop PC, even in the case of the treating the time domain. To further make the computational cost more "affordable", an implicit time integration scheme was used based on its well known superior stability compared to explicit methods. A selective quasi-Newton nonlinear solver was also deployed to aid in computational cost reduction, particularly in problems where the degrees of freedom becomes very large.

6.3 Original Contributions of This Work

Using the numerical approach with all of these selective methods, the numerical MI effect model has achieved the following:

1) We have constructed a numerical-based model that generally describes temperature, magnetization, magnetic field intensity, and other variables including the demagnetization potential in studying the MI effect. Using this, it was also shown that in

near room temperature, operating at the currents that are typically used (<20 mA), temperature effects are negligible and the temperature is practically uniform over the small MI element structure. This made way for the introduction of a coupled nonlinear harmonic model to describe the MI effect. Thus, numerical formulations that have been demonstrated as useful have been successfully formulated in an original way in this thesis research.

2) Using these modeling formulations, new information has been revealed about MI effect sensors. For example, the space-time model has been used to reveal that the mode of switching for the magnetization in the cylindrical amorphous wire is by way of a dynamic domain wall propagating radially inward, contrary to what decoupled models have suggested. Mechanisms explaining the peculiar rise in the MI voltage near room temperature were given as predicted by the more general formulation. The same mechanism (for temperature) was also used to explain the effects of frequency and its peak frequency, observed in MI sensors. This information had not been revealed prior to this work.

3) By operating in the conditions that make thermal effects negligible, an original nonlinear coupled harmonic formulation has been used successfully to show that a coupled nonlinear model provides an improvement in the modeling capability, particularly, when the magnitude of the magnetic field, H_e, is very weak. This was also shown to correlate to spatial dispersion in weak fields illustrating the importance of coupling in the weak field region. Improved accuracy was shown simulating the MI effect in response to the external field H_e as well as frequency, f. With this, the coupled

nonlinear harmonic numerical model was shown be useful for improving the ability to predict the MI effect.

4) In addition to improving prediction ability, the original coupled nonlinear harmonic formulation was also used in order to study, explicitly, the effects of experimentally observed domain structures in MI elements. It was shown that the effects of both Bloch walls and Neel walls formed during equilibrium tend to reduce the MI voltages, but in different ways. The Neel walls induce *flux cancellation*, while the Bloch wall *reduces the average transverse magnetization amplitude*. Such information is not obtainable from decoupled and linearized models, so this has helped to further enhance the understanding the observed MI effect in wires.

5) This work has also contributed by providing a numerical modeling approach in solving the more general set of equations that describe the MI effect. However, the equations also can be adapted to use with other magnetic sensors, as well. In particular, fluxgate and Hall effect sensors are good candidates. Thus, the approach has broader applications than just with MI sensors and may be useful in more research efforts than what has been carried out in this thesis research.

6.4 Recommendations for Future Work

In working to develop the numerical model in these research efforts in order to provide the kinds of contributions mentioned above, it was obviously found that not everything has worked perfectly. This leaves room for recommendations of future works that may be very useful extensions to what has been presented here. There are a few key areas of recommended focus that stand out from what has been learned in this research:

1) *Further Reduction of Computational Costs*: Although efforts were make to promote time savings, it is still possible to continue reducing the computational time considerably. One way is to build the numerical models using a binary code/language such as C, C++, or Fortran. These languages would be most impactful in the nonlinear solver and its implementation. This is currently the area of greatest demand in the numerical model. This would then enable much more efficient retrieval of data, hopefully speeding up the pace of learning, predictions, etc.

2) *Extended MI Element Geometries*: A more efficient model can also find use exploring other MI element geometries and configurations. In this work, single material amorphous cylindrical and ribbon structures were primarily studied, however, there is still a strong interest in composites and to date they have demonstrated the highest MI effect ratio compared to single materials. This includes circular composites with a single layer on a conductive core as well as a tri-layered ribbon structure, which has been shown experimentally to be better than more than a single symmetric ribbon layer. The original multilayered impedance model derived in Chapter 3 shows this to be the case, as well. Such a problem would also provide new challenges dealing with the interfaces in the materials. The good performance of these structures provides an impetus to further the understanding in these structures as they may be the likely candidates to meet the needs of the growing applications before the other structures.

3) *Extension of Methods to Other Sensors*: The modeling approach that has been outlined here is also applicable to other sensitive devices. The most logical extension from the MI effect sensor is the Fluxgate sensor, as both devices are very similar fundamentally as they are described by the same equations of motion under very similar

conditions. Therefore, minimal efforts would be required to use this approach to study these devices, which are widely studied right now. Miniature Hall effect sensors are also applicable candidates.

4) *Stress-Impedance Sensors*: The other part that has been omitted in this work that is extremely relevant is the modeling of the stress-impedance effect, which is an analog of the MI effect, however, a stress is applied to generate a voltage change instead of an external field. The SI effect has been shown to have very exciting potential and easily warrants the need for improved modeling capabilities. The modeling approach used here could be useful in studying the SI effect, as well.

APPENDIX A

A.1 Introduction and Review of Meshless Methods

We have mentioned that the equations of motion summarized in Chapter 2 are discretized spatially using a method known as *M*esh*L*ess *M*ethods (MLM). In this chapter, this spatial discretization method is introduced and several formulations are reviewed in order to emphasize that the choice of an MLM formulation is not arbitrary, but should depend on an understanding of the advantages and disadvantages of the various formulations. This discretization method has been more successfully developed over the last 10 to 20 years, thus is younger than its predecessor known as finite element methods (FEM). Thus, also, in light of the novelty of the method, a more broad discussion and introduction is given here where a focus is given to several more commonly used MLM shape function formulations while also drawing on a slightly historical perspective of the development, factoring in relevant contrasts, as well.

Meshless methods, also referred to as particle methods and meshfree methods, represent a set of more recently developed numerical discritization methods useful for approximating a "global" function, $u(\mathbf{x})$, usually defined on a bounded computational domain, Ω_C, using a set of "locally" defined approximation functions known as shape functions, the set of which is denoted here by $\left\{\Psi_j^s\right\}$. The method draws its name in reference to finite element methods (FEM), where the most significant contrast lies in the fact that MLMs do not require connected elements constructed by a meshing process, but rather only positional points, or "particles", representing the domain and its boundaries. The function, $u(\mathbf{x})$, to be approximated can be described either explicitly with discrete

functional values, $u(\mathbf{x}_j)$, or implicitly with a differential (or integral) operator, $\Im(\cdot)$. In this thesis, we investigate the use of various MLM shape functions in solving a particular set of differential equations, describing the degrees of freedom in a nonlinear micromagnetic system. We emphasize that by referring to the formulations as "meshless methods", this only refers to the mathematical and/or numerical processes by which the so called *shape functions* are derived. Another important and relevant topic is integration methods of the weak formulations resulting from an MLM formulation. Because a point collocation formulation is the method of choice here, where weak formulations are only used in a limited number of examples, we do not discuss the integration of MLM formulations in this thesis, which is generally distinct from integration of FEM formulations. Various discussions of integration techniques in MLMs can be found in [84]. However, similar to FEM, the shape functions designed in MLMs are defined as the finite set of functions, $\left\{\Psi_j^s\right\}$, where the approximation of u at a point $\mathbf{x}$ is defined in an approximation given by:

$$u(\mathrm{x}) \cong u^{\rho}(\mathrm{x}) \doteq \sum_j \Psi_j^S u(\mathbf{x}_j) \tag{A-1}$$

The index, j, counts the finite number of shape functions used in the approximation and this number is usually significantly less than the total number of equations in the problem to be solved, and reflects the total number of local support nodes in close proximity to $\mathbf{x}$. The superscript, $\boldsymbol{\rho}$, denotes a convergence parameter known as the *support radius* or *dilation parameter*. The convergence of the approximation depends on this parameter in the same way that uniform grid local estimations in FEM or finite difference methods (FDM) depend on the nodal spacing, h. Fig A-1 shows an illustration of a rectangular

MLM computational domain with general, boundary, and local support nodes of which are determined by the support radius, ρ, for a node in a computational domain.

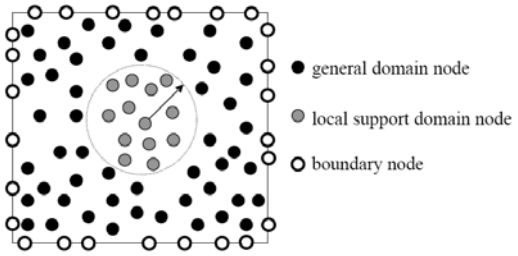

(a) illustration of mlm nodes for domain, boundary, and support

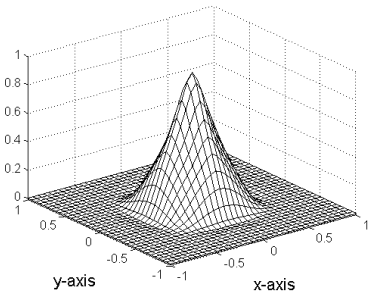

(b) qualitative illustration of a resulting *Hp*-cloud shape function

Figure A-1 MLM node illustration and shape function

The set of shape functions can naturally be separated into two distinct classes, namely, interpolating shape function (ISF), which equivalently possesses the Kronecker Delta function property (KDFP), and non-interpolating shape functions (NISF), which lack the KDFP. In practice, it is desirable to use shape functions that possess the KDFP (at least on the boundaries), as they lead to no special treatment of essential boundary conditions (EBCs) in the system of differential equations. When shape functions do not possess the KDFP directly, treatment can vary from modifying the equations of motion to include the EBCs as constraints or one can transform NISF into an ISF using a transformation matrix. Transformation matrices are particularly useful for point collocation schemes, however, prove to be temporally-compounding with computational time. Interpolation transformation matrices generally remove compactness; therefore, in order to restore compactness for weak formulations, we also introduce, in this work, the concept of a compaction transformation matrix, as well.

There are many MLM formulations for building shape functions for use in solving PDEs, however, we will explore and compare characteristics of six successfully used

MLM shape functions that together embody many important concepts and characteristics helpful in understanding strengths and weaknesses of MLMs. In particular, we compare the smooth particle hydrodynamics (SPH), the reproducing kernel particle method (RKPM), the moving-least-square reproducing kernel particle method (MLSRKPM), the element free galerkin (EFG), the Hp-Cloud (HpC), and radial point interpolation using radial basis functions (RBF). Transformations matrices are also discussed briefly.

Before moving forward to discuss MLM shape functions, let us mention two important attributes. The first is a prerequisite and necessary condition for MLM shape functions known as the Partition of Unity (POU) characteristic. This is defined by:

$$\sum_j \Psi_j^S(\mathrm{x}) = 1\,, \quad \forall \mathrm{x} \in \Omega_\mathrm{c} \tag{A-2}$$

Another characteristic that is not necessary, but is desirable, and is known as the Kronecker Delta Function property. In relation to MLM shape functions used in spatial discretization; this is equivalent to interpolating shape functions. The definition of the Kronecker Delta function is given by:

$$\delta_K(x) = \begin{cases} 1 & \text{if } x = 0 \\ 0 & \text{otherwise} \end{cases} \tag{A-3}$$

For MLM shape functions, this translates to the following:

$$\Psi_j^s(x) = \begin{cases} 1 & \text{if } x = 0 \\ 0 & \text{otherwise} \end{cases} \tag{A-4}$$

With this condition, the shape functions naturally handle EBCs, just as in FEM.

As already mentioned, not all (in fact very few) MLM shape functions possess the KDFP inherently in their formulation. We note that the lack of the KDFP does not generally mean less accuracy; however, the lack of KDFP can lead to larger errors when the interpolation at least at the boundaries is lacking.

Next we discuss one type of MLM formulation known as *kernel* formulations.

A.1.1 Kernel MLM Formulations

One method that inherently produces NISFs is often referred to as kernel methods. To introduce kernel methods, we begin by highlighting a few relevant mathematical observations intended to provide some understanding of the motivation behind kernel methods.

Recall that a continuous function can be "reconstructed" mathematically at a point, **x**, by the following integral representation:

$$u_k(\mathrm{x}) = \int_{-\infty}^{\infty} u(\mathrm{y}) \cdot \mathrm{K}(\mathrm{x}-\mathrm{y}) d\mathrm{y} \tag{A-5}$$

K is known as the kernel function and should possess certain properties for accurate reproduction. From this equation, we can make a few observations:

1) If K is exactly the Dirac delta function, $\delta(\cdot)$, then the statement is obviously valid from the following:

$$u_K(\mathrm{x}) = \int_{-\infty}^{\infty} u(\mathrm{y}) \cdot \delta(\mathrm{x}-\mathrm{y}) d\mathrm{y} = u(\mathrm{x}) \cdot \int_{-\infty}^{\infty} \delta(\mathrm{x}-\mathrm{y}) d\mathrm{y} = u(\mathrm{x}) \tag{A-6}$$

2) If we assume the kernel function behaves like the Dirac delta function by providing compact support i.e. nonzero values only *near* **x**, and zero away from or outside a local support, Ω_L, then the integral can be transparently replaced with a bounded domain integral representation given by:

$$u_K(\mathrm{x}) = \int_{\Omega_L} u(\mathrm{y}) \cdot \mathrm{K}(\mathrm{x}-\mathrm{y}) d\Omega_y \tag{A-7}$$

The kernel function must vanish at the boundary of Ω_L. This assumption has practical importance as it leads to the ability to build a sparse stiffness matrix which leads to better computational efficiency, as well.

3) In cases where finite spatial deviation is absent, *i.e.* if the function $u(\mathbf{x})$ were constant over the local support domain, it then follows that:

$$u_K(\mathrm{x}) = \int_{\Omega_{LS}} u(\mathrm{y})\mathrm{K}(\mathrm{x}-\mathrm{y})d\Omega_y = u(\mathrm{x})\int_{\Omega_S} \mathrm{K}(\mathrm{x}-\mathrm{y})d\Omega_y \tag{A-8}$$

As can be observed in the case of using the Dirac Delta function, in order for the formulation to handle a simple case like no variation, the following necessary condition must be met:

$$\int_{\Omega_{LS}} \mathrm{K}(\mathrm{x}-\mathrm{y})d\Omega_y = 1 \tag{A-9}$$

The condition in (A-9) is known as the normal condition. The satisfaction of this condition relates to the Partition of Unity (POU) property. Using equation (A-1) and (A-4), we can write:

$$u_K(\mathrm{x}) = \int_{\Omega_{LS}} \left(\sum_j \Psi_j^S(\mathrm{y}) u(\mathrm{y_j}) \right) \mathrm{K}(\mathrm{x}-\mathrm{y})d\Omega_y \tag{A-10}$$

Then, condition (A-10) is preserved because this leads to the following:

$$\begin{aligned}
&u_K(\mathrm{x}) = \int_{\Omega_L} \left(\sum_j \Psi_j^S(\mathrm{y}) u(\mathrm{y_j}) \right) \mathrm{K}(\mathrm{x}-\mathrm{y})d\Omega_y \\
&\Rightarrow u_K(\mathrm{x}) = u(\mathrm{x})\int_{\Omega_L} \left(\sum_i \Psi_i^S(\mathrm{y}) \right) \mathrm{K}(\mathrm{x}-\mathrm{y})d\Omega_y \\
&\Rightarrow u_K(\mathrm{x}) = u(\mathrm{x})\int_{\Omega_L} \mathrm{K}(\mathrm{x}-\mathrm{y})d\Omega_y \\
&\Rightarrow u_K(\mathrm{x}) = u(\mathrm{x})
\end{aligned} \tag{A-11}$$

Although the argument above only illustrates that the POU property is a sufficient condition for a kernel approximation to handle uniform degrees of freedom, it

helps to illustrate the importance of the role of the POU property. This condition is not unique to MLMs, but is also a condition of FEM and finite difference methods, as well. The condition has only been inherited by MLM shape functions.

4) Considering the spacing, Δ_k, between the two points, **x** and **y**, in the limiting case, $\Delta_k \to 0$, then we have:

$$\lim_{y \to x} \int_{-\infty}^{\infty} u(y) \cdot K(x - y) dy = u(x) \int_{-\infty}^{\infty} K(0) dy \tag{A-12}$$

Again, considering if the kernel function approaches the Dirac delta function results in a consistent convergent solution:

$$\lim_{\Delta_k \to 0} \int_{\Omega_L} u(y) \cdot K(\Delta_k) dy = u(x) \int_{-\infty}^{\infty} \delta(x - y) dy = u(x) \tag{A-13}$$

Argument (A-13) suggests that a "good" kernel function should not only have compact support like the *Dirac* delta function, but should converge, characteristically, to the Dirac delta function, as **y** values approaches **x**. This translates to the spacing between all the support nodes diminishing or "squeezing" closer to **x**.

We therefore see that good kernel functions begin with compact support, using normal kernel functions that converge to the Dirac Delta function with decreasing nodal spacing. These observations lend some insight into how kernel methods work as MLMs and lead to good convergence properties as well. This insight, and more, has lead researchers to the successful development and implementation of kernel methods in MLMs. Next, we review three particular kernel methods, starting with the Smooth Particle Hydrodynamics (SPH) shape functions, followed by an improved kernel method

known as the Reproducing Kernel Particle Method (RKPM), and then the Moving Least Squares Reproducing Kernel Particle Method.

Smooth Particle Hydrodynamics Method

The Smooth Particle Hydrodynamics method (SPH) was originally proposed by R. A. Gingold and J.J. Monaghan [44]. As the name suggests, the original application was astrophysical fluids. The formulation begins, theoretically, with a kernel approximation, given by

$$u^{\rho}(\mathrm{x}) \doteq \int_{\Omega_L} u(\mathrm{y}) K_s(\mathrm{x}-\mathrm{y}) d\mathrm{y}\ ,\ \Omega_L \subseteq \Omega_C \tag{A-14}$$

$u^{\rho}(\mathrm{x})$ is the function to be approximated at the point, **x**. The discrete form given in (A-1) is deliberately obtained by the numerical integration of (A-14) using a closed Newton-Cotes quadrature rule. The result gives a summation of the following form:

$$u^{\rho}(\mathrm{x}) = \sum_j w_j u(\mathrm{y_j}) K_s(\mathrm{x}-\mathrm{y_j}) dV_j \tag{A-15}$$

From the equation given in (A-15), the kernel shape functions are then defined by:

$$\Psi_j^{SPH}(\mathrm{x}) = w_j K_s(\mathrm{x}-\mathrm{y_j}) dV_j \tag{A-16}$$

A number of functions can be used as the kernel function that satisfies the conditions discussed above. For example, earlier works used a normalized Gaussian distribution given by:

$$K_s = \varepsilon e^{-\left\|\frac{\mathrm{x}-\mathrm{y}}{\rho}\right\|^2} \tag{A-17}$$

The coefficient, ε, depends on the dimension of the computational domain, where the scaling factor,

$$\varepsilon = \left[1/\left(\sqrt{\pi}\rho\right), 1/\left(\pi\rho^2\right), 1/\left(\pi\sqrt{\pi}\rho^3\right)\right] \text{for} \, \Omega_c \subseteq [1D, 2D, 3D] \tag{A-18}$$

A spline-type function has also been used, which is less computationally demanding than transcendental functions like that used in (A-17). For example, a quartic spline function yielding C^2 shape functions can be used and is given by:

$$K_s = \varepsilon \cdot \begin{cases} \left(2.5-s\right)^4 - 5\left(1.5-s\right)^4 + 10\left(0.5-s\right)^4 & 0.0 \le s < 0.5 \\ \left(2.5-s\right)^4 - 5\left(1.5-s\right)^4 & 0.5 \le s < 1.5 \\ \left(2.5-s\right)^4 & 1.5 \le s < 2.5 \\ 0 & 2.5 \le s \end{cases} \tag{A-19}$$

The scaling factors for the quartic spline are given by

$$\varepsilon = \left[1/\left(24\rho\right), 96/\left(1199\pi\rho^2\right), 1/\left(20\pi\rho^3\right)\right] \text{for} \, \Omega_c \subseteq [1D, 2D, 3D] \tag{A-20}$$

Figure A-2 shows an example of 1D SPH shape functions and 1st and 2nd derivatives using the quartic spline function.

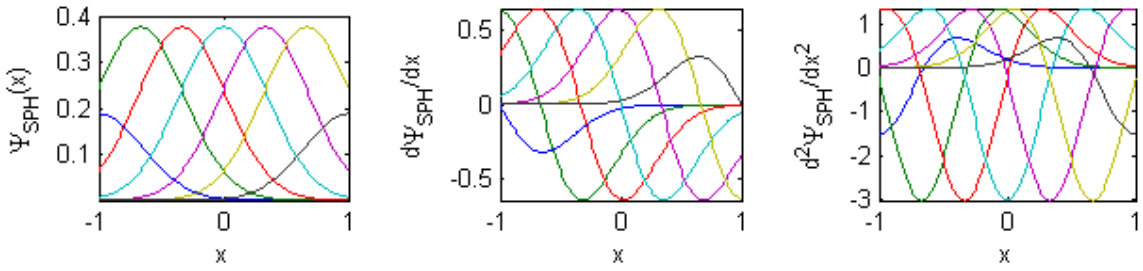

Figure A-2 SPH shape function using the normal Gaussian distribution.

The subsequently introduced reproducing kernel particle method (RKPM) formulation corrects an *Achilles heel* of the SPH functions relating to their inability to form partitions of unity near finite boundaries. Figure A-3 shows the summation of the shape functions at each point in the domain, where the POU property requires that each sum add to unity.

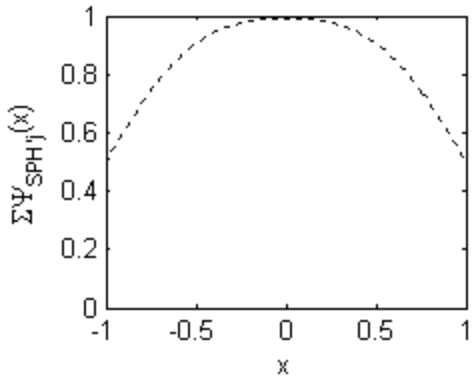

Figure A-3 POU characteristic for SPH shape functions using Gaussian weighting function

Figure A-3 shows, however, this is not the case for the SPH, i.e. the POU is not obtained over the entire computational range. This shall be discussed further in the formulation for the RKPM which follows.

Reproducing Kernel Particle Method

As an extension of the SPH formulation, the RKPM was originally introduced by Wing Kam Liu *et al*. [45], building on the observed weaknesses of the SPH shape functions. The key shortcoming observed in the SPH is the inability to represent a uniform function across the entire bounded computational domain. For example, Figure X. shows a plot of the sum of the shape functions evaluated over a computational domain from [-1, 1]. Recall from the arguments above that a POU is ideal to treat uniform degrees of freedom. However, Figure A-3. showed that near the boundaries, the POU property is not achieved very well by the SPH shape functions. The POU property relates to the ability of the shape functions to "reproduce" a polynomial. This means that if the function to be approximated is a polynomial of order k, then the shape functions should "reproduce" this exactly, everywhere in Ω_C. The POU property can be viewed as the minimum requirements of polynomial reproducibility, when the degree of freedom is

uniform in space and the function is a constant, or has C^0 continuity. With this understanding, the inability to "reproduce" polynomials, particularly near the boundaries, has been addressed in the RKPM by using a modified kernel function, given here by $\bar{K}_R$. In the RKPM, a kernel approximation form is still assumed in the kernel reproduction, given by:

$$u^{\rho}(\mathrm{y}) \doteq \int_{\Omega} u(\mathrm{y}) \bar{K}_R d\mathrm{y} \tag{A-21}$$

To correct for the POU problem near boundaries, the kernel function in the RKPM formulation, $\bar{K}_R$ is defined as:

$$\bar{K}_R = \left[\sum_{i=0}^{p} b_i(\mathbf{x};\rho) \left(\frac{\mathbf{x}-\mathbf{y}}{\rho} \right)^i \right] K_s(\mathrm{x}-\mathrm{y}) = \mathbf{B} \bullet \mathbf{P} K_s(\mathbf{x}-\mathbf{y}) \tag{A-22}$$

The vector, **B**, is the vector of coefficients, which need to be determined, while the vector, **P,** is the vector of monomial terms $\left[(\mathbf{x}-\mathbf{y})/\rho \right]^i$. The function K_s is the same as in SPH shape functions, ultimately controlling compactness and convergence towards the Dirac delta function. The added work in the RKPM formulation is to compute the coefficients, b_i. Lui *et al*. introduced these parameters as a way to implement polynomial reproducibility into the kernel formulation, thus restoring the POU property over the entire computational domain. The parameters are determined by solving a linear system constructed by using the so-called reproducibility conditions:

$$\mathrm{x}^{\alpha} = \int_{\Omega} \mathrm{y}^{\alpha} \bar{K}_s(\mathrm{x};\mathrm{x}-\mathrm{y}) d\mathrm{y}, \ \alpha \le n \tag{A-23}$$

Using equation (A-23) along with a Taylor series representation leads to a linear set of equations that define the coefficients, b_i. This process results in the full set of reproducing conditions, given by:

$$1 = \sum_{i=0}^{p} b_i(\mathrm{x}) \int_{\Omega} u(\mathrm{x}) \left(\frac{\mathrm{x}-\mathrm{y}}{\rho} \right)^i K_s(\mathrm{x}-\mathrm{y}) d\mathrm{y} \tag{A-24}$$

$$0 = \sum_{i=0}^{p} b_i(\mathrm{x}) \int_{\Omega} \left(\frac{\mathrm{x}-\mathrm{y}}{\rho} \right)^{i+1} K_s(\mathrm{x}-\mathrm{y}) d\mathrm{y} \tag{A-25}$$

$$\vdots \tag{A-26}$$

$$0 = \sum_{i=0}^{p} b_i(\mathbf{x}) \int_{\Omega} \left(\frac{\mathbf{x}-\mathbf{y}}{\rho} \right)^{i+p} K_s(\mathbf{x}-\mathbf{y}) d\mathbf{y} \tag{A-27}$$

From the reproducing conditions, the b_i coefficients are given by:

$$\mathbf{B} = \mathbf{M}^{-1} \begin{bmatrix} 1 & 0 & \cdots & 0 \end{bmatrix}^T = \mathbf{M}^{-1}\mathbf{C} \tag{A-28}$$

With **B** determined in this way, the approximation is given by:

$$u^{\rho}(\mathbf{x}) \doteq \int_{\Omega} u(\mathbf{y}) \mathbf{M}^{-1}(\mathbf{x}) \mathbf{C} \cdot \mathbf{P}(\mathbf{x}-\mathbf{y};\rho) K_s(\mathbf{x}-\mathbf{y};\rho) d\mathbf{y} \tag{A-29}$$

The construction of the final form of the approximation is given with the discretization of the integral:

$$u^{\rho}(\mathbf{x}) \cong \sum_{j=1}^{n} w_j \underbrace{\mathbf{M}^{-1}(\mathbf{x}) \mathbf{C} \cdot \mathbf{P}(\mathbf{x}-\mathbf{x}_j;\rho)}_{\text{Correction Function}} K_s(\mathbf{x}-\mathbf{x}_j;\rho) dV_j u(\mathbf{x}_j) \tag{A-30}$$

Lui *et al*. refers to the highlighted portion in (A-30) as the correction function, as it "corrects" the POU problem observed in the SPH near the boundaries and ensures a POU is made across the entire computational domain. Figure A-4 shows the resulting shape functions using the quartic weighting function,

(a) RKPM shape function (b) 1st derivative (c) 2nd derivative

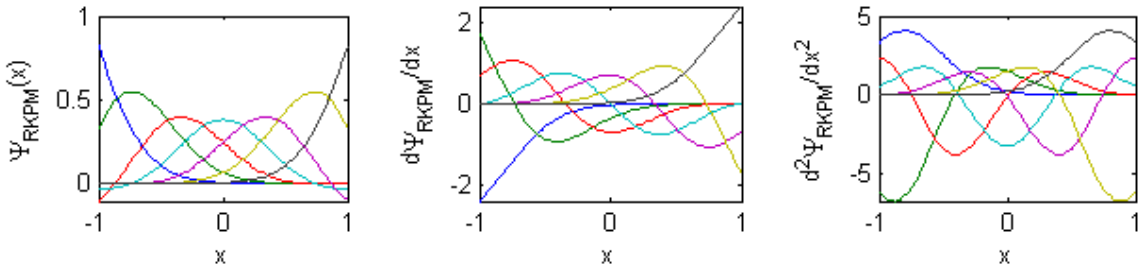

Figure A-4 RKPM shape functions, $p = 1$, with quartic shape functions.

Figure A-4 shows the POU values where the shape functions are added together over all points in the computational domain, and ideally, they should sum to unity. For comparisons, that for the non-corrected function (SPH) is shown, along with the actual values for the correction function.

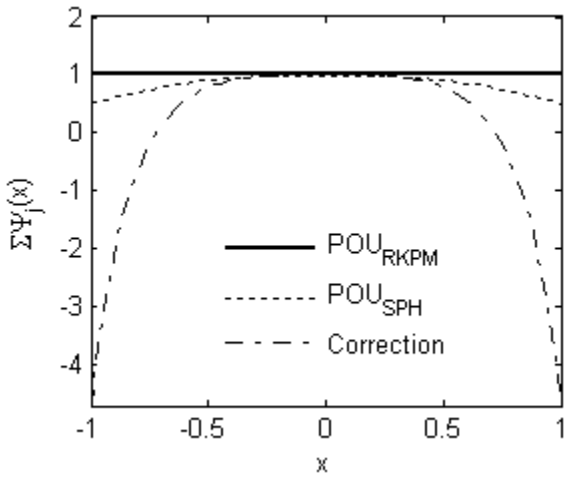

Figure A-5 POU sum for RKPM (POU_{RKPM}) with correction function shown compared to SPH ($POUs_{PH}$).

We can see that the RKPM makes the intended improvement by adding the correction function and the improvements are clear near the boundaries. However, even with these improvements, more were envisioned by Liu *et al*. and thus another formulation was subsequently introduced, known as the Moving Least Squares Reproducing Kernel Particle Method, discussed next.

Moving Least Squares Reproducing Kernel Particle Method

The Moving Least Square Reproducing Kernel Particle Method (MLSRKPM) actually constitutes a hybrid formulation (or cross-over), as the name suggests, where both, a kernel and an moving least squares (MLS) formulation are represented. We discuss MLS formulations formally in the next section, where the some of the remaining formulations fall into this category. The MLSRKPM formulation was also introduced by Lui *et al* [46]. It will be shown more clearly towards the end of this section how this formulation constitutes a kernel method, but let us begin with the standard kernel approximation form given by

$$u^{\rho}(\mathbf{x}) \doteq \int_{\Omega} u(\mathbf{x}\text{-}\bar{\mathbf{x}})\bar{K}_{\omega}(\mathbf{x}\text{-}\bar{\mathbf{x}})d\bar{\mathbf{x}} \tag{A-31}$$

In its current continuous form, $\bar{\mathbf{x}}$ is taken from Ω_L, while $\mathbf{x}$ is taken from Ω_C.

The derivation of the final shape functions, Ψ, is based on a continuous MLS solution for the basis function coefficients. The MLSRKPM formulation solves for the basis function coefficients by minimizing the continuous cost function, J, given by:

$$J := \int_{\Omega_L}\left(u(\bar{\mathbf{x}}) - \sum_{j=0}^{p} P_j\left(\frac{\mathbf{x}\text{-}\bar{\mathbf{x}}}{\rho}\right)b_j(\bar{\mathbf{x}})\right)^2 \omega\left(\frac{\mathbf{x}\text{-}\bar{\mathbf{x}}}{\rho}\right)d\Omega_{\bar{\mathbf{x}}} \tag{A-32}$$

The weighting function, $\omega(\mathbf{x})$, is chosen to provide properly normalized compact support. Minimizing the cost function, (A-32), results in the following normal equations relating the unknown coefficients, b_j with the degrees of freedom, ultimately to be determined:

$$\int_{\Omega_L} P_i\left(\frac{\mathbf{x}\text{-}\bar{\mathbf{x}}}{\rho}\right)\left(\sum_{j=1}^{p} P_j\left(\frac{\mathbf{x}\text{-}\bar{\mathbf{x}}}{\rho}\right)b_j(\bar{\mathbf{x}})\right)\omega\left(\frac{\mathbf{x}\text{-}\bar{\mathbf{x}}}{\rho}\right)d\Omega_{\bar{\mathbf{x}}} = \int_{\Omega_L}\omega\left(\frac{\mathbf{x}\text{-}\bar{\mathbf{x}}}{\rho}\right)P_i\left(\frac{\mathbf{x}\text{-}\bar{\mathbf{x}}}{\rho}\right)u(\bar{\mathbf{x}})d\Omega_{\bar{\mathbf{x}}} \tag{A-33}$$

Rearranging, (A-33) can be expressed as:

$$\sum_{j=1}^{m_p}\left[\int_{\Omega_L} P_i\left(\frac{\mathbf{x}-\bar{\mathbf{x}}}{\rho}\right)\omega\left(\frac{\mathbf{x}-\bar{\mathbf{x}}}{\rho}\right)P_j\left(\frac{\mathbf{x}-\bar{\mathbf{x}}}{\rho}\right)d\Omega_{\bar{\mathbf{x}}}\right]b_j = \int_{\Omega_L}\omega\left(\frac{\mathbf{x}-\bar{\mathbf{x}}}{\rho}\right)P_i\left(\frac{\mathbf{x}-\bar{\mathbf{x}}}{\rho}\right)u(\bar{\mathbf{x}})d\Omega_{\bar{\mathbf{x}}} \tag{A-34}$$

The moment matrix can then be defined by:

$$M_{ij} = \int_{\Omega_L} P_i\left(\frac{\mathbf{x}-\bar{\mathbf{x}}}{\rho}\right)\omega\left(\frac{\mathbf{x}-\bar{\mathbf{x}}}{\rho}\right)P_j\left(\frac{\mathbf{x}-\bar{\mathbf{x}}}{\rho}\right)d\Omega_{\bar{\mathbf{x}}} \text{ or } \mathbf{M}(\mathbf{x}) = \int_{\Omega_{LS}} \mathbf{P}^T\left(\frac{\mathbf{x}-\bar{\mathbf{x}}}{\rho}\right)\omega\left(\frac{\mathbf{x}-\bar{\mathbf{x}}}{\rho}\right)\mathbf{P}\left(\frac{\mathbf{x}-\bar{\mathbf{x}}}{\rho}\right)d\Omega_{\bar{\mathbf{x}}} \tag{A-35}$$

We can define a vector from the RHS given by:

$$\mathbf{A}(\mathbf{x}) = \int_{\Omega_L}\omega\left(\frac{\mathbf{x}-\bar{\mathbf{x}}}{\rho}\right)\mathbf{P}^T\left(\frac{\mathbf{x}-\bar{\mathbf{x}}}{\rho}\right)u(\bar{\mathbf{x}})d\Omega_{\bar{\mathbf{x}}} \tag{A-36}$$

Using (A-35) and (A-36), the nodal parameters are given by:

$$\mathbf{B}(\mathbf{x}) = \mathbf{M}^{-1}(\mathbf{x})\mathbf{A}(\mathbf{x}) \tag{A-37}$$

Using the solution for the vector of parameters, **B**, the approximation now becomes:

$$u^{\rho}(\mathbf{x},\bar{\mathbf{x}}) = \mathbf{P}\left(\frac{\mathbf{x}-\bar{\mathbf{x}}}{\rho}\right)\mathbf{M}^{-1}(\mathbf{x})\mathbf{A}(\mathbf{x}) \tag{A-38}$$

At this point in the derivation, Lui *et al*. refers to this step as introducing a so-called "global operator" which was defined to represent the "moving" of equation (A-38) arbitrarily within the computational domain. It is defined mathematically by taking the limit of (A-38) as $\bar{\mathbf{x}} \to \mathbf{x}$, resulting in:

$$u^{\rho} = \mathbf{P}(0)\mathbf{M}^{-1}(\mathbf{x})\int_{\Omega_L}\omega\left(\frac{\mathbf{x}-\bar{\mathbf{x}}}{\rho}\right)\mathrm{P}^T\left(\frac{\mathbf{x}-\bar{\mathbf{x}}}{\rho}\right)u(\bar{\mathbf{x}})d\Omega_{\bar{\mathbf{x}}} \tag{A-39}$$

Now, a kernel-like relationship emerges from (A-39) and is given by:

$$u^{\rho}(\mathrm{x}) = \int_{\Omega_L} u(\bar{\mathbf{x}})\underbrace{\mathbf{P}(0)\mathbf{M}^{-1}(\mathbf{x})\mathrm{P}^T\left(\frac{\mathbf{x}-\bar{\mathbf{x}}}{\rho}\right)\omega\left(\frac{\mathbf{x}-\bar{\mathbf{x}}}{\rho}\right)}_{K_\omega}d\Omega_{\bar{\mathbf{x}}} \tag{A-40}$$

Equation (A-40) takes a more obvious form of a kernel approximation, where we have:

$$u^{\rho}(\mathrm{x}) = \int_{\Omega_L} u(\mathrm{y})K_\omega\left(\frac{\mathrm{x}-\bar{\mathrm{x}}}{\rho}\right)d\Omega_{\bar{\mathrm{x}}} \tag{A-41}$$

Equation (A-41) takes a discrete form by implementation of a Newton-Cotes quadrature resulting in the final approximation given by:

$$u^{\rho}(\bar{x}) = \sum_{j=1}^{n} \underbrace{w_j K_{\omega}\left(\frac{x_j - \bar{x}}{\rho}\right) dV_j}_{\Psi_j^s} u(x_j) = \sum_{j=1}^{n} \Psi_j^s u_j \tag{A-42}$$

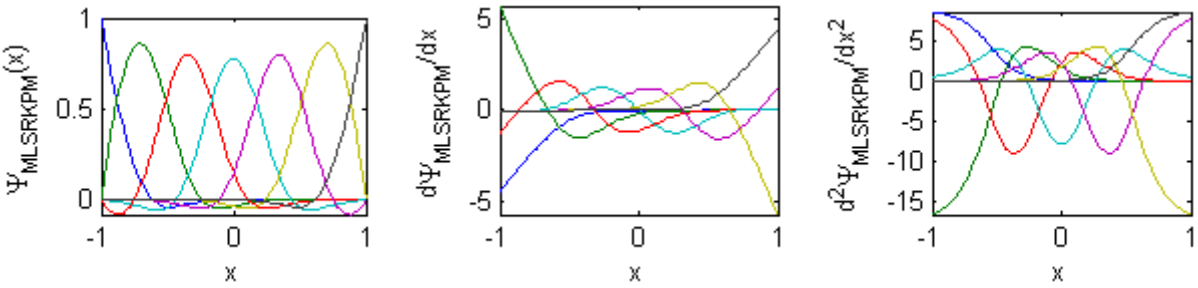

(a) shape function (b) first derivative (c) 2nd derivative

Figure A-6 MLSRKPM shape functions

A.1.2 Moving Least Squares Formulation

As an alternative to kernel methods, MLM shape functions can also be built using a method known as a moving least squares (MLS) formulation. This approach also offers shape functions that are inherently partitions of unity (POU), as well as compact, which are desirable particularly in weak formulations. We will also highlight in the context of one particular formulation known as the *Hp*-Cloud, that this type of formulation also offers better efficiency by not requiring explicit calculations of the derivatives of the shape functions, as well, if the basis functions are formed properly. The first MLS formulation reviewed is the *Hp*-Cloud (*Hp*-C) shape functions followed by the Element Free Galerkin (EFG) shape functions.

HP-Cloud Meshless Method

The *Hp*-Cloud meshless shape functions were originally introduced by Duarte and Oden [51] [85]. A distinguishing characteristic of MLS formulations* is that these shape functions are compact partitions of unity (POU) whose characteristics can readily be adapted to possess the Kronecker Delta Function (KDF) property on the boundaries, resulting in no need for special treatment for essential boundary conditions. This is not the case for Kernel methods, in general, and this is true for the EFG method, based on its original formulation. In MLS formulations, the approximation functions for any degree of freedom, u, are defined "up front" in a discrete form by:

$$u(\mathbf{x}) \cong u^{\rho}(\mathbf{x},\mathbf{x}_k;\rho) = \sum_{j=1}^{m} \varphi_j \, b_j = \varphi_v \bullet \mathbf{B} \tag{A-43}$$

For a 2nd order polynomial-reproducible formulation, for example, the p basis functions given in the most advantageous form, $\{\varphi\}$, are given by:

$$\{\varphi\} = \left\{ 1, \frac{x_k - x}{\rho_x}, \frac{y_k - y}{\rho_y}, \left(\frac{x_k - x}{\rho_x}\right)^2, \left(\frac{x_k - x}{\rho_x}\right)\left(\frac{y_k - y}{\rho_y}\right), \left(\frac{y_k - y}{\rho_y}\right)^2 \right\} \tag{A-44}$$

For the 2D domain, the dilation parameter becomes a vector, where each dimensions has a dilation parameter, ρ_i. The point $\mathbf{x} = (x,y)$ represents a position within the computational domain, Ω_C. The point $\mathbf{x}_k = (x_k,y_k)$ represents a point from the local support domain, Ω_L. A discrete MLS formulation is used to determine the coefficient vector, **B**, in the similar way as outlined in the MLSRKPM. The result for the vector of coefficients, here, is then given by:

$$\mathbf{B} = \mathbf{M}^{-1}\mathbf{T}\mathbf{U} \tag{A-45}$$

M is a $p \times p$ matrix whose elements are given by:

$$M_{ij} = \sum_{k=1}^{n} \varphi_i w\left(\mathbf{x}_k - \mathbf{x};\rho\right)\varphi_j \tag{A-46}$$

T is a $p \times n$ matrix, whose elements are given by:

$$T_{ik} = w\left(\mathbf{x}_k - \mathbf{x};\rho\right)\cdot\varphi_i\left(\mathbf{x}_k - \mathbf{x};\rho\right) \tag{A-47}$$

In (A-46) and (A-47), *w* is a compact weighting function, to be discussed later. Equation (A-45) allows the alternative representation of the approximation given by:

$$u^{\rho}\left(\mathbf{x}\right) = \varphi_v \mathbf{B} = \varphi_v \mathbf{M}^{-1}\mathbf{T}\mathbf{U} = \Psi_v^S \mathbf{U} \tag{A-48}$$

Because a point collocation scheme is considered here in 2nd order PDEs, the derivatives of the shape functions up to 2nd order are needed. This poses additional computational demands. At this point, we will show a key advantage of using MLS shape functions as it relates to determining shape function derivatives. The case is shown for the *Hp*-Cloud shape functions, however, the results are easily extended to other MLS shape functions, including the MLSRKPM formulation discussed above, as long as the basis functions have the "differential form" as given in (A-44). It can be shown that derivatives of the *Hp*-C shape functions do not need to be computed directly, but rather can be extracted from the same information used to compute the shape functions, given in (A-48). This can be shown by first writing a Taylor series expansion (in 2D) in a useful form for the unknown function, *u*, evaluated at the *n* local support nodes for a point, **x**, yielding:

$$\begin{aligned}
u(\mathrm{x}_1) &= u(\mathrm{x}) + \rho_x \frac{\partial u}{\partial x}\left(\frac{x_1 - x}{\rho_x}\right) + \rho_y \frac{\partial u}{\partial y}\left(\frac{y_1 - y}{\rho_y}\right) + \frac{\rho_x^2}{2!}\frac{\partial^2 u}{\partial x^2}\left(\frac{x_1 - x}{\rho_x}\right)^2 + \frac{2\rho_x\rho_y}{2!}\frac{\partial^2 u}{\partial x \partial y}\left(\frac{x_1 - x}{\rho_x}\right)\left(\frac{y_1 - y}{\rho_y}\right) + \frac{\rho_y^2}{2!}\frac{\partial^2 u}{\partial y^2}\left(\frac{y_1 - y}{\rho_y}\right)^2 + O\left(\rho^3\right) \\
u(\mathrm{x}_2) &= u(\mathrm{x}) + \rho_x \frac{\partial u}{\partial x}\left(\frac{x_2 - x}{\rho_x}\right) + \rho_y \frac{\partial u}{\partial y}\left(\frac{y_2 - y}{\rho_y}\right) + \frac{\rho_x^2}{2!}\frac{\partial^2 u}{\partial x^2}\left(\frac{x_2 - x}{\rho_x}\right)^2 + \frac{2\rho_x\rho_y}{2!}\frac{\partial^2 u}{\partial x \partial y}\left(\frac{x_2 - x}{\rho_x}\right)\left(\frac{y_2 - y}{\rho_y}\right) + \frac{\rho_y^2}{2!}\frac{\partial^2 u}{\partial y^2}\left(\frac{y_2 - y}{\rho_y}\right)^2 + O\left(\rho^3\right) \\
&\vdots \\
u(\mathrm{x}_n) &= u(\mathrm{x}) + \rho_x \left.\frac{\partial u}{\partial x}\right|_{\mathrm{x}}\left(\frac{x_n - x}{\rho_x}\right) + \rho_y \frac{\partial u}{\partial y}\left(\frac{y_n - y}{\rho_y}\right) + \frac{\rho_x^2}{2!}\frac{\partial^2 u}{\partial x^2}\left(\frac{x_n - x}{\rho_x}\right)^2 + \frac{2\rho_x\rho_y}{2!}\frac{\partial^2 u}{\partial x \partial y}\left(\frac{x_n - x}{\rho_x}\right)\left(\frac{y_{m_n} - y}{\rho_y}\right) + \frac{\rho_y^2}{2!}\frac{\partial^2 u}{\partial y^2}\left(\frac{y_n - y}{\rho_y}\right)^2 + O\left(\rho^3\right)
\end{aligned} \tag{A-49}$$

We can then express equations (A-49) in the following form:

$$\begin{bmatrix} u_1 \\ u_2 \\ \vdots \\ u_{m_n} \end{bmatrix} = \begin{bmatrix} 1 & \frac{x_1-x}{\rho_x} & \frac{y_1-y}{\rho_y} & \left(\frac{x_1-x}{\rho_x}\right)^2 & \left(\frac{x_1-x}{\rho_x}\right)\left(\frac{y_1-y}{\rho_y}\right) & \left(\frac{y_1-y}{\rho_y}\right)^2 \\ 1 & \frac{x_2-x}{\rho_x} & \frac{y_2-y}{\rho_y} & \left(\frac{x_2-x}{\rho_x}\right)^2 & \left(\frac{x_2-x}{\rho_x}\right)\left(\frac{y_2-y}{\rho_y}\right) & \left(\frac{y_2-y}{\rho_y}\right)^2 \\ \vdots & \vdots & \vdots & \vdots & \vdots & \vdots \\ 1 & \frac{x_{m_n}-x}{\rho_x} & \frac{y_{m_n}-y}{\rho_y} & \left(\frac{x_{m_n}-x}{\rho_x}\right)^2 & \left(\frac{x_{m_n}-x}{\rho_x}\right)\left(\frac{y_{m_n}-y}{\rho_y}\right) & \left(\frac{y_{m_n}-y}{\rho_y}\right)^2 \end{bmatrix} \underbrace{\begin{bmatrix} u^* \\ \frac{\partial u^*}{\partial x} \\ \frac{\partial u^*}{\partial y} \\ \frac{\partial^2 u^*}{\partial x^2} \\ \frac{\partial^2 u^*}{\partial x \partial y} \\ \frac{\partial^2 u^*}{\partial y^2} \end{bmatrix}}_{B^*} + \mathbf{O}\left(\rho^3\right) \tag{A-50}$$

In (A-50), a system of equations is formed after truncating the error term where the unknown is the RHS vector, **B***, where its components are given by

$$u^* = u, \frac{\partial u^*}{\partial x} = \rho_x \frac{\partial u}{\partial x}, \frac{\partial u^*}{\partial y} = \rho_y \frac{\partial u}{\partial y}, \frac{\partial^2 u^*}{\partial y^2} = \frac{\rho_y^2}{2!}, \frac{\rho_x^2}{2!}\frac{\partial^2 u}{\partial x^2}, \frac{\partial^2 u^*}{\partial x^2} = \frac{\rho_y^2}{2!}\frac{\partial^2 u}{\partial y^2} \tag{A-51}$$

Equation (A-51) then motivates the choice of basis functions used. Using the defined basis functions given in (A-44), it follows that **B**, used in the approximation function definition is also given by **B*** which was constructed using the Taylor series expansion. At first glance, one may be enticed to simply "invert" the matrix in (A-50) (or use an MLS without a compact weighting function) to determine **B***, however, beyond 1D domains, this problem inherits the complexities of singularities with computing interpolating polynomials in multidimensional space. In MLMs, these complexities are avoided by using an MLS formulation with a compact weighting function to solve for the unknowns. Hence, we then have, following the same process outlined in the MLSRKPM formulation:

$$\mathbf{B}^* = \mathbf{M}^{-1}\left(\mathbf{x}\right)\mathbf{T}\left(\mathbf{x}\right)\mathbf{U} \tag{A-52}$$

From (A-52), let us replace the terms in **B*** with the approximation functions for *u* and its derivatives:

$$\left[\Psi_v^s\cdot\mathbf{U}\quad \rho_x\partial\Psi_v^s/\partial x\cdot\mathbf{U}\quad \rho_y\partial\Psi_v^s/\partial y\cdot\mathbf{U}\quad \frac{\rho_x^2}{2!}\partial^2\Psi_v^s\Big/\partial x^2\cdot\mathbf{U}\quad \rho_x\rho_y\partial^2\Psi_v^s/\partial x\partial y\cdot\mathbf{U}\quad \frac{\rho_y^2}{2!}\partial^2\Psi_v^s\Big/\partial y^2\cdot\mathbf{U}\right]^T=\mathbf{M}^{-1}\mathbf{T}\mathbf{U} \tag{A-53}$$

By inspection, we can now write:

$$\begin{bmatrix}\Psi_v^s\\ \rho_x\partial\Psi_v^s/\partial x\\ \rho_y\partial\Psi_v^s/\partial y\\ \frac{\rho_x^2}{2!}\partial^2\Psi_v^s\Big/\partial x^2\\ \rho_x\rho_y\partial^2\Psi_v^s/\partial x\partial y\\ \frac{\rho_y^2}{2!}\partial^2\Psi_v^s\Big/\partial y^2\end{bmatrix}\mathrm{U}=\mathrm{M}^{-1}(\mathrm{x})\mathrm{T}(\mathrm{x})\mathrm{U} \tag{A-54}$$

Then, it follows that the shape functions and all relevant derivatives are explicitly given by:

$$\begin{aligned}
\Psi_v^s&=\begin{bmatrix}1&0&0&0&0&0\end{bmatrix}\mathbf{M}^{-1}(\mathrm{x})\mathbf{T}(\mathrm{x})\\
\partial\Psi_v^s/\partial x&=\begin{bmatrix}0&1/\rho_x&0&0&0&0\end{bmatrix}\mathbf{M}^{-1}(\mathbf{x})\mathbf{T}(\mathbf{x})\\
\partial\Psi_v^s/\partial y&=\begin{bmatrix}0&0&1/\rho_y&0&0&0\end{bmatrix}\mathbf{M}^{-1}(\mathbf{x})\mathbf{T}(\mathbf{x})\\
\partial^2\Psi_v^s/\partial x^2&=\begin{bmatrix}0&0&0&2!/\rho_x^2&0&0\end{bmatrix}\mathbf{M}^{-1}(\mathbf{x})\mathbf{T}(\mathbf{x})\\
\partial^2\Psi_v^s/\partial x\partial y&=\begin{bmatrix}0&0&0&0&1/\rho_x\rho_y&0\end{bmatrix}\mathbf{M}^{-1}(\mathbf{x})\mathbf{T}(\mathbf{x})\\
\partial^2\Psi_v^s/\partial y^2&=\begin{bmatrix}0&0&0&0&0&2!/\rho_y^2\end{bmatrix}\mathbf{M}^{-1}(\mathbf{x})\mathbf{T}(\mathbf{x})
\end{aligned} \tag{A-55}$$

The process is the same to obtain all derivatives in more general cases. Additionally, this is precisely the essence of the so-called "global operator" used in the MLSRKPM formulation. This property is an essential feature distinguishing it from kernel methods and even other point collocation formulations with the use of radial basis functions. It should be noted that computational efficiency is an important desired attribute in MLMs, as the shape function calculations are more demanding than using Lagrange polynomials, for example, as in FEM. The understanding summarized above that quickens derivative

calculations is not new as there have been other MLM shape functions using MLS that have taken advantage of this characteristic [47], however, the observation has only been applied for illustration to the to *Hp*-Cloud shape functions.

Moreover, this property relaxes the conditions of the weighting function used since no derivatives are explicitly required! This can be exploited to easily adapt the shape functions to possess *quasi*-KDF properties, where we refer to them as quasi because the interpolation is only precise on the boundaries, which is the minimum requirement. Let us consider the definition of the degree of freedom, *u*, given by:

$$u^{\rho}(\mathrm{x}) = \varphi_v \mathbf{M}^{-1}\mathbf{T}\mathbf{U} \tag{A-56}$$

It is then easy to see that:

$$\lim_{w(x)\to\delta_K(x)} \varphi_v \mathbf{M}^{-1}(w)\mathbf{T}(w) = \delta_K(x) \tag{A-57}$$

In (A-57), $\delta_K(x)$ is the Kronecker Delta function given in (A-). Therefore, MLS formulations posses the property that leads to an effective way to impose the KDFP on the shape functions by choosing a weighting function that possesses very near KDF properties. For example, a weighting function can take the form like that used in [47], and also used in this work, where we express w(**x**) in a tensor form in a 2D domain:

$$w(\mathrm{x}) = w_x(\mathrm{x})\, w_y(\mathrm{x}) = \left\{1 - \left[\frac{\|x - x_j\|}{\delta_x}\right]^{-2\eta}\right\}\left\{1 - \left[\frac{\|y - y_j\|}{\delta_y}\right]^{-2\eta}\right\},\ \eta \in \mathbf{N} \tag{A-58}$$

Figure A-7 shows computed *Hp*-C shape functions in a 1D computational domain of [-1,1], using the weighting function given in (A-58).

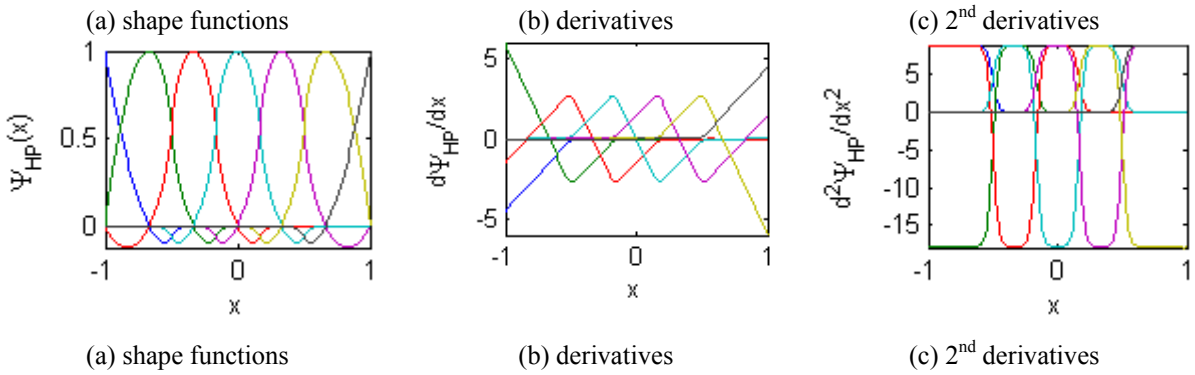

Figure A-7 *Hp*-cloud shape functions (top) derivatives using discontinuous w(x).

Element Free Galerkin Method

Another MLS formulation summarized here is known as the Element Free Galerkin (EFG) formulation. This formulation was first proposed by Belytschko *et al*. [49]. It was introduced as a improvement to the so-called Diffuse Element Method [50]. As with all MLM shape functions, the design of the shape functions used in EFG shape functions begins with the general assumption that each degree of freedom, u, is initially approximated by:

$$u(\mathrm{x}) \cong u^{\rho}(\mathrm{x}) = \sum_{j=1}^{m_p} \varphi_j(\mathbf{x}) b_j(\mathrm{x}) = \varphi_v \bullet \mathbf{B} \tag{A-59}$$

The basis function coefficients, b_j, are associated with each independent basis function, φ_j. Similar to the MLSRKPM, the basis functions, in 2D domains, φ_j is an element of the set given by $\{1, x, y, x^2, xy, y^2, \ldots\}$. The monomial functions, in the original EFG formulation are not scaled in the way of the previous formulation, but evaluated at the explicit position, **x**. Similar to Hp-C formulation, a weighted discrete cost function, J_d, is used:

$$J_d := \sum_{k=1}^{n} w\left(\frac{\mathrm{x}-\mathrm{x}_k}{\rho}\right)\left(u_k - \sum_{j=1}^{p}\varphi_j(\mathrm{x}_k)b_j\right)^2 \tag{A-60}$$

The approach taken in this formulation is analogous to that taken of previous MLS formulations, leading to the familiar solution for the vector coefficients, **B**:

$$\mathbf{B} = \mathbf{M}^{-1}(\mathbf{x})\mathbf{T}(\mathbf{x})\mathbf{U} \tag{A-61}$$

From this, the shape functions can be computed as:

$$u(\mathrm{x}) \cong \varphi_v \mathbf{M}^{-1}\mathbf{T}\mathbf{U} \tag{A-62}$$

M is a $p \times p$ matrix whose elements are given by:

$$M_{ij} = \sum_{k=1}^{n}\varphi_i(\mathrm{x}_k)w\left(\frac{\mathrm{x}-\mathrm{x}_k}{\rho}\right)\varphi_j(\mathrm{x}_k) \tag{A-63}$$

T is a $p \times n$ matrix, whose elements are given by:

$$T_{ij} = w\left(\frac{\mathrm{x}-\mathrm{x}_j}{\rho}\right)\cdot\varphi_i(\mathrm{x}_j) \tag{A-64}$$

Examples of EFG shape functions are shown in Figure A-8, below for the 1D domain, [-1,1].

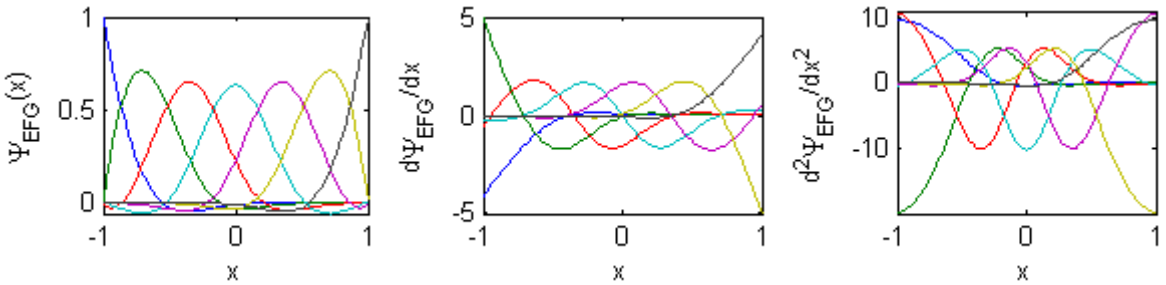

(a) shape functions (b) derivatives (c) 2nd derivatives

Figure A-8 Example of EFG shape functions (with 7 support nodes) using exponential weighting function.

A.1.3 Interpolating MLM Formulations

Radial Point Interpolation Method

The radial point interpolation method offers a unique formulation in that the resulting shape functions inherently form interpolating shape functions, exactly, and therefore, no weighting functions, transformations, or constraint treatments are necessary. In the simplest case, an approach to building a set of shape functions for an MLM formulation is to determine the coefficients for the basis function by simply forcing interpolation through each of the local support nodes, where the number of nodes in the support domain equals the number of basis functions, and we have an approximation of the form:

$$u^{\rho}(\mathrm{x}) = \sum_{j=1}^{p=n} R_j(\mathrm{x}) b_j = \mathbf{R}\cdot\mathbf{B} \tag{A-65}$$

R_j represents the general basis functions. A set of interpolating shape functions can then be constructed by forming the following linear system:

$$\begin{bmatrix} u(\mathrm{x}_1) \\ u(\mathrm{x}_2) \\ \vdots \\ u(\mathrm{x}_n) \end{bmatrix} = \begin{bmatrix} R_1(\mathrm{x}_1) & R_2(\mathrm{x}_1) & \cdots & R_n(\mathrm{x}_1) \\ R_1(\mathrm{x}_2) & R_2(\mathrm{x}_2) & \cdots & R_n(\mathrm{x}_2) \\ \vdots & \vdots & \ddots & \vdots \\ R_1(\mathrm{x}_n) & R_2(\mathrm{x}_n) & \cdots & R_n(\mathrm{x}_n) \end{bmatrix} \begin{bmatrix} b_1 \\ b_2 \\ \vdots \\ b_n \end{bmatrix} = \mathbf{MB} \quad \Rightarrow u^{\rho}(\mathbf{x}) = \mathbf{R}\cdot\mathbf{M}^{-1}\mathbf{U} \tag{A-66a,b}$$

One of the obvious concerns in equation (A-66) is the invertibility of the moment matrix, **M**. The ability to build a nonsingular moment matrix is highly dependent on the choice of basis functions. It can be shown that if the choice of basis functions is equal to the set of monomials, then only for the 1D case of unique nodes is **M** guaranteed nonsingular. In dimensions beyond 1D, singular matrices can certainly occur, depending on the choice of nodes. It is also important to note, however, that the simple approach above, *using at least one constant (and higher order monomials if desired)*, leads to a POU, as well. This

observation naturally leads to the question as to what choice of basis functions can be used that can guarantee a nonsingular moment matrix, computed using equation (A-66). Radial basis functions provide one answer to this question. It has been shown that the proper choice of radial basis functions along with suitable parameters can guarantee a nonsingular moment matrix [53]. Some of the RBFs that have been used are given in Table A-1:

Table A-1 Commonly used radial basis functions

Name	**Function**	**Parameter Domain**
Thin Plate spline(s) (1)	$(-1)^{1+m/2} r^m \log r$	$m \in 2\mathrm{N}$
(2)	$(-1)^{m/2} r^m$	$m \in \mathrm{R}_{>0} \setminus 2\mathrm{N}$
Gaussian	e^{mr^2}	$m \in R$
Multiquadric	$\sqrt{r^2 + m}$	$m \in R$

Selecting the basis functions, R_j, to come from the choice of RBFs from Table A-1, extricates the formulation from the problem of a singular moment matrix (given proper parameters). However, the question does remain as to whether strictly using RBFs results in a POU. In the form given by (A-66), using radial basis functions, a POU is not generally guaranteed. Figure A-9 shows the resulting shape functions for various values of the parameter, m, using thin plate spline radial basis functions (TPS). Additionally, Figure A-9 . shows the sum of the shape functions over the domain [-1, 1], using RBFs, with chosen parameters indicated. The shape functions clearly illustrate the lack of a POU, particularly, near the boundaries, although not the degree observed with SPH shape functions.

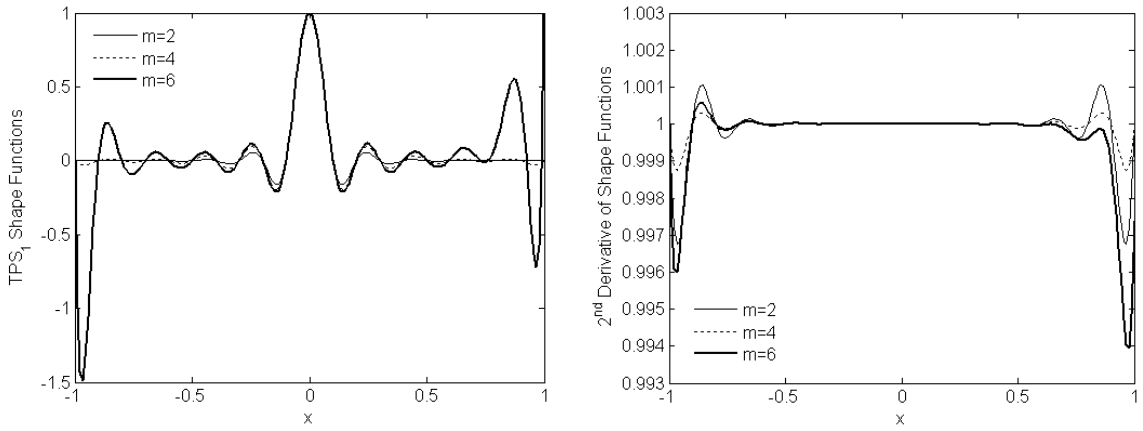

(a) (b)

Figure A-9 TPS shape functions and POU sums using strict radial basis functions showing lack of POU.

This issue is resolvable, however. There are two common ways that RBF shape functions can be modified to ensure a POU. First, taking an approach like that mentioned by Babuska *et al*. in the Partition of Unity method [52], normalization can be done in which:

$$\Psi^{POU}(\mathrm{x}) = \frac{\Psi^{s,NPOU}}{\sum_{j=1}^{n} \Psi_j^{s,NPOU}(\mathrm{x})} \tag{A-67}$$

This ensures a partition of unity, although, in our calculations, this approach proves to be less robust. Another approach, which has been successful in numerical implementation is to take the approach that was also suggested in [52] by Babuska *et al*., by "enriching" the shape functions by adding monomial terms to the set of basis function to achieve p^{th} order reproducibility. By achieving *p*th order reproducibility, 0^{th}, 1^{st}, up to p^{th} order can be exactly reproduced, thus restoring the POU characteristic easily. In practice, this is done in a strategic manner to preserve nonsingularness of the moment matrix [55]. In order to append monomial terms to the basis functions, the approximation becomes:

$$u^{\rho}(\mathrm{x}) = \sum_{j=1}^{p=n} R_j(\mathrm{x}) b_j + \sum_{j=1}^{k} M_j(\mathrm{x}) b_j^m = \bar{\mathbf{R}} \cdot \bar{\mathbf{B}} \tag{A-68}$$

The moment matrix is now modified and evaluated for the linear system given by:

$$\begin{bmatrix} u(\mathrm{x}_1) \\ u(\mathrm{x}_2) \\ \vdots \\ u(\mathrm{x}_n) \\ 0 \\ 0 \\ \vdots \\ 0 \end{bmatrix} = \begin{bmatrix} R_1(\mathrm{x}_1) & R_2(\mathrm{x}_1) & \cdots & R_n(\mathrm{x}_1) & M_1(\mathrm{x}_1) & M_2(\mathrm{x}_1) & \cdots & M_k(\mathrm{x}_1) \\ R_1(\mathrm{x}_2) & R_2(\mathrm{x}_2) & \cdots & R_n(\mathrm{x}_2) & M_1(\mathrm{x}_2) & M_2(\mathrm{x}_2) & \cdots & M_k(\mathrm{x}_2) \\ \vdots & \vdots & \ddots & \vdots & \vdots & \vdots & \ddots & \vdots \\ R_1(\mathrm{x}_n) & R_2(\mathrm{x}_n) & \cdots & R_n(\mathrm{x}_n) & M_1(\mathrm{x}_n) & M_2(\mathrm{x}_n) & \cdots & M_k(\mathrm{x}_n) \\ M_1(\mathrm{x}_1) & M_1(\mathrm{x}_2) & \cdots & M_1(\mathrm{x}_n) & 0 & 0 & \cdots & 0 \\ M_2(\mathrm{x}_1) & M_2(\mathrm{x}_2) & \cdots & M_2(\mathrm{x}_n) & 0 & 0 & \cdots & 0 \\ \vdots & \vdots & \vdots & \vdots & \vdots & \vdots & \ddots & \vdots \\ M_k(\mathrm{x}_1) & M_k(\mathrm{x}_2) & \cdots & M_k(\mathrm{x}_n) & 0 & 0 & \cdots & 0 \end{bmatrix} \begin{bmatrix} b_1 \\ b_2 \\ \vdots \\ b_n \\ b_1^m \\ b_2^m \\ \vdots \\ b_k^m \end{bmatrix} \tag{A-69}$$

The system can also be written in compact form as:

$$\begin{bmatrix} \mathbf{U} \\ 0 \end{bmatrix} = \begin{bmatrix} \mathbf{M} & \mathbf{M}_p \\ \mathbf{M}_p^T & 0 \end{bmatrix} \begin{bmatrix} \mathbf{B} \\ \mathbf{B}^m \end{bmatrix} = \mathbf{M}_{RBF} \bar{\mathbf{B}} \tag{A-70}$$

This leads to the solution for the basis function coefficients, given by:

$$\bar{\mathbf{B}} = \mathbf{M}_{\mathrm{RBF}}^{-1} \begin{bmatrix} \mathbf{U} \\ 0 \end{bmatrix} \tag{A-71}$$

$$\Rightarrow u^{\rho}(\mathrm{x}) = \bar{\mathbf{R}} \cdot \mathbf{M}_{\mathrm{RBF}}^{-1} \begin{bmatrix} \mathbf{U} \\ 0 \end{bmatrix} \tag{A-72}$$

The added equation to (A-70) is a *normal condition* between the added monomial terms and the original RBF coefficients specifying that:

$$\mathbf{M}_{\mathrm{p}}^{\mathrm{T}} \mathbf{B} = 0 \tag{A-73}$$

This formulation constitutes a polynomial-reproducing RBF formulation that interpolates and thus forms a POU naturally. Fig X shows the shape functions and POU properties in comparison, illustration the correction by this approach. This can be likened to the correction approach in the RPKM, with respect to the SPH formulation.

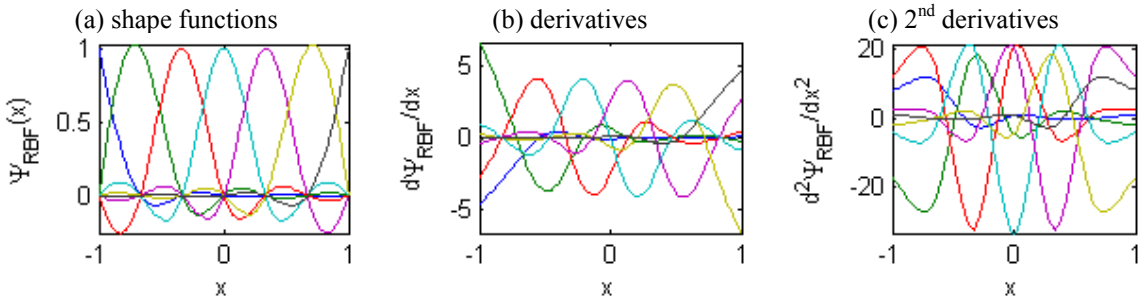

(a) shape functions (b) derivatives (c) 2nd derivatives

Figure A-10 Radial basis function shape functions using thin plate splines

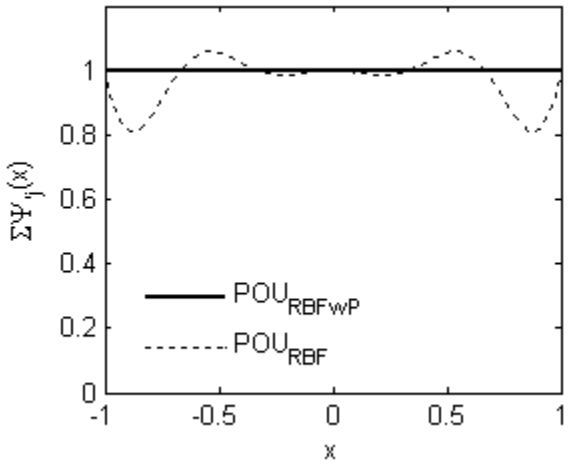

Figure A-11 RBF shape function POU sums with polynomial reproduction using thin plate spline (p=2).

For this reason, it is used in what can be considered a truly meshless process because the integration process in weak MLM formulations requires background cells, equivalent to a mesh. It is thus very suitable for point collocation (PC) schemes.

Interpolation Transformation Matrix

Although it was mentioned that many shape functions are not inherently exactly interpolating, except those using RBFs, this shortcoming can be resolved in any shape function by use of a transformation matrix, **T**. Essentially, the idea is to take the resulting non-interpolating shape functions given by the MLM formulation as a new set of basis functions in the manner done in the radial basis function formulation to force interpolation. Interpolation is then forced by the following linear relation:

$$\begin{bmatrix} u(\mathbf{x}_1) \\ u(\mathbf{x}_2) \\ \vdots \\ u(\mathbf{x}_n) \end{bmatrix} = \underbrace{\begin{bmatrix} \Psi_1^{NI}(\mathbf{x}_1) & \Psi_2^{NI}(\mathbf{x}_1) & \cdots & \Psi_n^{NI}(\mathbf{x}_1) \\ \Psi_1^{NI}(\mathbf{x}_2) & \Psi_2^{NI}(\mathbf{x}_2) & \cdots & \Psi_n^{NI}(\mathbf{x}_2) \\ \vdots & \vdots & \ddots & \vdots \\ \Psi_1^{NI}(\mathbf{x}_n) & \Psi_2^{NI}(\mathbf{x}_n) & \cdots & \Psi_n^{NI}(\mathbf{x}_n) \end{bmatrix}}_{\mathrm{T_I = transformation\ matrix}} \begin{bmatrix} u(\mathbf{x}_1) \\ u(\mathbf{x}_2) \\ \vdots \\ u(\mathbf{x}_n) \end{bmatrix} \tag{A-74}$$

This leads to an interpolating set of shape functions, Ψ_v^I, by using the following new relation:

$$\Psi_v^I = \mathbf{T}_I^{-1} \Psi_v^{NI} \tag{A-75}$$

Ψ_v^{NI} represents the original MLM shape functions that are non-interpolating. It should be noted that the resulting interpolating shape functions are generally no longer compact. This makes their use in PC schemes more straightforward, but can extend computational time considerably in weak formulations [43]. Figure A-12 shows the element free Galerkin (EFG) shape functions in 2D, with and without an applied interpolation transformation, **T**.

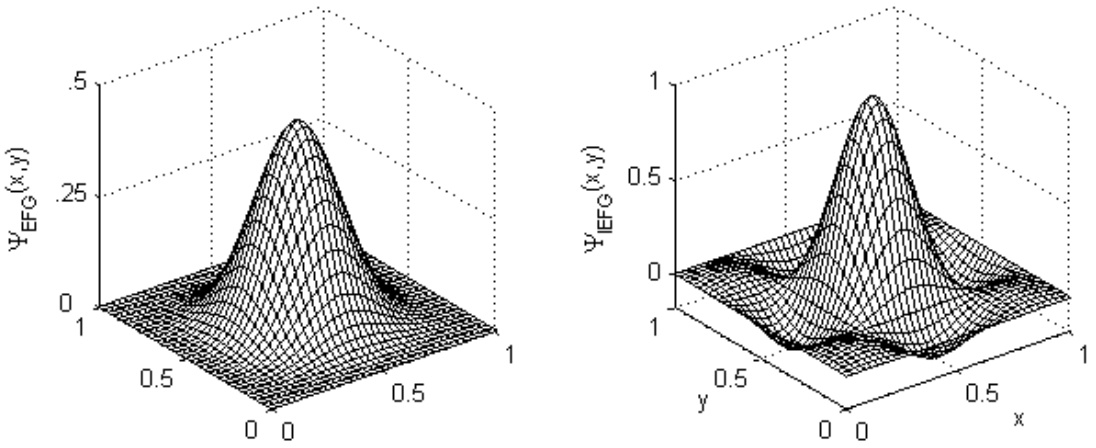

(a) EFG shape functions without interpolation (b) Interpolating EFG (IEFG) shape functions

Figure A-12 Element Free Galerkin shape function using interpolation transformation.

The interpolating shape functions could now be used in a point collocation scheme, for example. Next, we introduce the concept of the compaction transformation, for use in

weak formulations with interpolating shape functions. As mentioned earlier, compaction stabilizes the resulting stiffness matrix of the system for most numerical solvers.

Compaction Transformation

For weak formulations, the compactness of the shape functions can be restored by using an additional transformation matrix we refer to as a compaction transformation, $\mathbf{T}_c$. Equation (A-74) can be modified to form the following linear system to achieve compaction:

$$\underbrace{\begin{bmatrix} C(\mathrm{x}-\mathrm{x}_1) & 0 & \cdots & 0 \\ 0 & C(\mathrm{x}-\mathrm{x}_2) & \cdots & 0 \\ \vdots & \vdots & \ddots & \vdots \\ 0 & 0 & \cdots & C(\mathrm{x}-\mathrm{x}_m) \end{bmatrix}}_{\mathrm{T_C=compaction\ transformation}} \begin{bmatrix} u(\mathbf{x}_1) \\ u(\mathbf{x}_2) \\ \vdots \\ u(\mathbf{x}_n) \end{bmatrix} = \underbrace{\begin{bmatrix} \Psi_1^{NI}(\mathbf{x}_1) & \Psi_2^{NI}(\mathbf{x}_1) & \cdots & \Psi_n^{NI}(\mathbf{x}_1) \\ \Psi_1^{NI}(\mathbf{x}_2) & \Psi_2^{NI}(\mathbf{x}_2) & \cdots & \Psi_n^{NI}(\mathbf{x}_2) \\ \vdots & \vdots & \ddots & \vdots \\ \Psi_1^{NI}(\mathbf{x}_n) & \Psi_2^{NI}(\mathbf{x}_n) & \cdots & \Psi_n^{NI}(\mathbf{x}_n) \end{bmatrix}}_{\mathrm{T_I=transformation\ matrix}} \begin{bmatrix} u(\mathbf{x}_1) \\ u(\mathbf{x}_2) \\ \vdots \\ u(\mathbf{x}_n) \end{bmatrix} \tag{A-76}$$

The properties of the compaction transformation function, $\mathbf{T}_c$, are such that the compact function used should be sufficiently differentiable, and possess a maximum value of unity at the origin. From (A-76), we have

$$\mathbf{T}_\mathrm{I}^{-1}\mathbf{T}_\mathrm{C}\mathbf{U} = \mathbf{U} \tag{A-77}$$

The new approximations are then given by

$$u(\mathrm{x}) \cong \Psi_v^{NI}\mathbf{T}_\mathrm{I}^{-1}\mathbf{T}_\mathrm{C}\mathbf{U} \tag{A-78}$$

In general, such a transformation does not preserve the POU property; however, this can be restored by a proper normalization:

$$\Psi_j^{S,icp} = \frac{\Psi_j^{S,ic}}{\sum_k \Psi_k^{S,ic}} \tag{A-79}$$

(a) RBF shape functions without compaction (b) RBF shape functions with compaction

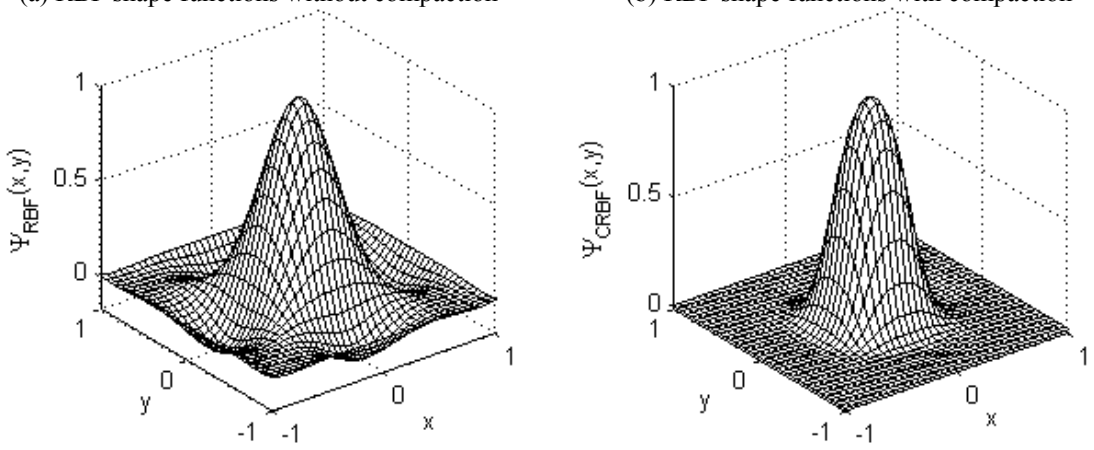

(a) RBF shape functions without compaction (b) RBF shape functions with compaction

Figure A-13 RBF shape functions using the compaction transformation.

We have tested the compaction transformation out using RBFs in weak formulations using an adaptive scheme designed by Li and Lee [60] and they worked very well. This leads to the a possibility of reducing the computation time in some problems by making the shape functions more compact.

At this point, we have reviewed the formulations for six MLM formulations including a bit of the historical development to introduce MLMs. The comparisons among them have helped to aid in the selection of the shape functions used in this work.

Table A-2 Summary of the considered shape function formulations

	POU	**KFDP**	**Kernel**	**MLS**	**PC**	**Weak**
SPH	Yes	No	Yes	No	No	Yes
RKPM	Yes	No	Yes	No	No	Yes
MLSRKPM	Yes	Yes*	Yes	Yes	Yes	Yes
HpC	Yes	Yes*	No	Yes	Yes	Yes
EFG	Yes	Yes*	No	Yes	No	Yes
reprod-**RBF**	Yes	Yes	No	No	Yes	Yes

Using MLMs provides the method for spatial discretization to equations to be solved in this work.

An instability due the norm preserving nature of the Gilbert equation was discussed in Chapter 2. Additionally, the time spans for the MI element (~1/*f*) is typically large compared to time constants of the magnetization. Thus, in order to use relatively large time steps for the problem considered, an implicit scheme is used. The disadvantage is that this approach leads to having to solve a nonlinear equation at each time step which extends the solution time at each iteration. In order to discretize the system in time, a well known 2^{nd} order time integration technique is used, known as the Newmark integration scheme and is described next.

APPENDIX B

B.1 Newmark Integration of 1st Order Temporal Systems

Although a more general treatment of the equations of motion considered in this work requires a formulation for integrating a 2nd order temporal derivative, the quasi-static conditions results in the need to discretize only a first order derivative formulation. With this, the system is generally expressed in the following form:

$$\frac{\partial \mathbf{y}}{\partial t} = \mathbf{f}\left(t, \mathbf{y}\right) \text{subject to } \mathbf{y}(0) = \mathbf{y}_0 \tag{B-1}$$

In (B-1), the time dependent solution $\mathbf{y}(t)$ is needed. In this thesis, equation (B-1) is discretized using a scheme known as the Newmark integration scheme. The Newmark integration scheme is an integration scheme that uses "averages" for the derivatives in order to arrive at an implicit integration scheme. In this work, the choice of an implicit time integration scheme is not arbitrary, but, is chosen because although implicit integration schemes are generally slower that explicit schemes, implicit schemes offer nearly global stability, unlike explicit time integration schemes like Euler schemes. This point is relevant here because the time constants of magnetization in the systems modeled in this work are much smaller than the characteristic times of the input current source. This leads to a requirement of very small time steps for a stable explicit integration scheme on the order of $1e^{-10}$. However, recall that the frequency inputs of the MI element are between 100 kHz and 10 MHz which result in electrodynamic waves with periods between $1e^{-7}$ and $1e^{-5}$, necessarily leading to a very large number of time steps for the problem considered. This problem is resolved by using an implicit scheme which allows for much smaller time steps and still converges to a stable solution.

The Newmark scheme used here begins by expressing the function of interest $\mathbf{y}(t)$ in a Taylor series expansion about a point in time, t_i. After truncating all terms of 2nd order and higher, we have the following:

$$y_{i+1} = y_i + \Delta t \left.\frac{\partial y}{\partial t}\right|_{avg} \tag{B-2}$$

Generally, the derivative in (B-2) is evaluated at t_i, however, in the Newmark scheme, it is replaced by a more "updated" term. Instead of a single evaluation at t_i, the average derivative is found using an average of the known value at t_i and the unknown value at t_{i+1}. Then, the average derivative is then defined in an approximation given by

$$\left.\frac{\partial y}{\partial t}\right|_{avg} = \frac{\partial y_{i+1/2}}{\partial t} = \left(1-\gamma\right)\frac{\partial y_i}{\partial t} + \gamma\frac{\partial y_{i+1}}{\partial t} \tag{B-3}$$

The subscript $i + ½$ is commonly used as it physically represents the derivative in the middle of the time interval $[t_i \;\; t_{i+1}]$. Also, (B-3) suggests that if $\gamma = 0.5$, the average will be exactly that in the "middle" when the derivative is linear in time. Further, a linear time derivative implies a constant "acceleration", and it is then easy to show that this scheme is exact for 2nd order systems and lower. Thus, the Newmark integration scheme is 2nd (with respect to time, t) for solving $\mathbf{y}(t)$. By having the time derivative function given in (B-1), the solution is then updated by the following rule:

$$y_{i+1} = y_i + \Delta t\left[\left(1-\gamma\right)\frac{\partial y_i}{\partial t} + \gamma\frac{\partial y_{i+1}}{\partial t}\right] \tag{B-4}$$

$\gamma = 0.5$ in all computations.

APPENDIX C

C.1 Broyden Nonlinear Solver

In this work, the nonlinear solver used is among the class of nonlinear solver methods known as Broyden's method. They are one type of quasi-Newton method. It draws this name in reference to its emulation of the more classical Newton's (or Newton-Raphson) method. However, as is demonstrated in this thesis research (Chapter 5), quasi-Newton schemes have significant advantages for systems with large numbers of unknowns, compared to Newton's method. For this reason, it is very suitable for some of the problem(s) considered here as there are as many as 14 degrees of freedom at each spatially discrete node in the computational domain.

The objective of a nonlinear solver is to find a vector **x** evaluated inside a homogeneous function **f**, which is generally posed as a root finding problem, where the homogeneous function **f** is expressed as:

$$\mathbf{f}(\mathbf{x}) = 0 \tag{C-1}$$

Assuming **f** is composted of n independent equations, where n = the length of **f**, the objective of finding the root is typically met using methods like the quadratically convergent (near the root) iterative method known as Newton's method.

Newton's update rule can be derived directly from a Taylor series expansion of **f** expressed as follows:

$$f_i(\mathbf{x}^{k+1}) = f_i(\mathbf{x}^k) + \sum_{j=1}^{n} \left.\frac{\partial f_i}{\partial x_j}\right|_{\mathbf{x}=\mathbf{x}^k} (x_j^{k+1} - x_j^k) + \sum_{j=1}^{n}\sum_{l=1}^{n} (x_j^{k+1} - x_j^k)^2 \left.\frac{\partial^2 f_i}{\partial x_j \partial x_l}\right|_{\mathbf{x}=\mathbf{x}^k} (x_l^{k+1} - x_l^k)^2 + O(\mathbf{h}^3) \tag{C-2}$$

To derive Newton's update rule, a truncation of 2nd and higher order terms is made in addition to the assumption of close proximity to the final solution, i.e.

$$f_i(\mathbf{x}^{k+1}) \approx f_i(\mathbf{x}_s) = 0 \tag{C-3}$$

With these assumptions, equation (C-2) can be rearranged as

$$f_i(\mathbf{x}^{k+1}) \approx 0 = f_i(\mathbf{x}^k) + \sum_{j=1}^{n} J_{ij}(x_j^{k+1} - x_j^k), \text{ where } J_{ij} = \left.\frac{\partial f_i}{\partial x_j}\right|_{\mathbf{x}=\mathbf{x}^k} \tag{C-4}$$

Expressing the equation for all the components of the function vector, ***f***, we have:

$$-\mathbf{f}(\mathbf{x}^k) = \mathbf{J}(\mathbf{x}^k)\left[\mathbf{x}^{k+1} - \mathbf{x}^k\right] \Rightarrow \mathbf{x}^{k+1} = \mathbf{x}^k - \mathbf{J}^{-1}(\mathbf{x}^k)\mathbf{f}(\mathbf{x}^k) \tag{C-5a,b}$$

One undesirable characteristic of Newton's method is the necessary condition that at each iteration, the Jacobian matrix, which is an *n* x *n* matrix, is needed as well as the need to solve the linear equation given in (C-5). For large systems, these calculations can be costly and lead to an inefficient computational process. For computing the Jacobian, on the order of n^2 algebraic operations are needed. In many problems, this number can be reduced, however, there are still many operations that are needed for each iteration and for complicated functions, even more time is needed independent of the number *n*.

In addition to computing the Jacobian, it must be inverted (or equivalently done such as using LU decomposition). Solving a linear system is known to take on the order of n^3 algebraic operations, and this number can easily dominate computation time, as well. Therefore, in each iteration, there are on the order of $n^3 + n^2$ arithmetic operations that must be performed, which amounts to a busy computer!

In an effort to remedy these shortcomings of the original Newton's method, a set of methods known as quasi-Newton methods have been developed and this class of methods is deployed in this work. These methods are summarized next.

In order to introduce these methods, first, note that if we omit the assumption (from the Taylor series expansion) that the updated function evaluation is close to zero, a general relation for the Jacobian like matrix is given by:

$$\mathbf{f}(\mathbf{x}^{k+1}) - \mathbf{f}(\mathbf{x}^{k}) = \mathbf{J}(\mathbf{x}^{k})(\mathbf{x}^{k+1} - \mathbf{x}^{k}) \text{ or } \mathbf{J}^{-1}\left[\mathbf{f}(\mathbf{x}^{k+1}) - \mathbf{f}(\mathbf{x}^{k})\right] = \mathbf{x}^{k+1} - \mathbf{x}^{k} \tag{C-6}$$

The condition in (C-6) is given as a necessary condition for any quasi-Newton method in approximating the Jacobian matrix as $\tilde{\mathbf{J}}$ that will replace the Jacobian matrix $\mathbf{J}$. The key to the quasi-Newton methods is that they *update* the Jacobian (or its inverse) from the previous step so no new Jacobian is computed and inverted at each iteration, but only the computation of a correction matrix is added to the previous Jacobian estimation which amounts to a total number of function evaluations on the order of n^2 at each iteration instead of $n^3 + n^2$! In order to rewrite the condition so that the estimated Jacobian can be updated from the previous step, (C-6) is alternatively expressed as

$$\mathbf{f}(\mathbf{x}^{k+1}) - \mathbf{f}(\mathbf{x}^{k}) = (\mathbf{J}^{k-1} + \mathbf{C}^{k-1})(\mathbf{x}^{k+1} - \mathbf{x}^{k}) \tag{C-7}$$

Equation (C-7) is more useful if expressed in such a way that the Jacobian inverse is the vector we are updating, so we then have

$$(\mathbf{J}^{-1,k-1} + \mathbf{C}^{k-1})\left[\mathbf{f}(\mathbf{x}^{k+1}) - \mathbf{f}(\mathbf{x}^{k})\right] = (\mathbf{x}^{k+1} - \mathbf{x}^{k}) \tag{C-8}$$

The condition given in (C-8) leads to the following rule for the correction matrix, **C**:

$$\mathbf{C}^{k-1}\boldsymbol{\gamma} = \boldsymbol{\delta} - \mathbf{J}^{-1,k-1}\boldsymbol{\gamma} \tag{C-9}$$

In (C-9), $\boldsymbol{\delta} = \mathbf{x}^{k+1} - \mathbf{x}^{k}$ and $\boldsymbol{\gamma} = \mathbf{f}(\mathbf{x}^{k+1}) - \mathbf{f}(\mathbf{x}^{k})$. Then, focusing on the correction term, satisfying equation (C-9) is equivalent to satisfying (C-6). It suffices to say that there are infinitely many matrix solutions to equation (C-9), and so the differences between quasi-Newton methods are the manner in which (C-9) is satisfied. In fact, a particular solution to (C-9) can readily by seen by substitution of the following

$$\mathbf{C}^{k-1} = \frac{(\boldsymbol{\delta} - \mathbf{J}^{-1,k-1}\boldsymbol{\gamma})\boldsymbol{\delta}^T \mathbf{J}^{-1,k-1}}{\left\|\boldsymbol{\delta}^T \mathbf{J}^{-1,k-1}\boldsymbol{\gamma}\right\|} \tag{C-10}$$

Since (C-10) is a particular solution to (C-9), it follows that infinitely many solutions also satisfy (C-9) if (C-10) is modified by augmenting a matrix resulting in the following:

$$\mathbf{C}^{k-1} = \frac{\left(\boldsymbol{\delta} - \mathbf{J}^{-1,k-1}\boldsymbol{\gamma}\right)\boldsymbol{\delta}^T \mathbf{J}^{-1,k-1}}{\left\|\boldsymbol{\delta}^T \mathbf{J}^{-1,k-1}\boldsymbol{\gamma}\right\|} + \upsilon \mathbf{a} \bullet \mathbf{b}^T \tag{C-11}$$

In (C-11), υ is an arbitrary scalar. The necessary condition for the additional matrix given on the RHS of (C-10) is given by the fact that the solution is preserved if the vector **b** is any vector perpendicular to **γ**, because then (C-9) is also readily satisfied because

$$\upsilon \mathbf{a} \bullet \mathbf{b}^T \bullet \boldsymbol{\delta} = 0 \tag{C-12}$$

In fact, the expression in (C-10) can expressed more generally by

$$\mathbf{C}^{k-1} = \frac{\left(\boldsymbol{\delta} - \mathbf{J}^{-1,k-1}\boldsymbol{\gamma}\right)\mathbf{c}^T}{\left\|\mathbf{c}^T \boldsymbol{\gamma}\right\|} + \upsilon \mathbf{a} \bullet \mathbf{b}^T \tag{C-13}$$

where $\mathbf{c}^T$ is any vector that is *not* perpendicular to **γ.** The choice of $\mathbf{c}^T$ is specified in (C-10), and this value is used in this work. It should be also expected that not all choices of the scalar υ and the additional matrix, $\mathbf{a}\mathbf{b}^T$ perform the same, thus different choices typically define the variations within the quasi-Newton family of nonlinear solver methods. Here, the choice of υ = 0 is used so the resulting update rule is given by (C-10). In the numerical implementation, equation (C-10) also uses an additional approximation. They are given by the following:

$$\boldsymbol{\delta} = \mathbf{x}^{k+1} - \mathbf{x}^k \approx \mathbf{x}^{k-1} - \mathbf{x}^{k-2} \text{ and } \boldsymbol{\gamma} = \mathbf{f}(\mathbf{x}^{k+1}) - \mathbf{f}(\mathbf{x}^k) \approx \mathbf{f}(\mathbf{x}^{k-1}) - \mathbf{f}(\mathbf{x}^{k-2}) \tag{C-14a,b}$$

The convergence rate of the quasi-Newton methods is *super*linear (near the root) instead of quadratic, as is the case in Newton's method.

The Broyden's method summarized above guarantees a direction that *can* lead to reducing the norm of the function, **f**, however, the amount of stepping in the determined direction is still not well defined. For "stiff" problems that vary a lot with **x**, the iterations can require smaller steps to ensure a reduction in **f**. At the same time, too small a step is undesirable as it slows down the convergence time. A solution to this is to determine an optimum length along the path determined above. This step is referred to as a *line search*. This approach is useful in both Newton's method as well as quasi-Newton methods. It stabilizes the algorithm by ensuring each step is reducing the norm of **f**, which is necessary to converge to the root, at which the norm of $\mathbf{f} = 0$.

Incorporating this stabilizing line search, the quasi-Newton schemes used here therefore involve two components:

1) *Jacobian* estimation
2) *Line search* algorithm

In general, the quasi-Newton update rule is given by:

$$\mathbf{x}^{k+1} = \mathbf{x}^k - \alpha^* \tilde{\mathbf{J}}^{-1}(\mathbf{x}^k)\mathbf{f}(\mathbf{x}^k) \tag{C-15}$$

The scalar parameter α^* is the result of the so-called *line search*. A simple interpretation of the line search is that it determines an optimal length or scaling amount, given by α^*, along the direction given by the vector $\tilde{\mathbf{J}}^{-1}\mathbf{f}$ that ensures the norm of the function $\mathbf{f}(\mathbf{x})$ is reduced. It is very common in practice that the line search is performed in such a way that approximates the optimal α^*. The true α, is defined by determining that α that minimizes $\|\mathbf{f}(\alpha)\|^2$, found by solving the following:

$$\frac{d\left\|\mathbf{f}(\alpha)\right\|^2}{d\alpha} = 0 \tag{C-16}$$

For large problems, the solution to (C-16) may be nontrivial. To avoid this extra computational burden, an approximation to $\left\|\mathbf{f}(\alpha)\right\|^2$, i.e. $\left\|\tilde{\mathbf{f}}(\alpha)\right\|^2$ is used by way of a second order interpolating polynomial. This approximation is used in the minimization and since it is second order, the solution to (C-16) is simple and easy to implement. The second order approximating polynomial is found by using a Newton's forward divided-difference interpolating polynomial, defining $\tilde{g} = \left\|\tilde{\mathbf{f}}(\alpha)\right\|^2$ as follows:

$$\tilde{g} = \tilde{g}(\alpha_0) + b_1\alpha + b_2\alpha(\alpha - \alpha_2) \tag{C-17}$$

In (C-17), the parameters b_1 and b_2 are given by

$$b_1 = \left[\frac{\tilde{g}(\alpha_1) - \tilde{g}(\alpha_0)}{\alpha_1 - \alpha_0}\right] \text{ and } b_2 = \frac{1}{\alpha_2 - \alpha_0}\left[\frac{\tilde{g}(\alpha_2) - \tilde{g}(\alpha_1)}{\alpha_2 - \alpha_1} - \frac{\tilde{g}(\alpha_1) - \tilde{g}(\alpha_0)}{\alpha_1 - \alpha_0}\right] \tag{C-18}$$

The polynomial given in (C-17) easily leads to a single critical point α^* given by

$$\alpha^* = \frac{1}{2}\left(\alpha_3 - \frac{b_1}{b_2}\right) \tag{C-19}$$

This provides the length of the step towards ensuring the approach to the root once the direction is obtained using the approximated Jacobian inverse.

A comment is also in order regarding the very first Jacobian estimation. Many choices are possible, and a few different choices were tested in this thesis research. For the MI effect problem, it was found that for larger than a 1D computational domain, the initial guess that is most robust is an approximated Jacobian using finite differences. However, for 1D problems, the identity matrix worked sufficiently, and was obviously more efficient.

APPENDIX D

D.1 Equivalence of Gilbert and Landau-Lifshitz-Gilbert Equation

The Gilbert equation is similar to (but not exactly the same as) an earlier micromagnetics formulation known as the Landau-Lifshitz micromagnetics formulation [11], which is considered one of the first proposed micromagnetics equations of motion. The Landau-Lifshitz-Gilbert equation is another micromagnetics formulation that has the form of the LL equation, and can be proven to be equivalent to the more intuitive relation, deployed in this work, given by the Gilbert equation. We show the equivalence between the Gilbert and Landau-Lifshitz-Gilbert equation, following the approach in [66]. The conversion starts by left crossing the Gilbert equation with the magnetization **M** giving

$$\mathbf{M}\times\frac{\partial\mathbf{M}}{\partial t}=-\gamma\mathbf{M}\times\mathbf{M}\times\mathbf{H}_T+\frac{\alpha}{M_s}\mathbf{M}\times\mathbf{M}\times\frac{\partial\mathbf{M}}{\partial t} \tag{D-1}$$

Replacement of the second term on the right hand side is done by using the vector calculus identity:

$$\mathbf{a}\times\mathbf{b}\times\mathbf{c}=\left(\mathbf{a}\cdot\mathbf{c}\right)\mathbf{b}-\left(\mathbf{a}\cdot\mathbf{b}\right)\mathbf{c} \tag{D-2}$$

Using (D-2), (D-1) now becomes

$$\mathbf{M}\times\frac{\partial\mathbf{M}}{\partial t}=-\gamma\mathbf{M}\times\mathbf{M}\times\mathbf{H}_T+\frac{\alpha}{M_s}\left[\left(\mathbf{M}\cdot\frac{\partial\mathbf{M}}{\partial t}\right)\mathbf{M}-\left(\mathbf{M}\cdot\mathbf{M}\right)\frac{\partial\mathbf{M}}{\partial t}\right] \tag{D-3}$$

Since the magnetization vector and its time derivative are always orthogonal to each other, (D-3) becomes

$$\mathbf{M}\times\frac{\partial\mathbf{M}}{\partial t}=-\gamma\mathbf{M}\times\mathbf{M}\times\mathbf{H}_T-\alpha M_s\frac{\partial\mathbf{M}}{\partial t} \tag{D-4}$$

The damping term can now be replaced yielding

$$\frac{\partial\mathbf{M}}{\partial t}=-\gamma\mathbf{M}\times\mathbf{H}_T-\frac{\alpha}{M_s}\left[\gamma\mathbf{M}\times\mathbf{M}\times\mathbf{H}_T+\alpha M_s\frac{\partial\mathbf{M}}{\partial t}\right] \tag{D-5}$$

Rearranging (D-5) gives

$$\frac{\partial\mathbf{M}}{\partial t}+\alpha^2\frac{\partial\mathbf{M}}{\partial t}=-\gamma\mathbf{M}\times\mathbf{H}_T-\frac{\alpha}{M_s}\left[\gamma\mathbf{M}\times\mathbf{M}\times\mathbf{H}_T\right] \tag{D-6}$$

From here, it follows that

$$\frac{\partial\mathbf{M}}{\partial t}=-\frac{\gamma}{1+\alpha^2}\mathbf{M}\times\mathbf{H}_T-\frac{\alpha\gamma}{\left(1+\alpha^2\right)M_s}\mathbf{M}\times\left(\mathbf{M}\times\mathbf{H}_T\right) \tag{D-7}$$

The final expression given in (D-7) is known as the Landau-Lifshitz-Gilbert equation and is also a commonly regarded micromagnetics formulation in addition to the earlier Landau-Lifshitz and Gilbert equations. In this work, the Gilbert equation is strictly used.

D.2 Magnitude Preservation by Micromagnetics

An important characteristic of the Gilbert equation (LL and LLG) is preservation of the norm of the magnetization vector **M** over time. This can be seen by performing a dot product of the Gilbert equation with the magnetization vector **M**, yielding

$$\mathbf{M}\cdot\frac{\partial\mathbf{M}}{\partial t}=\left(-\gamma\mathbf{M}\times\mathbf{H}+\frac{\alpha}{M_s}\mathbf{M}\times\frac{\partial\mathbf{M}}{\partial t}\right)\cdot\mathbf{M} \tag{D-8}$$

Because all vector components added on the RHS are orthogonal to **M**, the RHS vanishes. Additionally, on the LHS, we have

$$\mathbf{M}\cdot\frac{\partial\mathbf{M}}{\partial t}=M_1\frac{\partial M_1}{\partial t}+M_2\frac{\partial M_2}{\partial t}+M_3\frac{\partial M_3}{\partial t}=\frac{1}{2}\frac{\partial\|\mathbf{M}\|^2}{\partial t}=0 \tag{D-9}$$

This condition is analytically natural, but implicit, in the Gilbert equation of motion. However, in numerical implementation, often times, in order to avoid instability in the time integration, care must be taken in the integration to ensure this condition is met. The deviation from the norm preserving condition can be due to both numerical formulation error and/or round-off error. It is particularly important in explicit integration schemes such as Euler or Runge-Kutta methods. This point is discussed and illustrated by example in the next section.

D.3 Temporal Numerical Instability of Micromagnetics

As mentioned before, the implicit condition given by the preservation of the amplitude can lead to instabilities in the numerical integration of the equation. This is particularly relevant in explicit integration techniques, which typically are preferred due to their relative efficiency. However, in solving a system of equations that involves the micromagnetics equation, a typical numerical integration procedure often requires some modification to obtain a stable solution. Recall that the micromagnetics equation used takes the form:

$$\frac{\partial\mathbf{M}}{\partial t}=-\gamma\mathbf{M}\times\mathbf{H}_{\mathrm{T}}+\frac{\alpha}{M_s}\mathbf{M}\times\frac{\partial\mathbf{M}}{\partial t}$$

The stability can be examined by considering the simplest explicit forward stepping time integration scheme. First, the micromagnetics equation is expressed in a modified form:

$$\frac{\partial\mathbf{M}}{\partial t}=-\gamma\left[\mathbf{I}-\frac{\alpha}{M_s}\mathrm{skew}(\mathbf{M})\right]^{-1}\mathrm{skew}(\mathbf{H}_{\mathrm{T}})\mathbf{M}=\left[\mathbf{\Lambda}\right]\mathbf{M} \tag{D-10}$$

In (D-10), note that $\mathbf{\Lambda}$ depends on $\mathbf{M}$. Then, a first order linear time stepping scheme becomes

$$\mathbf{M}_{k+1} = \mathbf{M}_k + \Delta t\left[\mathbf{\Lambda}_k\right]\mathbf{M}_k = \left\{\mathbf{I} + \Delta t\left[\mathbf{\Lambda}_k\right]\right\}\mathbf{M}_k = \left[\bar{\mathbf{\Lambda}}_k\right]\mathbf{M}_k \tag{D-11}$$

Equation (D-11) is modified so that both vectors are normalized to have a length of unity and the formulation can be structured like an eigenvalue problem given by

$$\mathbf{m}_{k+1} = \frac{\left\|\mathbf{M}_{k+1}\right\|}{\left\|\mathbf{M}_k\right\|}\left[\bar{\mathbf{\Lambda}}_k\right]\mathbf{m}_k \tag{D-12}$$

In order to show the source of the numerical instability that arises from the condition of preserving the amplitude of $\mathbf{M}$, equation (D-12) can also equivalently interpreted to expresses a familiar numerical sequence resulting from solving an eigenvalue problem given by

$$\frac{\left\|\mathbf{M}_k\right\|}{\left\|\mathbf{M}_{k+1}\right\|}\left[\bar{\mathbf{\Lambda}}_k\right]^{-1}\mathbf{m} = \lambda\mathbf{m} \tag{D-13}$$

Such a discrete vector sequence is known to converge under the conditions of the spectral radius of the matrix in (D-13) and thus convergence is related to the condition:

$$\sqrt{\max\left(\lambda_i\left[\frac{\left\|\mathbf{M}_{k+1}\right\|}{\left\|\mathbf{M}_k\right\|}\left[\bar{\mathbf{\Lambda}}_k\right]\right]^{-T}\left[\frac{\left\|\mathbf{M}_{k+1}\right\|}{\left\|\mathbf{M}_k\right\|}\left[\bar{\mathbf{\Lambda}}_k\right]\right]^{-1}\right)} \le 1 \quad \forall t \tag{D-14}$$

Equation (D-14) provides a theoretical basis for the observed instability encountered in integrating the micromagnetics equation, particularly using explicit integration schemes.

One common approach to stabilizing the solution is to cast the form of the micromagnetics equation so that

1) $\mathbf{M} = |\mathbf{M}|/M_s$. Note that this is always possible with the micromagnetics equation.

2) In the discretization, each step forces a "projection" of a normalized form of $\mathbf{M}_{k+1}$ onto the unit circle (without changing the vector orientation). This means that the computed vector at each update is normalized by its length, $|\mathbf{M}_{k+1}|$. In this way, the real part of the eigenvalues (discussed above) tend to be kept within unity. A computational example using experimental parameter values typical in MI ribbon elements is shown in Figure D-1.

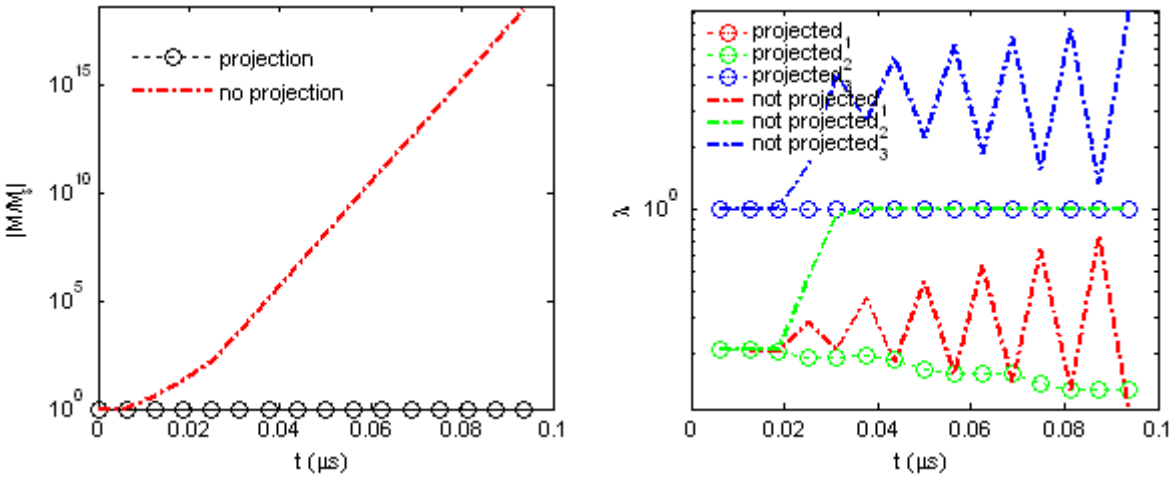

(a) **M** amplitude over time, *t* (b) inverse($\mathbf{\Lambda}_k$) eigenvalues over time, *t*

Figure D-1 Instability in Euler integration of Gilbert equation without projection. **Note**: red circles are coincident with green circles for projected solution.

Figure D-1 shows that for the case considered (which has been normalized), without projection, one of the eigenvalues exceeds 1, corresponding to the exponential "blow up" of the solution evident in Figure D-1(a). However, with the projection enforced at each time step, the solution is stable. The understanding of this problem could be critical in treating the temporal integration of the system considered in this thesis research. There are several alternatives to using an Euler type approach, of course, and this must be considered in making the selection. For example, it has been shown that using a midpoint method, which is 2nd order, naturally preserves the magnitude of **M** [61].

However, in this research, it has been found that projection still accelerates convergence in implicit algorithms.

Therefore, a careful approach must be taken when numerically solving the micromagnetics equation (with norm conservation) with integration. In most of the calculations performed in this work, a 2^{nd} order implicit integration scheme, similar to the midpoint method, is used along with projection to further stabilize the solution. The disadvantage to an implicit solver of this kind is that it leads to solving a nonlinear system at each time step, but near global stability is achieved. The selection of the nonlinear system solver used in most calculations in this work has been discussed in more detail in Appendix C. The time integration scheme, known as the Newmark integration scheme, has also been discussed in Appendix B.

APPENDIX E

E.1 Ribbon Impedance

The impedance for the ribbon element is derived analogously using Maxwell's equations. Consider Figure E-1 which shows the MI ribbon element geometry being modeled.

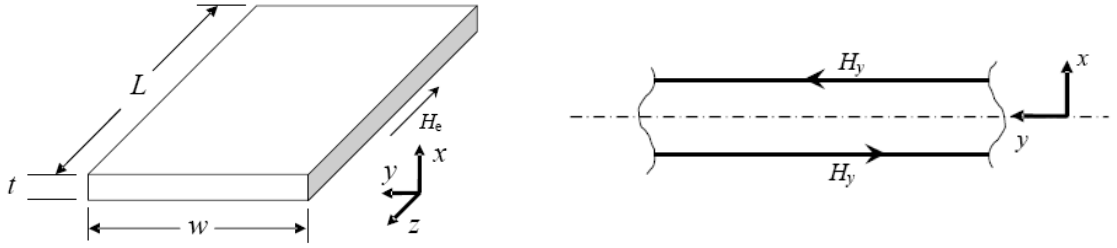

(a) Simplified ribbon MI element structure (b). Cross section for 1D model of ribbon MI element

Figure E-1 MI Ribbon element diagram.

The harmonic form of the equation of motion for the transverse magnetic field intensity, H_y, is given by

$$\frac{d^2 H_y}{dx^2} - k^2 H_y = 0 \tag{E-1}$$

The general solution to (3-17), owing to anti-symmetry, is given by

$$H_y = C_r \sinh kx \tag{E-2}$$

The constant, C_r, is again determined from a Dirichlet boundary condition for the ribbon element. By the same argument in the case of the circular wire, subjected to a fixed current source, I_s, the areal integration of Amperes law leads to an explicit Dirichlet boundary condition on the surface of the ribbon element. This is summarized as follows:

$$\int_S \nabla \times \mathbf{H} \cdot d\mathbf{S} = \int_S \mathbf{J} \cdot d\mathbf{S} = I_s \tag{E-3}$$

$$\int_S \mathbf{H} \cdot dl = \int_0^w \mathbf{H}_y\big|_{t/2} \cdot d\mathbf{y} + \int_{-t/2}^{t/2} \mathbf{H}_x\big|_w \cdot d\mathbf{x} + \int_w^0 \mathbf{H}_y\big|_{-t/2} \cdot d\mathbf{y} + \int_{t/2}^{-t/2} \mathbf{H}_x\big|_0 \cdot d\mathbf{x} + \approx 2\,wH_y\big|_{x=t/2} \tag{E-4}$$

The result in (E-4) follows from the condition that $t << w$. A Dirichlet boundary condition follows from (E-3) and (E-4) given by

$$H_y\big|_{x=t/2=t_h} \approx I_s / 2w \tag{E-5}$$

In (E-5), the half thickness, $t_h = t/2$, is introduced and thus using (E-2) and (E-5), the constant, C_r, is given by

$$C_r = \frac{I_s}{2w\sinh\left(kt_h\right)} \tag{E-6}$$

The electric field in the z-direction then follows from the transverse magnetic field intensity

$$\sigma E_z = \partial H_y / \partial x \Rightarrow E_z = C_r \cdot (k/\sigma) \cdot \cosh\left(kx\right) \tag{E-7}$$

Because E_z is assumed constant over the length of the ribbon as $L \ll c/f$, a positive voltage drop, in terms of the impedance, is then given by

$$I_s Z = LC_r \left(k/\sigma\right)\cosh\left(kt_h\right) \tag{E-8}$$

The impedance in the ribbon element is then given by

$$Z = \frac{Lk}{2w\sigma}\frac{\cosh\left(kt_h\right)}{\sinh\left(kt_h\right)} \tag{E-9}$$

In terms of the *dc* resistance, given by $R_{dc} = L/\sigma tw$, the impedance in the ribbon element is given by

$$Z = R_{dc} kt_h \frac{\cosh\left(kt_h\right)}{\sinh\left(kt_h\right)} = R_{dc} kt_h \coth\left(kt_h\right) \tag{E-10}$$

This is the same relation used in the literature [24] [86].

APPENDIX F

F.1 Circular Wire Impedance

The Landau Lifshitz impedance relation Z_c, for a circular magnetic wire [15] can be derived directly from Maxwell's equations. The reduced Maxwell's equations describing the amplitudes of the electric and magnetic field intensity, E_z and H_θ, in linear harmonic form, are given by

$$\frac{1}{r}\frac{\partial\left(rH_\theta\right)}{\partial r} = J_z \tag{F-1}$$

$$\frac{\partial E_z}{\partial r} = -j\omega\mu_\theta(H_e)H_\theta \tag{F-2}$$

H_θ is the circular or transverse component of the magnetic field intensity and J_z is the axial current density; j is the complex operator defined as $\sqrt{-1}$. μ_θ is the transverse permeability, which for the MI effect, should depend on the measured field H_e. The assumptions leading to (F-1) and (F-2) include that the permeability μ_θ is a scalar (complex or real). With the assumption of linear material properties, (F-1) and (F-2) leads to the following:

$$\frac{1}{r}\frac{\partial}{\partial r}\left(r\frac{\partial E_z}{\partial r}\right) = -j\omega\sigma\mu_\theta E_z \tag{F-3}$$

Equation (F-3) can alternatively be expressed as

$$\frac{1}{r}\frac{\partial}{\partial r}\left(r\frac{\partial E_z}{\partial r}\right) + k^2 E_z = 0 \tag{F-4}$$

In (F-4), the parameter k is then defined by $k = \sqrt{j\omega\sigma\mu_\theta}$. Equation (F-4) poses a particular case of the well known equation (the Bessel equation) where the solution is given by the zero order Bessel function of the first kind:

$$E_z = c_0 \cdot J_0\left(kr\right)e^{-j\omega t} \tag{F-5}$$

All the solutions have the complex exponential term, however, for brevity, it is omitted in the following equations. Then, with the solution for E_z, using (F-2), H_θ is given by

$$H_\theta = -j\frac{c_0 k}{\mu\omega} \cdot J_1\left(kr\right) \tag{F-6}$$

The constant c_0 is determined, here, by a Dirichlet boundary condition on the surface of the circular wire element. For the MI element, which is subjected to a fixed current source, I_s, and surrounded by air, the areal integration of Amperes law leads to an explicit Dirichlet boundary condition. This is summarized as follows:

$$\int_S \nabla \times \mathbf{H} \cdot d\mathbf{S} = \int_S \mathbf{J} \cdot d\mathbf{s} \tag{F-7}$$

Using Stokes theorem, relating the surface integral to the line integral around the wire, it follows that

$$\int_S \mathbf{H} \cdot dl = 2\pi r_0 H_\theta\big|_{r=r_0} \text{ and } \Rightarrow \int_S \mathbf{J} \cdot d\mathbf{S} = I_s \tag{F-8a,b}$$

Then, an explicit Dirichlet boundary condition is obtained for the MI element, given by

$$H_\theta\big|_{r=r_0} = I_s / 2\pi r_0 \tag{F-9}$$

The integration constant is then determined using the solution for the transverse magnetic field intensity leading to

$$I_s / 2\pi r_0 = -j\left(c_0 k / \mu\omega\right) J_1\left(kr_0\right) \Rightarrow c_0 = j\frac{I_s \mu\omega}{2\pi r_0 k J_1\left(kr_0\right)} \tag{F-10}$$

Using the definition of the electric potential, ($\partial V / \partial z = -E_z$), for a linear system of this kind with relatively large wavelengths compared to the wire length, L, i.e.:

$$c / f \gg L \Leftrightarrow 3e8 / 1e6 (= 300\text{m}) \gg 5e-3\,\text{m} \tag{F-11}$$

In condition (F-11), experimentally determined values [9] taken for the circular wire element have been substituted. It follows that

$$\frac{\partial V}{\partial z} = -c_0 J_0\left(kr\right) \tag{F-12}$$

Thus, a positive axial voltage drop across the MI element is then given by

$$\Delta V_z = ZI_s = c_0 J_0\left(kr_0\right) L \tag{F-13}$$

In order to solve for the impedance, the input current, I_s, is expressed as proportional to the constant, c_0, using (F-10), leading to the following for the impedance (first order approximation) in a circular magnetic conducting wire:

$$Z = \frac{c_0 J_0\left(kr_0\right) L}{-j\frac{c_0 2\pi r_0 k}{\mu\omega} \cdot J_1\left(kr_0\right)} = \frac{\mu\omega L}{-j2\pi r_0 k} \frac{J_0\left(kr_0\right)}{J_1\left(kr_0\right)} \tag{F-14}$$

Rearranging (F-14), the impedance is given by[7]

$$Z = \frac{j\mu\omega L}{2\pi r_0 k} \frac{J_0\left(kr_0\right)}{J_1\left(kr_0\right)} = \frac{1}{2} R_{\text{dc}} kr_0 \frac{J_0\left(kr_0\right)}{J_1\left(kr_0\right)} \tag{F-15}$$

[7] It is noted that the derivations here have been derived to deliberately be consistent with the literature yielding a positive real impedance component, however, the equations of motion should normally define a negative impedance because there is a always a voltage drop by convention and not a voltage increase as suggested by a "positive" impedance.

REFERENCES

[1] O. V. Lounasmaa and H. Seppa, "SQUIDs in neuro- and cardiomagnetism," *Journal of Low Temperature Physics,* vol. 135, pp. 295-335, 2004.

[2] D. S. Parasnis, *Magnetism:From Lodestone to Polar Wandering*: Harper and Brothers, 1961.

[3] M. Vopalensky, P. Ripka, and A. Platil, "Precise magnetic sensors," *Sensors and Actuators, A: Physical,* vol. 106, pp. 38-42, 2003.

[4] J. S. Stohr, H.C. Seigmann, *Magnetism:From Fundamentals to Nanoscale Dynamics*: Springer, 2006.

[5] A. Sandhu, A. Okamoto, I. Shibasaki, and A. Oral, "Nano and micro Hall-effect sensors for room-temperature scanning hall probe microscopy," *Microelectronic Engineering,* vol. 73-74, pp. 524-528, 2004.

[6] K. Mohri, T. Uchiyama, and L. V. Panina, "Recent advances of micro magnetic sensors and sensing application," *Sensors and Actuators, A: Physical,* vol. 59, pp. 1-8, 1997.

[7] N. A. Usov, A. S. Antonov, and A. N. Lagar'kov, "Theory of giant magneto-impedance effect in amorphous wires with different types of magnetic anisotropy," *Journal of Magnetism and Magnetic Materials,* vol. 185, pp. 159-173, 1998.

[8] K. Mohri, T. Uchiyama, L. P. Shen, C. M. Cai, Y. Honkura, and H. Aoyama, "Amorphous wire and CMOS IC based sensitive micro-magnetic sensors utilizing magneto-impedance (MI) and stress-impedance (SI) effects and applications," *Journal of Magnetism and Magnetic Materials,* in *MHS2001. Proceedings of the 2001 International Symposium on Micromechatronics and Human Science, 9-12 Sept. 2001*, Nagoya, Japan, 2001, pp. 25-34.

[9] K. Mohri, K. Bushida, M. Noda, H. Yoshida, L. V. Panina, and T. Uchiyama, "Magneto-impedance element," *IEEE Transactions on Magnetics,* vol. 31, pp. 2455-60, 1995/07/ 1995.

[10] C. Kittel, "Physical theory of ferromagnetic domains," *Reviews of Modern Physics,* vol. 21, pp. 541-583, 1949.

[11] A. G. Gurevich and G. A. Melkov, *Magnetization Oscillations and Waves*: CRC Press, Inc., 1996.

[12] N. A. Usov, A. S. Antonov, and A. B. Granovsky, "Theory of Giant Magneto-Impedance Effect in Composite Amorphous Wire," *Journal of Magnetism and Magnetic Materials,* vol. 171, pp. 64-68, 1997.

[13] P. J. Vulfovich and L. V. Panina, "Magneto-impedance in Co-based amorphous wires and circular domain dynamics," *Sensors and Actuators A (Physical),* vol. A81, pp. 111-16, 2000.

[14] K. Mohri, K. Bushida, M. Noda, H. Yoshida, L. V. Panina, and T. Uchiyama, "Magneto-impedance element," *IEEE Transactions on Magnetics,* vol. 31, pp. 2455-2460, 1995.

[15] L. D. Landau, E. M. Lifshitz, and L. P. Pitaevskii, "Electrodynamics of Continuous Media." vol. 8, Elsevier-Butterworth-Heinemann, MA, 1984.

[16] A. Antonov, S. Gadetsky, A. Granovsky, A. D'Yatckov, M. Sedova, N. Perov, N. Usov, T. Furmanova, and A. Lagar'kov, "High-frequency giant magneto-impedance in multilayered magnetic films," *Physica A:,* vol. 241, pp. 414-419, 1997.

[17] L. V. Panina and K. Mohri, "Magneto-impedance in multilayer films," *Sensors and Actuators, A: Physical,* vol. 81, pp. 71-77, 2000.

[18] Y. Zhou, J. Yu, X. Zhao, and C. Yang, "Giant magneto-impedance in multilayered FeSiB/Cu/FeSiB films," *Vacuum Science and Technology,* vol. 21, pp. 360-3, 2001.

[19] Z. Zhi-Yong, L. Zhong-Wen, Z. Huai-Wu, L. Ying-Li, and W. Hao-Cai, "Computation on giant magneto-impedance effects in ferromagnetic/non-ferromagnetic/ferromagnetic layered thin films," *Acta Physica Sinica,* vol. 50, pp. 1610-15, 2001// 2001.

[20] X. P. Li, Z. J. Zhao, C. Chua, H. L. Seet, and L. Lu, "Enhancement of giant magnetoimpedance effect of electroplated NiFe/Cu composite wires by dc Joule annealing," *Journal of Applied Physics,* vol. 94, pp. 7626-7630, 2003.

[21] K. Hika, L. V. Panina, and K. Mohri, "Magneto-impedance in sandwich film for magnetic sensor heads," *IEEE Transactions on Magnetics,* vol. 32, pp. 4594-4596, 1996.

[22] D. Menard, M. Britel, P. Ciureanu, and A. Yelon, "Giant magnetoimpedance in a cylindrical magnetic conductor," *Journal of Applied Physics,* vol. 84, pp. 2805-14, 1998.

[23] L. V. Panina and K. Mohri, "Magneto-impedance effect in amorphous wires," *Applied Physics Letters,* vol. 65, pp. 1189-91, 1994/08/29 1994.

[24] L. V. Panina, K. Mohri, T. Uchiyama, M. Noda, and K. Bushida, "Giant magneto-impedance in Co-rich amorphous wires and films," *IEEE Transactions on Magnetics,* vol. 31, pp. 1249-1260, 1995.

[25] F. L. A. Machado and S. M. Rezende, "A theoretical model for the giant magnetoimpedance in ribbons of amorphous soft-ferromagnetic alloys,", *J. Appl. Phys.*, Philadelphia, PA, USA, 1996, pp. 6558-60.

[26] S. S. Yoon, S. C. Yu, G. H. Ryu, and C. G. Kim, "Effect of annealing on anisotropy field in $Fe_{84}Zr_7B_8Cu_1$ amorphous ribbons evaluated by giant magnetoimpedance," *Journal of Applied Physics,* Miami, FL, USA, 1999, pp. 5432-4.

[27] K. Mohri, K. Kawashima, T. Kohzawa, and H. Yoshida, "Magneto-inductive element," *IEEE Transactions on Magnetics,* vol. 29, pp. 1245-8, 1993.

[28] T. Yoshinga, S. Furukawa, and K. Mohri, "Magneto-impedance effect in etched thin amorphous wires," *IEEE Transactions on MagneticsDigests of INTERMAG 99. 1999 IEEE International Magnetics Conference, 18-21 May 1999,* vol. 35, pp. 3613-15, Sept. 1999.

[29] H. Chiriac, C. S. Marinescu, and T. A. Ovari, "Temperature dependence of the magneto-impedance effect," *Journal of Magnetism and Magnetic Materials,* vol. 196, pp. 162-163, 1999.

[30] A. A. Rakhmanov, N. Perov, P. Sheverdyaeva, A. Granovsky, and A. S. Antonov, "The temperature dependence of the magneto-impedance effect in the Co-based amorphous wires," *Sensors and Actuators, A: Physical,* vol. 106, pp. 240-242, 2003.

[31] L. V. Panina, K. Mohri, T. Uchiyama, M. Noda, and K. Bushida, "Giant magneto-impedance in Co-rich amorphous wires and films," *IEEE Transactions on Magnetics Workshop on Rapidly Quenched Magnetic Wire and Applications, 24-25 June 1994,* vol. 31, pp. 1249-60, 1995/03/ 1995.

[32] R. S. Beach and A. E. Berkowitz, "Sensitive field- and frequency-dependent impedance spectra of amorphous FeCoSiB wire and ribbon," *Journal of Applied Physics,* vol. 76, pp. 6209-13, 1994.

[33] F. L. A. Machado, C. S. Martins, and S. M. Rezende, "Giant magnetoimpedance in the ferromagnetic alloy Co75-xFexSi15B10," *Physical Review B (Condensed Matter),* vol. 51, pp. 3926-9, 1995.

[34] D. Atkinson and P. T. Squire, "Phenonemological model for magnetoimpedance in soft ferromagnets," *Journal of Applied Physics,* vol. 83, p. 6569, 1998.

[35] L. Brunetti, M. Coisson, P. Tiberto, and F. Vinai, "Magneto-impedance measurements in amorphous Co-based magnetic wires at high frequency," in *International Workshop on Magnetic Wires, Jun 20-22 2001*, San Sebastian, Spain, 2002, pp. 310-314.

[36] S. Iida, D. Suzuki, S. Kambe, and O. Ishii, "Enhancement in the magneto-impedance (MI) effect of multi-ribbon," *IEEE*, vol. 36, pp. 3661-3, 2000.

[37] D. P. Makhnovskiy, A. N. Lagar'kov, L. V. Panina, and K. Mohri, "Effect of antisymmetric bias field on magneto-impedance in multilayers with crossed anisotropy [for sensing application]," *Sensors and Actuators A (Physical) Second European Magnetic Sensors and Actuators Conference. EMSA 98, 13-15 July 1998,* vol. A81, pp. 106-10, 2000/04/01 2000.

[38] G. Herzer, "Grain structure and magnetism of nanocrystalline ferromagnets," *IEEE Transactions on Magnetics,* vol. 25, pp. 3327-9, 1989.

[39] X. P. Li, Z. J. Zhao, T. B. Oh, and H. L. Seet, "Effect of magnetic field on the magnetic structure of nanocrystalline electroplated NiFe layers," *Journal of Metastable and Nanocrystalline Materials,* vol. 23, pp. 167-170, 2005.

[40] K. Mohri, T. Uchiyama, L. P. Shen, C. M. Cai, and L. V. Panina, "Sensitive micro magnetic sensor family utilizing magneto-impedance (MI) and stress-impedance (SI) effects for intelligent measurements and controls," Dresden, Germany, Elsevier 2001, pp. 85-90.

[41] K. Mohri, T. Uchiyama, L. P. Shen, C. M. Cai, and L. V. Panina, "Amorphous wire and CMOS IC-based sensitive micro-magnetic sensors (MI sensor and SI sensor) for intelligent measurements and controls," *Journal of Magnetism and Magnetic Materials,* vol. 249, pp. 351-6, 2002.

[42] G. R. Liu, *Mesh free methods: moving beyond the finite element method*: CRC Press, 2003.

[43] K.-M. Lee, Q. Li, and H. Sun, "Effects of numerical formulation on magnetic field computation using meshless methods," *IEEE Transactions on Magnetics,* vol. 42, pp. 2164-2171, 2006.

[44] R. A. Gingold and J. J. Monaghan, "Smoothed particle hydrodynamics: theory and application to non-spherical stars," *Monthly Notices of the Royal Astronomical Society,* vol. 181, pp. 375-89, 1977.

[45] W. K. Liu and Y. Chen, "Wavelet and multiple scale reproducing Kernel methods," *International Journal for Numerical Methods in Fluids,* vol. 21, p. 901, 1995.

[46] W.-K. Liu, S. Li, and T. Belytschko, "Moving least-square reproducing kernel methods (I) methodology and convergence," *Computer Methods in Applied Mechanics and Engineering,* vol. 143, pp. 113-154, 1997.

[47] D. W. Kim and Y. Kim, "Point collocation methods using the fast moving least-square reproducing kernel approximation," *International Journal for Numerical Methods in Engineering,* vol. 56, pp. 1445-1464, 2003.

[48] P. Lancaster and K. Salkauskas, "Surfaces generated by moving least squares methods," *Mathematics of Computation,* vol. 37, pp. 141-58, 1981.

[49] T. Belytschko, Y. Y. Lu, and L. Gu, "Crack propagation by element free Galerkin methods," New Orleans, LA, USA, ASME 1993, pp. 191-205.

[50] B. Nayroles, G. Touzot, and P. Villon, "Generalizing the finite element method: Diffuse approximation and diffuse elements," *Computational Mechanics,* vol. 10, pp. 307-318, 1992.

[51] C. A. M. Duarte and J. T. Oden, "HP Clouds---A Meshless Method to Solve Boundary-Value Problems," University of Texas at Austin, Technical Report 95-05, 1995.

[52] I. Babuska and J. M. Melenk, "Partition of unity method," *International Journal for Numerical Methods in Engineering,* vol. 40, pp. 727-758, 1997.

[53] H. Wendland, "Meshless Galerkin methods using radial basis functions," *Mathematics of Computation,* vol. 68, pp. 1521-31, 1999.

[54] C. Franke and R. Schaback, "Convergence order estimates of meshless collocation methods using radial basis functions," *Advances in Computational Mathematics,* vol. 8, pp. 381-99, 1998.

[55] X. Liu, G. R. Liu, K. Tai, and K. Y. Lam, "Radial point interpolation collocation method (RPICM) for partial differential equations," *Computers and Mathematics with Applications,* vol. 50, pp. 1425-1442, 2005.

[56] X. Liu, G. R. Liu, K. Tai, and K. Y. Lam, "Radial point interpolation collocation method (RPICM) for the solution of nonlinear poisson problems," *Computational Mechanics,* vol. 36, pp. 298-306, 2005.

[57] N. Sukumar, B. Moran, and T. Belytschko, "The natural element method in solid mechanics," *International Journal for Numerical Methods in Engineering,* vol. 43, pp. 839-87, 1998.

[58] B. Lu, X.-R. Ge, and S.-L. Wang, "Study on the numerical integration scheme with natural element method," *Yanshilixue Yu Gongcheng Xuebao/Chinese Journal of Rock Mechanics and Engineering,* vol. 24, pp. 1917-1924, 2005.

[59] G. R. Liu, B. B. T. Kee, and C. Lu, "A stabilized least-squares radial point collocation method (LS-RPCM) for adaptive analysis," *Computer Methods in Applied Mechanics and Engineering,* vol. 195, pp. 4843-61, 2006.

[60] Q. Li and K.-M. Lee, "An adaptive meshless method for magnetic field computation," *IEEE Transactions on Magnetics,* vol. 42, pp. 1996-2003, 2006.

[61] L. U. Banas, "Numerical methods for the Landau-Lifshitz-Gilbert equation," Rousse, Bulgaria, Springer Verlag, Heidelberg, D-69121, Germany, 2005, pp. 158-165.

[62] K. Eason and K. M. Lee, "Effects of Nonlinear Micromagnetic Coupling on the Weak-field Magneto-Impedance Sensors," *IEEE Transactions on Magnetics,* 2008 (to appear).

[63] K. Eason and K. M. Lee, "A Numerical Investigation of Neel Wall Effects in Amorphous MI Ribbons," *IEEE Transactions on Magnetics,* 2008 (to appear).

[64] F. P. Incropera and D. P. DeWitt, *Fundamentals of Heat and Mass Transfer*: John Wiley & Sons, Inc. 1996.

[65] J. D. Jackson, *Classical Electrodynamics*, John Wiley & Sons, Inc. 1999.

[66] B. Hillebrands and K. Ounadjela, *Spin Dynamics in Confined Magnetic Structures II (Topics in Applied Physics-87)*, Springer Berlin , Heidelberg, 2003.

[67] A. Hubert and R. Schafer, *Magnetic Domains:The Analysis of Magnetic Microstructures*, Springer-Verlag, Berlin, Heidelberg, New York 1998.

[68] K. Mohri, F. B. Humphrey, K. Kawashima, K. Kimura, and M. Mizutani, "Large Barkhausen and Matteucci effects in FeCoSiB, FeCrSiB, and FeNiSiB amorphous wires," *IEEE Transactions on Magnetics,* vol. 26, pp. 1789-1791, 1990.

[69] J. Yamasaki, F. B. Humphrey, K. Mohri, H. Kawamura, H. Takamure, and R. Malmhall, "Large Barkhausen discontinuities in Co-based amorphous wires with negative magnetostriction," *Journal of Applied Physics*, vol. 63, pp. 3949-51, 1988.

[70] A. D. Santos, L. G. C. Melo, C. S. Martins, F. P. Missell, Y. Souche, F. L. A. Machado, and S. M. Rezende, "Domains and giant magneto-impedance in amorphous ribbons by magneto-optical Kerr effect," *Journal of Applied Physics,* vol. 79, p. 6546, 1996.

[71] G. T. Rado and J. R. Weertman, "Spin-wave resonance in a ferromagnetic metal," *Journal of the Physics and Chemistry of Solids,* vol. 11, pp. 315-333, 1959.

[72] F. L. A. Machado and S. M. Rezende, "A theoretical model for the giant magnetoimpedance in ribbons of amorphous soft-ferromagnetic alloys," *Journal of Applied Physics* , vol. 79, pp. 6558-60, 1996.

[73] S. S. Yoon, S. C. Yu, G. H. Ryu, and C. G. Kim, "Effect of annealing on anisotropy field in Fe84Zr7B8Cu1 amorphous ribbons evaluated by giant magnetoimpedance," *Journal of Applied Physics Proceedings of the 43rd Annual Conference on Magnetism and Magnetic Materials, Nov 9-Nov 12 1998,* vol. 85, pp. 5432-5434, 1999.

[74] X. P. Li, Z. J. Zhao, S. Ang, S. J. Koh, T. B. Oh, J. Y. Lee, and W. X. Chen, "Effect of pH Values on the Magnetic Properties of Electroplated NiFe Layers," *Trans Tech Publications Ltd* in *Proceedings of the 2nd International Conference on Advanced Materials Processing, Dec 2-4 2002*, Singapore, Singapore, 2003, pp. 57-60.

[75] S. S. Yoon, C. G. Kim, H. C. Kim, K. J. Jang, and K. S. Ryu, "Analysis of giant magneto-impedance in terms of anisotropy field in annealed amorphous $Co_{66}Fe_4NiB_{14}Si_{15}$ ribbons," *Journal of Magnetism and Magnetic Materials Proceedings of the 1998 International Conference on Magnetism of Nanostructured Phases (MNP), Sep 4-Sep 6 1998,* vol. 203, pp. 301-303, 1999.

[76] W. F. Brown, *Micromagnetics*: Wiley & Sons, Inc., 1963.

[77] R. S. Turtelli and F. L. A. Machado, "Frequency-domain thermo-magnet memory effect in the $Co_{75-x}Fe_xSi_{15}B_{10}$ alloys," *IEEE Transactions on Magnetics*, Washington, DC, USA, 1989, pp. 3350-1.

[78] G. Bordin, G. Buttino, A. Cecchetti, and M. Poppi, "Temperature dependence of magnetic properties of a Co-based alloy in amorphous and nanostructured phase," *Journal of Magnetism and Magnetic Materials,* vol. 195, pp. 583-7, 1999.

[79] H. Chiriac, C. S. Marinescu, and T.-A. Ovari, "Temperature dependence of the magneto-impedance effect in Co-rich amorphous glass-covered wires," *Journal of Magnetism and Magnetic Materials,* vol. 215, pp. 539-541, 2000.

[80] F. L. A. Machado, B. L. da Silva, S. M. Rezende, and C. S. Martins, "Giant ac magnetoresistance in the soft ferromagnet Co70.4Fe4.6Si15B10," Minneapolis, MN, USA, 1994, pp. 6563-5.

[81] A. Prohl, *Computational Micromagnetism*: Teubner, 2001.

[82] R. L. Burden and J. D. Faires, *Numerical Analysis*: PWS Publishing Company, 1993.

[83] K. J. Beers, *Numerical Methods for Chemical Engineering:Applications in MATLAB*: Cambridge University Press, 2007.

[84] A. Carpinteri, G. Ferro, and G. Ventura, "The partition of unity quadrature in meshless methods," *International Journal for Numerical Methods in Engineering,* vol. 54, pp. 987-1006, 2002.

[85] C. A. Duarte and J. T. Oden, "H-p clouds - an h-p meshless method," *Numerical Methods for Partial Differential Equations,* vol. 12, pp. 673-705, 1996.

[86] C. Dong, S. Chen, T. Y. Hsu, and X. Zuyao, "A simple model of giant magneto-impedance effect in amorphous thin films," *Journal of Magnetism and Magnetic Materials,* vol. 250, pp. 288-94, Sept. 2002.